Università degli Studi di Ferrara

DOCTORAL COURSE IN "PHYSICS"

CYCLE XXXVI

COORDINATOR Prof. Luppi Eleonora

Study of the collectivity of intruder states in ^{83}Se and development of a new technique to measure lifetimes in the N=126 region

Scientific/Disciplinary Sector (SDS) FIS/04

Candidate

Pellumaj Julgen

Supervisors

Dr. Bettoni Diego

Dr. Valiente Dobón Jose Javier

Dr. Gottardo Andrea

Year 2020/2023

Mamit, babit, Gretes, Klodit
dhe veçanërisht nana Qokes.

Abstract

Along the N=49 isotones, intruder states with spins $1/2^+$ and $5/2^+$, originating from the promotion of one neutron in the $s_{1/2}$ and $d_{5/2}$ orbitals above the N=50 shell gap, were first observed in ^{83}Se and, later on, in other nuclei: ^{87}Kr, ^{81}Ge and ^{79}Zn. In the ^{83}Se, these intruder states have energies of around 500 keV, the lowest among the other N=49 isotones. The reduction of the N=50 shell gap towards ^{78}Ni favors the lowering in the energy of the deformed configurations and since ^{83}Se nucleus (Z=34) is in the middle of the proton fp-shell (28<Z<40), it should have the maximum quadrupole correlations driving the nucleus into deformed configurations. This makes the ^{83}Se nucleus a good candidate to understand the collectivity of the particle-hole intruder states in this region of the nuclear chart, lowered in energy by large quadrupole correlations. Large-scale shell-model calculations predict a quenching of the energy of the intruder states and even an island of inversion in ^{83}Se, at variance with the experimental data. Lifetime measurements of the intruder states of ^{83}Se would give an indication of their wave function, thus allowing one to estimate the degree of the N=50 core breaking in the ground state of Se isotopes. Moreover, such measurements could shed light on the behavior of the N=50 shell gap towards ^{78}Ni, a double-magic nucleus where intruder configurations competing in energy with the spherical ones have also been found.

This work, which represents the first part of the thesis, reports the results obtained from a recent experiment performed at the Laboratori Nazionali di Legnaro (LNL), where the lifetime of the 540-keV $1/2^+$ and 1100-keV $3/2^+$ intruder states of ^{83}Se were measured using the Recoil Distance Doppler-Shift Method and Doppler-Shift Attenuation Method, respectively. A beam of ^{82}Se, with an intensity of 0.02 pnA and with energy of 270 MeV provided by the TANDEM-XTU accelerator, impinged into a deuterated polyethylene (C_2D_4) target which was evaporated on a 6 mg/cm^2 thick gold layer. The GALILEO γ-ray array was coupled to the SPIDER silicon array, allowing one to obtain the needed channel selectivity through coincidence measurements between γ rays and the protons from the (d,p) reaction. The experimental results will be discussed in the framework of shell-model calculations and mean-field approaches, pointing out the role of the collectivity of low-lying intruder configurations.

***

The second part of the thesis is focused on describing a novel technique developed to measure the lifetimes of heavy neutron-rich nuclei, namely 'the reversed plunger configuration'. In heavy neutron-rich nuclei, information on the lifetimes of low-lying excited states is scarce since these nuclei are difficult to populate. Among different reaction mechanisms, multi-nucleon transfer reactions have shown to be the perfect tool to explore such regions. Therefore, profiting from the kinematics of such reactions and the plunger device in the reversed configuration, lifetimes of excited nuclear states of the order of picoseconds can be measured.

This technique was employed for the first time to measure lifetimes of low-lying excited states of nuclei with a mass of around 190, where shape transitions from prolate to oblate are expected to occur along different isotopic chains while approaching the N=126 shell closure. The experiment took place at Laboratori Nazionali di Legnaro with the aim to measure the lifetime of the 2^+ and 4^+ state of ^{196}Os. A beam of ^{136}Xe with the energy of 1134 MeV passed through a degrader foil of ^{93}Nb with a thickness of 3.2 mg/cm^2 and impinged into a ^{198}Pt target 1.4 mg/cm^2 thick. Beam-like fragments entered the PRISMA spectrometer where they were identified in mass, atomic number, and velocity, while the target-like fragments (the heavy nuclei of interest) traveled towards the degrader foil where they were stopped. Gamma rays were measured with the AGATA γ-ray tracking array composed of 33 segmented HPGe detectors. Among the nuclei populated in this experiment is ^{198}Pt, for which the lifetimes of the low-lying excited states are known, and can be used as a benchmark to validate the use of the proposed technique.

This work reports the lifetimes measured with the reversed plunger configuration for the 2_1^+, 2_2^+ and the 4^+ states of ^{198}Pt, employing the standard analysis procedures: the Decay Curve Method and the Differential Decay Curve Method. The agreement of our results with the literature data demonstrates the capability of this technique to further investigate the nuclear structure of heavy neutron-rich nuclei.

Contents

List of Tables

List of Figures

Abbrevations

ADC	**A**nalog to **D**igital **C**onverter
APCAD	**A**nalysis **P**rogram for the **C**ontinous-**A**ngle **D**SAM
AGATA	**A**dvanced **GA**mma ray **T**racking **A**rray
ALPI	**A**cceleratore **L**ineare **P**er **I**oni
ATC	**A**GATA **T**riple **C**luster
DCM	**D**ecay **C**urve **M**ethod
DCMD	**D**ifferential **D**ecay **C**urve **M**ethod
DSAM	**D**oppler **S**hift **A**ttenuation **M**ethod
DWBA	**D**istorted **W**ave **B**orn **A**pproximation
ECR	**E**lectron **C**yclotron **R**esonance
FPGA	**F**ield **P**rogrammable **G**ate **A**rray
FWHM	**F**ull **W**idth at **H**alf **M**aximum
GGP	**G**lobal **G**igabit **P**rocessor
GSC	**G**ALILEO **S**ingle **C**rystal
GTS	**G**lobal **T**rigger and **S**yncronization
GTC	**G**ALILEO **T**riple **C**luster
HFB	**H**artree **F**ock **B**ogoliubov
HPGe	**H**igh **P**urity **G**ermanium
IC	**I**onization **C**hamber
LNL	**L**aboratori **N**azionionali di **L**egnaro
MCP	**M**ulti **C**hannel **P**late
MNT	**M**ulti **N**ucleon **T**ransfer
MWPPAC	**M**ulti **W**ire **P**arallel **P**late **A**valanche **C**ounter
OFT	**O**rsay **F**orward **T**racking
PGCM	**P**rojected **G**enerator **C**oordinate **M**ethod
QWR	**Q**uarter **W**ave **R**esonator
RFQ	**R**adio **F**requency **Q**uadrupole
RDDS	**R**ecoil **D**istance **D**oppler **S**hift
SEM	**S**canning **E**lectron **M**icroscope
TAC	**T**ime to **A**mplitude **C**onverter
ToF	**T**ime **o**f **F**light

Chapter 1

Introduction

The nucleus is a system composed of interacting nucleons: Z protons and N neutrons. Its existence was first suggested by Rutherford and confirmed by the experiments of Geiger and Marsden in 1911. Since then, the nucleus has been studied extensively, pushing further our understanding of the fundamental interactions and revealing many of its properties. Even though a lot of progress has been achieved since its discovery, many questions still need to be addressed.

There are hundreds of stable nuclei which exist in nature and radioactive ones can be produced in the laboratory via nuclear reactions. The development in the detection techniques and the availability of several accelerated ion beams allowed the production of around 3,000 nuclei in the laboratory. Up to 6,000 nuclei are predicted to exist by different models. The known nuclei can be organized in what is called "the Segre chart", shown in Fig. 1.1, a two-dimensional matrix where the x-axis is the neutron number and the y-axis is the proton number. The black squares in the nuclear chart represent the stable nuclei, forming the valley of stability, while the colors indicate different decay modes of the unstable nuclei.

Gamma-ray spectroscopy is one of the most powerful tools for investigating nuclear structure properties because the de-excitation of the excited energy levels proceeds mainly via γ decay. Different observables can be measured by γ-ray spectroscopy, like energy, parity, angular momentum, and angular distributions. One of the observables is also the lifetime of the nuclear-excited states, which is inversely proportional to the transition probability. Measuring the lifetimes experimentally allows one to compare these values with the results obtained from the calculations based on nuclear models, advancing our knowledge of nuclear structure.

Experimental evidences pointed to the existence of nuclear shells similar to the atomic ones where electrons orbit around the nucleus. The shell gaps that appeared at some particular proton and neutron numbers were called "magic numbers" and the nuclei with

a magic number of protons and neutrons were called doubly magic. Basic models were developed to describe the properties of nuclear matter and to predict new ones. The magic numbers could be first described by the "shell model" proposed by Maria Geoppert Meyer and Otto Haxel in 1949, providing a further understanding of the structure of the nucleus. The exploration of nuclei towards the drip lines has revealed new nuclear phenomena: the magic numbers can disappear and new ones appear, deformed configurations lower their energy and sometimes even become the ground state of a nucleus. These are some of the nuclear phenomena that triggered research on understanding the properties of the nucleon-nucleon interaction that drives the nucleus towards these structural changes.

One of the regions of the nuclear chart that is nowadays attracting great interest is the region in the vicinity of ^{78}Ni where deformed configurations can become very low in energy and compete with spherical ones. The magicity of the ^{78}Ni was not proven until 2019. Several studies showed the possibility that the N=50 shell gap vanishes but others confirmed its stability. The evolution of the N=50 shell gap towards ^{78}Ni is under study but the data in the region are still scarce. This shell gap is particularly important because of its role in the r-process nucleosynthesis, with ^{78}Ni being a possible waiting point. Moreover, the influence of three-body forces and the role of the monopole interaction on its evolution could be tested. This would help in a better understanding of the nuclear structure of these very neutron-rich nuclei.

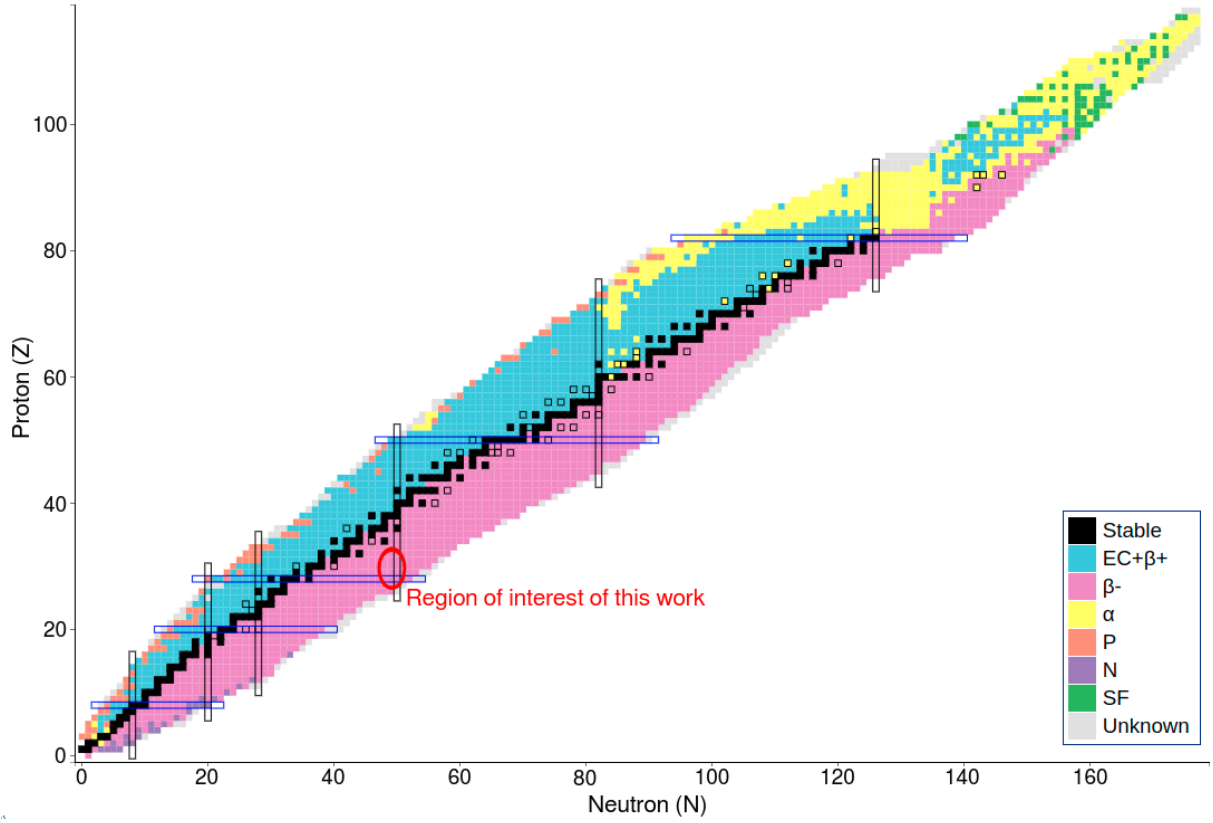

Figure 1.1: The nuclear chart where the x-axis is the neutron number and the y-axis is the proton number. The decay modes are indicated with the corresponding colors.

This work attempts to shed some light on the stability of the N=50 shell gap and its evolution towards ^{78}Ni by investigating the intruder states in ^{83}Se (N=49). Intruder states with spin $1/2^+$ and $5/2^+$, emerging from the excitation of one neutron from the $1g_{9/2}$ shell towards the $2s_{1/2}$ and $2d_{5/2}$ shells, appear not only in ^{83}Se but all along the N=49 isotones, ^{79}Zn, ^{81}Ge, ^{85}Kr. These intruder states were known since early 70s and were studied by several methods. In ^{83}Se, the excitation energy of these states reaches the minimum along the N=49 isotones, at around 500 keV. The energy of the intruder configurations results from a delicate balance between the monopole properties of the N=50 shell gap and the quadrupole correlations, which are at a maximum in ^{83}Se since it is at the middle of the proton shell (Z=28-40). These states still need to be characterized in terms of quadrupole collectivity. Thus, in this work, the lifetimes of several intruder states of ^{83}Se have been measured using the Doppler Shift Attenuation method and the Recoil Distance Doppler Shift technique. A (d,p) reaction was used to populate the excited states of the nucleus of interest. The setup employed to reach the goals of this work was composed of the GALILEO γ-ray array in phase II configuration coupled to the SPIDER silicon array and a plunger device for lifetime measurements. Comparison of the results of this work with theoretical calculations provided by the shell model and mean-field approaches will help to understand the role of the quadrupole correlations in the reduction of the N=50 shell gap towards ^{78}Ni and the emergence of the quadrupole deformation in this region.

This first part of the thesis is focused on the study of the intruder states of ^{83}Se and is divided into six chapters. The outline is as follows:

Chapter 2 - Introduction to shell evolution and shape coexistence and the factors that drive the nucleus towards these structural changes. The main observables that probe the appearance of such phenomena and the available experimental data, especially focused on the region near ^{78}Ni, are reported. The motivation for this work is described in detail.
Chapter 3 - This chapter conveys the experimental setup and techniques used in this work. The basic principles of the experimental techniques used for lifetime measurements of nuclear-excited states, Recoil Distance Doppler Shift and Doppler Shift Attenuation Method, are introduced.
Chapter 4 - The presorting of the data for each apparatus of the experimental setup, GALILEO and SPIDER, is described in detail.
Chapter 5 - The analysis performed to extract the lifetimes of the intruder states of ^{83}Se from the experimental data is described, and the results are reported.
Chapter 6 - The nuclear models used to interpret the results are briefly introduced, and a comparison of the experimental results with theoretical calculations is shown.
Chapter 7 - Summary of the results and conclusions.

***

The heavy region with mass of around 190 exhibits signatures of prolate-oblate shape transitions, γ-softness, and triaxiality. Prolate-to-oblate shape transitions are predicted to occur for the W, Os, and Pt while moving along the isotopic chains from the less towards the more neutron-rich elements, approaching the N=126 shell closure. Moreover, the isotopic chains of Er, Yb, Hf, W, Os, and Pt, with a mass of ∼190, constitute a playground for the nuclear models aiming to describe collectivity and deformation.

Experimental data vanish on this region as approaching the N=126 shell closure. Figure 1.2 shows the nuclei in the region at A≈190 for which spectroscopic information is known. With the green color are shown the even-even isotopes where spectroscopic information for the low-lying energy states is available, and with the blue are marked the isotopes for which lifetimes of low-lying nuclear-excited states are known.

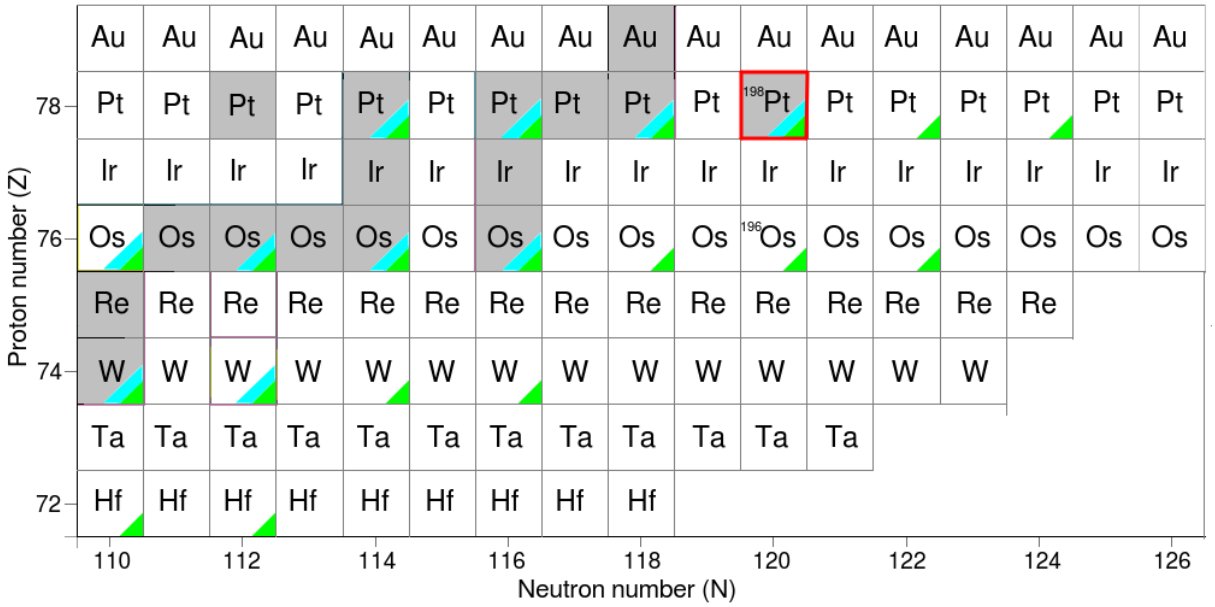

Figure 1.2: The region with A≈190 of the nuclear chart. The stable nuclei are marked with gray color, and the isotopes for which there is available information on the lifetime of the excited states are marked with blue color. The isotopes for which there is information on the excitation energy of the low-lying states are marked with the green color. The ^{198}Pt nucleus, the nucleus of interest in this work is marked in red.

The nuclei in this region cannot be populated with fusion-evaporation reactions and are too heavy to be populated via fission. Deep inelastic reactions have been successfully used to populate the high-spin states of these nuclei, but this reaction mechanism does not allow a clear identification of the reaction channels. Excited states of nuclei in this region can be studied using multi-nucleon transfer reactions or isomeric-decay spectroscopy. In the past, fast-timing measurements were performed for several nuclei in this region, populating the states of interest using fragmentation reactions. With this technique, lifetimes up to hundreds of picoseconds can be measured, while shorter lifetimes require Doppler-based techniques.

Multi-Nucleon Transfer (MNT) reactions have been extensively used to populate excited states of neutron-rich nuclei. For nuclei with Z<50 populated via MNT reactions, the lifetimes of nuclear-excited states were measured using the differential plunger device coupled to large magnetic spectrometers and γ-ray arrays. Such setup and reaction mechanism could not be employed to study heavier ions with Z>54, because of the limitations of the identification capabilities of the magnetic spectrometer. A new plunger configuration is proposed in this work to overcome these limits, the so-called "reversed plunger configuration". This configuration of the plunger device was tested for the first time at Laboratori Nazionali di Legnaro. The known lifetimes of the ^{198}Pt could be used as a benchmark to validate the technique. Getting profit from the kinematics of the MNT reactions and the geometrical arrangement of the setup, the experiment with the reversed plunger configuration proved that it is possible to separate the shifted and the unshifted component of a γ-ray transition, which decays from a state with the lifetime in the range of picoseconds. technique.

This second part of the thesis, which describes the measurement of the low-lying excited states of ^{198}Pt employing the reversed plunger configuration, is divided into five chapters. The outline is given as follows:

Chapter 8 - Introduction to the previously used techniques to measure lifetimes of nuclear-excited states employing large magnetic spectrometers and the motivation for the development of a new technique.
Chapter 9 - Optimization of the geometry of the experimental setup based in Geant4 Monte Carlo simulations and GRAZING calculations. A description of the experiment carried out at the LNL laboratories and the experimental setup.
Chapter 10 - The pre-processing of the data of AGATA data is presented: calibrations, time alignment, cross-talk, and neutron damage correction. The detectors of the PRISMA spectrometer have been calibrated, gates and thresholds optimized, and ions are identified in atomic number, charge state, and mass.
Chapter 11 - Analysis of the data from the reversed plunger using the Decay Curve Method and the Differential Decay Curve Method. The lifetimes of the 2_1^+, 2_2^+ and 4^+ are measured and compared with the reported values from previous works.
Chapter 12 - Summary of the work, conclusions, and future perspectives.

Part I

Study of intruder states towards ^{78}Ni via lifetime measurements in ^{83}Se following ^{82}Se(d,p)^{83}Se

Chapter 2

Theoretical background

This chapter introduces concepts relevant to the work presented in this thesis and raises unsettled questions concerning the nuclear structure in the region of interest, emphasizing the help that this experimental study and our results could provide. Section 2.1 introduces the shell evolution and the effect of the monopole force on its appearance. The appearance of shape coexistence in nuclei is discussed in Section 2.2 based on experimental evidences along the nuclear chart and theoretical calculations, focusing primarily on the region in the vicinity of ^{78}Ni. Section 2.3 reports on the previous studies of the ^{83}Se nucleus and the importance of characterizing its intruder states in terms of collectivity by performing lifetime measurement.

2.1 Shell model and shell evolution

Some basic properties of the nucleus and the nuclear force could be pictured based on simple empirical facts and several attempts were made to describe them analytically [1,2]. The possibility of the existence of nuclear shells similar to the ones of the atom was proved when the shell model was able to reproduce some elementary properties of the nuclear medium, but later on, it was found that this picture was a rough approximation. To describe nuclei far from stability, the system must be treated by considering other properties of the interaction like three-body forces, the tensor component, etc., revealing the complexity of the nuclear force. Experimental studies proved that the properties of nuclei can change drastically just by adding or removing one or a few nucleons from the system.

2.1.1 Shell model

The nucleus is a system made of interacting nucleons: N neutrons and Z protons. To find out that the nucleus has an internal structure, it took a very long time. At the beginning of the 20th century, attempts were made to describe the nucleus analytically. Nuclear models

were constructed, aiming to explain and reproduce the properties of nuclear matter using different approaches. The liquid drop model of the nucleus was proposed in 1935 [3] and could describe several of its properties, like the nuclear binding energies or the trend of the proton and neutron separation energy. This model does not consider the internal structure of the nucleus but tries to describe its properties on a macroscopic scale, considering the nucleus as a liquid drop.

Several experimental evidences pointed out the existence of nuclear shells similar to those of the atomic structure:

- The proton and neutron separation energy increases smoothly along an isotopic or isotonic chain except for several sharp drops at some particular nucleon numbers. Figure 2.1 (Left panel) shows the difference between the experimental two-neutron separation energy and the predicted value from the mass formula of the liquid drop model for several nuclei. The general trend is well reproduced, but not the deviation at the neutron number N=8, 20, 28, 50, 82, and 126. This behavior of the two-neutron separation energy is similar to that of atomic shells of noble gases. The ionization energy, as a function of the proton number, drops at a particular Z due to transitions from one fully occupied shell to another.

- The neutron-capture cross-section of isotopic chains for various nuclei shows some deviation from the trend, appearing precisely at the same neutron numbers as those mentioned previously [1].

- The nuclear charge radius also shows the same behavior. To emphasize the shell effects, as shown in Fig. 2.1 (Right panel), the experimental nuclear radii as a function of the neutron number divided by the predicted value from liquid drop model, $R=r_0A^{1/3}$ [4].

- The excitation energy of the first excited 2^+ state for even-even nuclei increases drastically for the nuclei close to a particular neutron and atomic number. Such behavior can be seen in Fig. 2.2.

The sudden discontinuity of several observables at the same proton and neutron number, the so-called magic numbers (Z or N = 2, 8, 20, 28, 50, 82, 126), had to be related to the internal structure of the nucleus itself. The liquid drop model could not describe the sharp drops of the experimental neutron and proton separation energies appearing at nuclei with magic numbers of protons or neutrons. A microscopic description of the nucleus had to be considered.

Since many experimental evidences pointed out the possibility of the existence of nuclear shells, a theory similar to that of the atoms was developed for describing the structure of the nucleus, even though the two systems are drastically different. In the case

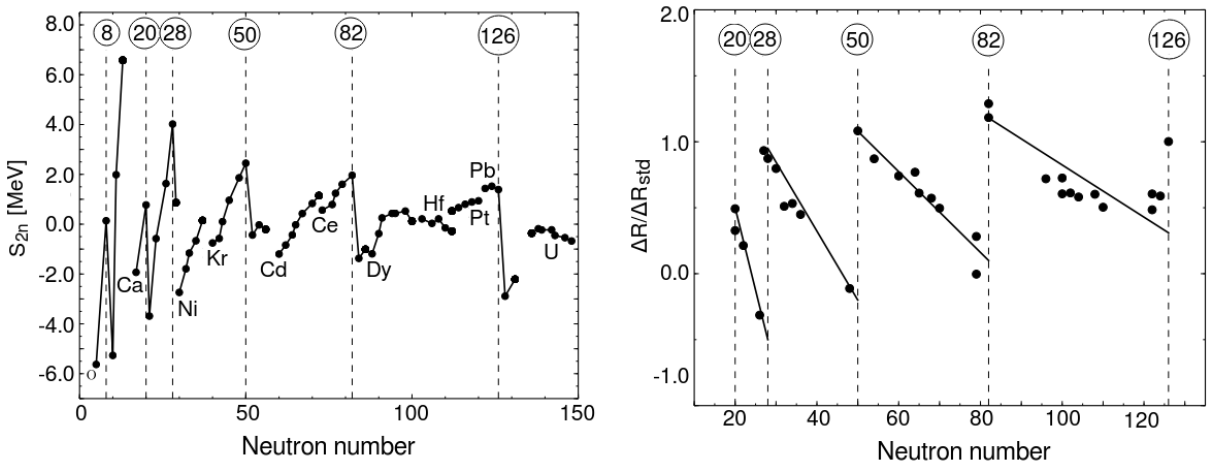

Figure 2.1: (Left) The difference between the experimental two neutron separation energy and the prediction of the empirical mass formula as a function of the neutron number. The sudden changes in the trend of this observable indicate the magic numbers. (Right) The difference between the experimental data for the nuclear charge radii and the prediction of the liquid drop model as a function of the neutron number. The sudden changes in the trend of this observable indicate the magic numbers as marked in the figure. Figures adapted from [5].

of the atomic model, the potential is supplied by the positive charge of the nuclues and the Schrödinger equation can be solved for such potential (Coulomb potential), providing the energies of the subshells where the electrons move. In the case of the nucleus, no external agent is producing a field where the nucleons move.

The idea of the existence of nuclear shells was first put forward by Maria Goeppert Mayer [7] and Hans Jensen [8]. In 1949, they developed the shell model with nucleons distributed in shells with different energy levels. As in atomic physics, the shells are labeled with the quantum numbers (n, l, m, j). To study this system, the Schrödinger equation has to be solved:

$$\hat{H}\psi(r_1, r2, ..., r_A) = (\hat{T} + \hat{V})\psi = E\psi(r_1, r2, ..., r_A) \tag{2.1}$$

where $\hat{H}$ is the Hamiltonian describing the system, $\hat{T}$ is the kinetic energy operator, $\hat{V}$ the nuclear potential, ψ is the wave function which characterizes the nuclear state and E its energy.

In the case of the nuclear shell model, the nucleons are assumed to be in the presence of a potential (nuclear potential) created from the nucleon-nucleon interaction itself. Attempts were made to solve the Schrödinger equation (Eq. 2.1) using an infinite well and an harmonic oscillator potential but in both cases, the magic numbers were not reproduced. For an infinite well potential it is evident that an infinite energy is required to separate a proton or neutron from the system which experimentally is not valid. Moreover, the potential should have a smooth edge when approaching zero beyond the mean radius but

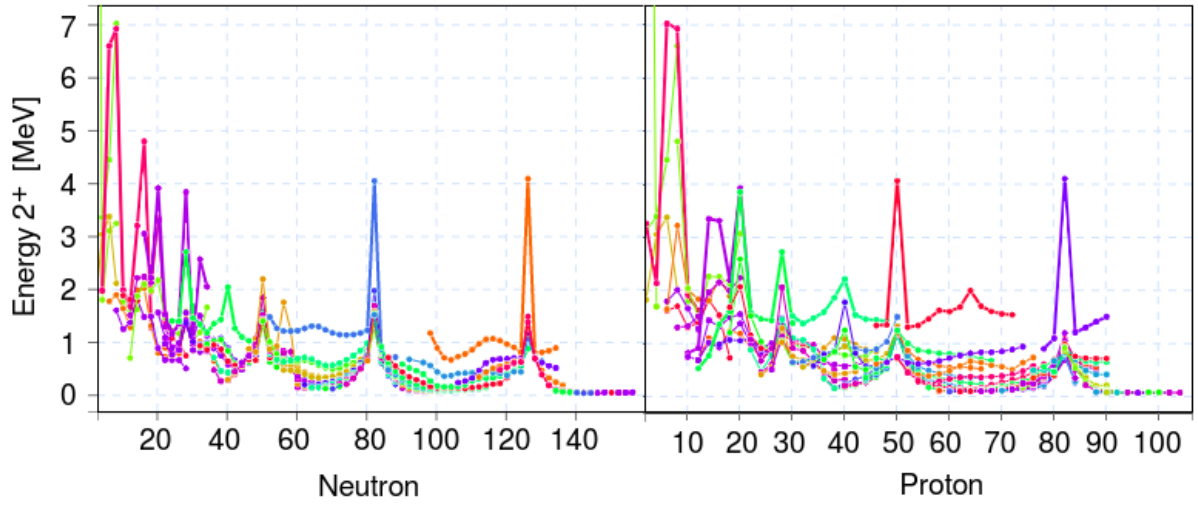

Figure 2.2: The evolution in the energy of the first 2^+ state along different isotopic (Left) and isotonic (Right) chains. The peaks correspond to the proton and neutron magic numbers. The data for the two plots are taken from [6].

none of the previously mentioned potentials fulfill this property. A more realistic potential that meets the mentioned conditions is the Wood-Sakson potential which is given by the expression:

$$V_{ws}(r) = \frac{-V_0}{1 + exp[(r - R)/a]} \tag{2.2}$$

where V_0 is the well depth adjusted approximately at 50 MeV to give the proper separation energies, a is the skin thickness defined as the distance in which the potential changes from $0.9V_0$ to $0.1V_0$ and is approximately 0.5 fm, R is the mean radius given by the expression: $R=1.25A^{1/3}$. However, even by using a more realistic potential it was possible to reproduce the magic numbers 2, 8, and 20 but not the higher ones like 28, 50, 82, and 116.

Many unsuccessful attempts were made to find the needed correction by adding a term on the potential in order to break the degeneracy of the levels and to be able to reproduce the magic numbers. This was achieved in 1949 by Mayer and Haxel [7], who showed that the inclusion of a phenomenologic spin-orbit potential breaks the degeneracy of the levels and reproduces the magic numbers. The Hamiltonian of the system is given by the equation:

$$H = -\frac{\hbar^2}{2m}\nabla^2 + V_{ws} + V_{so} + V_c \tag{2.3}$$

where V_c is the Coulomb potential due to the repulsive interaction of the protons in the nucleus, V_{ws} the Wood-Saxon potential, and the V_{so} the spin-orbit term. By solving the Schrödinger equation using the Hamiltonian given at Eq. 2.3, the degeneracy of the energy levels breaks, and the shell model reproduces the magic numbers [1]. This is shown

schematically in Fig. 2.3.

The nucleons interact not only through mutual two-body forces but also through three-body forces as well. Solving this many-body problem is challenging from the mathematical point of view due to the nature of the nuclear force. Thus, nuclear models are constructed to allow more straightforward mathematically solvable problems able to reproduce the known properties of the nuclear medium and to predict new ones. Over the years, the shell model has proved to be able to describe successfully several properties of nuclei like: magic numbers, excitation energies, transition probabilities, and the spins and parities of nuclear-excited states.

2.1.2 Collective behavior of the nucleus

The shell model describes the formation of nuclear shells and nuclear shell gaps by considering the motion of a nucleon in a spherical potential. The model considers the nucleus a perfectly spherical body without any deformation, and its properties depend only on the movement of the valence nucleons. This approach is successful in reproducing the structure of the nuclei near shell closures. The contribution of only the valence nucleons in defining the wave function of the nuclear state is a very strong assumption when one deals with the development of collective behavior for nuclei at the mid-shell. Shell-model calculations can correctly reproduce these structures if a large enough valence space is provided in order to allow for coherent contribution from many nucleons in the wave function of the nuclear state.

The appearance of collective properties originate from the collective motion of all the nucleons in the nucleus, and they all constructively contribute to the nuclear state and the nuclear wave function. The display of such properties in nuclei is well known: for example, it is how the low-lying energy of the 2_1^+ state for nuclei at the mid-proton and neutron shell is explained. The collective properties of the nucleus are portrayed by considering a vibration of the nuclear shape about a spherical equilibrium shape or by the rotation of the nucleus around the symmetry axis. Considering the rotational and vibrational modes, it is possible to reproduce the low-lying excited energy levels of the nuclei at the mid-shell.

A nucleus with a non-zero quadrupole moment (nucleon density distribution is not spherically symmetric) can have excited energy levels because of its rotation perpendicularly to the axis of symmetry. These states have energies:

$$E = \frac{J(J+1)\hbar}{2I} \tag{2.4}$$

where J is the total angular momentum and I is the moment of inertia of the nucleus with respect to the rotating axis. The energy levels in the rotational band are proportional to the $J(J+1)$.

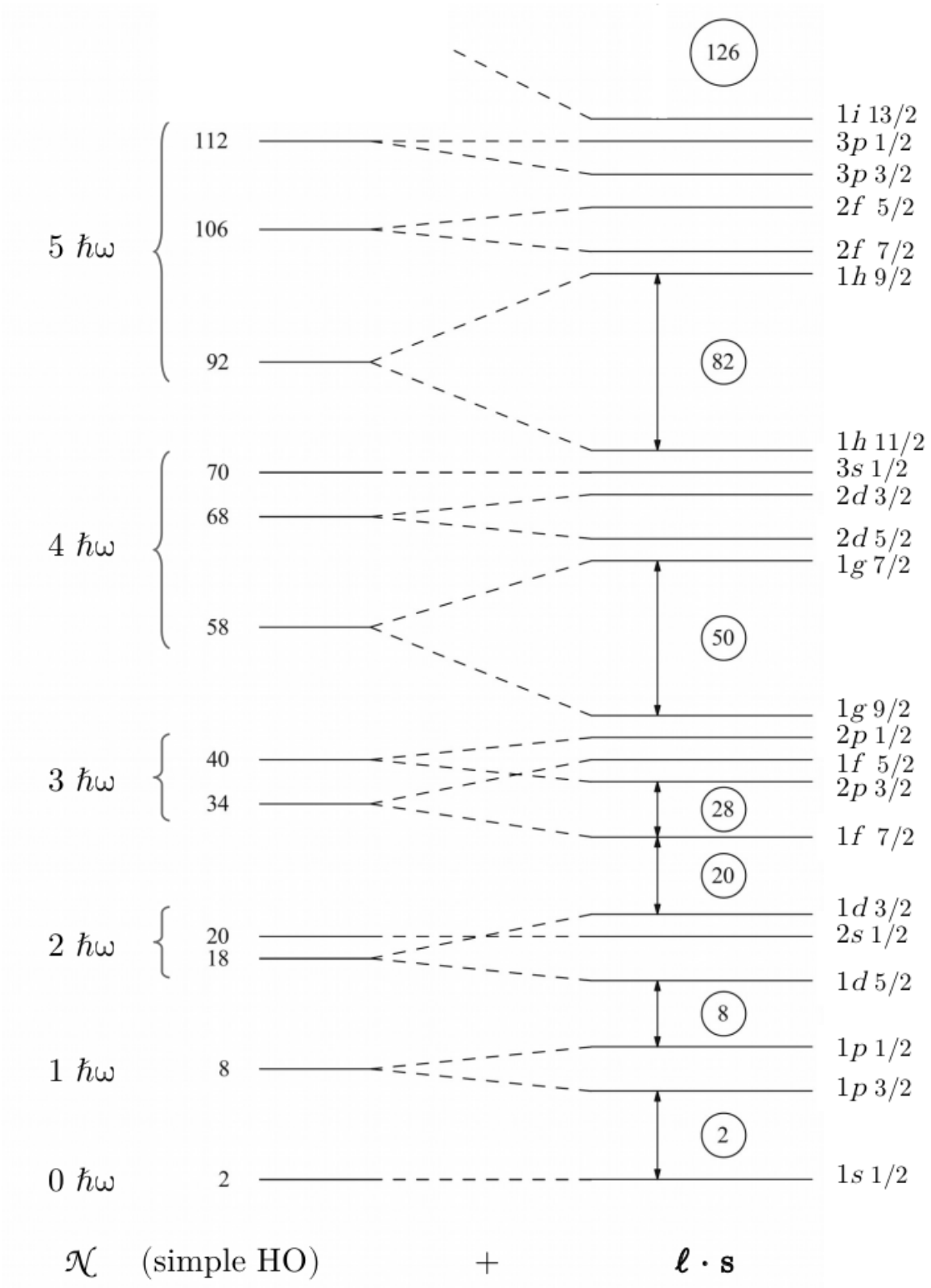

Figure 2.3: Shell-model level structure when a harmonic oscillator is chosen as potential and the breaking of the degeneracy when a phenomenological spin-orbit term is included in the potential. Figure taken from Ref. [5].

When the deformation of a nucleus oscillates around its mean value, is called vibrational mode. There are different modes of vibration and in most cases, the quadrupole vibration is the lowest and the most relevant one. The small oscillations about the equilibrium shape, interpreted as shape oscillations, give rise to a simple harmonic motion which results on spreading equidistantly from each other the excitation energy levels.

Besides the macroscopic description of the deformed and collective behavior of the nucleus, a microscopic description was formalized by Nilsson in the 60s [9]. This formalism is based on the idea of a potential that is not spherical but deformed. For the deformed nuclei, the shell model potential should approximate the actual nuclear shape, a rotational ellipsoid. The deformation parameter β_2 determines the degree of the deformation.

$$\beta_2 = \frac{4}{3}\sqrt{\frac{\pi}{5}}\frac{\Delta R}{r} \tag{2.5}$$

where ΔR is the difference between the semi-major and semi-minor axes, and r is the radius of the spherical shape determined by the same volume as the one of the ellipsoid. When $\beta_2 = 0$, the shape is spherical while the nuclear shapes with $\beta_2 < 0$ and $\beta_2 > 0$ are known as oblate and prolate shapes, respectively. The nuclear shapes are discussed in more detail in Section 2.2.1.

In the case of a deformed potential, the energy levels of the single-particle states depend on the projection of the total angular momentum along the symmetry axis. The potential that each nucleon experiences depends on the orientation of the orbit where the nucleon is placed, at variance with the case of the spherical potential where there is no preferred direction in space. The magnitude and the direction of the shift of the single-particle energy compared to the spherical potential depend on the orientation of the angular momentum vector with respect to the deformed core. Some orbits will significantly overlap with the core, resulting in a strong interaction. Thus, these orbits will lower their energy compared to the case of a spherical potential since the particle is more tightly bound. The opposite is true for the particles occupying states that overlap less with the core and consequently have a weaker interaction. Since these particles will be less bound, the energy of the orbit will increase. The increase or decrease of the energy of the orbital will depend on the deformation parameter β_2 of the potential.

The Nilsson model is one of the most successful models able to account for most of the features observed in hundreds of deformed nuclei [2].

2.1.3 Shell evolution

The shell model reproduced the magic numbers for nuclei in the valley of stability and such numbers were believed to remain the same along the nuclear chart. Later on, with the developments of new beams and detection techniques, it was possible to produce in the laboratory nuclei far from the valley of stability. The new isotopes showed phenomena

that were not expected, such as the disappearance of the known magic numbers and the appearance of new ones, proving that the nuclear properties evolve with the proton and the neutron numbers.

Evidences of such behavior were found in ^{12}Be [10], where the measured spectroscopic factors showed that N=8 is not a good shell closure for this nucleus. The only two bounded states of ^{12}Be seem to be significantly influenced by contribution of the $1d_{5/2}$ and $2s_{1/2}$ orbits above the N=8 shell closure.

A breakdown of the N=20 shell closure was first reported from β decay studies, which revealed a 2^+ state very low in energy while approaching N=20 in the Mg isotopes [11]. This was confirmed later from the large deformation of the first 2^+ state suggested by the low excitation energy and the large B(E2) value [12], pointing to a vanishing of the N=20 shell gap. Also, a reduction of the N=28 shell gap was suggested by a very low excitation energy of the first 2^+ state in ^{32}Si, which is supposed to be a semi-magic nucleus [13].

The first evidence indicating the appearance of a new magic number far from the line of stability was found in ^{24}O. The very high excitation energy of the first 2^+ state in this nucleus and the small B(E2) value, implying a small β_2 parameter (0.15±0.04), suggested a N=16 spherical sub-shell closure in ^{24}O [14]. This experimental result agreed with the prediction from shell model calculations [15]. In other mass regions, γ-ray spectroscopy and mass measurements in the exotic Ca isotopes revealed the appearance of a new subshell closure at N=32 and N=34 [16, 17].

What are the factors that drive the nucleus towards these structural changes? This question has triggered a lot of theoretical and experimental work, aiming to pin down the factors included in the process. One of the open questions in nuclear structure remains the evolution of the shell gaps from the line of stability toward the drip lines. The shell gaps not only become larger or smaller as a function of the proton and neutron number, giving rise to the disappearance of the known magic numbers and the appearance of new ones, but also the ordering of the orbitals may even exchange. Several cases are known for displaying the latter behavior, for example, the ^{32}Mg nucleus which has a deformed ground state. The nuclei where the deformed configurations become the ground state of the system instead of spherical configurations constitute "the island of inversion" [18].

2.1.4 Shell evolution driven by the monopole force

Monopole, quadrupole, and pairing are the three main contributions to the nuclear Hamiltonian [19]. The pairing and quadrupole interactions are the most important short and long-range correlations. The quadrupole interaction, which dominates for near mid-shell nuclei, is responsible for inducing deformations and is essential in describing rotational spectra [20]. The pairing part corresponds to proton-proton and neutron-neutron interactions coupled to angular momentum J=0. It allows for an explanation of the energy gap

of about 1 MeV, which occurs between the J^{π} =0^{+} ground state and a set of relatively degenerate states ($J^{\pi} = 2^{+}$,4^{+},6^{+} ....), in the spectra of even-even nuclei that are just a few nucleons above or below closed-shell systems. The monopole part of the nucleon-nucleon interaction generates the shell evolution [19].

As anticipated, the atomic nuclei show shell structure expressed in terms of single-particle orbits of protons and neutrons similar to the electrons in the atom. From a shell-model point of view, the nucleus can be seen as a closed core and valence nucleons. The orbits outside of the inert core can be specified by a set of single-particle energies and adding or removing nucleons from the valence orbits may change the single-particle energies due to the interaction between the valence nucleons. These changes in the shell structure are called shell evolution.

The matrix element of the monopole component of a two-body interaction is given by the expression:

$$\nu_m(j,j') = \frac{\sum_{\mu\mu'}\langle j,\mu,j',\mu'|\hat{\nu}|j,\mu,j',\mu'\rangle}{\sum_{\mu\mu'}1} \tag{2.6}$$

where j and j' is the notation for a pair of orbits standing for the (n, l, j) quantum numbers characterizing the orbit, and μ and μ' is the magnetic substrate for each of the orbits, respectively. The denominator in the expression of the monopole interaction stands for all the possible orientations of the two-particle states, $\mu \oplus \mu'$. After considering all the possible orientations of the two magnetic substates for the j and j', one gets:

$$\nu_m(j,j') = \frac{\sum_J (2J+1)\langle j,j',J|\hat{\nu}|j,j',J\rangle}{\sum_J (2J+1)} \tag{2.7}$$

where J is the coupling of the angular momentum of the two orbits: $\vec{J} = \vec{j} + \vec{j'}$. The degeneracy of the two-particle states is (2J+1). If only the proton-neutron part of the monopole interaction is being considered, there are no values of J that are forbidden, and there is no need for the antisymmetrization. Finally, the monopole component $\hat{\nu}$ can be derived from the matrix element. The monopole interaction between a proton in the orbit j and a neutron in the orbit j', or vice versa is given by:

$$\hat{\nu} = \sum_{j,j'} \nu_m(j,j')\hat{n}_j\hat{n}_{j'} \tag{2.8}$$

where $\hat{n}_j$ and $\hat{n}_{j'}$ are the operators that account for the occupancy of the orbits j and j'.

As mentioned previously, the effect of the monopole interaction is on the single-particle energies. The energy of the orbit j changes due to the occupancy of the orbit j'.

$$\Delta\epsilon_j = \nu_m(j,j')n_{j'} \tag{2.9}$$

From the relation 2.9, it is clear that the single-particle energy of the orbit j changes depending on the occupation of the orbit j'. The more particles are added in the j' orbit, the stronger the monopole interaction between j and j' becomes. If the nuclear force is an attractive central force, then the monopole effect given by Eq. 2.9 is always attractive. This means that if more neutrons are added in the j' shell, the protons in the orbit j become more and more bound, but the proton shell is conserved [21]. One of the components of the nuclear force, which seems to significantly impact the shell evolution and the appearance and disappearance of the magic numbers, is the tensor force [22]. The tensor force is a non central component of the nucleon-nucleon interaction, responsible, for example, of the non zero quadrupole momentum of deuterium. The effects of the monopole part of the tensor force in the shell evolution are divided into two cases: The type I shell evolution and the type II shell evolution.

2.1.4.1 Type I shell evolution

The proton orbits with total angular momentum $j_> = (l + 1/2)$ and $j_< = (l - 1/2)$, and the neutron orbits with $j'_>$ are represented schematically in Fig. 2.4.a. For the tensor force, the interaction between the $j_<$ and the $j'_>$ orbit is attractive, while the interaction between the $j_>$ and the $j'_>$ orbit is repulsive. Due to the attractive force, the energy of the $j_<$ orbit gets lower. On the other hand, due to the repulsive force, the energy of the $j_>$ orbit gets higher. This is represented schematically in Fig. 2.4.b. By adding more neutrons in the $j'_>$ orbit, the single particle energies get more affected because the monopole effect is linear with the number of nucleons. So the spin orbiting splitting between the $j_>$ and $j_<$ proton orbits becomes larger and larger by adding more neutrons in the $j'_>$, as illustrated in Fig. 2.4.c. If enough neutrons are added in the j' orbit, the ordering of the $j_<$ and $j_>$ orbit can change. This effect of the tensor force differs from the effects discussed previously in Section 2.1.4. The shell evolution brought by the tensor force may lead to the disappearance of the known magic numbers and the appearance of new ones. In the former case, the attractive force only brought closer the orbits, creating a more bound system (See Section 2.1.4). The strength of the tensor force also depends on the radial functions of the j and j' orbit. A larger magnitude of interaction is expected for the same orbits ($j = j'$). The structural changes caused by the change in the number of nucleons in the system are defined as 'type I shell evolution' [22].

2.1.4.2 Type II shell evolution

As discussed in Section 2.1.4.1, shell evolution may appear along an isotopic chain by adding or removing particles from one orbital. Type II shell evolution can appear within the same nucleus without changing the number of particles which are present in the system. The promotion of particles from one shell to another leads to the appearance of

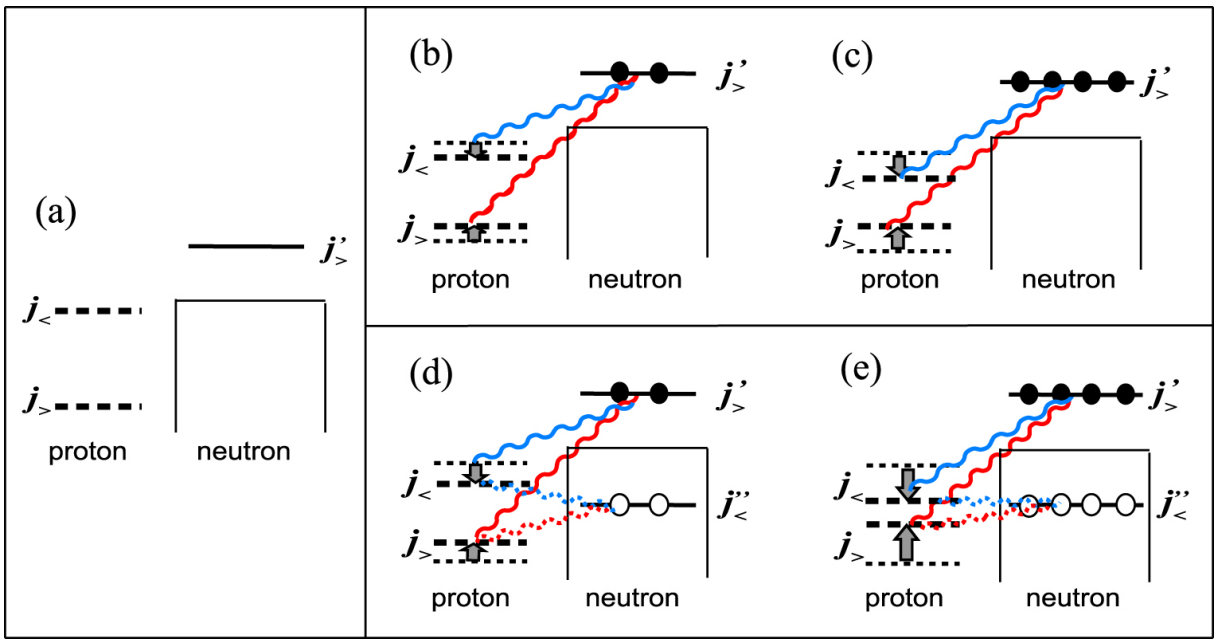

Figure 2.4: Illustration of type I (b and c) and type II (d and e) shell evolution driven by the monopole component of the tensor force. Figure taken from [23].

attractive and repulsive interaction due to the tensor force. The situation is illustrated in Fig. 2.4.d. The promotion of two neutrons from the $j''_<$ orbit to the $j'_>$ one, will affect the proton orbit splitting as discussed previously. Moreover, the two vacancies in the $j''_<$ orbit will induce another effect: the neutron holes will lower the energy of the $j_<$ orbit and bring higher the energy of the $j_>$ orbit. This means that, the proton spin–orbit splitting between the $j_>$ and $j_<$ orbits is reduced even more compared to the type I shell evolution. Promoting more neutrons from the $j''_<$ orbit to the $j'_>$ orbit would impact further the spin-orbit splitting as represented in Fig. 2.4.e.

These properties of the tensor force have been verified with spectroscopic data, like, for example, in the ^{68}Ni nucleus [24]. In this nucleus, a second 0^+ state is found a few hundred keVs below the first 2^+_1 excited state, and a third 0^+ state is located just above the 2^+_1 level. The first 0^+ state corresponds to fully occupied $\pi f_{7/2}$ and fully occupied pf shell for the neutrons. The second 2^+ state is due to the breaking of the Z=28 shell gap by one proton and a breaking of the N=40 shell gap by two neutrons. Instead, the third 0^+ excited state results from the excitation of three protons across the Z=28 gap and more than four neutrons across the N=40 gap. The type II shell evolution could explain such large deformation for this state. The promotion of four neutrons to the $1g_{9/2}$ shell as well as the neutron vacancies in the pf shell affect the spin-orbit splitting between the $1f_{7/2}$ and $1f_{5/2}$ proton orbitals. Similar behavior was also found in other nickel isotopes, $^{62-66}$Ni [25]. The appearance of the deformed 0^+ state at low energies could be explained by the tensor force.

2.1.5 Observables probing shell evolution

Several observables are used as possible signatures of shell closure evolution when following isotopic or isotonic chains.

Masses and separation energies

The mass of an atomic nucleus is a direct and essential property of the system that one can measure. The most precise mass spectroscopy is achieved through frequency measurements. The revolution frequency of ions in magnetic fields is measured to determine the mass over charge ratio in Penning traps [26] or storage rings [27].

The separation energies are the simplest observables to probe shell evolution. The two-nucleon separation energy in even-even nuclei can be easily calculated from the total binding energy. The two-proton separation energy is given by the expression:

$$S_{2p}(Z,N) = E(Z-2,N) - E(Z,N) \tag{2.10}$$

where $E(Z,N)$ is the total binding energy of the nucleus Z, N. The two-neutron separation energy is given by the formula:

$$S_{2n}(Z,N) = E(Z,N-2) - E(Z,N) \tag{2.11}$$

A change in the two-nucleon separation energy along isotopic or isotonic chains directly indicates a sudden increase in the ground-state binding energy of a given nucleus that often originates from a shell closure. The neutron separation energy is typically related to the ground-state properties.

Excitation energies

High excitation energies of the first excited states in nuclei are typically related to the appearance of a shell closure. A clear example is given by the excitation energy of the 2_1^+ state along the isotopic and isotonic chain for several even-even nuclei in Fig. 2.2, or as it will be shown later for the Ni isotopic chain in Fig. 2.6 (Left panel). Excited states of nuclei decay predominantly by emission of γ-rays. Excitation energies are measured with great precision using γ-ray spectroscopy.

Reduced transition probabilities

The collective degrees of freedom of a nucleus can be studied via the reduced transition probabilities. The reduced electromagnetic transition matrix element B(σL) can be derived from cross sections measured in Coulomb excitation experiments or by lifetime measurements of nuclear-excited states. Reduced transition probabilities provide information on the wave function of the nuclear-excited states.

Magnetic dipole and electric quadrupole moments

The magnetic dipole moment give information on the evolution of the single-particle states of nucleons when experimental values are compared with the ones obtained from theoretical calculations. The effective one-body operator of the nuclear magnetic moment is given by:

$$\mu = \sum_i \mu_i = \sum_i g_l^i l_i + g_s^i s_i \tag{2.12}$$

where g_l is the orbital gyromagnetic factor g_l^π=1 for protons and g_l^ν=0 for neutrons and g_s the spin gyromagnetic factors. The magnetic moments remain very sensitive to the orbitals occupied by the valence nucleons.

The deviation from the sphericity of a nucleus with non-zero spin can be quantified through its electric quadrupole moment. The electric quadrupole moment can be derived from the measured spectroscopic quadrupole moment or calculated from estimated B(E2) values. A relation of the electric quadrupole moment with the deformation parameter β_2 will be introduced in Section 6.3.

Direct reactions

Direct reactions can probe the nuclear wave function and are the tool of choice for the spectroscopy of the single-particle states, being able to investigate the shell evolution. In these reactions, one or only a few nucleons are transferred between the projectile and the target nucleus, avoiding the formation of an intermediate compound system. Measured cross-sections are compared with theoretical calculations involving the 'Distorted Wave Born Approximation (DWBA)' [28] or higher-order formalisms dependent on the entrance and exit channel optical model potentials, providing an insight to the shell structure.

2.1.6 The stability of N=50 shell gap

The magic number 50 originates from the spin-orbit part of the nuclear interaction, which lowers the energy of the $1g_{9/2}$ orbit from the N=4 major shell so that it is located close to the orbits from the N=3 major shell (See Fig. 2.3). The size of the N=50 shell gap is evolving with the proton number (from Z=28 to Z=50) depending on proton-neutron interactions between the proton fp and neutron $g_{9/2}$ shells and the neutron orbits around the N=50 shell gap, i.e. $\nu g_{9/2}$ below and $\nu d_{5/2}$, $\nu g_{7/2}$, $\nu s_{1/2}$ and $\nu d_{3/2}$ above.

So far, a considerable amount of experimental data has been accumulated concerning the structural changes of nuclei in the vicinity of N=8 [29], N=20 [30], and N=28 [31] and theoretical calculations are able to reproduce reasonably well such properties. On the contrary, at N=50, the available data in the region is scarce due to the experimental difficulties in populating these nuclei.

The evolution of the N=50 shell gap along the proton number is one of the key points of the present nuclear structure studies far from stability, as it will be discussed in Section 2.1.7. The stability of the N=50 shell closure remains an open question, and different studies draw different conclusions about what concerns this topic. Studies in the even-even nuclei along N=50 show that one-particle one-hole (1p-1h) configurations with spin 5^+, 6^+ and 7^+ emerge from the excitation of one neutron from the $1g_{9/2}$ to the $2d_{5/2}$ shell. The energy evolution of these states along N=50 mirrors the evolution of the shell gap. Measurements of these states were performed up to ^{82}Ge (Z=32). A comparison of their energy with the one of ^{84}Se (Z=34) and ^{86}Kr (Z=36) leads to the conclusion that the shell gap is reducing towards ^{78}Ni [32,33].

Another spectroscopic study of excited states in ^{83,84,85}Ga showed a possible reduction of the N=50 shell gap towards the ^{78}Ni and beyond. Moreover, in this study the authors predict the disappearance of the N=50 shell gap and the appearance of a new one at N=58 from the splitting of the $3s_{1/2}$ and $2d_{5/2}$ orbitals [34].

A study on ^{81}Ga found a stable, not reduced, N=50 shell gap. The excited states of this nucleus are coherent with the data of heavier odd-proton nuclei along the N=50 isotonic chain up to the stability. The first excited states along the N=50 odd isotones down to Z=31 could be described by assuming a double Z=28 and N=50 shell closure [35]. Another study was performed along the N=50 isotones including ^{83}As, ^{82}Ge and ^{81}Ga [36]. The experimental spectra of these nuclei were reproduced from shell model calculations, seen as evidence for an adequate description of the residual nucleon-nucleon interaction and the single-particle energies (shell gap), thus confirming the stability of the N=50 shell gap in the vicinity of ^{78}Ni [36].

Reduced transition probabilities were measured along the $^{74-80}$Zn isotopes, just two protons above ^{78}Ni, using low-energy Coulomb excitation. No evidences could support a possible breaking of the N=50 shell gap by comparing the experimental data with theoretical shell-model calculations [37].

As introduced previously, mass measurements are one of the primary probes to test the evolution of shell closures [38]. The experimental two-neutron separation energies (S_{2n}) across N=50 indicated the reduction of the shell gap, i.e., the difference of S_{2n} values between the N=50 and N=52 isotones, from Z=40 down to Z=34 [39]. Experimental evidences prove that the gap has a minimum at Z=32 and then increases again at Z=30 [40,41] as shown in Fig. 2.5.

Large-scale shell-model calculations performed for nuclei in the vicinity of ^{78}Ni involving the π(fp)-ν(fpgd) model space allowed to study simultaneous excitations across the Z=28 and N=50 shell gaps [43]. The calculations point to a minimum of the mass gap in Z=32 consistent with the experimental data [40,41]. Its increase toward Z=28 indicates a robustness of the N=50 gap in ^{78}Ni. From the theoretical calculations, the evolution of the N=50 shell gap shows similarities with the oxygen and the calcium isotopic chain [43],

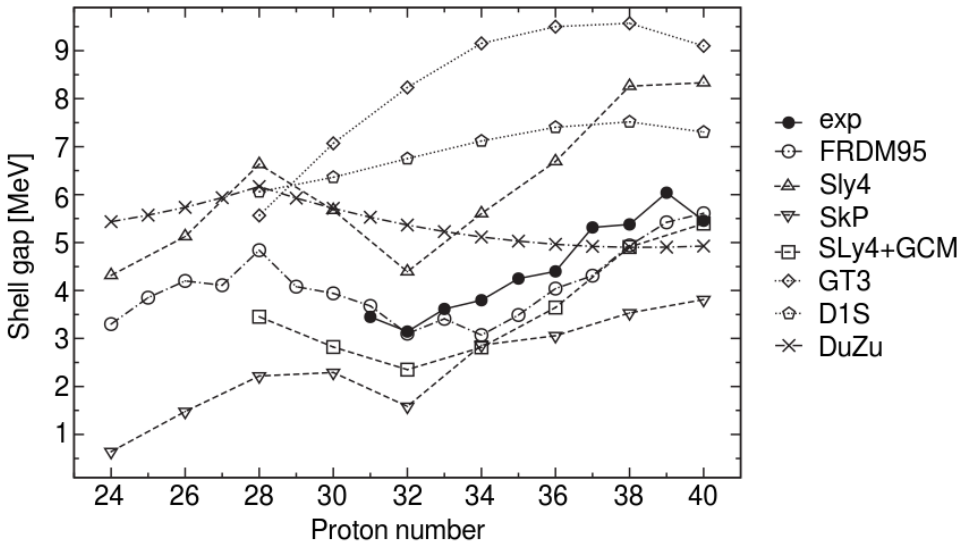

Figure 2.5: The evolution of the N=50 shell gap based on experimental data from mass measurements and compared with predictions from different theoretical models. Figure adapted from [42].

but requires a renormalization of the interaction monopoles.

2.1.7 The importance of the evolution of the N=50 shell gap

The N=50 shell gap evolution is of key importance for many aspects [44]:

- an understanding of the nuclear structure in this region and especially of the doubly-magic ^{78}Ni, whose spectroscopy is still unknown

- very neutron-rich nuclei play an essential role in r-process nucleosynthesis, and ^{78}Ni is one of its possible waiting points [41]

- the evolution of the N=50 shell gap may be a result of the repulsive three-body forces as in the case of O and Ca isotopes. Constraining its size is of paramount importance for future developments and tests of state-of-the-art effective interactions with the inclusion of many-body forces, as well as for validation of empirical universal monopole interactions

- the knowledge of single-particle energies in shell-model valence space which takes ^{78}Ni as a closed core

- ^{78}Ni, with the largest N/Z ratio in a doubly magic nucleus, represents a unique possibility of exploring the properties of very neutron-rich nuclei

2.1.8 Magicity of ^{78}Ni

Magic nuclei have always been the scope of nuclear structure studies, especially those with both proton and neutron magic numbers. There are only a few double magic nuclei, and ^{78}Ni (28 protons and 50 neutrons) is the most neutron-reach double magic nucleus in the nuclear chart known at present. Predictions on the position of the neutron drip-line also confirm that this nucleus is the most neutron-rich double-magic nucleus ever existing. Spectroscopic information of ^{78}Ni is still scarce even though significant experimental and theoretical work has been done recently in this region. ^{78}Ni is a nucleus far from the valley of stability and hard to populate: it is one of the goals of the state-of-the-art radioactive ion beams facilities like Radioactive Isotope Beam Factory (RIBF) in Japan [45], the Facility for Antiproton and Ion Research (FAIR) in Germany [46], the Facility for Rare Isotope Beams (FRIB) [47].

Previous studies questioned the double magic nature of ^{78}Ni [32–34]. The double magic character of this nucleus was confirmed in 2019 when it was populated using radioactive ion beams in the RIBF facility [48]. The observed γ ray with energy of 2.6 MeV was tentatively assigned as the $2_1^+ \rightarrow 0^+$ transition. Figure 2.6 (Left panel) shows the evolution of the energy of the 2_1^+ state along the Ni isotopic chain, where two sharp deviations from the systematics are seen: at N=40, indicating the appearance of the N=40 subshell closure, which is well-known from previous studies, and also a sharp increase at N=50, confirming the doubly magic character of ^{78}Ni.

Besides the first 2^+ state, coincidence measurements allowed the construction of the ^{78}Ni level scheme based on a tentative assignment of spin and parity to the states. A low-lying state with energy 2.91 MeV was assigned to a spin-parity 2_2^+ and a γ ray with energy 580 keV was assigned to the $4^+ \rightarrow 2_1^+$ transition, as shown in the proposed level scheme in Fig. 2.6. The appearance of the low-lying 2_2^+ just a few hundreds keV above the 2_1^+ state needs to be verified in future measurements, as also pointed out by the authors. Shell-model calculations predict the appearance of a well-deformed 2^+ excited state below spherical 2^+ level.

2.2 Shape coexistence

2.2.1 Nuclear shapes

Differently from the atomic systems, which appear in spherical shapes due to the $1/r$ term of the Coulomb potential, the spatial arrangement of the nucleons in a nucleus can be different from spherical [2]. The most crucial contribution to deviations from spherical shapes comes from the quadrupole correlations, the lowest order in the decomposition in multipoles of the nuclear shape, but there might also be octupole and hexadecapole shapes. Octupole and higher orders of deformation are however out of the scope of this

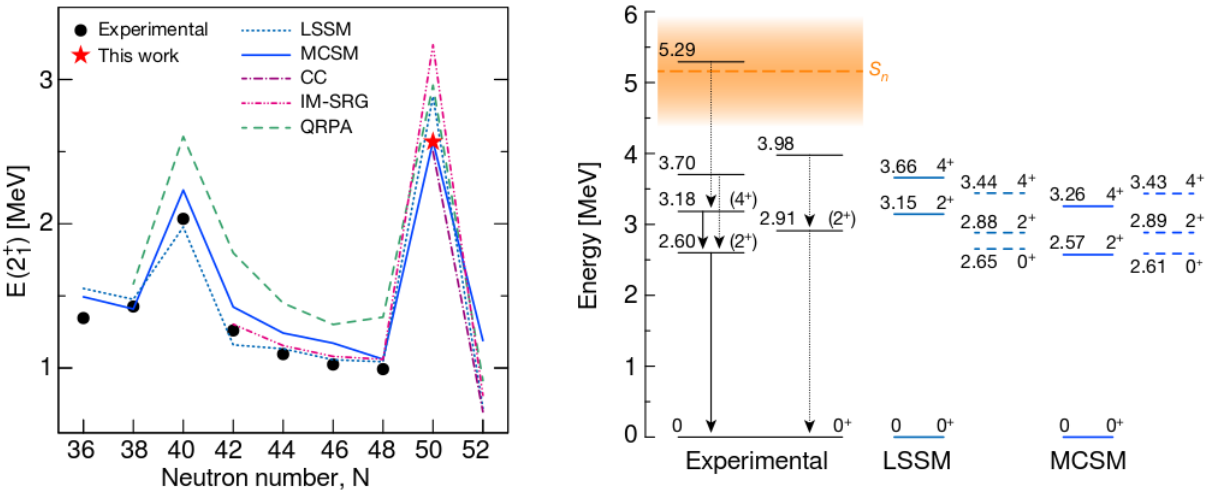

Figure 2.6: (Left) Evolution of the energy of the first 2^+ excited state measured experimentally along the Ni isotopic chain and compared to shell model calculations. The two sharp increases correspond to the N=40 subshell closure and the N=50 shell closure, proving the double-magic nature of ^{78}Ni. (Right) The proposed level scheme for ^{78}Ni and a comparison with shell-model calculations. Figures adapted from [48].

work: the attention is focused on the nuclei that exhibit quadrupole deformation.

Assuming the nucleus can be modeled as a liquid drop, the nuclear surface can be described as a series of spherical harmonics. Considering the quadrupole deformation as the main contributor to the change of the shape from spherical to deformed, the radius of a nucleus can be written as the expression:

$$R = R_0 \left[1 + \sum_{\mu} \alpha_\mu Y_{2\mu}(\theta, \phi) \right] \tag{2.13}$$

where R_0 is the radius of the spherical nucleus of the same volume, $Y_{2\mu}$ are spherical harmonics of order 2, and the α_μ are expansion coefficients describing the deformation of the nuclear shape.

Equation 2.13 describes the nuclear shape with arbitrary orientation in space. It is more convenient the description which can be achieved by applying a transformation into the principal axis frame, using the Wigner rotation matrices [42], $D^J_{\nu\mu}(\alpha\beta\gamma)$:

$$a_{2\mu} = \sum_{\nu} D^2_{\nu\mu}(\alpha\beta\gamma)\alpha_{2\nu} \tag{2.14}$$

where (α, β, γ) are the Euler angles chosen in such a way that $a_{2\pm1} = 0$. The most common deformation parameters are a_{20} and a_{22} defined as:

$$a_{20} = \beta_2 cos\gamma, \qquad a_{22} = \frac{1}{\sqrt{2}}\beta_2 sin\gamma \tag{2.15}$$

The radii along the k principal-axis directions are:

$$R_k = R_0 + \sqrt{\frac{5}{4\pi}} R_0 \beta_2 cos\left(\gamma - \frac{2\pi k}{3}\right) \tag{2.16}$$

By writing α_μ in terms of three Euler angles and two intrinsic variables, $\alpha_0 = \beta cos\gamma$ and $\alpha_2 = \beta sin\gamma$, the nuclear shape can be specified in terms of the parameters of β and γ. The variable β stands for the extent of quadrupole deformation, while γ represents the degree of axial asymmetry. The parameter γ ranges from 0° (axially symmetric) to 60°, with maximum axial asymmetry at 30°. Prolate nuclei have $\beta > 0$, the nucleus is extended in one direction and squeezed in two, and oblate nuclei have $\beta < 0$, the nucleus shape is extended in two directions and compressed in one. Figure 2.7 visualizes the oblate and the prolate shapes.

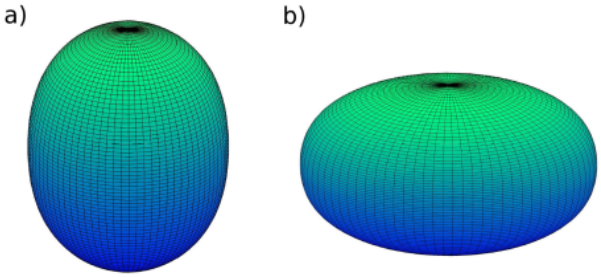

Figure 2.7: Prolate and oblate shapes calculated with β_2=0.35 for γ=0° and γ=60°. Figure adapted from [42].

Two of the most important quantities to describe a quadrupole-deformed nucleus are the moment of inertia and the quadrupole moment. These quantities can be written in terms of the deformation β. Considering the moment of inertia for a rigid body rotor:

$$I = \frac{2}{5} M r^2 \tag{2.17}$$

and if one integrates over the radius of the nuclear surface for an ellipsoidal shape gets the expression for the moment of inertia of an ellipsoidal shape:

$$I = \frac{2}{5} A M R_0^2 (1 + 0.31\beta) \tag{2.18}$$

where $R_0 \sim A^{1/3}$. From Eq. 2.18, one derives that the moment of inertia is a linear function of the deformation parameter β.

The quadrupole moment of the nucleus with an ellipsoidal shape is given by Eq. 2.19.

$$Q_0 = \frac{3}{\sqrt{5\pi}} Z R_0^2 \beta (1 + 0.16\beta) \tag{2.19}$$

2.2.2 Shape coexistence

Shape coexistence is an ubiquitous feature of the nucleus that has been studied both theoretically and experimentally. It is a concept that was introduced in nuclear physics in the 70s, with the discovery of a 0_2^+ state in ^{16}O, the energy of which could not be explained and understood at that time. For even-even nuclei, it is accepted that the ground state is a 0^+ state because the valence protons and neutrons couple to total angular momentum J=0. The energy of the second 0_2^+ state could not be reproduced from shell-model calculations without including a deformation $\beta \approx 0.2$ for this state. The manifestation of such property is unique for finite many-body systems. Over the years, a lot of effort was spent to understand the mechanisms that drive the nucleus towards the coexistence of different shapes and to find evidence of its appearance in nuclei. Shape coexistence manifests itself in the nuclear landscape because of the interplay between two opposing tendencies: the stabilizing effect of closed shells, which causes the nucleus to retain a spherical shape, and the residual quadrupole interaction between protons and neutrons, which drives the nucleus into deformed configurations at low excitation energies [49].

Hints that probe the shape coexistence

Several experimental hints that one can be used to probe the shape coexistence:

- A first indication can be obtained from the energy levels of a nucleus itself. The observation of a low-lying 0_2^+ state in an even-even nucleus is interpreted as a hint of the appearance of shape coexistence.

- Deformed particle-hole configurations across a shell gap appear due to the strong quadrupole correlations. These particle-hole excitations are called intruder states or just intruders. These configurations may become favored in energy over the spherical configurations and, in some cases, become the ground states, giving rise to what is called 'the island of inversion'. Known islands of inversion appear around N=8, 20, and 28 nuclei.

- Rotational bands are a typical sign of deformation. The energy difference of the rotational energy levels can provide information on the moment of inertia and of the enhanced deformation of the nucleus.

- Another observable one can measure to probe shape coexistence is the root mean square $< l^2 >$ of the charge distribution of different states.

- Electromagnetic transition rates of low-lying states may also reveal information on the deformation of the nuclei.

- Measurements of E0 transition strengths would provide additional data to draw conclusions about the structure of a nuclear state. E0 transitions, which are only allowed for $0^+ \rightarrow 0^+$ transitions, are sensitive to the changes in the nuclear charge-squared radii.

- Besides γ-ray spectroscopy, reactions like (d,p) can be used to deduce the wave function of single-particle states. The spectroscopic factors are a quasi-observable which allows one to deduce the single-particle strength distribution.

Experimental evidences of shape coexistence

Experimental evidences were found in several regions of the nuclear chart. The regions of the nuclear chart where shape coexistence has been found are shown in Fig. 2.8. In the N=50 region, in the vicinity of ^{78}Ni, there is a lack of proofs from the experimental point of view.

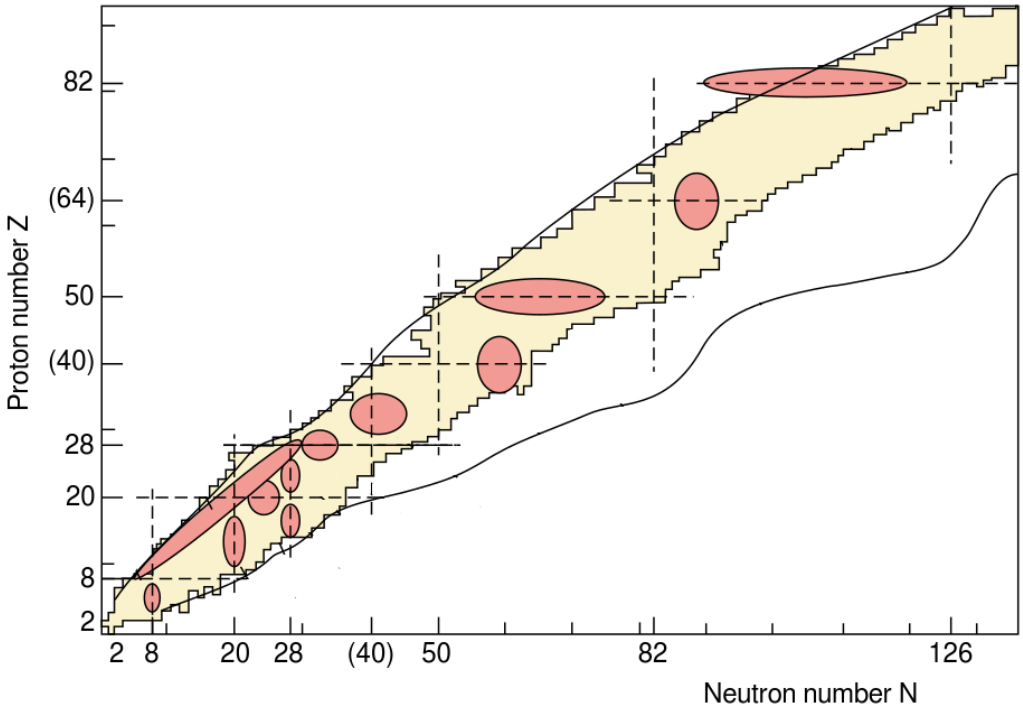

Figure 2.8: The regions of the nuclear chart where the appearance of shape coexistence has been observed. Figure adopted from [49].

The first indications of shape coexistence in the Z∼82 region were found in the mercury isotopes where significant isotope shifts were observed [50]. Further investigation revealed 0_2^+ states and rotational bands built on top of them [51]. This region has been explored quite a lot in recent years, even though the population of the isotopes was not easy. The behavior seen in the Hg isotopes raised the question about the survival of the Z=82 shell gap in the region, which resulted in an extensive study of the Pb isotopes.

Also in the Pb isotopes measurements performed with γ-ray and α-decay spectroscopy revealed the presence of coexisting structures [52].

In the Z$\sim$50 region, the first evidences of shape coexistence were found in the Sn isotopes employing γ-ray spectroscopy methods [53]. Intruder states appear at very low excitation energies, not only in Sn but also in Te, Ru, and Pd isotopes [54]. This region has been extensively studied theoretically and experimentally through γ-ray spectroscopy and lifetime measurements in recent years.

The region of nuclei with Z$\sim$40 and N$\sim$60 is known to display a large deformation [55]. Large two-neutron separation energies and significant isotope shifts pointed out the change in the structure of the nuclei in this region when compared to the neighboring ones. The Mo, Zr, Sr, Pd, and Ru isotopes are some of the nuclei in this region that exhibit well-defined shape coexistence [49]. Second 0^+ states appear very close in energy with the ground state for several elements and strong E0 transitions are present, especially in ^{96}Sr, among the strongest known in the nuclear chart. All the just-mentioned nuclei that exhibit shape coexistence are all near mid-shell. Shape coexistence in this region cannot be explained by the appearance of intruder configurations across a shell gap but instead by the role of the subshell closure. The same patterns are also followed by nuclei in Z$\sim$64 and N$\sim$90 regions that show large isotope shifts and two-neutron separations energies [54].

Shape coexistence in the region with Z$\sim$34 and N$\sim$40 was quite evident when studying ^{72}Se [54,56] where it was found that the role of subshells is essential for understanding the appearance of collectivity and coexistence. Shape coexistence is also observed in the vicinity of nuclei along N=Z, like in ^{16}O or ^{40}Ca [49].

In the N=50 region, intruder states appearing at low excitation energies were known since long time; however this region remains quite unexplored, and the spectroscopic information on intruder states is scarce.

2.2.3 Shape coexistence in the N$\sim$50 region

Indications of the presence of low energy intruder states in the region around ^{78}Ni were known since the early 70s. First, intruder states with spin $1/2^+$ and $5/2^+$ originating from the $s_{1/2}$ and $d_{5/2}$ orbitals were observed in ^{83}Se and later on in other N=49 isotones like ^{79}Zn, ^{81}Ge etc [57–60]. Intruder states, which appear as multiparticle-multihole excitations across a closed shell gap, become lower in energy, especially for nuclei with a nearly closed proton or neutron shell and with the partner nucleon having a near mid-shell nucleon number [61]. The evolution in the energy of the intruder states with spin $1/2^+$ and $5/2^+$ along the N=49 isotonic chain is shown in Fig. 2.9. In ^{83}Se, these intruder states have energies of around 500 keV, the lowest among the other N=49 isotones. The spectroscopic information known for the intruder states with spin $1/2^+$ and $5/2^+$ is given in Tab. 6.1. No information is available in the literature for the lifetime of states built

over the $1/2^+$ and $5/2^+$ intruder configurations in ^{83}Se: such as the 1100-keV $3/2^+$ state.

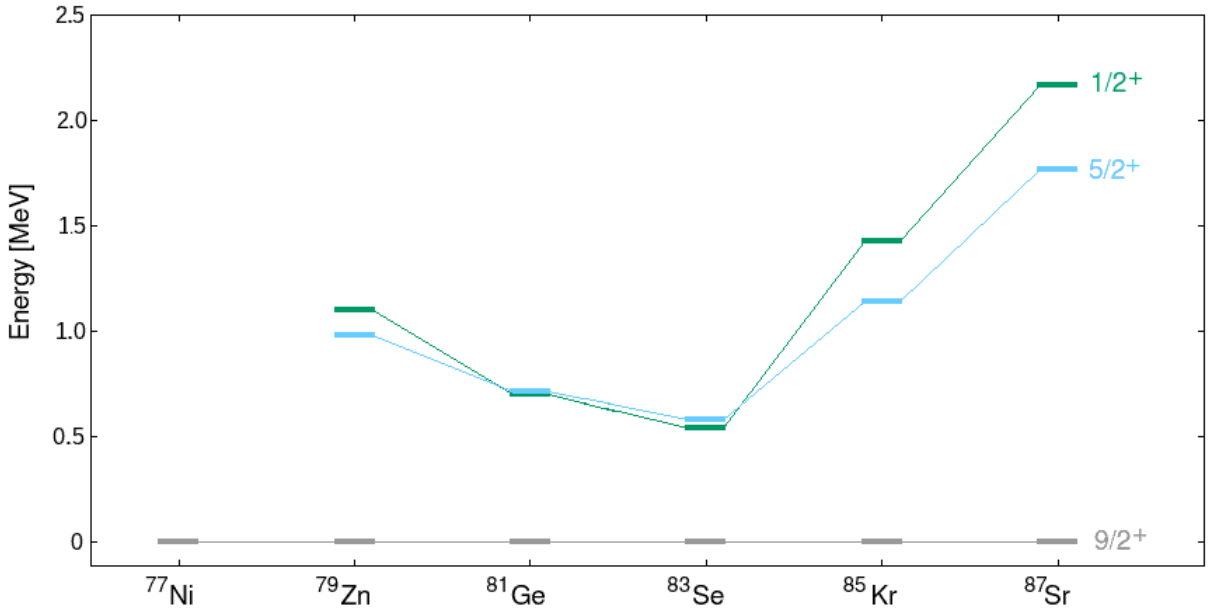

Figure 2.9: The evolution in the energy of the intruder states with spin $1/2^+$ and $5/2^+$ along the N=49 isotonic chain. No experimental information exists so far for the ^{77}Ni nucleus. Data taken from [6].

Table 2.1: The known experimental information on the excitation energy and the half-life of the intruder states with spin $1/2^+$ and $5/2^+$ along N=49 isotones based on Ref. [6].

Nucleus	$E_{lev}(1/2^+)$ [keV]	$t_{1/2}(1/2^+)$	$E_{lev}(5/2^+)$ [keV]	$t_{1/2}(5/2^+)$
^{77}Ni	-	-	-	-
^{79}Zn	1100 (15)	$\geq$ 200 ms	983 (3)	-
^{81}Ge	679.14 (4)	7.6 (6) s	711.21 (2)	3.9 (2) ns
^{83}Se	539.74 (9)	-	582.22 (6)	3.6 (6) ns
^{85}Kr	1430.6 (10)	-	1140.73 (7)	3.5^{+28}_{-14} ps
^{87}Sr	2169.43 (2)	$\geq$ 0.15 ps	1770.48 (2)	5.5^{+63}_{-21} ps

The appearance of shape coexistence close to ^{78}Ni was indicated by a strong isomer shift found in ^{79}Zn. This isomer with energy 1.1 MeV corresponds to the $1/2^+$ intruder state. From the measured spectroscopic factors, this state results to be a 2p-1h configuration. If the measured isomer shift is entirely attributed to an increase in deformation, it leads to an estimate of $\beta_2 = 0.22$ for the isomer [61].

Another evidence of shape coexistence in the N$\sim$50 region was found in ^{80}Ge where β-decay measurements revealed a tentative 0_2^+ state just below the first 2^+ state [62]. Theoretical calculations showed the role of quadrupole correlations as one of the main factors for the appearance of shape coexistence in this nucleus. This 639 keV $E0$ transition depopulating the tentative 0_2^+ state was not observed in a later experimental work [63].

Several other studies beyond N=50 show the possibility of shape coexistence. In ^{82}Zn, a state lying between the 2^+_1 and 4^+_1 was identified. This state was assigned as a possible 0^+_2 state decaying to the 2^+_1 state. Calculations were performed with the shell model using three different interactions. One of the calculations reproduces these results very well, while the other two interactions are not able to reproduce the proposed level scheme [64].

Similar conclusions were also drawn for ^{81}Ge where the intruder states with spin $1/2^+$ and $5/2^+$ are interpreted as 2p-1h configurations with a significant contribution of the $s_{1/2}$ and $d_{5/2}$ orbital above the N=50 shell gap, probing in this way the shape coexistence in the vicinity of ^{78}Ni [65]. In ^{76}Ni, a new excited state was observed decaying via a γ ray of 2004.5 keV. This excited state was assigned to a possible second 0^+ state or a second 2^+ state. Theoretical shell-model calculations support both scenarios when including in the valence space the neutron $p_{1/2}$ and the proton $f_{7/2}$ shells [66]. The first 2^+ excited state of ^{76}Ni is located at 990 keV.

The nuclei around the N∼50 region where shape coexistence has been observed are shown schematically in Fig. 2.10.

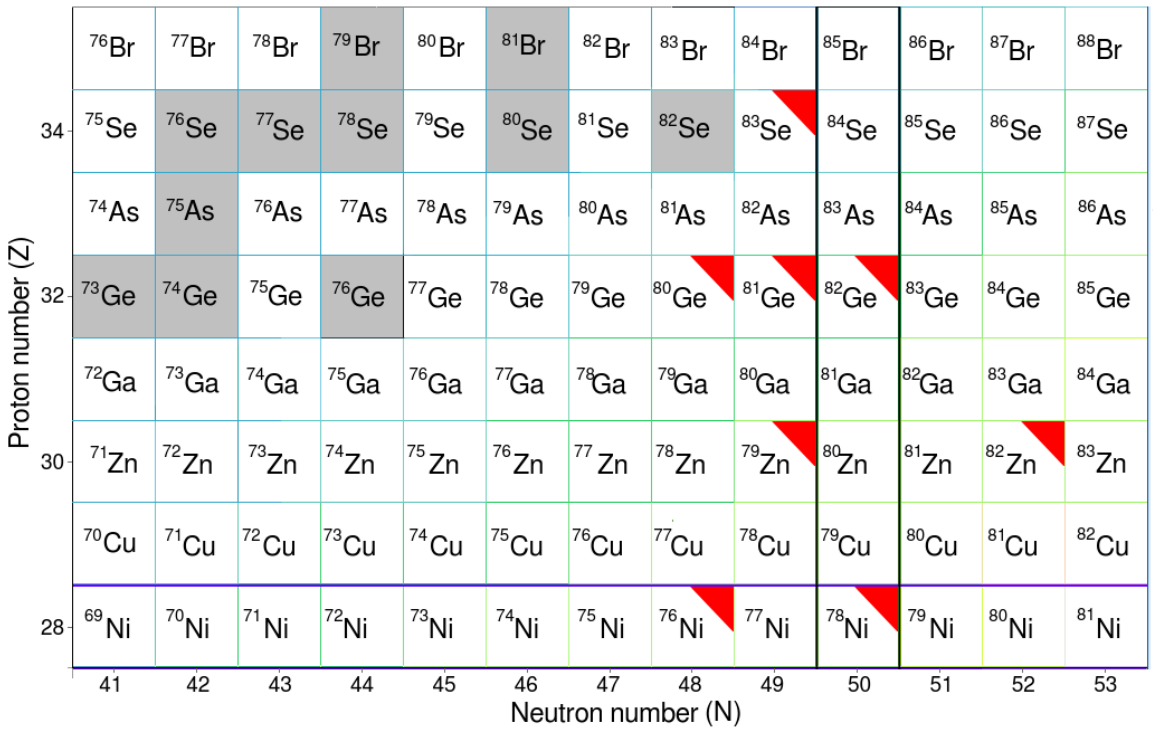

Figure 2.10: The nuclei which display shape coexistence in the N=50 region are marked with the red triangles.

2.3 Physics motivation

This work is focused on the study of intruder states in ^{83}Se, where information on the deformation of intruder configurations is crucial, as introduced in the following sections.

2.3.1 Previous studies of the ^{83}Se nucleus

Studies in ^{83}Se date early in the 60s when low-lying intruder states were found for the first time. A study using a (d,p) reaction revealed a $2d_{5/2}$ particle state in ^{83}Se [60]. Values of the transferred neutron angular momenta and spectroscopic factors for the energy levels were derived by comparing the experimental data with theoretical calculations using the DWBA. The angular distributions confirmed the ground state spin assignment of $9/2^+$. This work of E. K. Lin et al [60] also identified an isomer with spin $1/2^-$ and energy 220 keV and moreover this experiment indicated that the $d_{5/2}$ orbital above the N=50 gap is partially occupied ($\sim$0.6 particles) in the Se nuclei leaving the lower shells below N=50 not full. Other states were identified with excitation energies up to 5 MeV and interpreted as a coupling of the ground state of ^{82}Se with the various single-particle states above the N=50.

Montestruque et al. reached also the same conclusions from an experiment performed in the 70s [67] where the setup was similar to the one of the former, but instead, a polarized deuteron beam was used. Comparison of angular distributions with DWBA allowed to assign spin and parities to fifteen states of ^{83}Se, among them the intruder state with spin $1/2^+$ at an excitation energy of 540 keV.

Several studies were focused on the β decay of the ground state of ^{83}Se and of the $1/2^-$ isomer at 229 keV for which half-lives of 22 minutes and 70 seconds, respectively, were confirmed in several works [68, 69].

Concerning positive-parity intruder states, calculations were performed with a Nilsson+Coriolis coupling model by S.L. Heller and J.N. Friedman to study the energy of the $5/2^+$ intruder state in ^{83}Se as a function of deformation [59]. The calculations showed that a deformation of β $\sim$0.2 was necessary to reproduce the energy of the $5/2^+$ at 582-keV state in ^{83}Se.

Other studies of ^{83}Se followed afterwards by means of β decay [57]. The information obtained by β-delayed γ-ray spectroscopy in combination with the previous knowledge gained by the (d,p) reaction experiments allowed one to establish for the first time the 1p-2h intruder states along N=49 [57]. The appearance of the intruder states along the N=49 was associated with the existence of the proton subshell closure at Z=40. This subshell gap blocks the collectivity necessary for the formation of low-lying intruder states in ^{89}Zr at difference with ^{83}Se. The half-life of the 582-keV level $5/2^+$ intruder state was confirmed to be around 3 ns as it was measured previously by another experiment [58].

More recent works focused on the spectroscopic study of high spin states of ^{83}Se

[70,71]. The first four high-spin states above the $9/2^+$ ground state in ^{83}Se were established by N. Fotiades et al. [71]. ^{83}Se was populated by the fission of a compound nucleus formed in a fusion evaporation reaction. These states were interpreted as originating from neutron configurations involving the coupling of the $g_{9/2}$ hole to the first-excited states in the ^{84}Se core. An experiment aiming to study the low spin states of ^{83}Se and angular correlations of γ rays in this nucleus was performed recently [72]. The results of this work which complement the ones of this thesis are explained in more detail in Section 6.3.

2.3.2 Why ^{83}Se?

^{83}Se is a N=49 isotone with a neutron hole with respect to the magic N=50 shell. Hence, the number of single-particle-hole configurations available to construct the level scheme is limited. The ground state of ^{83}Se originates from the neutron hole in the $1g_{9/2}$ orbital. The other excited states are expected to arise from the coupling of this hole to the orbitals beyond the N=50 shell gap.

The energy of the intruder configuration results from the delicate balance between the monopole properties of the N=50 gap (which is reducing towards Z=32) and the quadrupole correlations, significantly lowering the energy of intruder particle-hole configurations. ^{83}Se is at the mid of the $f_{5/2}$, $p_{3/2}$ and $p_{1/2}$ proton shell (28<Z<40), and so it should have the maximum of quadrupole correlations, which makes it an excellent candidate to understand the collectivity of the particle-hole intruder states in this region [62]. Indeed, large-scale shell-model calculations predict a quenching of the energy of the intruder states in ^{83}Se, at variance with the experimental data [73] as it can be seen in Fig. 2.11. On the other hand, the same theoretical model can reproduce quite well the excitation energy of the intruder states in other N=49 isotones.

The ^{83}Se nucleus appears to be a unique candidate to help answer to several questions about the stability of the N=50 gap and the nature of particle-hole intruder states. Lifetime measurements of the intruder states of ^{83}Se will give information about their wave function and would allow to estimate the degree of the N=50 core breaking in the ground state of Se isotopes. Moreover, such measurements could shed light on the behavior of the N=50 shell gap towards ^{78}Ni.

2.3.3 Purpose of the present work

The main goal of this work is to perform lifetime measurements of the intruder states in ^{83}Se. The $1/2^+$ intruder state of ^{83}Se, originating from the promotion of one neutron from the $g_{9/2}$ across the N=50 shell gap towards the $s_{1/2}$ orbital, decays by an E1 transition with the energy of 311 keV to the $1/2^-$ state (See Fig. 2.12).

The $1/2^-$ state has a $\nu p_{1/2}^{-1}\nu g_{9/2}^{10}$ wave function, and it is a long-lived isomer since it is the first-excited state above the $9/2^+$ ground state. The 311-keV transition ($1/2^+ \rightarrow 1/2^-$)

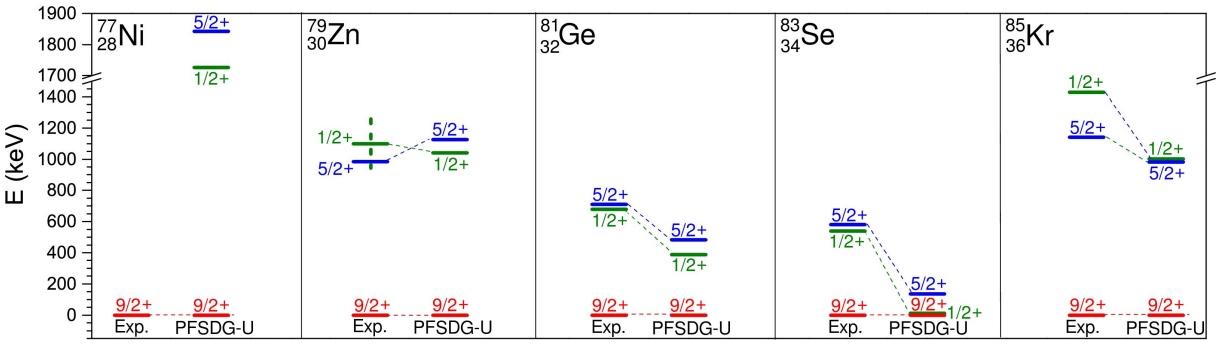

Figure 2.11: Energies of the $1/2^+$ and $5/2^+$ intruder state along the N=49 isotonic chain compared with results obtained from large-scale shell-model calculations. The decreasing trend of the energy of the intruder states towards ^{83}Se is well reproduced from the data. An island of inversion is predicted in ^{83}Se, which is not seen experimentally. Figure taken from [73]

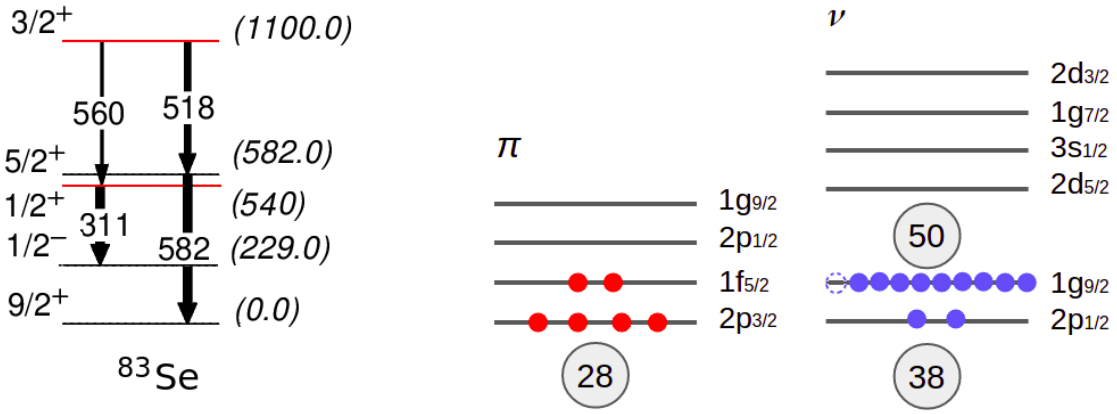

Figure 2.12: (Left) Partial level scheme of ^{83}Se. (Right) Single particle orbits for ^{83}Se

connects an intruder state with a spherical one. The lifetime of this state provides information on the reduced transition probability, which then can be compared with theoretical calculations to get further insight into the mixing of spherical and intruder configurations in ^{83}Se.

The 1100-keV $3/2^+$ level is also an intruder state which decays to the $1/2^+$ intruder state via a 560-keV γ-ray, and to the $5/2^+$ intruder state via a 518-keV transition. The information on the lifetime of this excited state will provide the reduced transition probability and subsequently the deformation parameter of the intruder states in ^{83}Se. This $3/2^+$ state can decay via M1 and/or E2 transition: and therefore also a mixing ratio measurement is needed to complement the experimental data.

Chapter 3

The experimental setup

This chapter describes in detail the experimental setup used to reach the goals of this work. A brief overview of the experiment, the setup, the target, and the reaction mechanism chosen to populate the states of interest is given in Sections 3.1 and 3.2. Section 3.3 introduces the GALILEO γ-ray array coupled to a plunger device for lifetime measurements and the SPIDER detector used in our setup to provide a channel selectivity event-by-event, leading to the reduction of possible sources of systematic errors in the lifetime determination. The working principles of the two techniques used to measure the lifetimes of the intruder states of ^{83}Se, the Recoil Distance Doppler Shift method (RDDS) and the Doppler Shift Attenuation method (DSAM), are introduced in Section 3.4.

3.1 Overview of the experiment

The experiment described in this work took place at Laboratori Nazionali di Legnaro (LNL-INFN) in Italy in 2021 with the purpose of studying the intruder states in ^{83}Se. The excited states of this nucleus were populated via a (d,p) reaction performed in inverse kinematics: ^{82}Se(d,p)^{83}Se. The beam of ^{82}Se with an intensity of 0.02 pnA and an energy of 270 MeV was provided by the Tandem-XTU accelerator [74]. This machine has been operating in this laboratory since the 80s and delivers a variety of stable beams, starting from protons up to Au. The beam energies for heavy ions reach up to 4 MeV/u. It has two acceleration steps: first, the ions extracted from the ion source with a weakly positive charge interact with a gas (cesium) and get a net negative charge. Afterwards, the ions are accelerated in an electrostatic field up to 14 MV. In the middle of the accelerator, a stripper foil is placed, which changes the charge state of the particles from negative to positive and then the ions are post-accelerated towards the terminal of the TANDEM and then transmitted to the experimental setup. Since the charge state of the ions in the second stage of the acceleration is higher, this acceleration stage is much more effective with respect to the first.

The beam impinged into a deuterated target (C_2D_4) produced in the laboratory

of LNL-INFN using a novel technique allowing these kind of targets to be suitable for performing lifetime measurements exploiting the RDDS technique. Since the lifetimes of the intruder states are expected to lay in two different time ranges, the beam time allocated to the experiment was divided into two parts. In-beam measurements were performed in seven days using the RDDS technique. This technique requires a plunger device [75] which is used to hold the target and the stopper foil at a particular distance. The target foil where the reaction takes place faces the beam, followed by the stopper, a thick foil of a high Z material used to stop the reaction products. In the RDDS experiment for the study of the intruder states of ^{83}Se, a deuterated polyethylene foil with a thickness of 1 mg/cm^2 was evaporated into a gold backing with a thickness of 6 mg/cm^2. A gold foil with a thickness of 30 mg/cm^2 was used as a stopper. Measurements of the lifetime of 540-keV $1/2^+$ intruder state were carried out for several distances between the target and the stopper foil, varying from tens of micrometers to a few millimeters.

Another three days of beam time were dedicated to measure the lifetimes of other intruder states, such as the 1100-keV $3/2^+$ and the 1472-keV $3/2^+$ state, employing the Doppler-Shift Attenuation Method. The deuterated-polyethylene foil with a thickness of 1 mg/cm^2 was evaporated on a gold foil with a thickness of 30 mg/cm^2. This technique is similar to the RDDS, but the target and the stopper are attached to each other, making it suitable for measuring shorter lifetimes ranging from femtoseconds to picoseconds. More details on both techniques used for lifetime measurements of nuclear-excited states are given in Section 3.4.

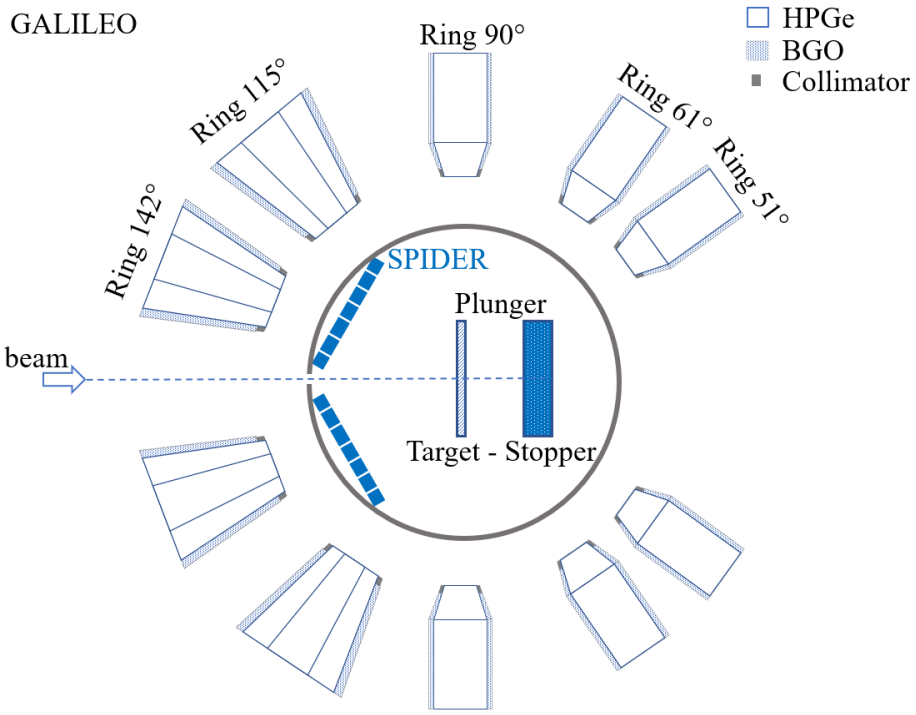

Figure 3.1: Schematic representation of the experimental setup composed of GALILEO (γ-ray detector array) + SPIDER (charged particle detector) + Plunger device.

The GALILEO γ-ray detector array in the phase II configuration [76] was used to detect the emitted γ rays. It is a Compton-Suppressed γ-ray array composed of 50 HPGe crystals arranged in rings as represented in the schematic view of Fig. 3.1. To reach the desired channel selectivity, the GALILEO γ-ray array was coupled to SPIDER [77], a silicon-stripped detector designed to work as an ancillary device coupled with γ-ray detector arrays, and it is used for detecting charged particles. In this experiment, this detector was used for the proton tagging of the (d,p) transfer reaction. SPIDER was placed inside the vacuum chamber, covering backward angles with respect to the beam direction, as shown in Fig. 3.1. The experimental setup is described in detail in the following sections of this chapter.

3.2 Reaction and C_2D_4 target

The ^{83}Se nucleus has been studied previously using different reactions like neutron capture [78], direct reactions [60, 67], β decay of ^{83}As [57, 79] and fusion-fission reactions [80, 81]. In this work, a deuteron stripping reaction (d,p) was chosen to populate the states of interest of ^{83}Se.

3.2.1 Direct reactions

In a direct nuclear reaction, the target nucleus and the projectile experience a short interaction in time, of the order of 10^{-22} s, and the interaction is limited only to a specific degree of freedom (one single nucleon or one collective coordinate) that changes during the process, thus the initial and the final states do not differ much. Only one or a few nucleons near the surface of the nuclei are involved in the reaction mechanism [82]. The direct reactions are divided into two classes: when one nucleon or cluster is transferred to the target nucleus, it is called a stripping reaction and when nucleons are transferred from the target to the projectile nucleus, it is called a pickup reaction. The stripping and pickup reactions provide a direct measure of the single particle character of the nuclear states, probing the shell-model description of the nucleus.

Figure 3.2 shows schematically the reaction: A(d,p)B*. The deuteron collides with the target nucleus A and loses the neutron. The recoil nucleus B is produced in an excited state B* and the proton is scattered at the angle θ.

The momentum diagram of the reaction is also shown in Fig. 3.2, where the momentum of the incident deuteron is $k_d\hbar$, the momentum of the emitted proton is $k_p\hbar$ and $k_n\hbar$ is the momentum of the stripped neutron. From the conservation of momentum, following the diagram in the figure, one gets the relation:

$$k_n^2\hbar^2 = k_d^2\hbar^2 + k_p^2\hbar^2 - 2k_dk_p\hbar^2 cos\theta \tag{3.1}$$

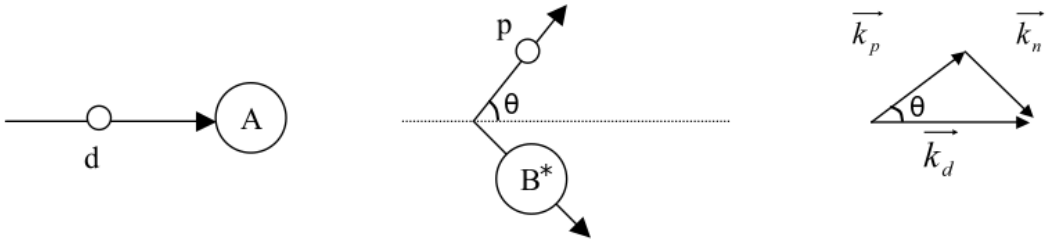

Figure 3.2: Schematic representation of a (d,p) reaction: A(d,p)B*. The deuteron collides with the target nucleus A and loses the neutron. The proton is emitted at an angle θ and the recoil nucleus B is produced in an excited state B*. The momentum diagram for the reaction is shown on the right.

where θ is the angle between the direction of the outgoing proton and the incident deuteron direction.

If the neutron is captured at impact parameter b, which is approximately the radius of the target nucleus (b≈R), the angular momentum transferred to the nucleus is given by the expression:

$$l_n\hbar = Rk_n\hbar l_n = Rk_n \tag{3.2}$$

From the two relations above, it results that the orbital angular momentum transfer in the reaction can be associated with a given angle θ corresponding to the direction of the outgoing proton with respect to the incident deuteron direction. The excited state of the residual nucleus and the angular momentum transfer in the reaction can be deduced by measuring the energy and the scattering angle of the outgoing proton. From the perspective of lifetime measurements, the use of (d,p) reactions to populate the nucleus of interest provides the possibility to select a particular excited state of the residual nucleus based on the energy of the outgoing nucleon. This offers a better control on the feeding of the state of interest, which is one of the most significant contributors to systematic errors when performing lifetime measurements of nuclear-excited states, as it will be further explained in this work.

Based on Eq. 3.1 and 3.2, one can conclude that the angular momenta l=0,1,2,3,4... transferred in a direct (d,p) reaction are forward-focused ($\theta < 90°$). In this work, the reaction is performed in inverse kinematics. In inverse kinematics, the proton is scattered in the backward angles in the laboratory frame of reference. Mechanical constraints of the reaction chamber of GALILEO do not allow to host at once the plunger device and the SPIDER detector at forward angles.

Angular distributions of the differential cross-section have been calculated with the Fresco code [83, 84] for different excited states of ^{83}Se populated following the reaction ^{82}Se(d,p)^{83}Se at 270 MeV beam energy. The volume, the surface, and the spin-orbit potentials for the deuteron were used in the calculations as defined by A. Haixia and

C. Chonghai [85] and for the proton, the potentials defined in A.J Koning and J.P Delaroche [86]. The calculated differential cross-sections for several excited states of ^{83}Se are shown in the left panel of Fig. 3.3. The angular range covered by SPIDER is indicated in the figure with the dashed lines. The scattered protons are expected to have an energy of a few MeV as shown in the kinematics plot calculated by the Lise++ program [87, 88] in Fig. 3.3 (Right panel). The recoil nucleus, ^{83}Se, is scattered at very small angles in the forward direction.

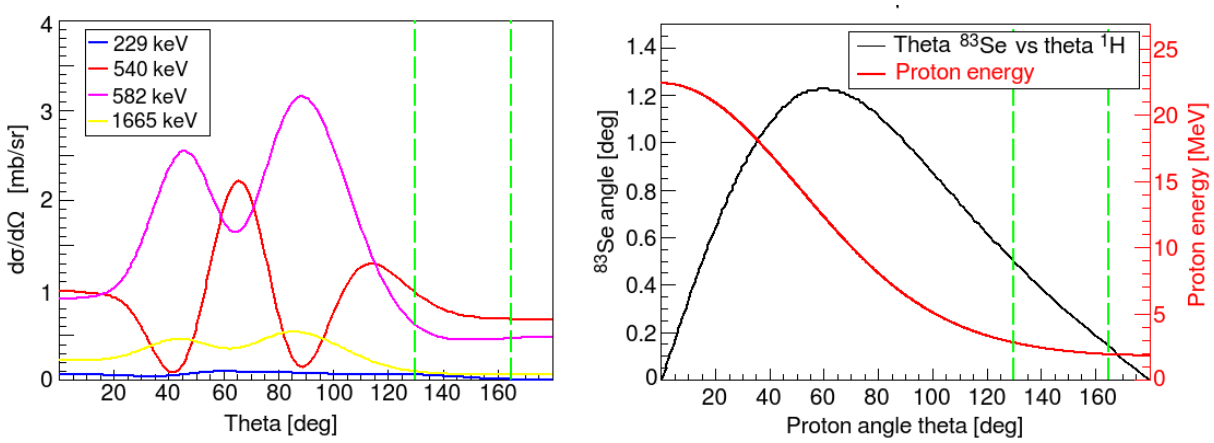

Figure 3.3: (Left) Angular distribution of the differential cross-section calculated with the Fresco code for different excited states of ^{83}Se. The angular coverage by SPIDER is shown with the green vertical lines. (Right) The kinematic line of the reaction was calculated with Lise++ program. The scattered protons are expected to have energy of a few MeV and the recoil nucleus, ^{83}Se, is scattered at angles smaller than 2°.

3.2.2 C_2D_4 target for RDDS measurements

Deuteron-induced reactions such as (d,p) have been used for decades, typically exploiting deuteron beams into stable targets. Developments of radioactive beams or also the need to measure lifetimes of neutron-rich elements, as in the case of this work, imposed the request to produce deuterated targets and perform deuteron-induced reactions in inverse kinematics (incident beams upon a deuterated target).

The C_2D_4 targets can be produced as self-supporting targets by several techniques such as: vacuum deposition, hot press, and most typically solvent casting [89]. In the case of the latter technique, the C_2D_4 powder is dissolved in a solvent (generally xylene) and poured over a level surface. Heating the mixture above the melting point of C_2D_4 (around 125°C) evaporates the solvent, producing a thin film of C_2D_4.

For lifetime measurements with C_2D_4 targets using the RDDS technique, the target has to be stretched into the target holder support of the plunger device. A tension force is applied on the sides of the target, making its surface as flat as possible. Self-supporting C_2D_4 targets are not capable of resisting this tension, thus making impossible their use for

such measurements. Moreover, this material is not conductive, so no distance feedback can be provided by the plunger device as explained in Section 3.3.3. C_2D_4 targets suitable for RDDS experiments were produced at LNL-INFN. The C_2D_4 foil with a thickness of 1 mg/cm^2 was evaporated into a 6 mg/cm^2 thick gold layer mounted and stretched previously on the target holder of the plunger device. The evaporation of the C_2D_4 material was at first performed at a temperature of 200°C but the target was deformed at the end of the process, as seen in Fig. 3.4 (Left panel). This was caused by a tension of the polyethylene foil, which was left attached to the gold foil after the evaporation of the substrate. Additionally, the gold foil was only partially covered by the C_2D_4 layer (the dark areas in the figure represent the gold surface). Changing the temperature during the evaporation process at a very low rate, increasing by 90°C/h up to 230°C and decreasing after 30 minutes with a rate of 25°C/h until room temperature, improved the homogeneity of the target as shown by the Scanning Electron Microscope (SEM) analysis and cleared out the wrinkles from the stretched surface as seen in Fig. 3.4 (Right panel). The C_2D_4 target produced at LNL-INFN by this novel technique allowed the deuterated targets to be used for plunger measurements.

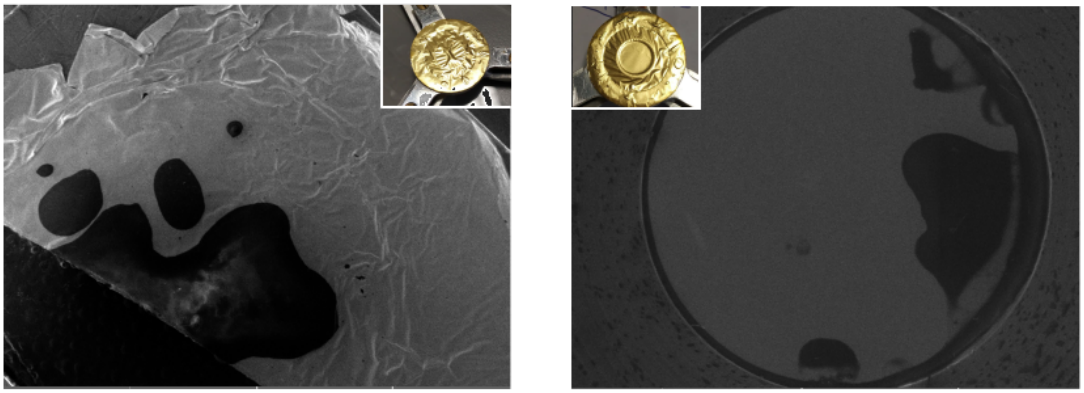

Figure 3.4: The C_2D_4 target produced at LNL-INFN using a novel technique allowing the deuterated targets to be used for plunger measurements. Comparison of the target produced by changing with different rates the temperature during the evaporation process of the substrate. Decreasing the rate (Right) improved the homogeneity of the target (as shown from the SEM analysis, the dark color represents the uncovered gold areas) and wrinkles do not appear on the stretched surface.

3.3 Experimental setup

The experimental setup consisted of the GALILEO γ-ray array coupled with SPIDER and the plunger device. The different parts of the setup are described in the following sections.

3.3.1 GALILEO phase II configuration

GALILEO is a 4π Compton-suppressed γ-ray array of HPGe detectors designed and installed at LNL-INFN. With respect to the Phase I configuration, ten triple clusters (three encapsulated HPGe crystals mounted in a common cryostat) were added to the array at backward angles. The presence of the triple clusters increases the efficiency and the sensitivity of the array for lifetime measurements employing Doppler shift-based techniques. The GALILEO γ-ray array in the phase II configuration is also hosting 25 GASP detectors [90] together with the BGO shielding placed at 23.5 cm from the target position. Ten GALILEO Single Crystals (GSC) are mounted at 90° rings with respect to the beam direction, five detectors at 51°, five detectors at 61° and another five detectors at 21° ring. Five Euroball HPGe triple clusters [91] together with their BGO shielding are arranged at 115° and other five at 142°. The GALILEO Triple Clusters (GTC) are placed at 24.5 cm from the target position. The detectors are mounted in two shells and one ring between them, as shown in the CAD drawing in Fig. 3.5. The upstream shell accommodates the GTC detectors, and the downstream shell hosts the single detectors at forward angles. The downstream shell can be shifted back and forth, allowing access to the reaction chamber. The reaction chamber, with a radius of 15 cm, is made of a layer of aluminum with a thickness of 2 mm to limit the absorption of γ rays at low energies. The geometrical arrangement of the detectors and the mechanics are shown in Fig. 3.5.

The GSC detectors of the 21° ring of GALILEO were not present in the experimental configuration of this work.

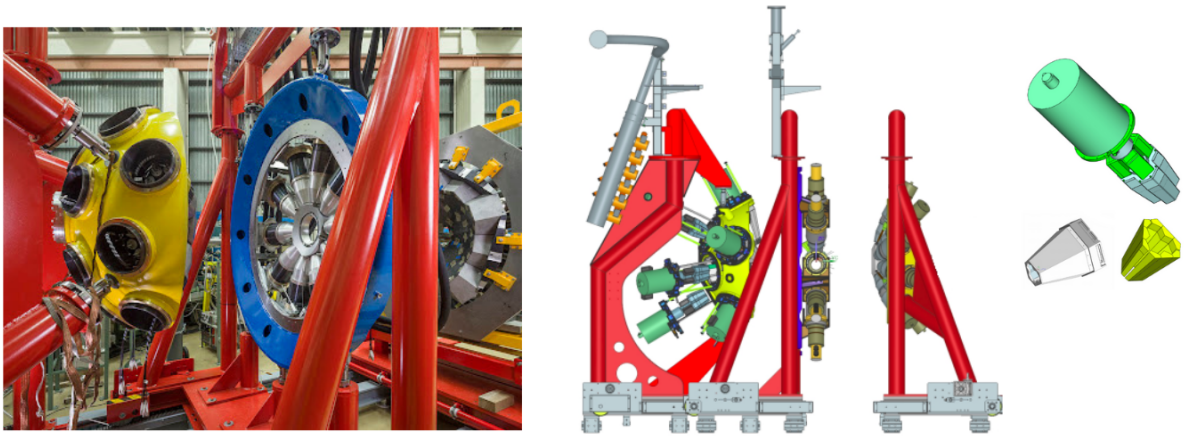

Figure 3.5: (Left) Picture of the GALILEO array at LNL-INFN. (Right) CAD drawing of the GALILEO detector array and of the triple cluster together with the corresponding BGO anti-Compton shielding. Figure adapted from [76].

Gamma rays in the energy range from hundreds of keV to a few MeV interact with the highest probability with the HPGe detectors via Compton scattering. The Compton background emerging in the spectrum because of γ rays that do not fully deposit their energy in the detector can be reduced by using the anti-Compton shielding. All the

HPGe detectors of the GALILEO array, the single crystals, and the triple clusters are surrounded by Bismuth Germanium Oxide (BGO) scintillators, acting as anti-Compton shields. Gamma rays measured in coincidence between the HPGe and its surrounding BGO are discarded, significantly improving the Peak-To-Total ratio (P/T). The BGO scintillator material is ideal to be used as an anti-Compton shield. The high Z and high density of this material improve the veto condition efficiency. Additionally, the possibility of having the BGO crystals in small dimensions does not affect much the solid angle coverage of the HPGe detectors. The anti-Compton shield of the GSC detectors is composed of eight BGO crystals coupled to eight photomultiplier tubes. The direct interaction of the γ rays with the BGO material is prevented by lead shielding between the BGO crystal and the reaction chamber. Consequently, only scattered events from the interaction with the HPGe material can be detected. The anti-Compton shield of the GTC detectors is made of nine BGO crystals coupled to twelve photomultipliers. Hevimet collimators (an alloy of 90% tungsten, 6% nickel, and 4% copper) are used to avoid the direct interaction of γ rays with the BGO crystal. In the case of GTC detectors, Compton scattered events of γ rays may appear not only between the BGO and the HPGe but also inside the germanium volume itself. These events may be reconstructed, improving further the P/T ratio and the efficiency of the array.

The hit pattern of the GALILEO detector generated from simulations with the Geant4 toolkit is shown in Fig. 3.6. The labels of the detectors and the rings are indicated in the figure. For simplicity, each detector is assigned an ID number as shown in Tab. 3.1.

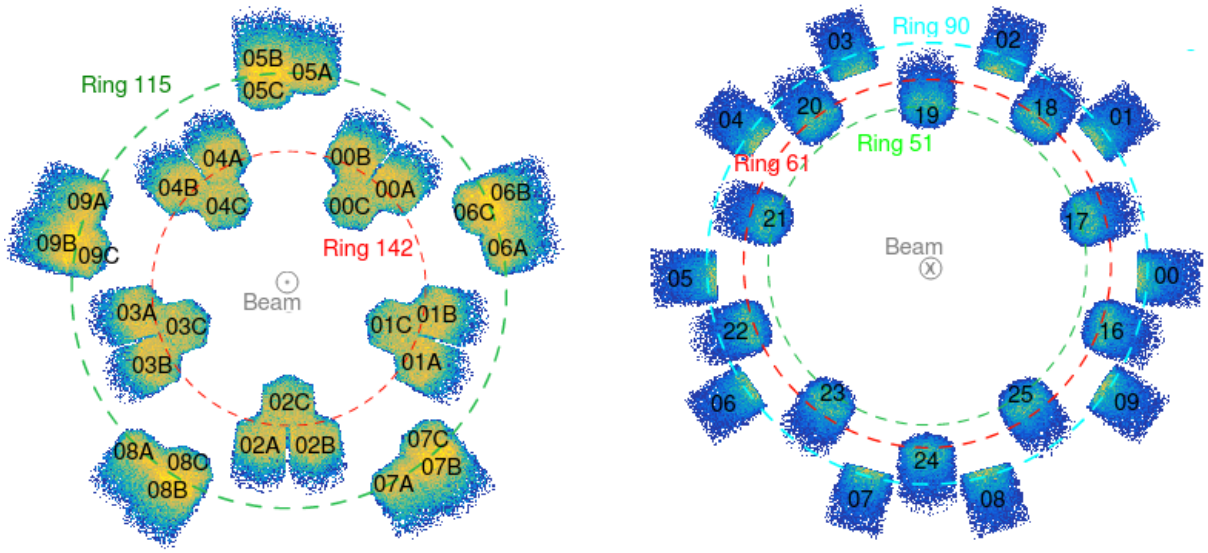

Figure 3.6: Hit pattern of the triple cluster detectors (Left) and of the GALILEO single detectors (Right) generated from Geant4 simulations. The detectors and the rings are indicated.

GALILEO can be coupled to other ancillary devices like SPIDER, EUCLIDES [92],

GAL-TRACE [93], and Neutron Wall [94]. Coincidence measurements between γ rays and the emitted ejectiles allow one to select the reaction channel. Lifetime measurements can be performed by coupling GALILEO with a plunger device. The array is equipped with a fully digital read-out electronic chain and customized DAQ, introduced in further detail in Section 3.3.4.

Table 3.1: The ID number for each detector of the GALILEO array. The position of each detector in the array is shown in Fig. 3.6

						Ring 51°									
Det	17	19	21	23	25										
ID	17	19	21	23	25										
						Ring 61°									
Det	16	18	20	22	24										
ID	16	18	20	22	24										
						Ring 90°									
Det	00	01	02	03	04	05	06	07	08	09					
ID	0	1	2	3	4	5	6	7	8	9					
							Ring 115°								
Det	05A	05B	05C	06A	06B	06C	07A	07B	07C	08A	08B	08C	09A	09B	09C
ID	111	112	113	114	115	116	117	118	119	120	121	122	123	124	125
							Ring 142°								
Det	00A	00B	00C	01A	01B	01C	02A	02B	02C	03A	03B	03C	04A	04B	04C
ID	96	97	98	99	100	101	102	103	104	105	106	107	108	109	110

3.3.2 SPIDER

SPIDER is a segmented silicon detector designed to work in conjunction with γ-ray arrays like GALILEO and is typically used for low-energy Coulomb-excitation experiments. This detector is a modular array made of eight single units, shaped in a trapezoidal form, each covering one-eighth of 2π in the azimuthal angle. A flat disc-shaped array with a diameter of 21 cm can be constructed with eight detector modules. Each detector unit is segmented into eight annular strips surrounded by a guard ring, reducing the charge-splitting effect. The thickness of the silicon crystals is around 300 μm with dead layers of 50 nm on the surface side and around 350 nm on the ohmic side. Since the detector units are independent, reducing the number of modules of the array turns it into a cone-shaped device, making it possible to fit different dimensions of the reaction chamber where it is used. A CAD drawing of the SPIDER array with seven detector units is shown in the left panel of Fig. 3.7

In our experimental configuration, SPIDER consists of seven detector units placed inside the vacuum chamber in the backward direction with respect to the beamline and

covering angles from 130° to 165°. Because of the mechanical constraints of the GALILEO reaction chamber, SPIDER can be mounted only in the backward direction when coupled with the plunger device. SPIDER mounted in the GALILEO chamber is shown in Fig. 3.7 (Right panel). The solid angle covered by the entire array equals 17% of 4π [95].

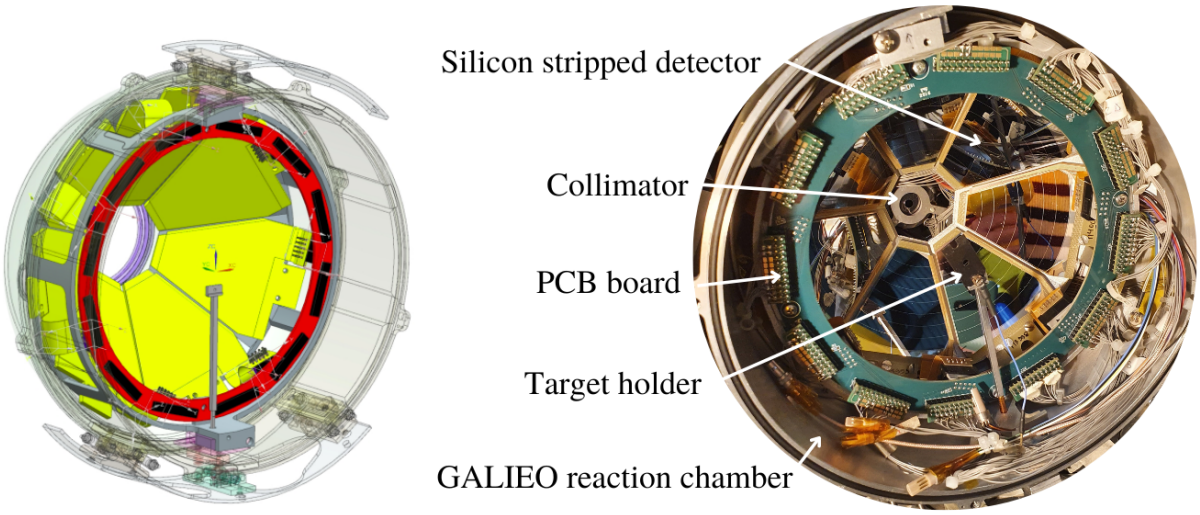

Figure 3.7: (Left) CAD drawing of the SPIDER array with seven detector units and of the holding support for the GALILEO reaction chamber. Figure taken from Ref. [77] (Right) SPIDER mounted in the GALILEO reaction chamber.

Gamma rays are measured in coincidence with protons from the (d,p) reaction allowing a high selectivity in the reaction channel. Besides that, thanks to the segmented silicon pad detectors, SPIDER provides information on the energy of the protons and on their angle of emission, enabling the possibility of choosing a particular excited state of ^{83}Se nucleus.

The mapping of the SPIDER array is shown in Fig. 3.8 where each of the seven detector pads is identified with the letter D followed by a number from 1 to 7 and each segment of the sector is numbered from 1 to 8. The ID number which will be used to refer to the SPIDER segments in the rest of the thesis is shown in the figure.

The processing of the signals of the SPIDER detectors and the electronic chain is described later in Section 3.3.4.

3.3.3 Plunger

The plunger is a mechanical device used as a holder of the target and the stopper foil at a particular distance in RDDS experiments with a precision of sub-micrometers. A dedicated plunger device was designed for the reaction chamber of GALILEO in a compact design that allows its coupling with other ancillary devices like EUCLIDES [92], GALTRACE [93], or SPIDER, as in this experiment. The target and the stopper foil are stretched in the conic support of the plunger and are placed in front of each other as

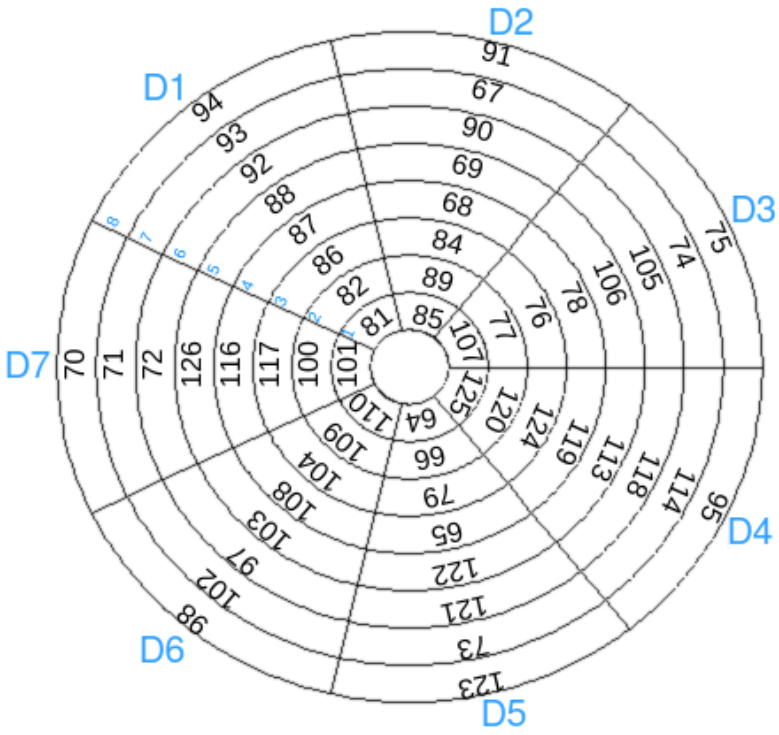

Figure 3.8: Mapping of the SPIDER array. Each detector pad is identified with the letter D followed by a number from 1 to 7. The segments of each sector are marked with numbers from 1 to 8. The number ID of each segment is marked in the figure.

parallel as possible by attaching the conic support to a holder (See Fig. 3.9). The stopper foil is placed in a fixed position in the holder. The target is attached to a piezo motor, which allows the distance between the foils to change. The position sensor of the engine has a resolution of 20 nm, precise enough for measurements in the RDDS experiments where the distance between the foils ranges from a few micrometers up to 15 mm. The distance between the foils is measured using the capacitance signal. A pulse generator signal is applied in one foil, inducing a voltage to the other one. The induced voltage is then monitored from an automatic feedback system, constantly maintaining the two foils at a fixed position. A calibration of the distance between the two foils is performed before the experiment by using the position information of the motor. The calibration process is explained further in Section 4.3. The holder is then mounted in the reaction chamber with the target at the geometrical center of the array. The plunger device accommodated in the GALILEO reaction chamber is shown in Fig. 3.9.

In front of the target, a tantalum collimator with 4 mm diameter is placed to allow the focusing of the beam in the center of the target. The plunger support is manufactured with the minimum material possible in order not to shadow the HPGe or the particle detectors. Due to its dimensions, the motor may shadow the 90° ring of GALILEO, but since the γ rays measured in this ring are not affected by the Doppler effect, thus this ring is not sensitive to lifetime measurements.

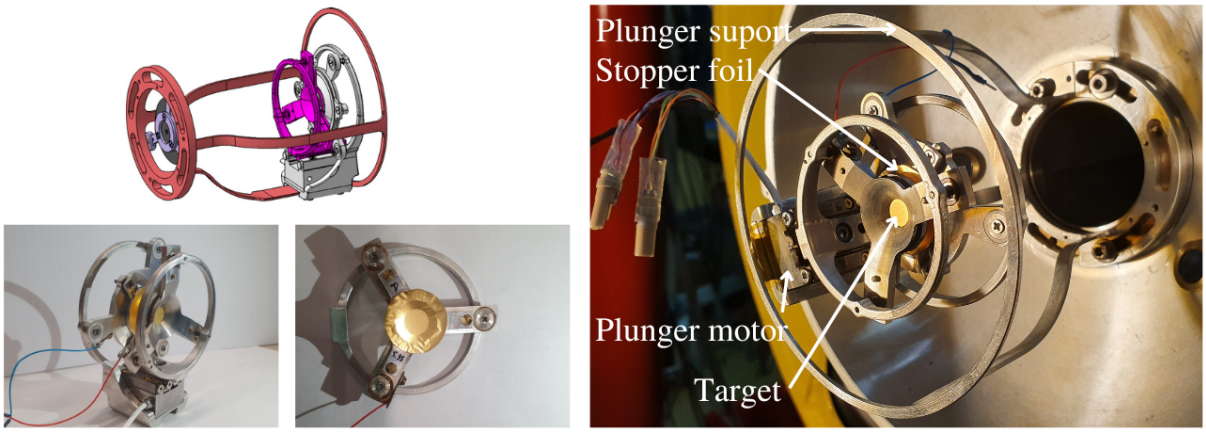

Figure 3.9: (Top left) CAD drawing of the plunger device. Figure taken from Ref. [75]. (Bottom left and right panel) Pictures of the target and the holding structure of the plunger device installed in the reaction chamber of GALILEO.

3.3.4 Data Acquisition and electronics

The signals of the GALILEO detectors are read out by charge-sensitive preamplifiers designed especially for this γ-ray array. These preamplifiers employ the fast reset circuitry when the output signals exceed a given threshold, allowing to optimize significantly the dynamic range and reducing the dead time [96]. The differential signals from the preamplifiers and the BGOs are sent to the GALILEO digitizers. The digitizers developed within the AGATA community, also being used as part of the AGATA array electronics [97], perform a shaping of the signals and convert them to digital at a 10 Msps rate. Each digitizer is composed of the control card [98] and three DigiOpt12 boards [99] with twelve input channels each. The control card manages the DigiOpt12 boards by receiving and distributing the synchronization signal from the pre-processing electronics. The digitized signals are transmitted via optical links to the pre-processing board, a custom PCI express board namely the Global Gigabit Processor (GGP). The GGP is furnished with an FPGA (Field Programmable Gate Array) which takes care of the processing, time stamping, formatting, and distributing of the data to the hosting servers [100]. If the signals are above a certain threshold, they get processed by a moving window deconvolution algorithm generating the energy of the event by means of a trapezoidal shaper adjusted by a set of parameters. Because of the limits of the FPGA dimensions the channels are distributed into domains consisting of one master and n-slave. In the case of the single GASP detectors, the domain is built by two channels, one as a master trigger (the HPGe signal) and one slave (the corresponding surrounding BGO). Meanwhile, in the case of the triple cluster detectors, the domain is built by four channels. The trigger is performed on the sum of the three HPGe detectors and the BGO signal is acquired as a slave. The absolute time to the events is distributed by the Global Trigger and Synchronization system (GTS) with a frequency of 100 MHz [101]. Thus, the time stamp of each signal has

a resolution of 10 ns. The preprocessed digital signals contain information on the channel, amplitude, timestamp, and trace (100 samples for each triggered waveform). At this stage, a local trigger request is sent to the GTS. The GTS also collects the trigger request and sends back validation of rejection to the corresponding local server. The further flow of GALILEOs data is handled by several XDAQ applications: read-out units, filter units, builder units, and merger units. The read-out unit distributes the data from the preprocessing board to the local filter. The local filter unit runs dedicated algorithms on the acquired data like pile-up rejection, Compton scattering, pulse shape analysis, or other codes for online analysis. Events in coincidence between GALILEO and the BGOs in a time window of 100 ns are discarded before the data is saved in the disk, whereas, all the other events are recorded allowing the user to improve further the Compton suppression and the P/T ratio. After the local filter, the data are sent to the builder unit, which orders the signals in time and builds events based on the configured coincidence window. The merger unit combines the data from all the builder units and organizes the events within a time window of 500 ns. Before the data are stored on disk, a final filter is applied to the data able to select data based on the time coincidence between GALILEO and other ancillary devices.

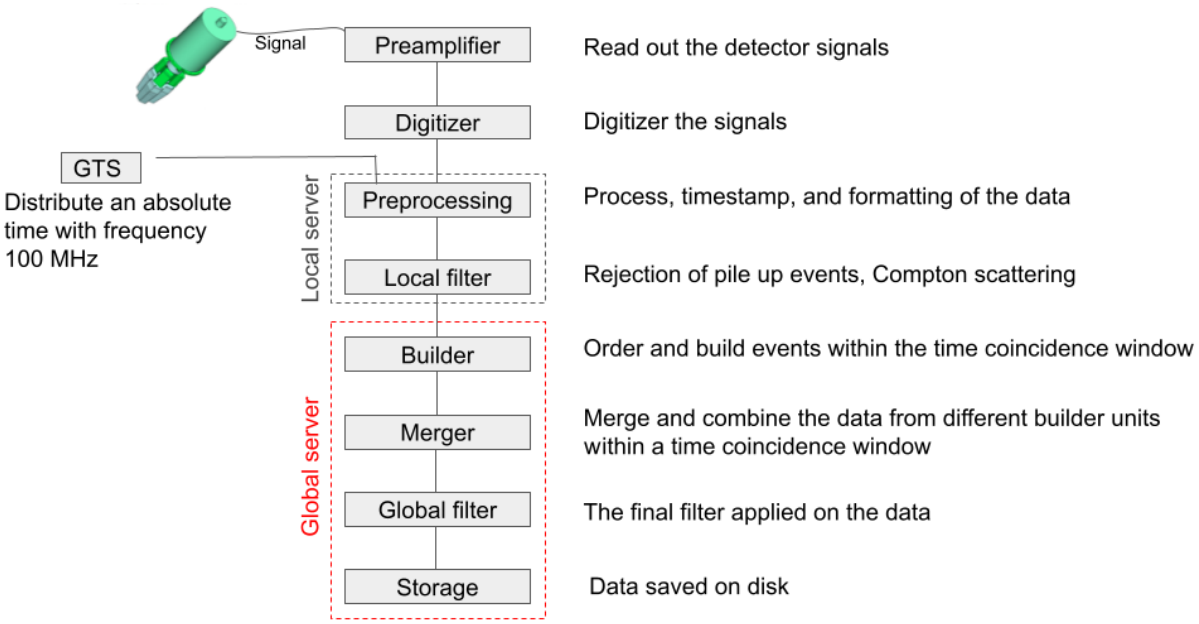

Figure 3.10: The flow of the GALILEO data along the electronic chain.

The signals of the SPIDER detector are read out by home-designed charge-sensitive preamplifiers [92] located outside the reaction chamber. The signal from the detector is transmitted to the preamplifier via 120-cm-long cables. Afterwards, the differential output signal from the preamplifier is sent to the GALILEO digitizer following the same path as described in the case of the HPGe signals. GALILEO and SPIDER are aligned thanks to

the GTS system allowing to construct the coincidence events. Each of the 56 acquisition channels of SPIDER is self-triggering and the events of interest are reconstructed in the off-line analysis. A schematic representation of the data flow is given in Fig. 3.10.

3.4 Lifetime measurements of nuclear excited states

The lifetimes of the nuclear-excited states that decay by γ-ray emission vary from 10^{-16} to 10^{-3} seconds, depending on the strength and the energy of the transition. The most typical range of the lifetimes for single-particle states varies from picoseconds to nanoseconds. Different techniques have been developed to measure lifetimes in various ranges and they are classified into two groups: techniques involving the direct measurement of the time difference between two successive γ rays and those based on the Doppler shift effects. In the former case, there are limitations because of the rise time of the detector signals, but still, with these techniques, it is possible to measure lifetimes of the order of nanoseconds, or even tens of picoseconds with the "fast timing" technique [102].

Doppler-based techniques are typically used to measure shorter lifetimes with respect to the latter techniques, varying from hundreds of picoseconds down to a few femtoseconds. The most commonly used are the RDDS and DSAM, both exploited in this work to measure lifetimes of intruder states of the ^{83}Se nucleus.

3.4.1 Recoil Distance Doppler Shift method

Recoil Distance Doppler Shift method (RDDS) is a Doppler-based technique used for measuring lifetimes of the order of picoseconds that was employed in this work to measure the lifetime of the $1/2^+$ intruder state of ^{83}Se.

This technique consists of a thin target where the reaction takes place, followed by another foil placed parallel to the target at a particular distance d from it, used to stop the reaction products. As described previously, the two foils are mounted in the plunger device at a defined distance between them. The reaction products leave the thin target at a given velocity v defined by the kinematics of the reaction and the energy losses in the target. Let's assume the nuclei leave the target in an excited state and decay by γ-ray emission with a lifetime on the range of the sensitivity of the technique. If the γ decay takes place when the nucleus is in flight, the detectors would measure higher or smaller energy of the γ ray, depending on the detection angle due to the Doppler effect. The energy measured is given by the relation below:

$$E'_\gamma = E_\gamma \frac{\sqrt{1-\beta^2}}{1-\beta cos\theta} \tag{3.3}$$

where $\beta = v/c$, E_γ is the energy of the γ-ray photon, β the velocity of the emitting nucleus, and θ the angle between the recoil and the γ-ray photon. Higher energy would be measured at forward angles and smaller at backward angles while at 90°, the Doppler effect would not be observed as long as the β values are small. Since the γ decay is a statistical process, the emission of γ-rays may occur in flight or when the emitting nucleus is at rest in the stopper. Consequently, two γ-ray peaks belonging to the same transition may be observed in the γ-ray spectrum (if the detection angle of the photon is different from 90°). A schematic representation of the reaction kinematics and the observed γ-ray spectrum is shown in Fig. 3.11.

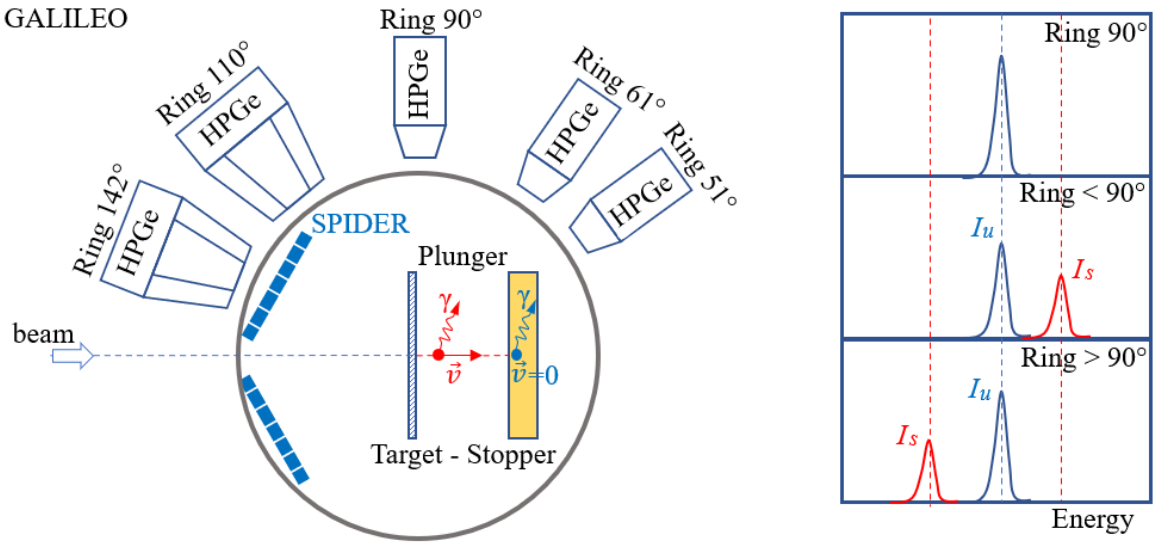

Figure 3.11: A schematic representation of RDDS technique within the setup configuration used in this experiment and the expected γ-ray energy spectrum at different rings.

By varying the distance between the stopper and the degrader, the intensities of the two peaks (which belong to the same transition) will change. At closer distances the stopped component is dominant, meanwhile, at large distances, the events decaying in flight dominate. The change in intensity between the two peaks (the shifted and the unshifted component) allows one to construct the decay curve of the state, which depends on the lifetime of the nuclear-excited state. Fitting the decay curve obtained from the experimental data points provides information on the lifetime of the nuclear state. More details on the analysis of RDDS data are given in Chapter 5.

3.4.2 Doppler Shift Attenuation method

The Doppler Shift Attenuation method is a Doppler-based technique for measuring lifetimes from a few femtoseconds to tens of picoseconds. This technique is similar to RDDS, but in this case, the target is deposited to the stopper foil, so $d = 0$. Slowing down the reaction products immediately after the reaction allows one to measure shorter lifetimes of nuclear-excited states compared to RDDS. If the lifetime of an excited energy level is

comparable with the time it takes for the nucleus to stop entirely in the backing, its γ-ray decay can occur when it is still slowing down inside the stopper material or when it is at rest.

Being the slowing down process of the particles inside the medium continuous and the γ-ray emission statistical, the measured spectrum of the γ-ray energies corresponding to a particular transition is a continuous distribution. This distribution ranges from the nominal rest energy and the maximum Doppler shift, at difference with the RDSS technique where only two separated peaks are present in the spectrum. A schematic representation of the setup and of the expected γ-ray spectrum is shown in Fig. 3.12. The lineshape (distribution) depends on the lifetime of the level, on the kinematics of the emitting nuclei, on the slowing down properties of the absorbing medium, and also on the angle between the beamline and the detector.

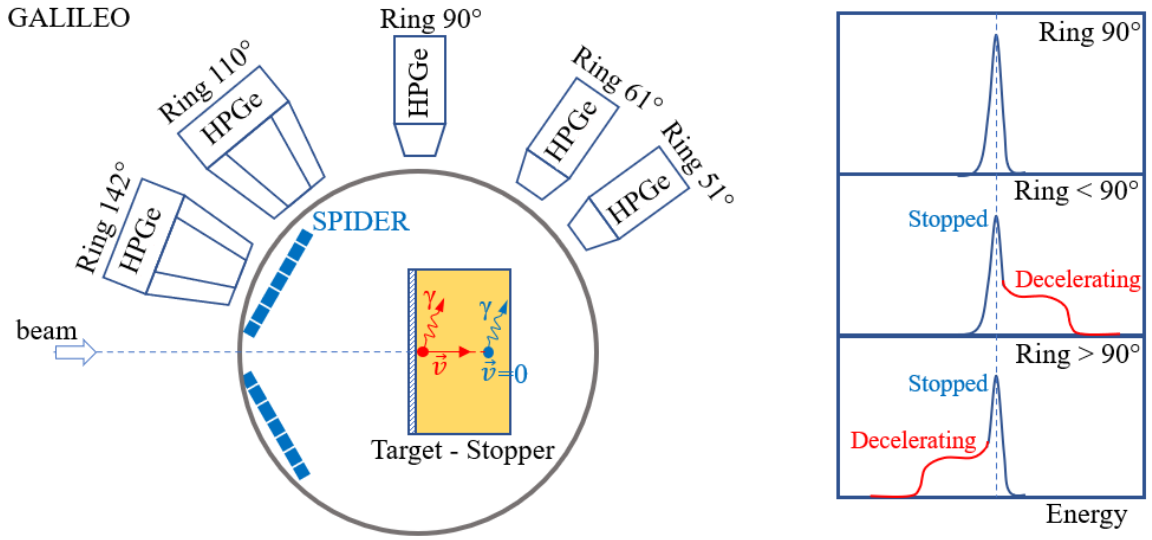

Figure 3.12: A schematic representation of DSAM technique within the setup configuration used in this experiment and the expected γ-ray energy spectrum at different rings.

The lifetime of the excited state decaying by a particular γ-ray transition is extracted from the experimental data by performing simulations that try to reproduce the shape of the experimental spectrum. These simulations take into account the geometry of the setup, resolution of the detectors, stopping power of the reaction products in the stopper, the population of the nuclear-excited states from the reaction, the decay of the nucleus of interest, and most important the lifetime of the excited state. Changing these parameters allows one to reproduce the experimental peak shape and helps in deriving the lifetime of the state of interest.

As primary sources of uncertainty and limitations of the Doppler Shift Attenuation method, one can mention the kinematics of the nuclei inside the stopper, the side feeding, and the limited knowledge of the population of the energy levels from the reaction. These sources of uncertainty are discussed further in Section 5.4

Chapter 4

Data pre-processing

Before starting the data analysis for measuring the lifetimes of the nuclear-excited states of interest, a pre-processing of the data is needed. The GALILEO detectors have been calibrated, the performance of each detector has been evaluated in terms of energy resolution, and the whole array has been characterized in terms of efficiency. Gates to reduce pile-up events were set and thresholds to improve the rejection of the Compton events were updated with respect to the conditions during the experiment, as described in Section 4.1. The SPIDER detectors were calibrated and aligned in time with the HPGe detectors. The silicon strips of SPIDER were characterized in terms of energy resolution and their status is reported in Section 4.2. The calibration procedure of the plunger device is briefly described in the last section of this chapter, Section 4.3.

4.1 Pre-processing of the GALILEO data

The energy calibration for the HPGe detectors was performed and, if present, the drifts in time of the detected γ-ray energies have been corrected. The energy thresholds have been optimized to improve the rejection of the Compton scattered events and the add-back procedure was performed in the GTC detectors. The GALILEO array was characterized in terms of efficiency and the results are given in the following sections.

4.1.1 Energy calibration and energy resolution of the HPGe detectors

The energy deposited by the γ rays in the HPGe detector is proportional to the charge collected by the electrodes. To calibrate the signals produced by the detector from ADC channels into energy, source data with known γ-ray energies such as ^{60}Co, ^{133}Ba, ^{152}Eu, and ^{226}Ra were employed, covering a wide energy range from tens of keV up to 3 MeV.

For HPGe detectors, the energy as a function of the ADC channel does not always behave linearly. This effect is typically observed at low energies, where the energy grows

exponentially with respect to the ADC channel, followed by a linear increase. Thus, to account for this effect, the Eq. 4.1 is used for the energy calibration of the HPGe detectors:

$$E(x) = ax + b(1 + e^{-\lambda x}) \tag{4.1}$$

where x is the ADC channel, a is the slope, b is the offset, and λ is the exponential parameter. The γ rays at low energies, $E_\gamma < 300$ keV, are very sensitive to the exponential term of the function while the linear dependence dominates for higher energy γ rays. A test was performed to evaluate the adequate performance of this function on the calibrated spectrum. The raw data were calibrated using a first-order polynomial and a linear plus an exponential function as given by the Eq. 4.1. The difference between the γ-ray energy of the corresponding sources with the centroid obtained from the fit of the γ-ray peak after calibrating the spectrum is shown in Fig.4.1 as a function of the ADC channel.

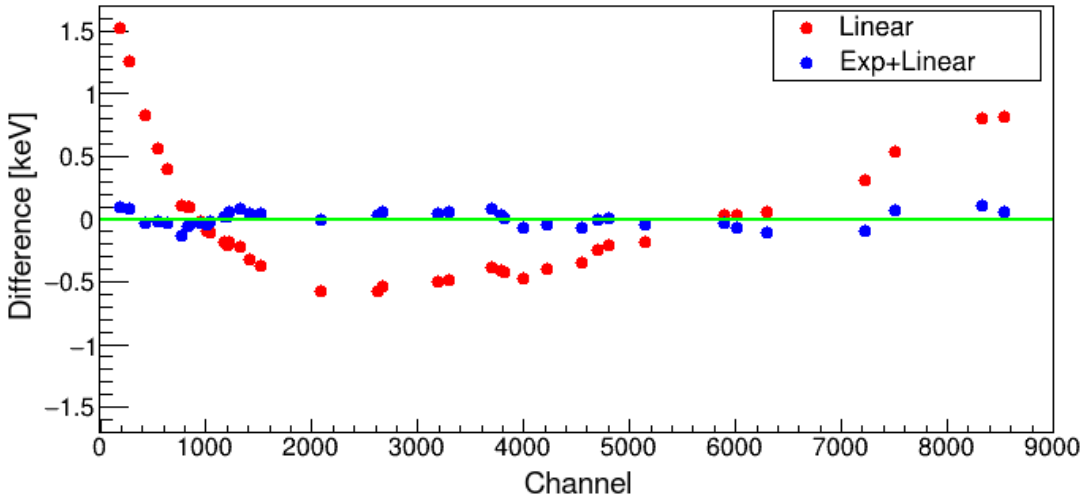

Figure 4.1: The calibrated energy spectrum using a first-order polynomial and that obtained by a linear plus exponential function are compared. The difference between the known energy of the γ-ray and the centroid obtained from the fit of the γ-ray peak is plotted with respect to the ADC channel for one of the detectors of the GALILEO array. The energy calibration performed with the linear plus exponential function is more effective than a first-order polynomial.

It is clear from the figure that the use of a non-linear function improves the energy calibration of the detector. It has to be pointed out that the non-linear behavior of the detected γ-ray energy with respect to the ADC channel was present in most of the detectors of the GALILEO array, while a few of them showed a linear behavior, thus a first-order polynomial was used to calibrate them in energy.

Figure 4.2 shows the energy resolution in full-width at half maximum (FWHM) at 1332 keV for every HPGe detector of the GALILEO array. The average energy resolution of the detectors is around 2.5 keV. The detector with ID 105, corresponding to detector 03A, shows an FWHM of around 4 keV at 1.3 MeV, so this detector was excluded from the

analysis since its resolution is 60% above the average value. The detectors with ID 102, 115, and 121 were physically present in the array but excluded from the data acquisition (refer to Fig. 3.6 and Tab. 3.1 for the position of these detectors in the array). Finally, the data accumulated from the 46 remaining HPGe detectors of the GALILEO γ-ray array was processed further in the analysis.

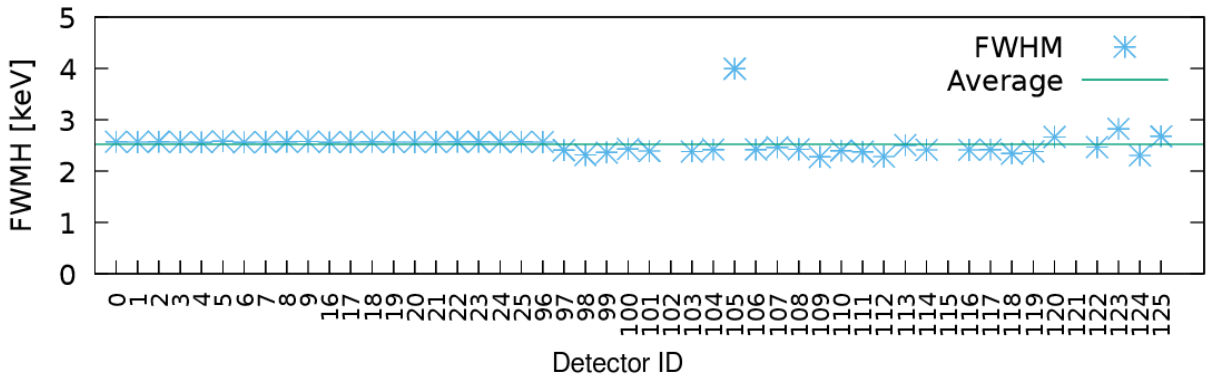

Figure 4.2: The energy resolution of all the HPGe of the GALILEO array in FWHM at 1332 keV. The average value is represented with the green line. The detector with ID 105 showed an energy resolution around 60% above the average value and was excluded from the analysis. The detectors with ID 102, 115, and 121 were absent in the acquisition.

4.1.2 Time alignment of the HPGe detectors

Gamma rays that reach the detectors within a given time window are defined to be in coincidence with each other. Transitions belonging to the same cascade can be observed in coincidence only if the detectors are aligned in time, thus the signals of the GALILEO detectors were aligned and the time window for $\gamma\gamma$ coincidence measurements was defined. In the acquisition, a time window of 1 μs is set but a narrower gate is set in the offline analysis in order to avoid random coincidences.

The time difference between the first event detected in the crystal with ID=0, chosen as a reference, and the events seen by the rest of the detectors is shown in Fig. 4.3. The time difference has been aligned to zero by applying an offset for all the detectors, and a time window ranging from $\pm$50 ns was chosen for setting the $\gamma\gamma$ coincidences. The γ-ray spectrum obtained in coincidence with the 582-keV transition in ^{83}Se is used to measure the lifetime of the 1100-keV level, as it will be shown in the analysis in Chapter 5.

4.1.3 Pile-up rejection

As mentioned in the previous chapter, thanks to the electronics of GALILEO, the energy of the γ rays may be measured by applying a trapezoidal filter to the signals (long trace energy) or by computing the pulse-height information (short trace energy). The energy obtained by the long traces is more accurate, but using the short traces may be more useful

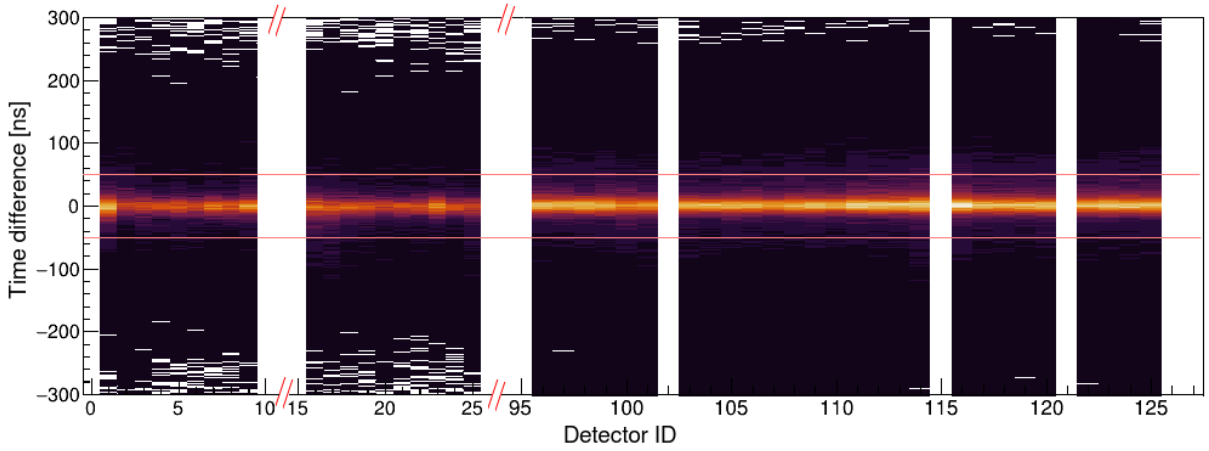

Figure 4.3: Time alignment of the HPGe detectors of the GALILEO array. The time difference between one detected event in the reference detector with the events seen by all the rest has been aligned to zero. A time window from ±50 ns was chosen to set up the $\gamma\gamma$ coincidences.

when dealing with pile-up events due to high counting rates. Pile-up is the superposition of the pulses due to the slow decay time of the signal compared to the incoming flux of photons.

The effect of the pile-up can be seen in the matrix of Fig. 4.4 (Left panel). The energy of the γ-rays measured by the short traces is plotted with respect to the energy measured by the long traces. The events lying outside the diagonal line are due to pile-up. In the offline analysis, cuts may be applied by selecting the diagonal line, as shown in the figure, in order to reject such events. In this work, the counting rate of the detectors was close to hundreds of Hz: due to the low counting rate, the effects of pile-up are not present in the data, as can be seen in the right panel of Fig. 4.4 where the energy measured by the short or the long traces lays in the diagonal line of the matrix.

4.1.4 Compton background reduction

The Compton scattering is the dominant process of interaction of the germanium material with γ-ray photons in the energy range from a few hundreds of keV up to a few MeV. To reduce those events where the photon energy is only partially deposited in the detector, the BGO crystal scintillator surrounds the triple clusters and the single crystals of GALILEO. The BGO acts as a veto in the acquisition, rejecting all the events in coincidence with the HPGe detectors. A time window of 150 ns was set for rejecting the Compton scattered events. The energy of the events triggered by an HPGe detector and seen by its surrounding BGO outside this time window is stored and used afterwards in the offline procedure to further improve the rejection of the Compton-scattered events.

Setting a threshold on the energy of the BGO helps to reduce the number of events in random coincidence with the HPGe detectors. The threshold will affect the efficiency

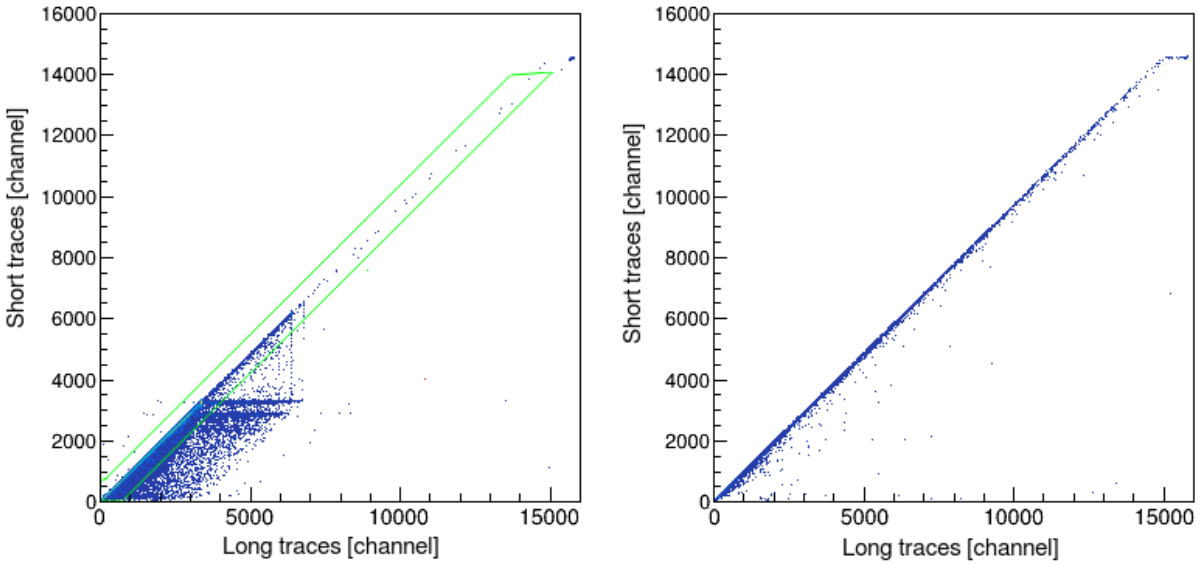

Figure 4.4: The energy measured from short traces as a function of the energy measured from the long traces. The data points outside the diagonal emerge from pile-up events. (Left) Acquired Co-source data. The detector rates close to 1 kHz. The gate for the rejection of the pile-up events is shown in green color. (Right) Data was acquired during the present experiment where no pile-up events are visible. The detector rates were a few hundreds of Hz.

and the Peak-To-Total ratio. The efficiency and the P/T ratio for one of the GALILEO detectors are plotted with respect to the BGO threshold and are shown in Fig. 4.5. A high threshold results in a lowering of the P/T ratio, whereas, a low threshold would negatively impact the efficiency curve, therefore, setting the threshold is a compromise between efficiency and the P/T ratio. The optimal value of the BGO energy threshold is chosen at the start of the plateau in the efficiency curve as shown with the dashed line in the figure. The procedure to optimize the rejection of Compton scattered events was applied to all the detectors present in the array. A comparison of the energy spectrum with and without the rejection of the Compton scattered events is shown for the same detector in Fig. 4.6.

4.1.5 Addback

As mentioned earlier, because of the Compton scattering process, γ rays escape the germanium volume without depositing all the energy, giving rise to a huge continuous background in the γ-ray energy spectrum. For the triple cluster detectors, where three HPGe crystals are in next to each other, the energy of these events may be recovered with the add-back procedure. This procedure involves γ-ray events that interact with one HPGe crystal via the Compton effect, escape to the neighboring germanium crystal, and get absorbed. These events measured in coincidence between two or three HPGe crystals that belong to the same triple cluster may be summed together, allowing one to reduce the

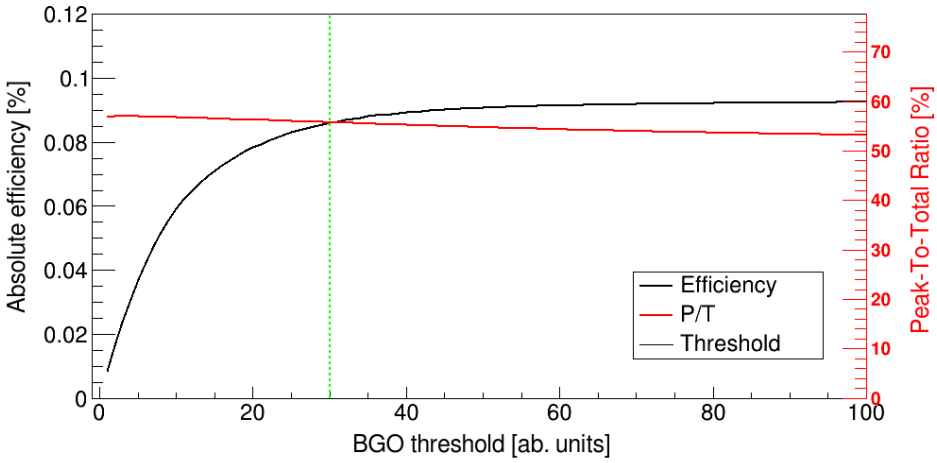

Figure 4.5: The efficiency curve and the P/T ratio as a function of the BGO energy threshold for one detector of the GALILEO array. The detection efficiency and the P/T ratio are affected in opposite tendencies by the change of the BGO threshold.The optimal threshold is chosen at the start of the plateau in the efficiency curve. The vertical line represents the optimal value of the BGO threshold.

Compton background and increase the efficiency in the photopeak. Events appearing in neighboring HPGe crystals of a triple cluster within a time window of 100 ns and not in coincidence with the surrounding BGO detector are summed together. Figure 4.6 shows a comparison of the γ-ray energy spectrum for one triple cluster of the GALILEO array without any condition, with Compton suppression, and add-back procedure applied. From the figure, it is evident that the number of counts in the photopeak has increased and the Compton background has reduced after applying the add-back procedure. The efficiency in the 1332-keV peak increased from 0.20% to 0.23% and the P/T ratio changed from 18% to 37% compared to the γ-ray spectrum where no conditions are applied.

4.1.6 Gamma-ray detection efficiency of the GALILEO array

The detection efficiency depends on the energy of a γ-ray photon. The efficiency is at maximum for γ ray energies of around 200 keV where the probability of the γ-ray to deposit the total energy inside the detector volume is higher.

At the end of the experiment described in this thesis, an efficiency run was taken with an ^{152}Eu source with known activity placed at the target position of the GALILEO reaction chamber. The SPIDER detector and the plunger device were also placed in the chamber in order to account for the possible absorption of γ rays from their material. The absolute detection efficiency for γ rays with energy E_γ is calculated with the formula:

$$E_{ff}(E_\gamma) = \frac{C}{A \cdot t_m \cdot P_\gamma \cdot (1 - D_t)} \tag{4.2}$$

where C is the number of the detected counts in the photopeak with energy E_γ, A is the

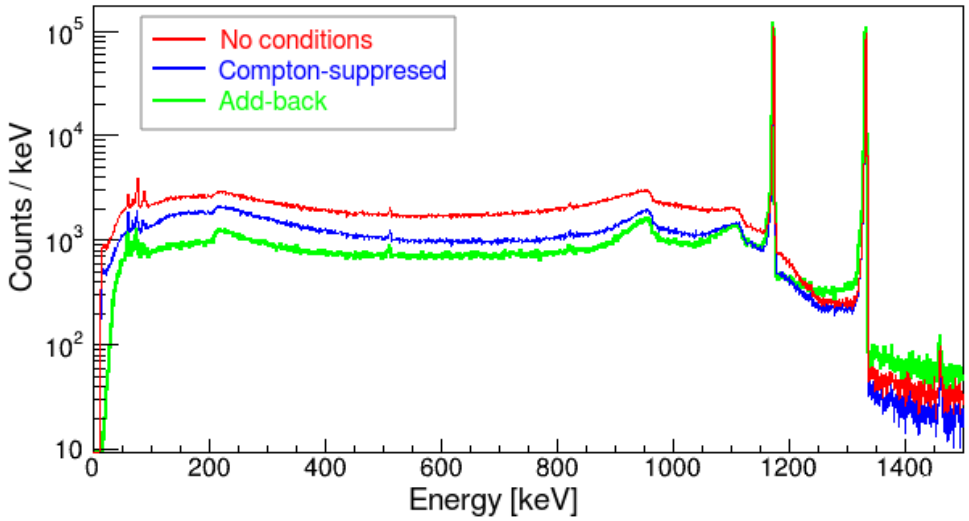

Figure 4.6: Comparison of the ^{60}Co γ-ray spectrum without any conditions, with Compton suppression, and add-back procedure applied, for one triple cluster detector of GALILEO. After the add-back procedure is applied to the data, the photopeak efficiency increases, and the P/T ratio improves.

activity of the source, t_m is the time of measurement time with the γ-ray source, P_γ is the probability the source to decay by the γ-ray transition with energy E_γ and D_t is the 'dead time' of the acquisition system. The probabilities P_γ used to calculate the efficiency were taken from the reference [6]. The dead time of the DAQ was approximately 0.4%. The experimental data points for the calculated efficiency using Eq. 4.2 are shown in Fig. 4.7. The main contribution to the error bars of the experimental data points is the uncertainty of the activity of the source, around 3%. The experimental data points obtained from the ^{152}Eu measurement are fitted with the Eq. 4.3:

$$E_{ff}(x) = ax^b \cdot exp\Big\{-\Big(\frac{x}{c}\Big)^d\Big\} \tag{4.3}$$

where x is the energy of the γ ray, and a, b, c, and d are parameters of the fit. The absolute efficiency curve of the GALILEO γ array is shown in Fig. 4.7 with the red line.

The efficiency curves of the GTC and GASP detectors are shown with the blue and green lines, respectively. The efficiency curve of the 90° ring of GALILEO is displayed with a light blue line. The efficiency of the 90° ring is particularly important in the analysis procedure for the determination of the lifetimes of the nuclear-excited states, as it will be discussed in Chapter 5.

4.1.7 Stability of the HPGe detectors during the experiment

Due to several factors, such as the high counting rate, temperature, or humidity, the stability of the HPGe signals may be affected and consequently, the energy measured by the detectors can drift over time. To check the stability, the measured energy of the γ

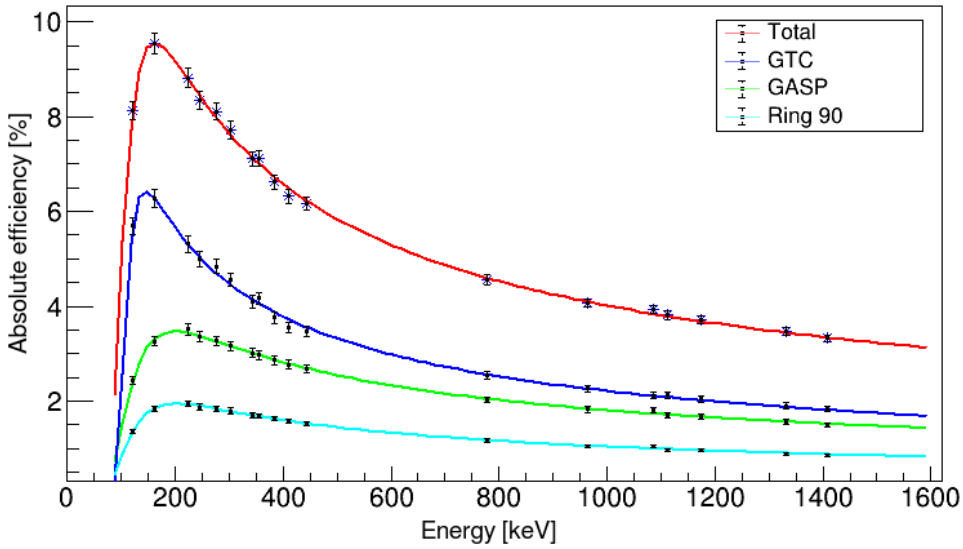

Figure 4.7: The total absolute efficiency curve of the full GALILEO γ-ray array compared with the efficiency curve of its components, the GTC, GASP, and 90° ring detectors.

rays by every detector is plotted as a function of the time stamp of the event. Figure 4.8 (Right panel) shows the energy of the $2^+ \rightarrow 0^+$ transition of ^{82}Se (654 keV) measured by every crystal in a time interval of 10 minutes for all the duration of the experiment. As can be seen from the figure, for several detectors the measured γ-ray energy oscillates over time up to 1 keV.

To correct these small drifts, three γ-ray peaks of the energy spectrum of known transitions are selected and fitted every 10 minutes of accumulated data. The selected peaks correspond to γ-ray transitions of ^{197}Au (279 keV), ^{82}Se (654.5 keV), and the 1460 keV transition from the decay of ^{40}K. The three centroids are fitted with a linear function, and the coefficients are used to recalibrate the spectrum. The correction of the energy drifts over time is shown for the 654.5-keV peak in the left panels of Fig. 4.8.

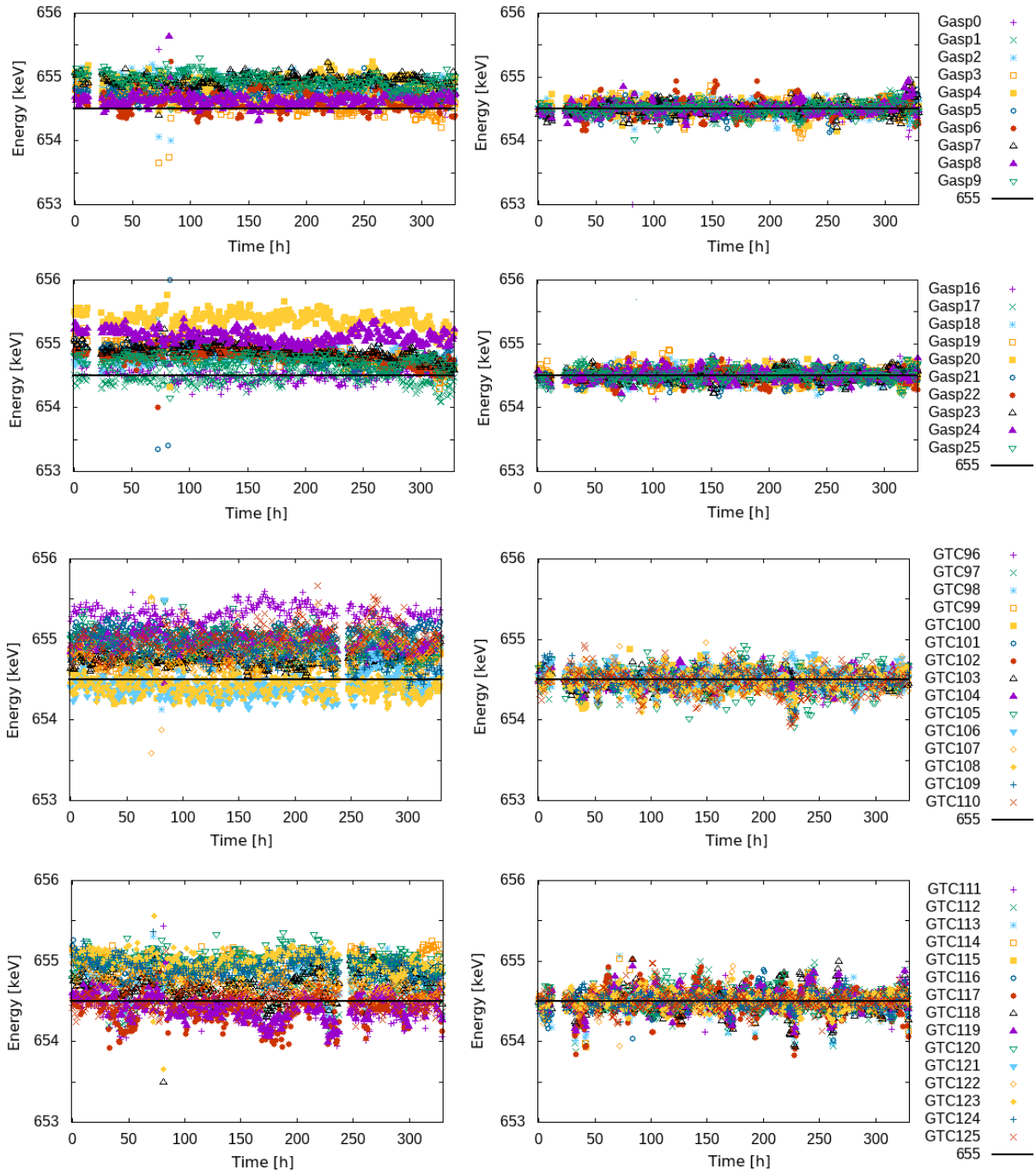

Figure 4.8: The detected energy of the 654-keV $2^+ \rightarrow 0^+$ transition of ^{82}Se as a function of time during the duration of the experiment. (Left) Before applying the correction. (Right) After applying the correction.

4.2 Pre-processing of SPIDER data

All the segments of the SPIDER detector have been characterized in terms of energy resolution and calibrated by using an alpha source. To measure γ rays in coincidence with protons, the signals of the SPIDER detectors were aligned in time with the ones of the GALILEO array, and a narrow time window was set to avoid random coincidences.

4.2.1 Energy calibration

For the energy calibration of the SPIDER detector, a triple α source was used: ^{239}Pu, ^{241}Am, ^{244}Cm. The energies of the most intense α particles emitted from these sources are 4805 keV, 5055 keV, and 5480 keV, respectively. A linear function fitting the centroids of the three α peaks was used to convert ADC channels into energy. Figure 4.9 shows the calibrated spectrum of each detector. As can be seen from the figure, the three peaks of the alpha source are well separated from each other and well aligned in energy. The segments of SPIDER with ID numbers 70, 97, 98, 102, 113, 114, 118, 120, 122, 125, and 126, showed the presence of noise in the signal or a low resolution, and therefore they were excluded from the analysis.

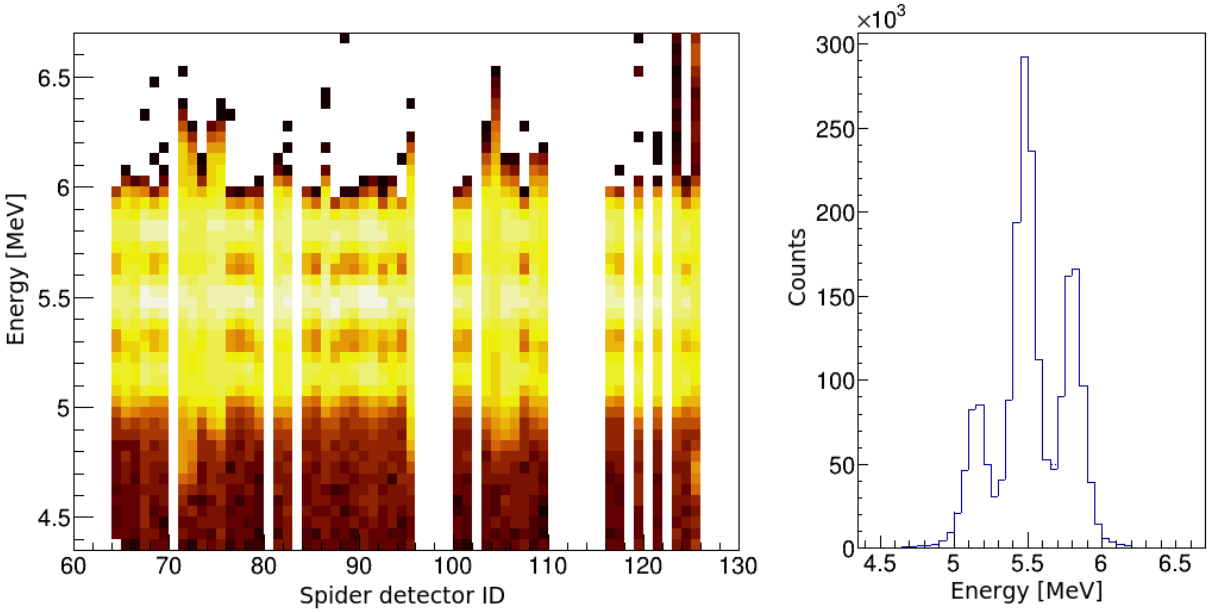

Figure 4.9: (Left) Energy of the alpha particles versus the ID of the segments of SPIDER. Data acquired with a triple alpha source: ^{239}Pu, ^{241}Am, ^{244}Cm. The energies of the most intense α particles emitted from these sources are 4805 keV, 5055 keV, and 5480 keV, respectively. (Right) Projection of the matrix on the energy axis.

The energy resolution in FWHM of the ^{241}Am peak (5055 keV) of every segment is presented in Fig. 4.10. The overall resolution at 5 MeV is around 0.15 MeV.

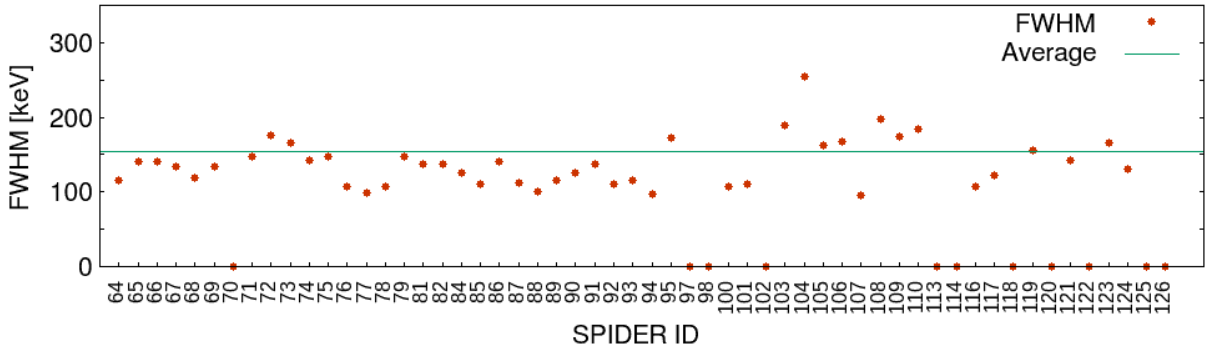

Figure 4.10: Energy resolution at FWHM of the SPIDER segments at 5 MeV. The segments excluded from the analysis are indicated with energy resolution zero.

4.2.2 Time alignment of SPIDER with HPGe

To perform coincidence measurements between the protons and the γ rays, a time alignment of each SPIDER detector with the HPGe crystals has to be performed. As anticipated, a time window of 1 μs is used in the acquisition for accepting events in coincidence. A higher selectivity and reduction of random coincidences can be achieved by setting a narrower time window. The time difference between events detected in SPIDER and the GALILEO array is plotted for all the SPIDER detectors in Fig. 4.11. The top panel shows this quantity during the experiment, while the bottom panel of the figure shows the time alignment performed offline by applying an offset on the time difference of the signals to align the coincidence peak to zero. The detectors of GALILEO were already aligned in time previously so each detector or the whole array could be used as a reference. The time window set for the proton-γ coincidence ranges from -60 ns up to +100 ns.

4.3 Plunger calibration

The target and the stopper foil of the plunger device are electrically insulated. When placed at a short distance, the two parallel plates act like a capacitor and the capacitance C is related to the distance between the two foils by the equation:

$$C(d) = \epsilon \frac{A}{d} \tag{4.4}$$

where A is the area of the foils seen from each other, ϵ is the absolute permittivity of the dielectric material between the two foils, and d is the distance between them. A pulse with an amplitude of 5 V is applied to the target foil. The charge Q generated is proportional to the voltage V and the capacitance C:

$$Q(d) = C(d)V \tag{4.5}$$

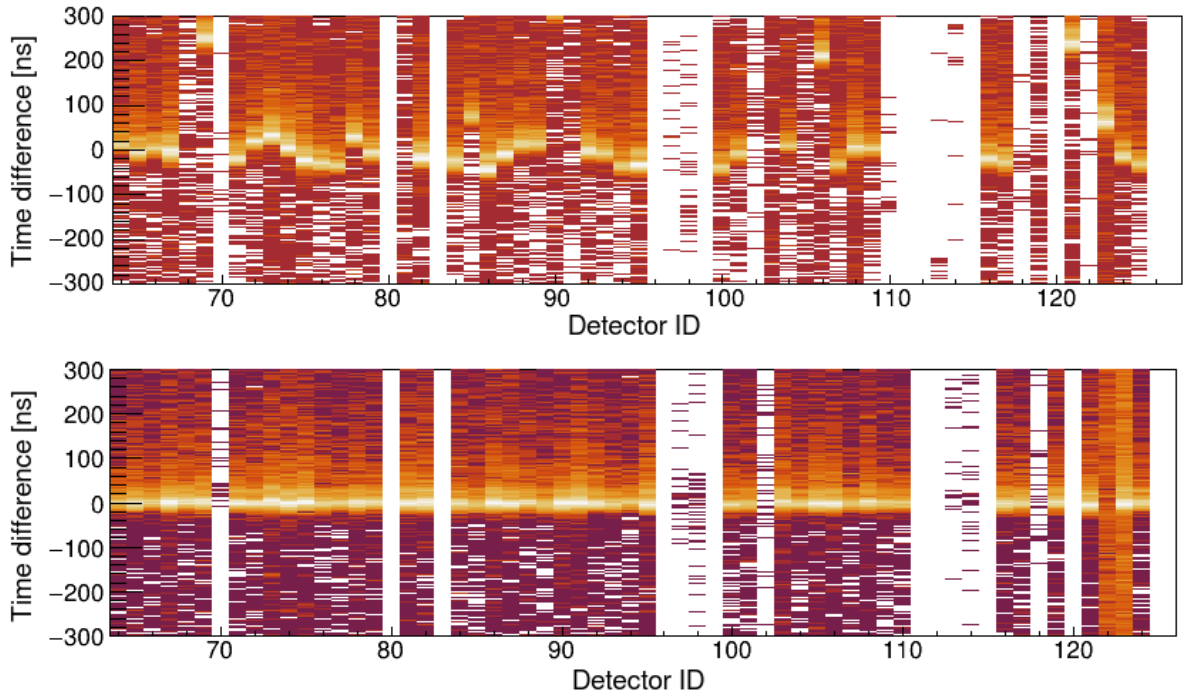

Figure 4.11: The time difference between the signals of each SPIDER segment with those of the HPGe detectors. (Top) The time alignment during the experiment. (Bottom) The time difference between the events detected in SPIDER and in the GALILEO array aligned to zero in the offline analysis.

The zero distance between the foils is found by reducing the distance between the two foils until there is a mechanical contact. At this position, the capacitance suffers a sudden change. As mentioned previously, the plunger device is connected to a step motor. Thus, after setting the zero point, the motor position is used to convert the capacitance to distance in μm. The plunger is calibrated after being mounted inside the reaction chamber, and the vacuum level reaches the optimal value.

Chapter 5

Data analysis

The analysis for measuring the lifetime of the 311-keV $1/2^+$ and 1100-keV $5/2^+$ intruder states is presented in this chapter.The observed γ-rays and their intensities are shown in Section 5.1. The RDDS data set has been analyzed using the standard techniques, the Decay Curve Method and the Differential Decay Curve Method introduced in Section 5.2 and 5.3. For the data collected with the DSAM technique, realistic simulations were performed to extract the lifetimes of the nuclear-excited states as introduced in Section 5.3. Systematic uncertainties are discussed in Section 5.4, and the final results are summarized in Section 5.5.

5.1 Level scheme of ^{83}Se

Before starting the analysis procedure for the lifetime measurement one needs information on the population of the levels of interest and the identification of possible background sources that may impact the final results. Known γ-ray lines were identified in the spectrum by means of $\gamma\gamma$ coincidence. Since many excited states of ^{83}Se have lifetimes in the region of sensitivity of the RDDS and DSAM technique, the coincidence is set between the full GALILEO array and the ring at 90°, avoiding the presence in the spectrum of γ-ray peaks shifted in energy due to the decay of the nucleus in flight and making in this way easier to identify the γ-ray transitions.

A γ-ray spectrum in coincidence with the protons is shown in Fig. 5.1.a where one of the most intense peaks is the 582-keV peak, an E2 transition of ^{83}Se connecting the 582-keV $5/2^+$ intruder state with the ground state. The γ-ray spectrum in coincidence with the 582-keV transition is shown in Fig. 5.1.b. The γ-ray peaks belonging to ^{83}Se are marked with the dashed line in the figure. No γ-ray transitions belonging to other reaction channels are found, making this an excellent gate for the analysis.

The spectrum gated on the 518-keV transition is shown in Fig. 5.1.c where the transition at 357 keV indicated with an asterisk belongs to ^{83}Br. The intensity of this peak is much smaller compared to the intensity of the transitions that belong to ^{83}Se. The

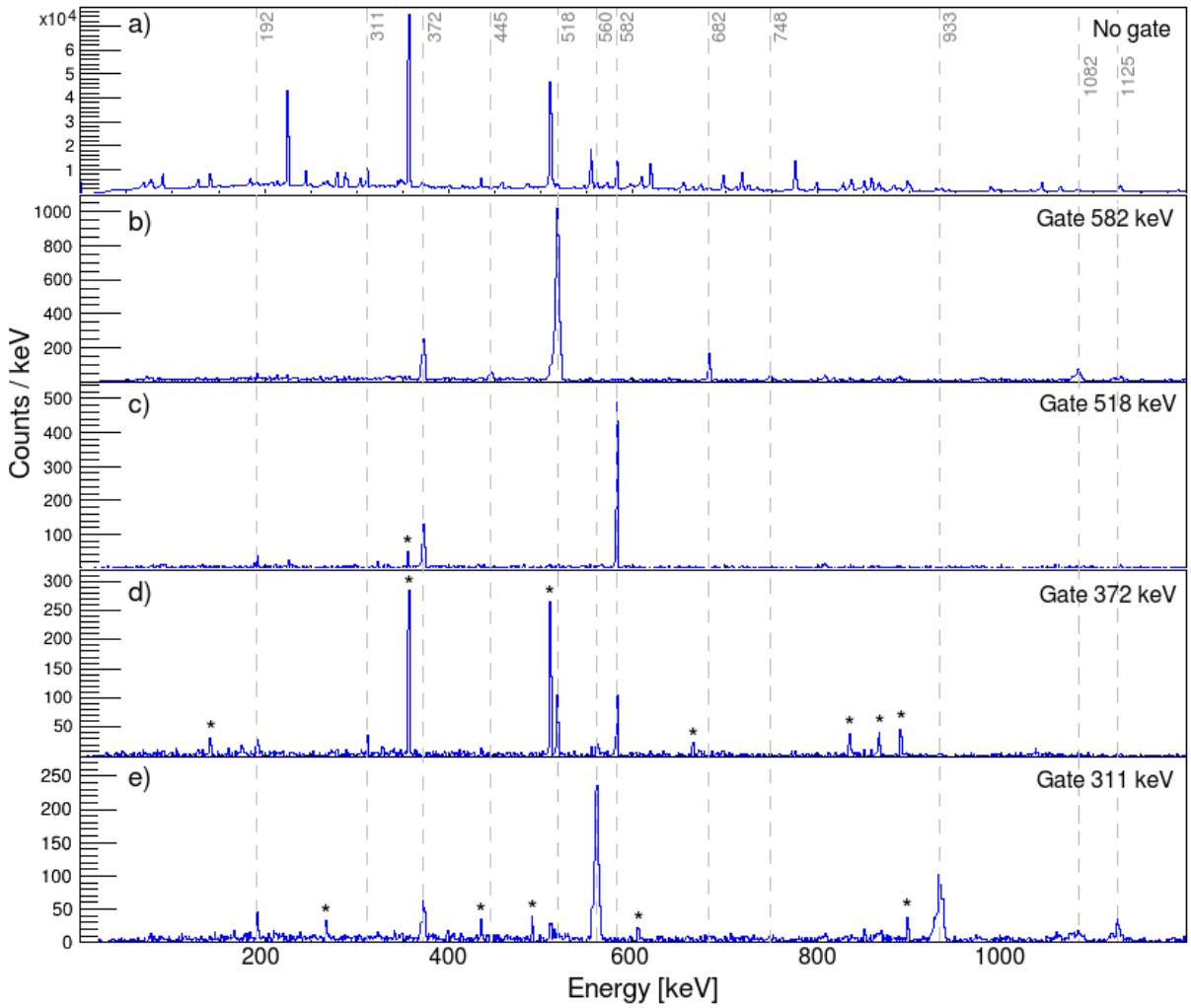

Figure 5.1: a) Gamma-ray spectra obtained by the coincidence with the protons. Gamma-ray spectra b) gated on 582 keV, c) gated on 518 keV, d) gated on 372 keV, and e) gated on 311 keV. The coincidence is set between the full GALILEO array and the 90° ring to avoid the Doppler effect. The peaks that are marked with an asterisk are contaminants or not identified, while the peaks marked with the dashed lines indicate transitions belonging to ^{83}Se.

situation differs when gating on other weak transitions of ^{83}Se. The γ-ray spectrum gated on the 372-keV and 311-keV transitions show the presence of contaminants (See Fig. 5.1.d and 5.1.e) with intensities that dominate over the transitions of ^{83}Se. The transitions are identified to belong to ^{83}Br (356, 510, 835, 889 keV), ^{197}Au (267 keV), ^{90}Zr (141 keV) or ^{88}Sr (434 keV). The presence of these transitions results from the composition of the target and the presence of the Au backing. Gamma-ray peaks belonging to ^{90}Zr or ^{88}Sr arise in the γ-ray spectrum from the fusion evaporation reaction of the beam with the ^{12}C present in the target while the gold peaks are due to the Coulex reaction between the ^{82}Se beam and the Au backing of the target.

The transitions identified in the γ-ray gated spectrum belonging to ^{83}Se are already known from previous studies. The energies measured in this experiment coincide with

the values in the literature [6, 60, 67]. A partial level scheme of ^{83}Se was constructed, containing all the transitions identified in the γ-ray spectra. Spin and parities of the levels were assigned based on the existing database [6]. The width of the arrows representing the γ-ray transitions is proportional to the measured intensity, corrected by the efficiency curve introduced in Chapter 4 and relative to the intensity of the 582-keV transition of ^{83}Se. As seen from the level scheme in Fig. 5.2, low-lying states are populated with higher intensity and excited states are seen up to 2 MeV excitation energy.

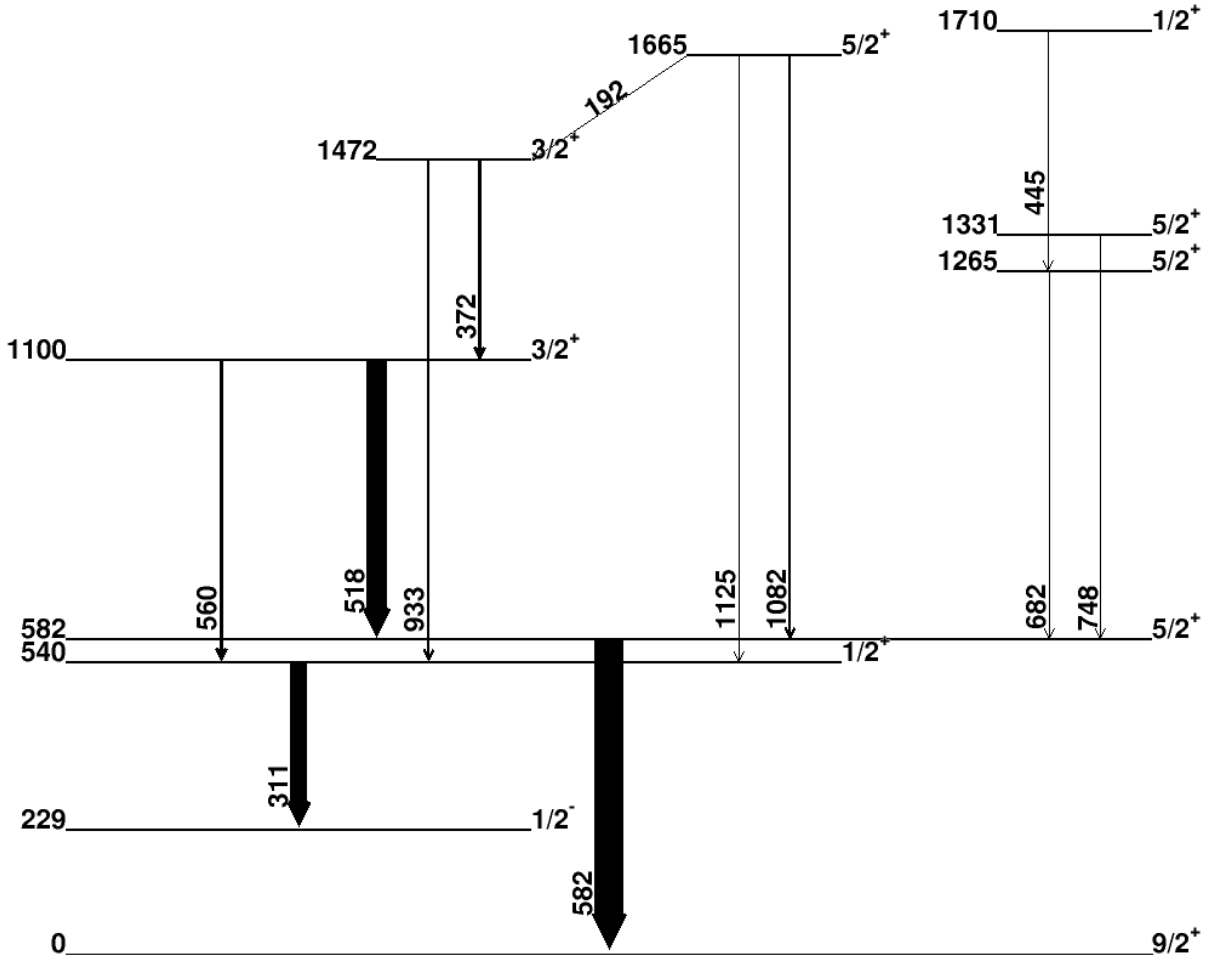

Figure 5.2: Partial level scheme of ^{83}Se constructed from the γ-ray transitions observed in the present work. The assignment of spin, parity, and excitation energies is based on the existing literature. The width of the arrows representing the γ-ray transitions is proportional to their intensity.

Table 5.1 summarizes energies, spin, parities, and intensities of the identified transitions relative to the intensity of the 582-keV transition.

5.2 Analysis of the RDDS data

As introduced in the previous chapter, the lifetime of the 540-keV $1/2^+$ intruder state of ^{83}Se was measured by using the RDDS technique. Measurements were performed for

Table 5.1: Energies and intensities of the ^{83}Se γ-ray transitions observed in this experiment. Spin and parities of the levels involved are also given. The intensities are relative to the E_γ=582 keV.

E_i [keV]	J_i^π	E_f [keV]	J_f^π	E_γ [keV]	Iγ [%]
540	$1/2^+$	229	$1/2^-$	311.1 (8)	59.53(3)
582	$5/2^+$	0	$9/2^+$	582.4 (8)	100.00 (5)
1100	$3/2^+$	582	$5/2^+$	517.9 (8)	69.23 (4)
1100	$3/2^+$	540	$1/2^+$	560.7 (8)	11.81(1)
1265	$5/2^+$	582	$5/2^+$	682.5 (8)	4.90 (1)
1331	$5/2^+$	582	$5/2^+$	748.9 (9)	2.57 (1)
1472	$3/2^+$	540	$1/2^+$	933.6 (9)	9.12(1)
1472	$3/2^+$	1100	$3/2^+$	372.2 (8)	11.43 (1)
1665	$5/2^+$	1472	$3/2^+$	192.5 (7)	0.87 (3)
1665	$5/2^+$	582	$5/2^+$	1082 (1)	7.88 (1)
1665	$5/2^+$	540	$1/2^+$	1125 (1)	1.53(4)
1710	$1/2^+$	1331	$5/2^+$	445.6 (8)	3.03 (1)

several distances between the target and the stopper. Thanks to the setup used in this experiment, GALILEO coupled to SPIDER, one can achieve a high selectivity event-by-event and an effective control on the side feeding of the state of interest by γ-particle coincidences.

5.2.1 The kinematic line of the 540-keV state

One of the main factors contributing to uncertainties when performing lifetime measurements of nuclear-excited states is the population of the state of interest from higher energy levels. The ideal situation would be to directly populate the state of interest, but one cannot have such control in a nuclear reaction. With the proper experimental setup, it is possible to limit such effects and to select events directly populating the state of interest.

In a two-body nuclear reaction, the measurement of the angle of emission and the energy of one of the partners allows the reconstruction of the trajectory of the other. Moreover, in a (d,p) reaction a particular excited state of the nucleus of interest can be selected by measuring the energy of the outgoing proton [1], as discussed in Section 2.3. Thanks to the segmentation of the silicon detector used in this experiment to detect the protons coming from the (d,p) reaction, the angles of emission and the energy can be measured with enough precision to allow the reconstruction of the kinematic lines.

The 540-keV state decays by emitting a 311-keV γ ray, as shown in the level scheme in Fig. 5.2. This energy level is fed from the 1100-keV, 1472-keV, and 1665-keV states via γ-ray transitions with energy of 560 keV, 933 keV, and 1125 keV, respectively. The kinematic line derived from the energy of the protons measured by SPIDER as a function

of its angle of emission is drawn by selecting coincidences with γ-rays in the energy range from 300 to 350 keV and is shown in Fig. 5.3 (Left panel). The experimental data have been compared with the kinematic line calculated from the NPTools (blue line) [103] and as shown in the plot, the experimental kinematic line of the 540-keV state is compatible with the expected one. No kinematic line could be observed without the gate on the γ-rays. Since the 540-keV level is very close in energy to the 582-keV excited state, their kinematic lines are similar (compare the right and the left panel of Fig. 5.3). Still, this will not impact the lifetime determination of the 540-keV state since these two levels are not connected by any known γ-ray transition.

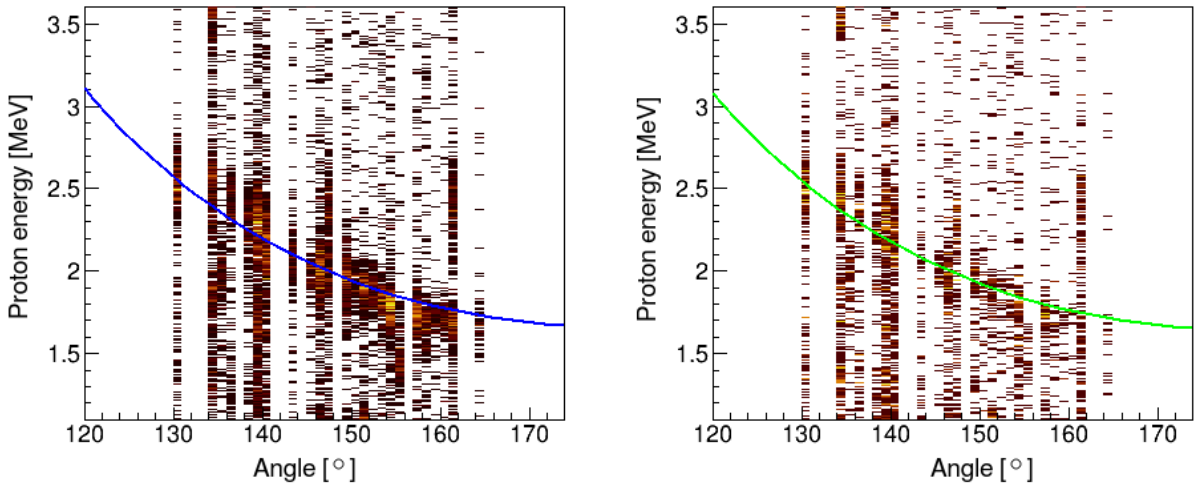

Figure 5.3: (Left) The kinematic line of the 540-keV state of ^{83}Se, i.e. the energy of the protons as a function of its angle of emission in coincidence with γ rays in the energy range from 300 to 350 keV. The experimental data are compared with the kinematic line calculated from NPTools (red line). (Right) The kinematic line of the 582-keV state of ^{83}Se in coincidence with γ rays with energy from 570 up to 590 keV. The experimental data are compared with the kinematic line calculated from NPTools (green line).

A 2D gate is applied, isolating the events in the kinematic line of the 540-keV state, and γ-rays are measured in coincidence. The gated γ-ray spectrum is shown in Fig. 5.4, with the blue color, and is compared with the non-gated spectrum for the 90° ring of GALILEO shown in red color. As can be seen from the figure, the background has reduced significantly in the gated γ-ray spectrum. The γ-ray peak in the gated spectrum corresponds to the 311-keV transition depopulating the 540-keV excited state. Using a (d,p) reaction with a gate on the energy of the ejectile and, hence, on the excitation energy of the state of interest eliminates any influence from the feeding transitions.

5.2.2 Gamma-ray spectra from the RDDS data set

The γ-ray energy spectrum obtained in coincidence with the 2D gate on the kinematic line of the 540-keV state for each distance between the plunger and the stopper (0.1, 2,

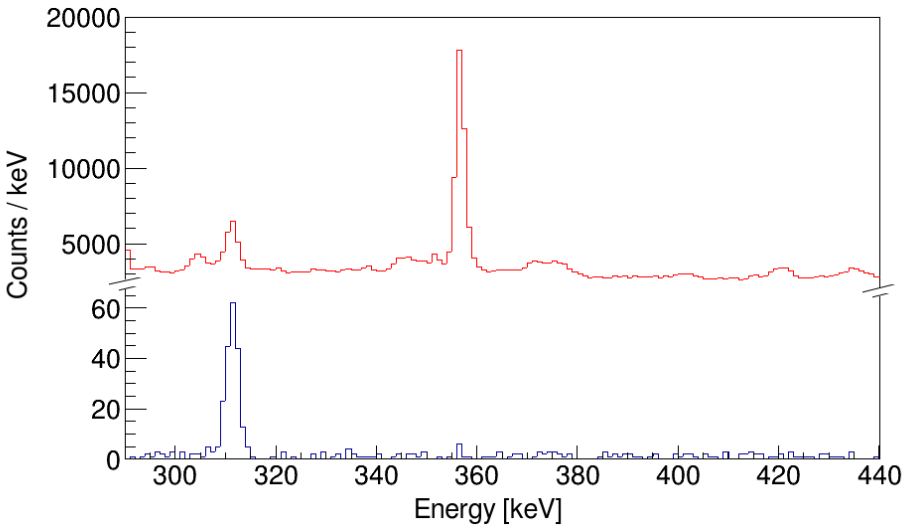

Figure 5.4: Energy γ-ray spectrum gated with the kinematic line of the 540-keV state compared to the non-gated spectrum for the 90° ring of GALILEO. The background is reduced significantly.

2.8, 3, 4, 5, and 7 mm) is presented in Fig. 5.5 for the transition of interest. The spectra are shown for the rings of GALILEO at 118, 146°, whereas, due to the low statistics, the data from the forward rings at 51° and 61° are added together. For these two rings, the sum spectra are analyzed by assuming an average angle between the two (56°).

In the γ-ray spectra at Fig. 5.5, the 311-keV peak is marked with a red line. This peak corresponds to the decay events depopulating the 540-keV intruder state when ^{83}Se is at rest in the stopper foil. The shifted component of the 311-keV transition appears at different energies for different rings. Because of the Doppler effect, a larger or smaller γ-ray energy will be measured depending on the observation angle of the γ ray (at higher energies for the 56° ring and at lower energies for the 118 and 146° rings). As seen from the spectra in Fig. 5.5, at short distances, the stopped component is dominant because the nucleus reaches the stopper before it undergoes γ decay. At long distances, the probability of decay between the target and the stopper is higher. The intensity of the shifted and the unshifted components which varies with the distance is due to the finite lifetime of the nuclear energy level. The intensities of these two peaks depend on the lifetime of the state.

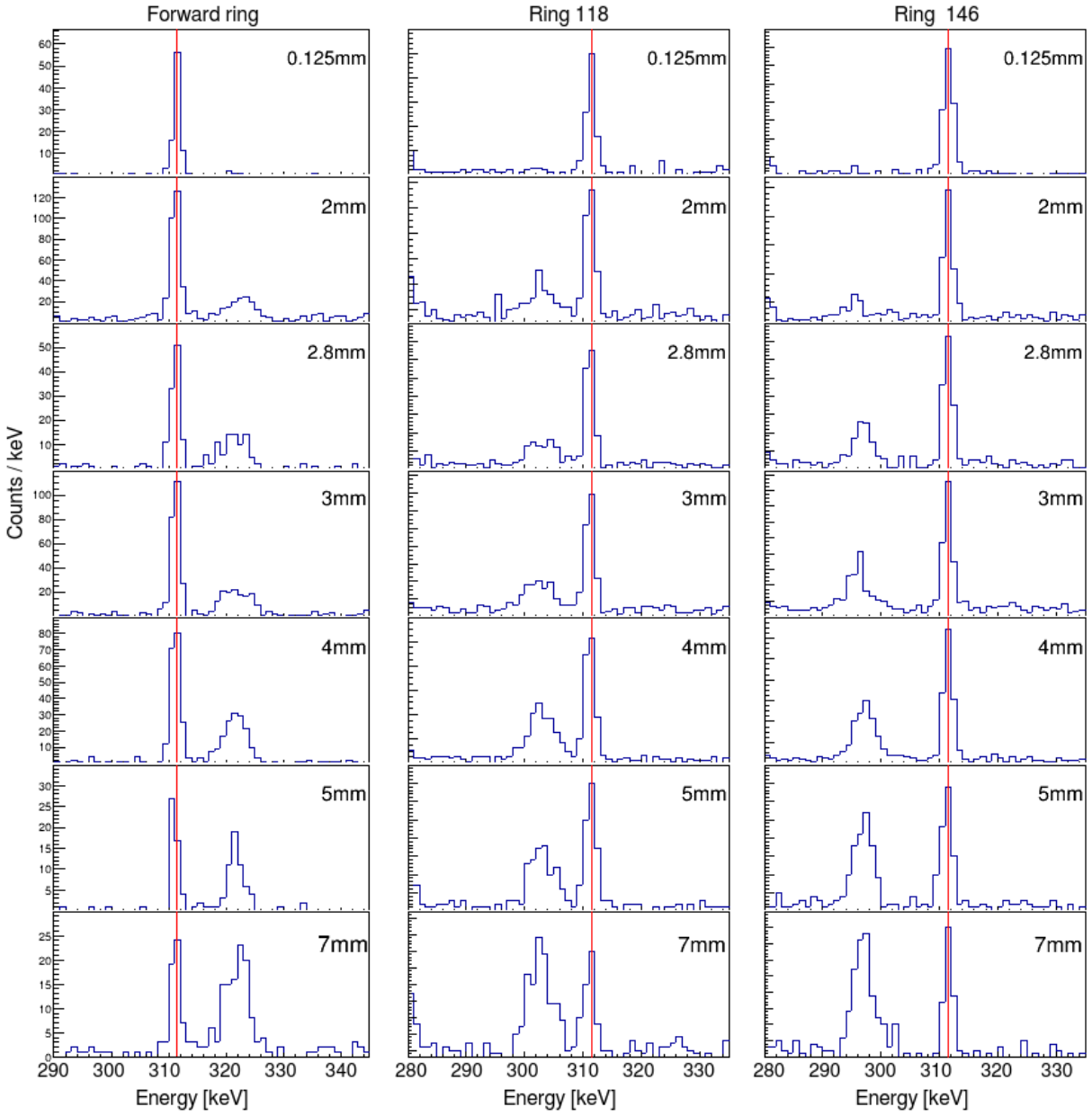

Figure 5.5: Gamma-ray energy spectra for different plunger distances between the target and the stopper for different rings of the GALILEO array, at 56 degrees, 118, and 146. The energy spectrum for the 311 keV transition depopulating the $1/2^+$ state was obtained in coincidence with one proton and with a 2D gate on the kinematic line of the 540-keV state. The red line represents the unshifted component while the second peak is the shifted one. The intensity of the shifted component increases with the distance, as expected.

5.2.3 Analysis of RDDS data

The RDDS data are typically analyzed using two different techniques: the Decay Curve Method (DCM) and the Differential Decay Curve Method (DDCM), that we have both applied in this work. A brief description of both techniques and their formalism is introduced in this section.

The DCM method

Assuming that a t=0, N_0 nuclei are produced in an excited state in the thin target and start to travel towards the stopper foil with a given velocity, its de-excitation may occur in flight or when the nucleus comes at rest in the stopper foil. Based on the radioactive decay law, the number of decays in flight will be given by:

$$I_s = N_0 \cdot exp\left(-\frac{t}{\tau}\right) = N_0 \cdot exp\left(-\frac{d}{v c \tau}\right) \tag{5.1}$$

where t is the time the nucleus is traveling between the target and the stopper, d is the distance between the target and the stopper, v is the velocity of the emitting nucleus, and τ is the lifetime of the nuclear-excited state. Considering Eq. 5.1, the number of nuclei decaying when stopped in the stopper foil, I_u, is given by the expression:

$$I_u = N_0 - I_s = N_0\left(1 - exp\left(-\frac{d}{v\tau}\right)\right) \tag{5.2}$$

As seen from the formula above, the intensities of the shifted and the unshifted components can be expressed in terms of variables known from the experimental data except N_0. To avoid this dependence, the ratio between the counts of the unshifted component and the total counts is defined as:

$$R(d) = \frac{I_u(d)}{I_u(d) + I_s(d)} \tag{5.3}$$

Combining Eq. 5.1 and 5.2, one obtains:

$$R(d) = exp\left(-\frac{d}{v\tau}\right) \tag{5.4}$$

The ratio $R(d)$ can be easily deduced from the experimental data, the distance between the stopper and the target is known and β can be obtained from the observed γ-ray spectra as it will be shown in Section 1.2.4. Thus, one ends up with one equation, Eq. 5.4, where the only unknown variable is τ, the lifetime of the state of interest which can be expressed as:

$$\tau = \frac{d}{v} ln\left(\frac{1}{R}\right) \tag{5.5}$$

To derive these equations, one has to assume that a given nucleus was directly populated in the state of interest. This is a strong assumption that can lead to an overestimation of the lifetime of the nuclear state. Many excited states are populated in a nuclear reaction, and the state of interest may be fed by higher-lying states with a finite lifetime. The feeding of the state of interest has to be considered unless there are experimental techniques that one can use to control it. This was the case in this work: GALILEO was coupled with the SPIDER detector, allowing one to select only events directly populating the state of interest. When the feeding cannot be controlled, a mathematical formalism can be used to deduce the lifetime of the state of interest [104].

The DDCM method

Another technique used in the analysis is the Differential Decay Curve Method (DDCM) [104, 105]. Different from DCM, it does not require the absolute distance between the target and the stopper, providing an advantage with respect to the standard analysis. With this technique, systematic errors can be easily identified, resulting in a reduction in the error of the measurement. For every distance between the target and the stopper, a lifetime is derived.

The Differential Decay Curve Method (DDCM) [104,105] is an alternative to analyze RDDS experimental data. Different from DCM, it does not require the absolute distance between the target and the stopper, providing an advantage with respect to the standard analysis. With this technique, some types of systematic errors can be easily identified, and for every distance between the target and the stopper where measurements are performed, a lifetime is derived.

The equation of the lifetime of the level i can be written as in Ref. [104]:

$$\tau_i = \frac{-N_i(t) + \sum b_{ki} N_k(t)}{\frac{dN_i(t)}{dt}} \tag{5.6}$$

In terms of the experimental observables, this equation turns to:

$$\tau_i = \frac{-R_i(t) + \sum b_{ki} \alpha_{ki} R_k(t)}{\frac{dR_i(t)}{dt}} \tag{5.7}$$

where $Ri(\mathrm{t})$ is the normalized ratio of the unshifted component as shown in Eq. 5.3 for the level i, which depends on $t = d/v$, the term $\sum b_{ki}\alpha_{ki}R_k(t)$ accounts for the contribution of the feeding of the level of interest i from higher lying states k, α_{ki} is a factor of proportionality depending on the detector efficiency and the angular distributions of the depopulating γ-ray transitions, b_{ki} is the branching ratio of the $k \rightarrow i$ transition. In this equation, the numerator is determined experimentally while the denominator is

obtained from the derivative of the fitted function to the ratio $R_i(t)$.The lifetime is deduced independently for each distance between the target and the stopper, and these results are fitted with a constant function τ(t).

Since in this work, the feeding can be controlled by the coincidences between GALILEO and SPIDER, this equation is simplified to:

$$\tau_t = \frac{-R_i(t)}{\frac{dR_i(t)}{dt}} \tag{5.8}$$

5.2.4 Velocity determination

As seen from the equations introduced in the previous section, the velocity of the recoils from the target to the stopper is needed in order to deduce the lifetimes of the levels of interest. This information can be obtained by exploiting the γ-ray spectrum measured in each ring of GALILEO. The energy difference between the shifted and the unshifted component changes depending on the Doppler shift formula (see Eq. 3.3). Knowing the angle of each ring and the energy splitting from the γ-ray spectra of the two peaks, the velocity of the recoils is obtained.

Figure 5.6 shows the energy spectrum gated in the kinematic line of the 540-keV state, for every ring of GALILEO. As seen from the figure, depending on the angle, the energy difference between the shifted and the unshifted changes as expected. The energies of the shifted and the unshifted component and the results, in terms of β=v/c are reported for every ring in Tab. 5.2.

The weighted average of the β value obtained independently for each ring gives β=(5.8±0.5)%. This value is the one used in the analysis for the determination of the lifetime of the 540-keV state of ^{83}Se. This value of β is also confirmed by the calculations of the energy losses of the beam and reaction product in the target, performed with the Lise++ program [87].

Table 5.2: The β value determined for each ring of the GALILEO array based on the energy of the shifted and unshifted component of the 311 keV transition. The weighted average of these results obtained independently for each ring gives β=(5.8±0.5). This value of the β is used in the analysis.

Ring [°]	$E_{unshifted}$ [keV]	$E_{shifted}$ [keV]	β [%]
51	311.2±0.8	323.1±1.5	5.7±0.8
61	311.1±0.8	320.5±1.5	5.8±1.0
115	311.2±0.8	302.8±2.3	5.7±1.6
142	311.4±0.8	296.6±1.9	5.7±0.8

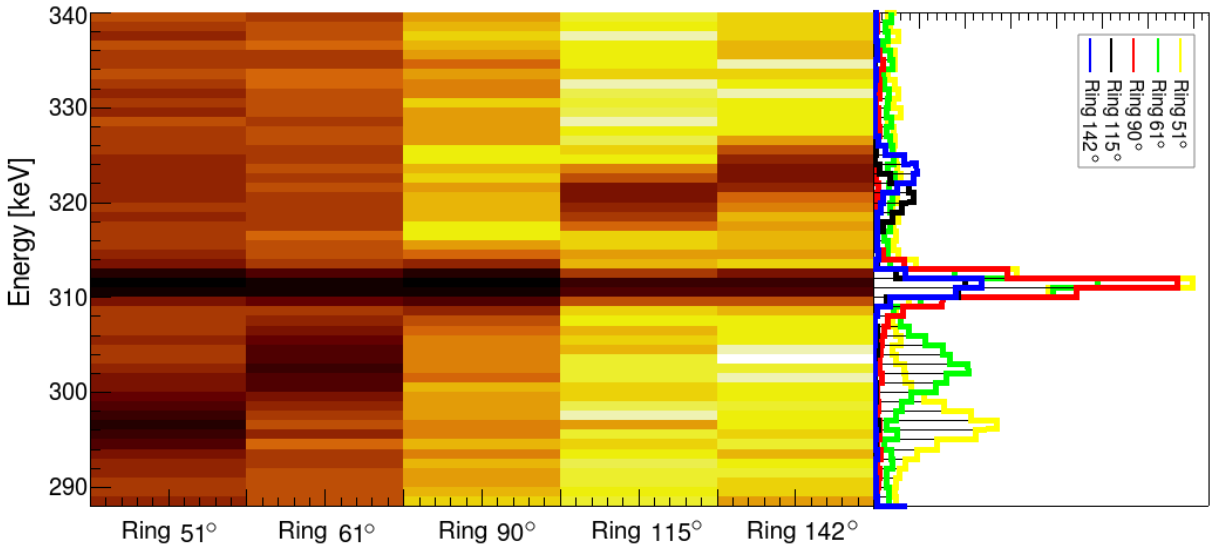

Figure 5.6: (Left) Gamma-ray energy spectrum versus the GALILEO ring. (Right) Projection of the matrix on the energy axis.

5.2.5 The half-life of the 540-keV state using the DCM analysis

The intensities of the shifted and unshifted components of the 311-keV transition are measured for every distance and for each ring of GALILEO independently and by using Eq. 5.3 the ratio R(d) is obtained. The data point from the 0.1 mm plunger-stopper distance was not included in the analysis since the shifted component in the spectrum is not visible due to the very small intensity. Using Eq. 5.4 and the relations between the lifetime and the half-life, $t_{1/2} = \tau \cdot ln(2)$, one gets:

$$ln\left(\frac{1}{R}\right) = \frac{dln(2)}{vt_{1/2}} \tag{5.9}$$

the ln(1/R) is plotted as a function of the distance in Fig. 5.7, and the data points are fitted using Eq. 5.9. The error in the distance is considered to be 0.1 μm. The half-life of the 540-keV state obtained from the fit for each ring of GALILEO is marked in the figure, and as noticed the results are compatible within 1σ. The weighted average of the results of each ring returns a value of the half-life of the 540-keV state $t_{1/2}$=(248±9) ps.

5.2.6 The half-life of the 540-keV state from the DDCM analysis

From the DDCM technique, a lifetime is obtained for each distance between the plunger and the stopper using Eq. 5.8. The results obtained for every ring of GALILEO are shown in Fig. 5.8. The data points are fitted with a constant function, which is the half-life of the nuclear-excited state. The results from the fit are summarized in Tab. 5.3. The results obtained for the rings of GALILEO are compatible with each other within the error bars.

As mentioned, the DDCM technique gives smaller statistical uncertainty compared

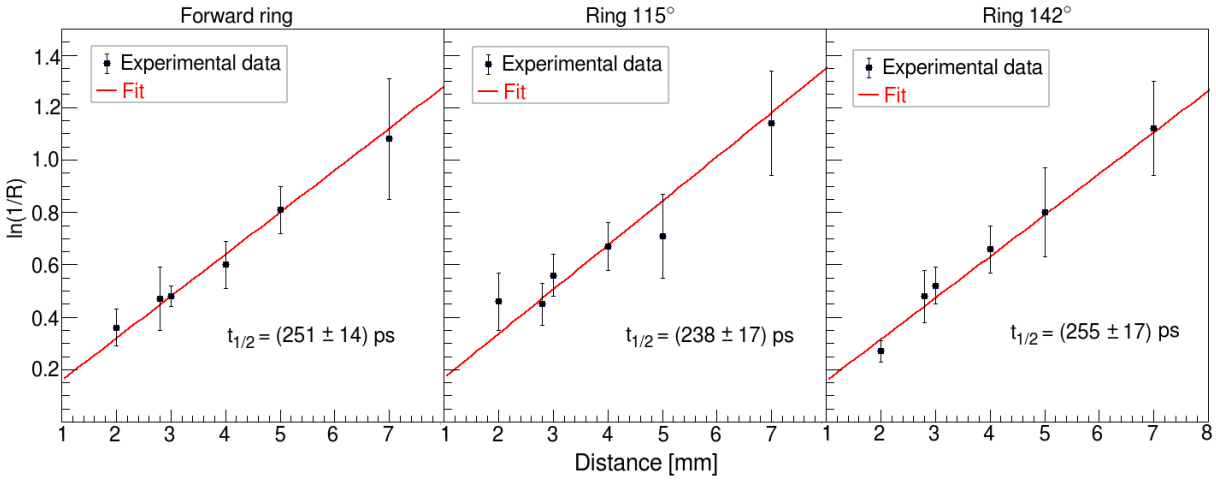

Figure 5.7: The ln(1/R) of the shifted and the unshifted component with respect to the distance target-stopper for the rings of the GALILEO array and the half-life of the 540-keV state obtained when fitting the experimental data using the DCM technique. The error in the distance is considered to be 0.1 μm but is not visible in the figure due to the scale of the X-axis.

to the DCM method. This is because the derivation of the lifetime is based only on the measured quantities, and only the relative distance between the plunger and the stopper is needed. To summarize, the half-life of the 540-state is $t_{1/2}$=(246±5) ps. This result was obtained by taking the weighted average of the results obtained independently from each of the three rings.

Table 5.3: The half-life of the 540-keV state obtained from the DDCM analysis independently in each ring. The weighted average gives $t_{1/2}$=(246±5) ps.

Ring (°)	$t_{1/2}$ (ps)
56	247 ± 7
115	234 ± 10
142	251 ± 8

5.3 Analysis of the DSAM data

The lifetime of the 1100-keV $3/2^+$ intruder state was measured using the DSAM technique. This energy level decays by two γ-ray transitions of 518-keV and 560-keV, to the $5/2^+$ and $1/2^+$ states, respectively. Since the statistics are higher for the 518-keV peak, the lifetime of the state is derived based on the lineshape of this transition.

5.3.1 Gamma-ray spectrum from DSAM data

The 2D gate on the kinematic line, as introduced in the previous section, not only reduces the background in the γ-ray spectrum but also, as demonstrated, is a potent tool to select

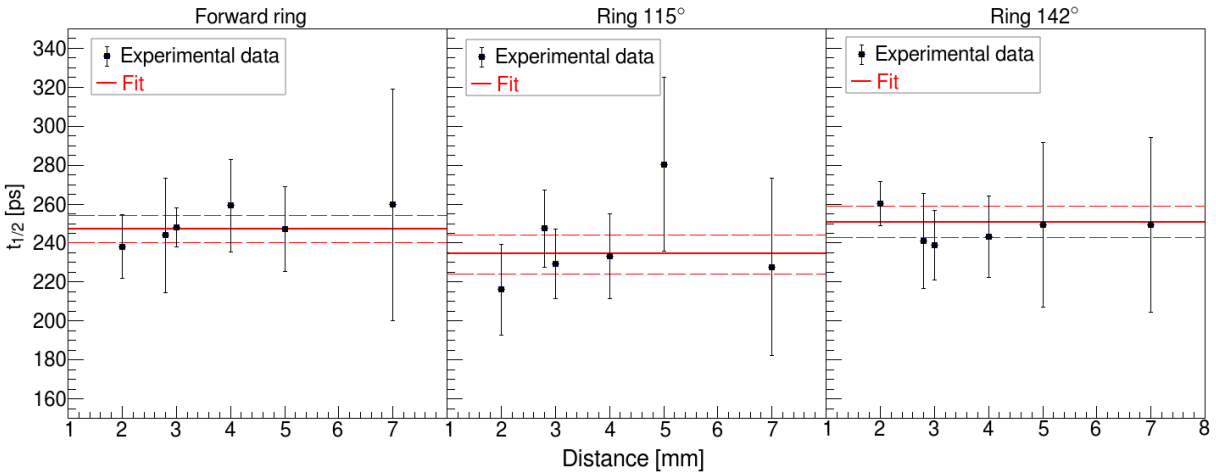

Figure 5.8: The half-life of the $1/2^+$ intruder state of ^{83}Se measured at various distances with the DDCM technique. The fit to the experimental results is shown with the red line and the dashed red line represents the experimental uncertainty at standard deviation level.

events where the state of interest is directly populated. However, for the 1100-keV state, this method cannot be used. The energy of the protons as a function of their angle of emission in coincidence with the 518-keV γ-ray transition, is shown in Fig. 5.9 as a function of the angle of emission. No kinematic line is observed in this cases, due to the low cross section of direct population of the 1100-keV energy level from the (d,p) reaction.

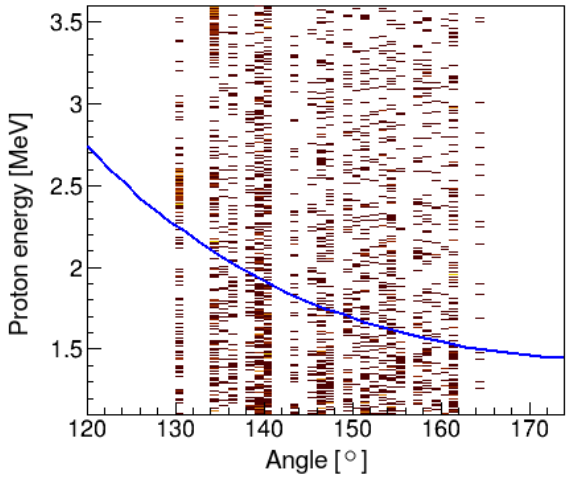

Figure 5.9: The kinematic lines of the 1100-keV state obtained in coincidence with the 518-keV γ-ray transition. In blue is shown the kinematic line of the 1100-keV state calculated by NPTools [103].

Instead, $\gamma\gamma$ coincidences were used to reduce the background in the γ-ray spectrum. The coincidence is set between the full GALILEO array and each ring. When gating in the 582-keV $5/2^+ \rightarrow 9/2^+$ transition, the γ rays with energies 372-keV and 518-keV show characteristic lineshapes, (See Fig. 5.10). The stopped component is marked with a red line in the spectrum. The lineshapes result from the γ-ray de-excitation when the nucleus

decelerates inside the stopper material. As expected, at 90°, the Doppler effect does not affect the energy spectrum. The 372-keV and the 518-keV transitions depopulate the 1472-keV and the 1100-keV states, respectively. The lineshapes indicate that both states have lifetimes in the range of femtoseconds and they lay in the same cascade as shown in Fig. 5.2. The 1472-keV level decays via 372-keV γ ray to the 1100-keV level. The feeding of the 1100-keV level from the 1472-keV state has to be taken into account in the analysis for the proper lifetime determination.

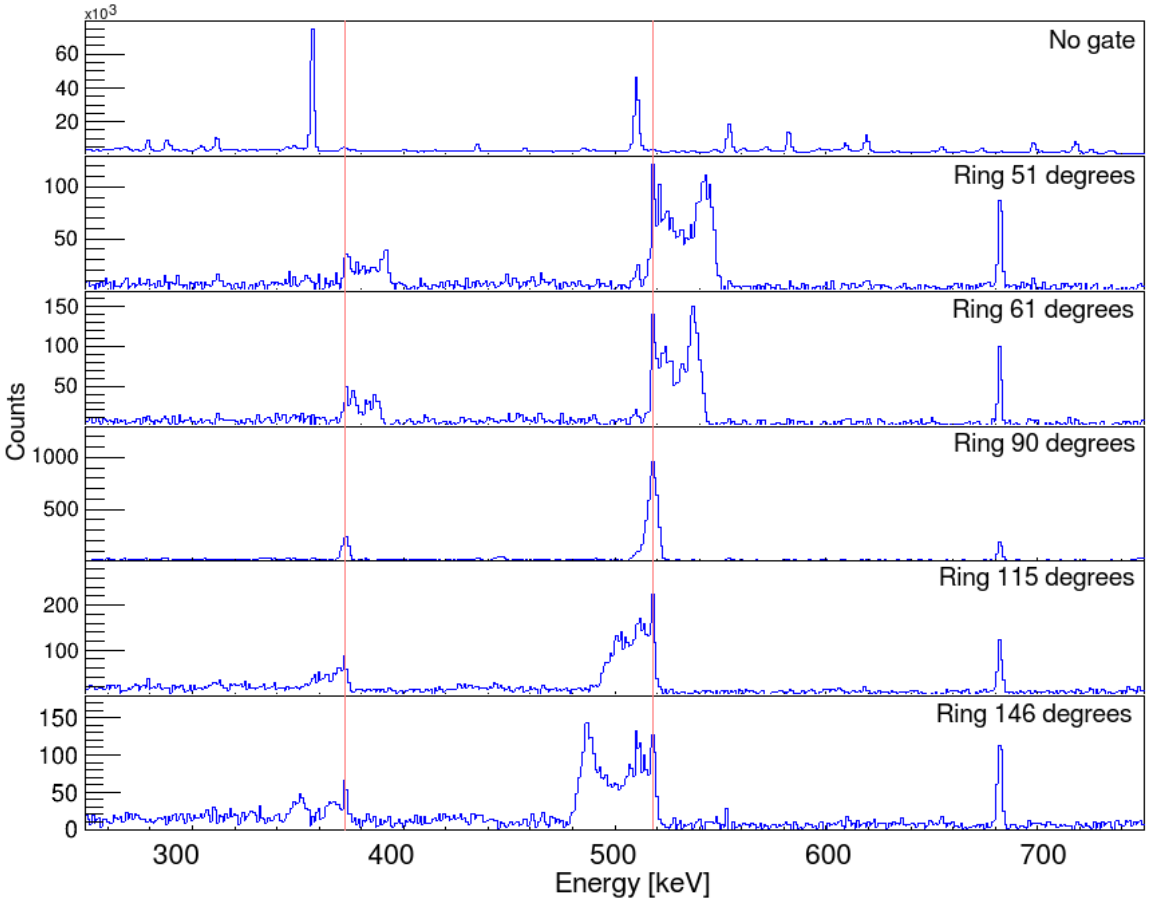

Figure 5.10: Gamma-ray spectrum measured in singles and γ-ray spectra for each ring of the GALILEO array measured in coincidence with the 582-keV $5/2^+ \rightarrow 9/2^+$ transition of ^{83}Se. The coincidence is set between the full GALILEO array versus each ring. The peaks at 372 keV and 518 keV show characteristic lineshapes. The red line in the figure indicates the energies at 372 and 518 keV.

5.3.2 Lifetime measurement from DSAM data

The lifetimes are extracted from the experimental data via a comparison of the γ-ray spectrum with a model calculation. Detailed Monte Carlo simulations have been performed with the Geant4 toolkit [106] and the AGATA simulation package [107] to produce the model spectrum. Geant4 is a powerful code used commonly to plan and analyze experiments in nuclear physics. Thanks to the possibility of describing complex geometries

and interactions of particles or γ rays with the matter, the user can simulate all the needed information from a physics process. Furthermore, the AGATA simulation package based on C++ classes of Geant4 contains important implementations that can be used for performing lifetime measurements with the Doppler shift techniques, as for example:

- reaction mechanism in the target - The particles can interact with the target via transfer, fusion evaporation, Coulex, and fusion-fission reactions.
- interaction of the reaction products with the stopper - The reaction products can also interact with other materials placed after the target, like a stopper foil, decelerate in the material and undergo γ decay while decelerating or stopped.
- reaction kinematics - Angular distribution of cross section and the energies of the reaction products can be included in the simulation.
- de-excitation of excited nuclei following complex decay patterns - The γ-ray cascades and branching ratios are well taken into account.
- the lifetime of the nuclear-excited states governs the γ decay process.

The power of this simulation package in the analysis of DSAM spectra has been successfully demonstrated in previous works [108–111].

To extract lifetimes from the DSAM data, the spectrum obtained from the simulation is compared with the experimental one. Parameters as the lifetime of the state of interest are modified in the codes until a good agreement between the two is achieved and the characteristic lineshapes are reproduced. The quality of the fit between the two histograms is characterized by the least-χ^2 method. The χ^2 is defined as:

$$\chi^2 = \sum_i \left(\frac{n_{exp}(i) - n_{sim}(i)}{\sigma_{exp}(i)} \right)^2 \tag{5.10}$$

where i indicates the number of bins where the fit is performed (region of sensitivity), $n_{exp}(i)$ denotes the number of events in the bin i of the experimental histogram, $n_{sim}(i)$ is the number of events in the bin i of the simulated histogram, and σ is the error on the experimental spectrum. Since the content of the bins of a raw spectrum is considered to be ruled by the Poisson statistics, the variance for each bin is regarded to be the channel content, $(\sigma_{exp}(i))^2 = n_{exp}(\mathrm{i})$. In principle, an error should be considered for the simulated data, but this error is neglected since the number of simulated events is much larger than the number of events in the experimental data.

Performing simulations by varying the lifetime of the state of interest, a χ^2 curve is obtained. The simulation for which the χ^2 has the minimum value is the one that better reproduces the experimental data and the half-life used in the simulation is the one retained.

5.3.3 The response function of the HPGe detectors

The lineshapes in the γ-ray peaks in the DSAM data are directly related to the lifetime of the level of interest. This means that the intrinsic energy resolution of the HPGe detectors must be taken into account in the simulations in order to measure the lifetime of the state of interest without including any systematic error in the analysis. Thus, a smearing function, defined as a Gaussian with an exponential left or right tail, is applied to the simulated data to reproduce the response function of the detectors. Experimental data taken with an ^{152}Eu source are used to properly calibrate the resolution of the detectors as a function of energy. The average resolution in FWHM of all the HPGe detectors of the GALILEO array is plotted as a function of the energy in Fig. 5.11 (black circles) and fitted with a second-order polynomial (red line). This function is then used as a weight function to control the amount of the smearing effect on the simulated data, defining the resolution of the γ-ray peaks versus the energy.

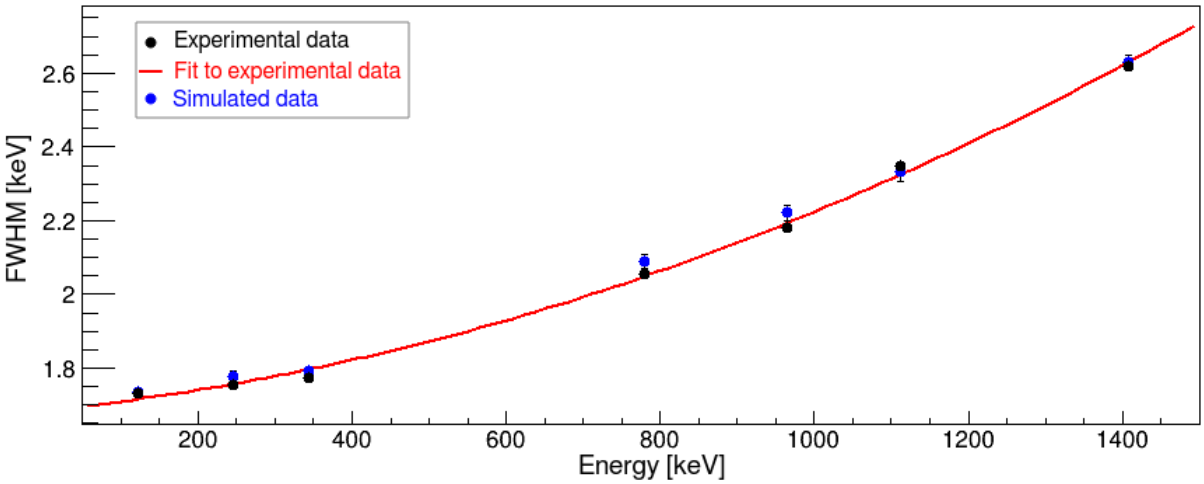

Figure 5.11: The resolution of the HPGe detectors as a function of the energy. The experimental data have been compared with the simulated ones for a ^{152}Eu source.

The response function was implemented in the simulated ^{152}Eu source data. The resolution in FWHM of the simulated γ-ray peaks is compatible with the experimental values, as seen in Fig. 5.11. A comparison of the simulated ^{152}Eu spectrum with the experimental one is shown in Fig. 5.12. As was shown in Fig. 4.2 of the previous chapter, the HPGe crystals of GALILEO have a very similar energy resolution. Therefore, a general response function was used in the simulations instead of using a particular function for every crystal.

5.3.4 The half-life of the 1472-keV state

The γ rays with energy 372 keV, which depopulates the 1472-keV energy level of ^{83}Se (see Fig. 5.2), appear in the DSAM spectra with a characteristic lineshape (see Fig. 5.10). The

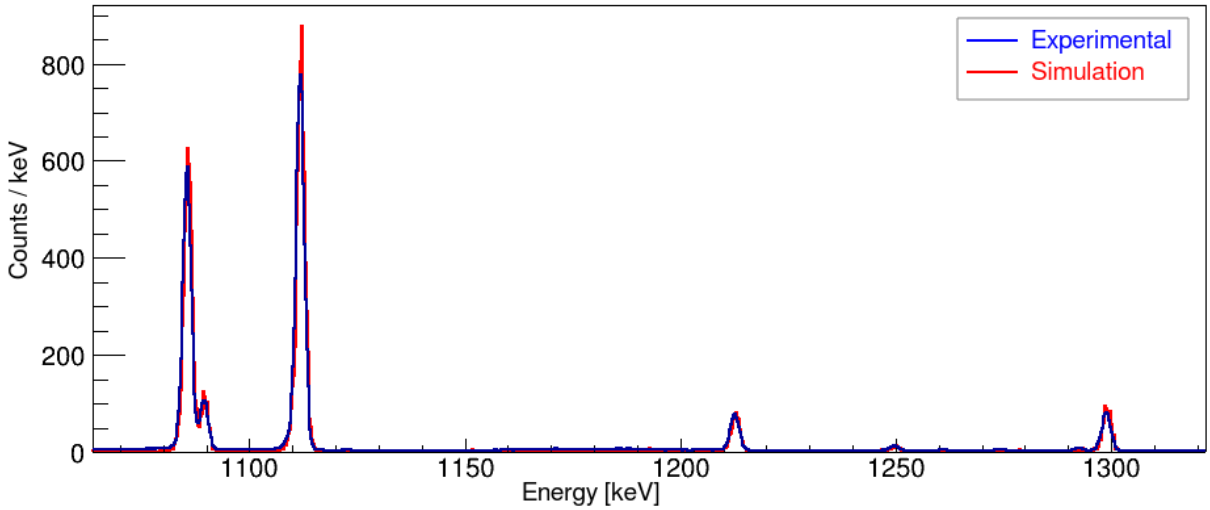

Figure 5.12: Comparison of the experimental and simulated γ-ray spectrum of ^{152}Eu source.

1472-keV level is the highest in energy in the γ-ray cascade built above the 582-keV level to display a lifetime in the sensitive region of the DSAM technique, thus, it is convenient to start the analysis by deriving first the lifetime of this state since the lower energy levels are influenced by its feeding. The analysis for the lifetime measurement was performed independently for the rings of the GALILEO array, except for those at forward angles. Due to low statistics, the data from the 51° and 61° rings were added together. On the contrary, the two rings on the backward are treated separately.

To define the range of sensitivity for the χ^2 analysis, simulations were performed for a very short and long lifetime of the 1472-keV state, 1 fs, and 10 ps. The γ-ray spectra obtained from the simulation are shown in Fig. 5.13. At 10 ps lifetime of the 1472-keV state, the 372-keV transition appears as a stopped component in the spectra. At 1 fs lifetime, the 372-keV γ-ray is emitted in flight and its measured energy depends on the angle of detection. The region between the two peaks for every ring is the region where the χ^2 analysis is performed using Eq. 5.10. This region is represented with the green dashed lines in Fig. 5.13 for all the rings of GALILEO.

As seen in Fig. 5.2, the 1665-keV level decays to the 1472-keV state via a 192 keV γ ray. Since this level contributes with less than 1% of the intensity of the 372-keV peak, its influence on the lifetime of the 1472-keV state is not significant.

Simulations were performed for a range of lifetimes from 300 to 500 fs in steps of 10 fs. The simulated spectrum was normalized to the experimental one using the intensity of the 372-keV peak itself. The χ^2 is calculated using the Equation 5.10 in each case by comparing the simulated spectrum with the experimental one in the region of sensitivity as described in Fig. 5.13. The χ^2 as a function of the lifetime of the 1472-keV state is shown in Fig. 5.14. One sigma in the level of confidence is provided by the expression $\Delta\chi^2=|\chi^2\text{-}\chi^2_{min}|=1$. In Fig. 5.14, the simulation that minimizes the χ^2 is shown for all the

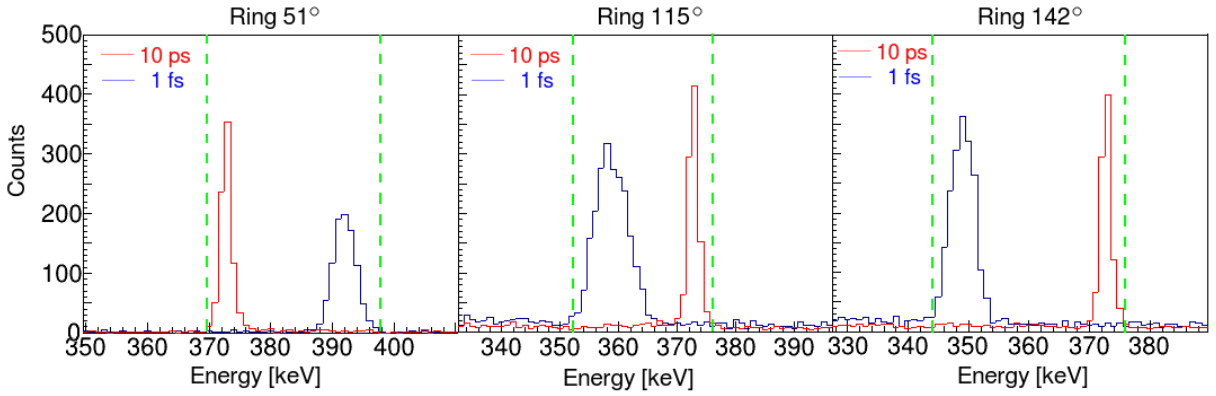

Figure 5.13: The range of sensitivity of the χ^2 for the 1472-keV state. Simulations for a short and a long lifetime of this state, 10 ps, and 1 fs, are performed to define the range of sensitivity, which is represented by the dashed lines for the forward ring and the rings at 115° and 142°.

rings, as well as the region where $\Delta\chi^2$=1. The results obtained for each ring for the 1472-keV state of ^{83}Se are summarized in Tab. 5.4. These results include only the statistical uncertainty. The addition of the systematic uncertainties is discussed in Sec. 5.4.

Table 5.4: The half-life of the 1472-keV state of ^{83}Se and the corresponding statistical uncertainty measured independently in every ring of the GALILEO array.

Ring (°)	$t_{1/2}$ (fs)
51+61	398 ± 14
115	427 ± 16
142	419 ± 16

5.3.5 Simulation for the γ-ray cascade 372-518 keV

The 1472-keV state decays via a γ-ray transition of 372-keV to the 1100-keV level. This feeding to the 1100-keV state has to be accounted on its lifetime determination. Thanks to the AGATA simulation package, simulations can be performed for several levels in a γ-ray cascade taking into account the lifetime of each one. One of the parameters to be appropriately set in the code is the population of the levels from the reaction. In an experiment, several states are populated and an estimate of the population of each level is obtained by investigating the intensities of the γ-ray peaks in the spectrum and by constructing the levels scheme with the observed transitions. This was performed already for ^{83}Se, as it was shown in Section 5.1. The estimates of the population of the 1472-keV and 1100-keV energy levels, which decay by 372-keV and 518-keV transitions, respectively, are shown in Tab. 5.5, taking into account the γ-decay branching ratios and the efficiency of the GALILEO array. For the 1100-keV level, 28% of its intensity results from the feeding of the higher lying state at 1472-keV state, while 78% is the direct

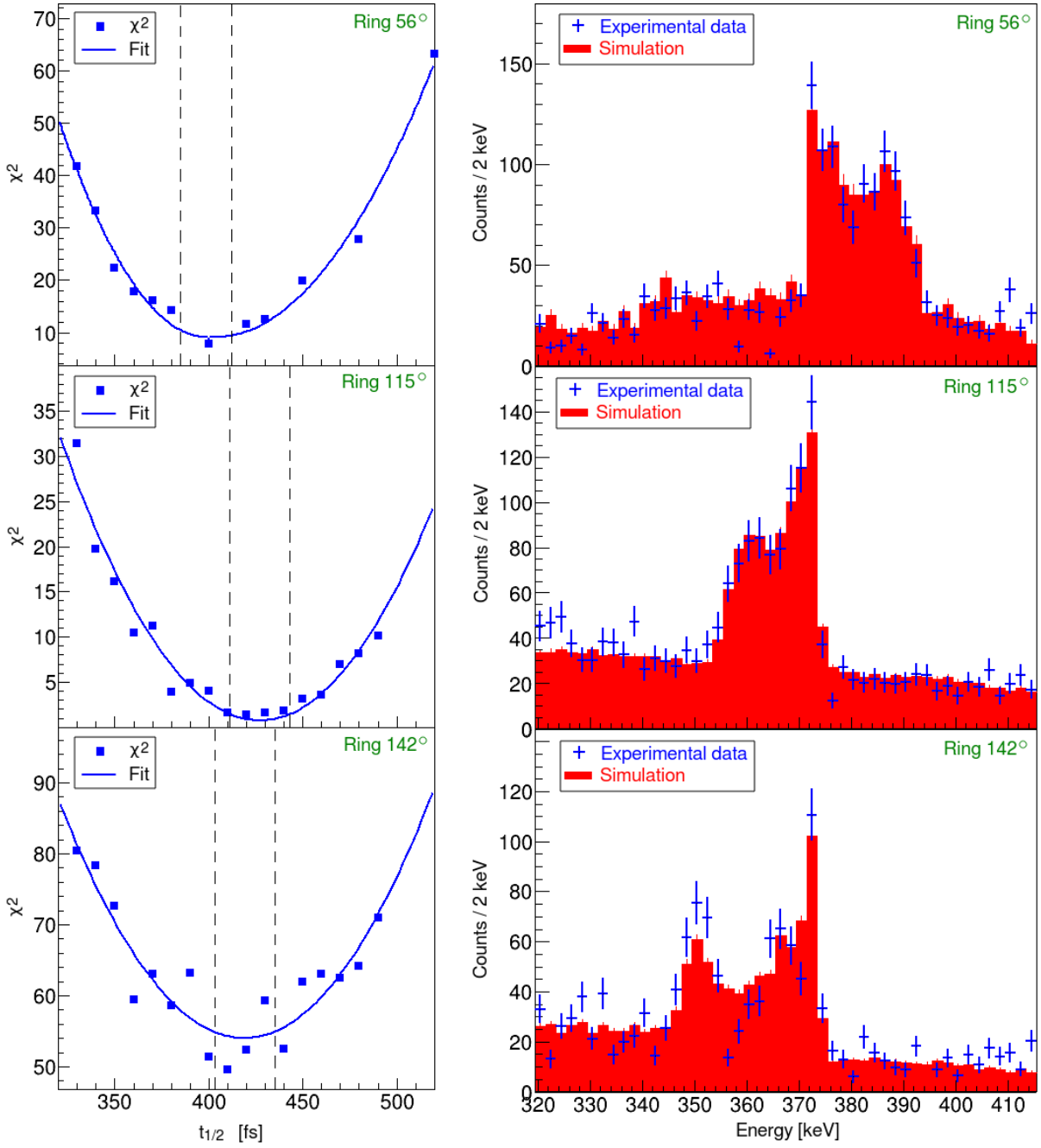

Figure 5.14: (Left) The χ^2 curves as a function of the half-life of the 1472-keV state obtained by comparing the Geant4 simulations with the experimental spectrum for the forward ring of GALILEO (top) and the rings at 115° (middle) and 142° (bottom). The vertical dashed line indicates the $\chi^2 - \chi^2_{min}$=1 range. (Right) Comparison of the best-simulated spectrum with the experimental one for each ring of GALILEO. The dark dashed line indicates the bins where the least-χ^2 analysis is performed.

reaction population.

Table 5.5: The population of the 1472-keV and 1100-keV energy levels of ^{83}Se based on the intensities of the 372-keV and 518-keV γ-ray transitions.

Peak keV	Counts	Eff %	B ratio %	Corrected	Level	Pop	Pop %
372	875	0.0164	0.45	53354	117912	117912	22
518	5095	0.0142	0.75	358803	477208	42061	78

To confirm the population of the 1472 and 1100-keV levels of ^{83}Se, a series of simulations were performed for the 90° ring, populating the states of interest simultaneously. Since the 1472-keV level is the highest in the simulated cascade and decays to the 1100-keV level by a γ ray with an energy of 372 keV, the counts of this γ-ray peak are used to normalize the simulated spectrum to the experimental one. The fit between the simulated and experimental spectra is evaluated based on the minimization of the χ^2, calculated for the peak at 518 keV. The range of the fit for the 518-keV peak is performed from 513 to 521 keV. The results are shown in Fig. 5.15. As seen from the figure, the χ^2 reaches its minimum value at 78%, compatible with what was deduced from the intensities of the peaks in the experimental data. This result indicates that the branching ratios for the γ decay and the efficiency of the detectors are well taken into account in the simulation.

The simulation that better reproduces the experimental spectrum is shown in Fig. 5.15 (Right panel). Besides the intensities, the energy resolution of the γ-ray peaks in the simulated spectrum is in perfect agreement with the one of the experimental data. Even though the data used in this case are those of the 90° ring and thus not sensitive to the Doppler effect, the aperture of the detector increases the peak FWHM compared to the case of emission of γ rays at rest. This behavior is also well reproduced from the simulation.

5.3.6 The half-life of the $3/2^+$ 1100-keV state in ^{83}Se

A similar procedure as in Section 5.3.4 was followed to determine the lifetime of the 1100-keV state, which decays by emitting a γ ray with an energy of 518 keV. At first, the region of sensitivity for the χ^2 analysis is defined by performing simulations with a lifetime of 1 fs and 10 ps for the 1100-keV level. The region of sensitivity for each ring is shown in Fig. 5.16.

The 1472 keV and the 1100-keV state are simulated at the same time to account for the feeding from above. Simulations are performed by varying the lifetime of the 1100-keV level from 200 to 400 fs with a step of 10 fs. The lifetime of the 1472-keV is the one already obtained from the analysis of the previous section.

The χ^2 as a function of the lifetime of the 1100-keV state for every ring of GALILEO

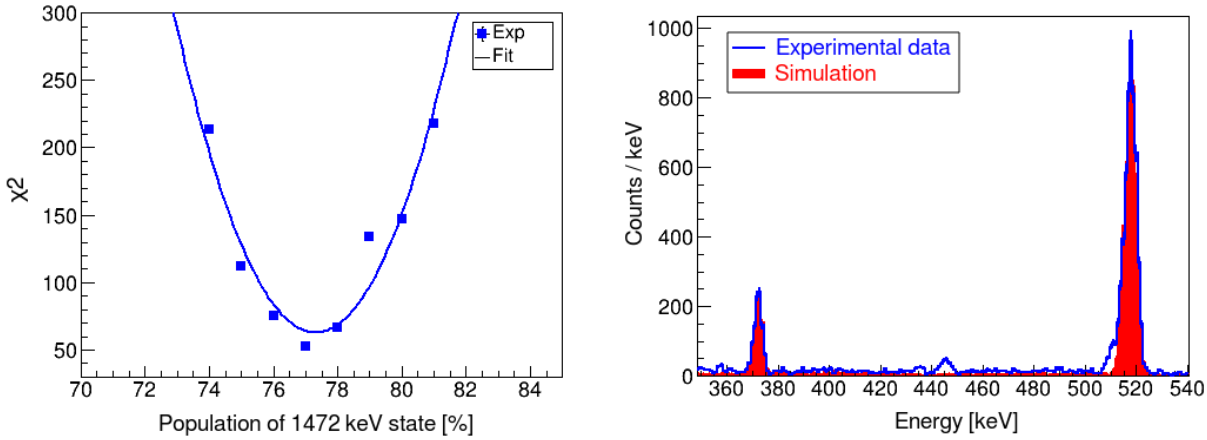

Figure 5.15: (Left) The χ^2 obtained as a function of the ratio of the population of the 1472-keV and 1100-keV state. (Right) Comparison of the experimental spectrum and the simulation for the 90° ring of GALILEO. The peak at 440 keV is a transition of ^{83}Se, and since it doesn't belong to the cascade is not included in the simulation. The peak at 511 keV is not included in the simulation either. The states of interest were populated with the value suggested from the minimization of χ^2.

is shown in Fig. 5.17 (Left panel). The region where $\Delta\chi^2 = \chi^2 - \chi^2_{min} = 1$ is indicated in the figure with the dashed lines. The simulated spectrum is scaled to the experimental one by the intensity of the 372-keV γ-ray transition. The simulation which better reproduces the experimental spectrum is shown in Fig. 5.17 (Right panel).

A summary of the results for each ring is presented in Tab. 5.6. Taking the weighted average of the values measured in each ring, the half-life of the 1100-keV state of ^{83}Se results to be $t_{1/2}$ = (298±4) fs. The uncertainty of the measurement is only statistical, obtained from the analysis with the least-χ^2 method. The systematic uncertainties are discussed in Sec. 5.4

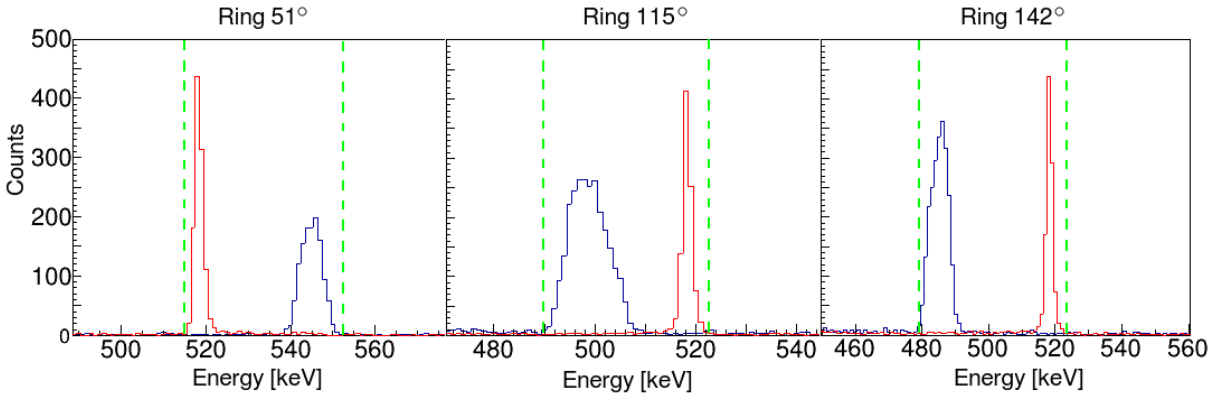

Figure 5.16: The range of sensitivity of χ^2 for the 1100-keV state decaying through the 518-keV γ ray.

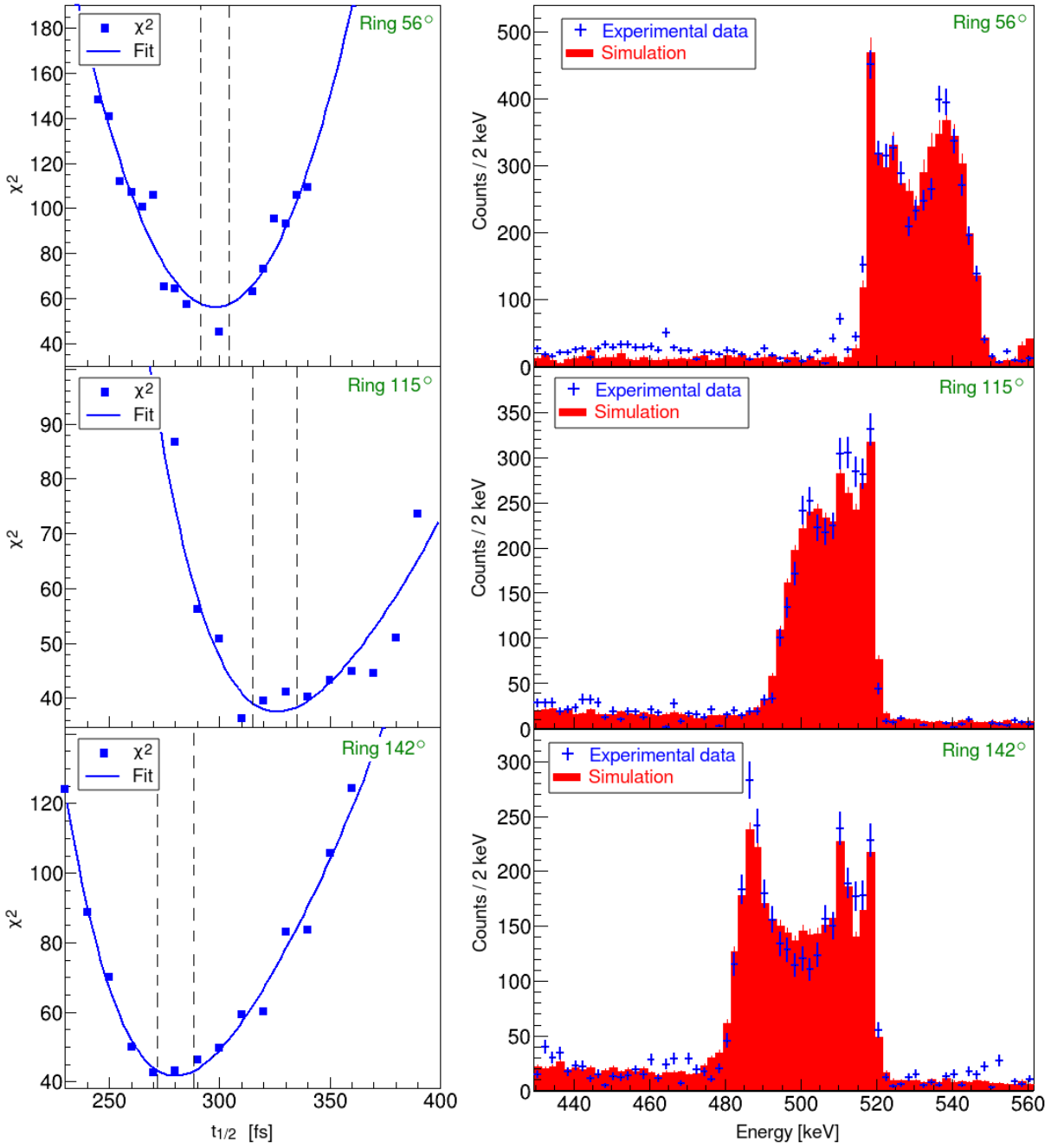

Figure 5.17: (Left) The χ^2 curves as a function of the half-life of the 1100-keV state obtained by comparing the Geant4 simulations with the experimental spectrum for the forward ring of GALILEO (top) and the rings at 115° (middle) and 142° (bottom). The vertical dashed line indicates the $\chi^2 - \chi^2_{min}$=1 range. (Right) Comparison of the best-simulated spectrum with the experimental one for each ring of GALILEO. The dark dashed line indicates the bins where the least-χ^2 analysis is performed.

Table 5.6: The half-life of the 1100-keV state of ^{83}Se and the corresponding statistical uncertainty measured independently in every ring of the GALILEO array.

Ring [°]	$t_{1/2}$ [fs]
51+61	298 ± 6
115	330± 11
142	280± 8

5.4 Systematic uncertainties

The uncertainties given so far to the measured half-lives are only statistical. Several factors may produce systematic errors in the measurement:

- The target thickness
- The stopping power of the stopper
- The number of simulated events
- The feeding

5.4.1 Uncertainties from the target thickness

Depending on the technique to produce the deuterated polyethylene targets, the plastic material's density or homogeneity can vary. This would influence the energy loss of the particles inside the target, thus affecting the lifetime measurement. To account for these effects, simulations were performed for the ring at 146° of the GALILEO array by varying the target thickness by ±0.1 mg/cm^2. The results from the least-χ^2 method are shown in Fig. 5.18. The variation on the lifetime deduced from the χ^2 minimization is 2%. It is important to note that a variation of ±1 mg/cm^2 on the target thickness is quite large with respect to the target thickness measurement precision. Since the density of the target is small, the effect of the energy loss in the target is not very significant in our case.

5.4.2 Uncertainties from the stopping power

The lineshape displayed by the γ-ray peaks in DSAM data is not only the result of the lifetime of the energy level. The kinematics of the reaction and the stopping power properties of the stopper material also have an important role. To be able to reproduce the lineshape, the simulation has to account for these effects. As mentioned previously, the AGATA simulation package accounts for the slowing down process of the nucleus of interest inside the stopper material, and the γ decay may occur while the nucleus is de-accelerating. The stopping power of ^{83}Se into Au has not been measured experimentally. The ^{84}Kr isotope is the closest isotope to ^{83}Se where the stopping power in Au is known.

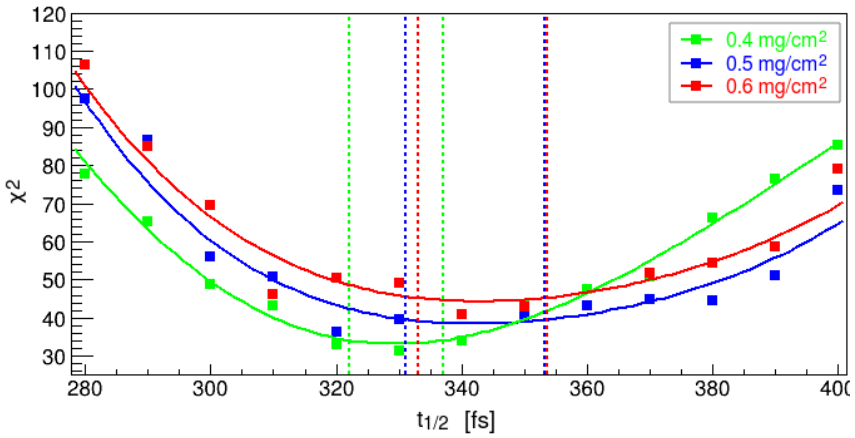

Figure 5.18: The χ^2 as a function of the half-life of the 1100-keV state for the 115° ring, calculated by varying ± 0.1 mg/cm^2 the target thickness. The dashed lines correspond to χ^2-χ^2_{min}=1 range for each target thickness.

A comparison of the experimental stopping power of ^{84}Kr into Au with the one calculated for ^{83}Se with SRIM2013 [112] and Geant4 is shown in Fig. 5.19. The stopping power calculated with Geant4 for ^{83}Se shows slight differences with respect to the one calculated with SRIM2013 in the energy range from 0.5 to 1 MeV/A, instead it shows a similarity over the full energy range with the experimental data of ^{84}Kr

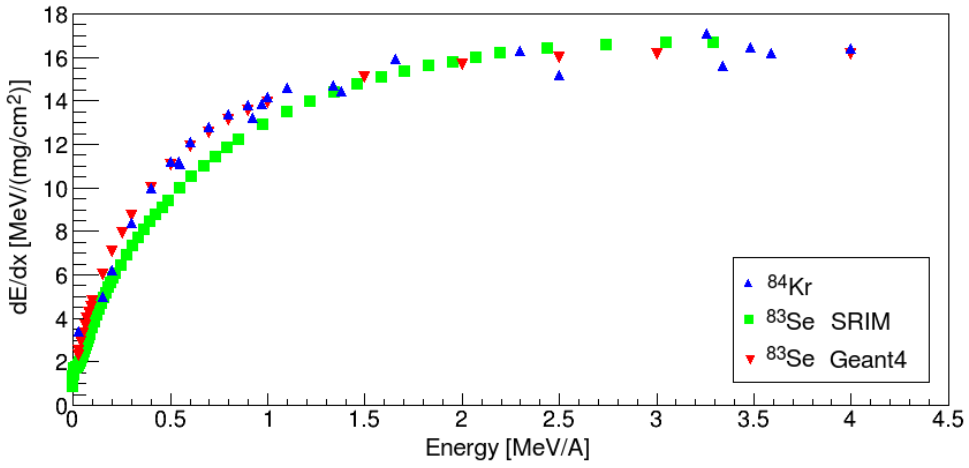

Figure 5.19: Stopping power as a function of the particle energy for ^{84}Kr (experimental), ^{83}Se (calculated from SRIM2013), and the one used (calculated by Geant4 Monte Carlo simulations).

Simulations performed with both functions show no difference in the lineshapes. Besides the electronic stopping power, SRIM and Monte Carlo calculations also account for the nuclear-stopping power, which becomes significant at low energies. Following an educated guess, a systematic error of 3% is added in the final half-life due to the uncertainty on the stopping power.

5.4.3 Number of simulated events

The number of the events simulated in the Monte Carlo for the analysis was $2.5{\cdot}10^6$. In these analysis, the simulations are considered without any error. To test the influence of the number of the simulated events on the results, additional simulations were performed with $0.5{\cdot}10^6$ and $1.5{\cdot}10^6$ events. The corresponding χ^2 curve as a function of the half-life of the 1100-keV state is shown in Fig. 5.20.

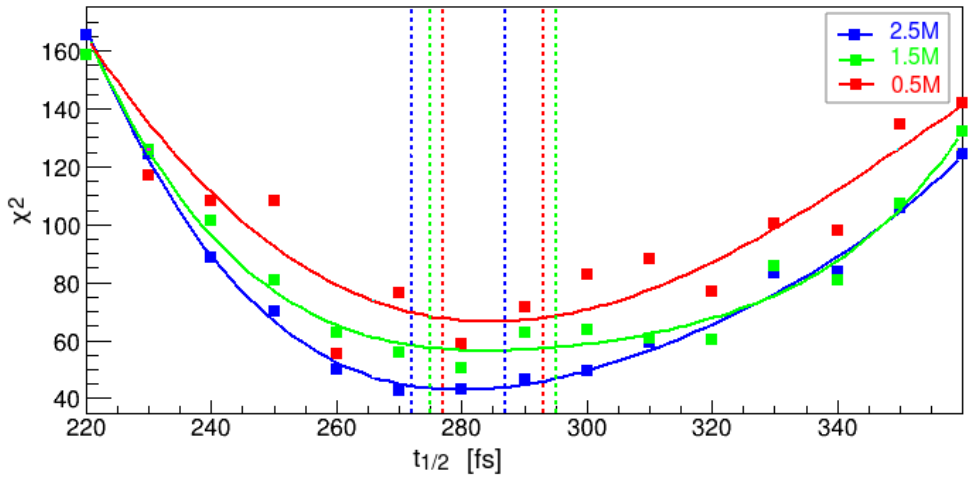

Figure 5.20: The χ^2 curve as a function of the half-life of the 1100-keV state obtained by comparing the experimental spectrum with the simulated one using a different number of events, 2.5, 1.5 and 0.5 million.

As shown in the figure, the influence of the number of events in the measured half-life is negligible. Reducing the number of events, the χ^2 starts to oscillate: this is due to statistical fluctuations. The number of simulated events is chosen such that the χ^2 follows a smooth trend and does not suffer oscillations.

5.4.4 Side feeding

The 1472-keV and 1100-keV levels, whose lifetime was measured using the DSAM technique, are connected by the 372 keV transition. The branching ratio for the decay of the 1472-keV level via this γ-ray is around 47%, meaning that only some of the events populating this state undergo γ decay to the 1100 keV state. In the analysis performed in this work, such feeding was taken into account thanks to the AGATA simulation packages, which allow to simulate the population of several levels and a complex level scheme of the nucleus of interest. Even though the contribution of the feeding of the 1100-keV transition is low, it may still lead to some systematic uncertainties when determining the lifetime. The contribution of the 1472-keV level in the 1100-keV state is shown schematically in Fig. 5.21. The experimental data are compared with the simulated spectrum where only the 1472-keV level is populated. The simulated spectrum is scaled to the experimental one by the intensity of the 372 keV peak.

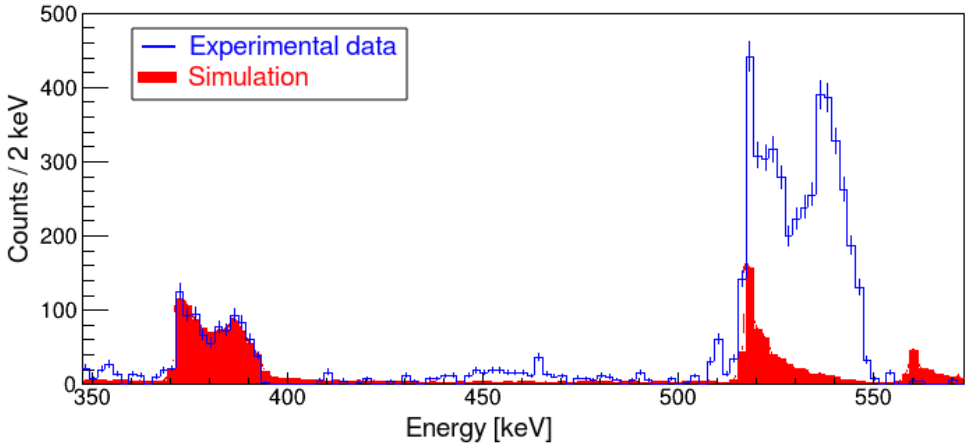

Figure 5.21: Gamma-ray spectrum resulting from the gate on the 582-keV transition where the decays of the 1472 and 1100-keV state can be observed with their lineshape (blue line). The simulated spectrum (red) shows the effect of the direct feeding of the 1100-keV state from the 1472-keV state. In the simulation, only the 1472-keV has been directly populated.

To understand the contribution of the half-life of the 1472-keV level to the half-life of the 1100-keV state, simulations were performed by varying the half-life of the feeder. The half-life of the 1472-keV peak was found to be (414±36) fs when considering the results shown in Tab. 5.4 and the previously mentioned contributions to the systematic errors. Simulations were performed with the half-life of the 1472-keV level at the two extremes, 380 and 450 fs. In both cases, the half-life of the 1100-keV level was varied with a step of 10 fs from 210 to 350 fs. From the comparison of the simulated spectrum with the experimental data, a χ^2 curve as a function of the half-life of the 1100-keV level was obtained. The results are shown in Fig. 5.22 where from the minimization of the χ^2 it results that the difference in the half-life is within 3%.

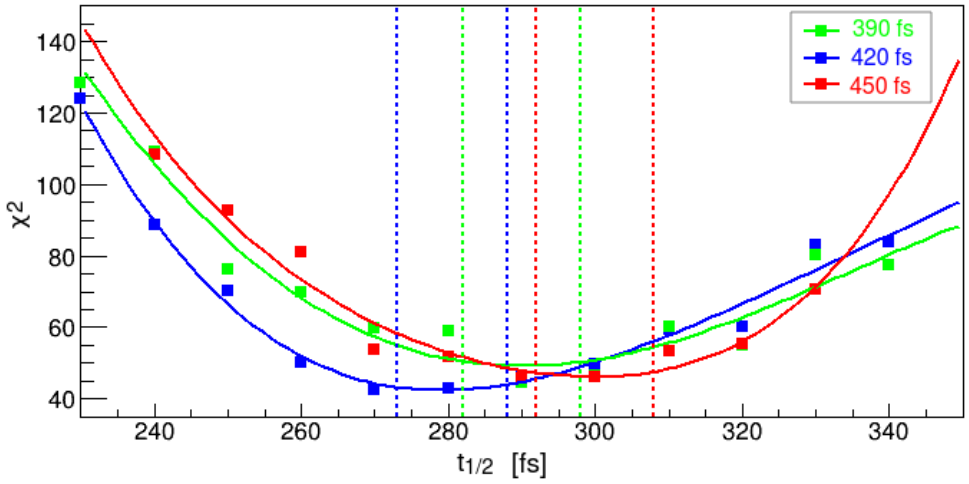

Figure 5.22: The χ^2 curve as a function of the half-life of the 1100-keV state for three different half-lives of the 1472-keV state, 390 fs, 420 fs, and 450 fs.

Therefore, for the 1100-keV state, a systematic error of 3% is considered as a contribution from the uncertainty of the finite half-life of the feeder.

5.5 Summary of the measured lifetimes in ^{83}Se

The half-lives of intruder states of ^{83}Se were measured for the first time using the RDDS and the DSAM method. The half-lives of each state measured in this work are summarized in Tab. 5.7. The half-life of the 1472-keV and 1100-keV states measured with the DSAM technique were obtained by taking the weighted average of the measurement performed independently in each ring (See Tab. 5.4 and Tab. 5.6) considering also the systematic errors discussed in this chapter.

Table 5.7: The half-life of excited states of ^{83}Se measured in this work.

E_{level} [MeV]	J^{π}	$t_{1/2}$ [ps]
540	$1/2^{+}$	246(5)
1100	$3/2^{+}$	0.298(28)
1472	$3/2^{+}$	0.414(42)

Chapter 6

Results and discussions

In this chapter, the experimental results of this work are compared with theoretical calculations. The definition of reduced transition probabilities and their determination for pure and mixed E2/M1 transitions is given in Sections 6.1 and 6.2. The reduced transition probabilities derived from the experimental lifetimes of the 540-keV $1/2^+$ and 1100-keV $3/2^+$ intruder states of ^{83}Se are reported in Section 6.3. A brief introduction to the shell-model and the mean-field approaches used to perform theoretical calculations is shown in Section 6.4. Results from the shell model using the GWB interaction from the Oxbash library, mean-field calculations with the Gogny energy-density-functional, and calculations with the PFSDG-U interaction using the TAURUS code are reported in Section 6.5 of this chapter.

6.1 Reduced transition probabilities

Gamma-ray transitions connect an initial and a final nuclear state, $i \rightarrow f$. The emitted photon carries away from the system an amount of angular momentum L such that $\vec{J_f} = \vec{J_i} + \vec{L}$. Therefore, L can take values from $(|J_i - J_f|)$ increasing by one unit up to $(J_i + J_f)$. Considering the fact that photons have an intrinsic spin of one, transitions with $L = 0$ are forbidden. The value of the angular momentum L carried from the photon determines the multipolarity of the radiation. A dipole transition has $L = 1$, a quadrupole transition carries angular momentum $L = 2$, an octupole has $L = 3$, and so on. Electromagnetic radiation is classified as electric or magnetic depending on the parity of the initial and final nuclear state. The protons and neutrons are held together by the strong interaction, which conserves the parity, so nuclear states are characterized by a defined parity. If the parity of the initial and final state is the same, then the electric transitions have $L = even$ and magnetic transitions have $L = odd$. If the parity of the initial state differs from the one of the final state, then electric transitions have $L = odd$ and magnetic transitions have $L = even$. The lowest orders of multipolarity allowed in a transition are the dominant ones. A transition with angular momentum L is more

likely than a transition with angular momentum $(L+1)$ by a factor of 10^5. For the same multipolarity, the electric character of the radiation is approximately 10^2 times stronger compared to the magnetic character [1].

The reduced transition probability, derived from the experimental lifetimes, is a measure of the overlap between the wave function of two nuclear states connected by an electromagnetic transition:

$$B(\sigma L : J_i \rightarrow J_f) = \frac{| < J_f|\hat{O}(\sigma L)|J_i > |^2}{2L+1} \tag{6.1}$$

where B is the reduced transition probability, σ is the character of the electromagnetic radiation (E-electric or M-magnetic), and L is the angular momentum carried by the transition connecting the initial J_i and the final state J_f. The operator $\hat{O}$ expresses the interaction of electromagnetic radiation with the nucleons and it is equal to the sum of the magnetic and electric multipole operators, $\hat{O} = \hat{O}(\mathrm{E}\lambda)\mu + \hat{O}(\mathrm{M}\lambda)\mu$. The electric operator depends on the effective charges of the proton and of the neutron while the magnetic operator depends on the magnetic moments (g-factors) of the proton and the neutron.

For pure E1 and E2 transition, the reduced transition probability is given by the expression:

$$B(E1) = \frac{0.629 \cdot 10^{-3} \cdot ln(2)}{E_\gamma^3 \cdot t_{1/2}} br \quad [e^2 fm^2] \tag{6.2}$$

$$B(E2) = \frac{816 \cdot ln(2)}{E_\gamma^5 \cdot t_{1/2}} br \quad [e^2 fm^4] \tag{6.3}$$

where E_γ is the energy of the γ-ray photon in MeV, $t_{1/2}$ is the half-life of the nuclear state in picoseconds, and br is the branching ratio of the γ-ray transition. As can be seen from the formula, the overlap between the wave functions of the initial and the final state connected by the electromagnetic transition is given in terms of experimental observables such as energy, and lifetime.

For a pure M1 transition, the relation of the reduced transition probability with the lifetime of the nuclear state is given by the formula:

$$B(M1) = \frac{56.8 \cdot ln(2)}{E_\gamma^3 \cdot t_{1/2}} br \quad [\mu_N^2] \tag{6.4}$$

where E_γ is the energy of the γ ray in MeV, $t_{1/2}$ is the half-life of the state in femtoseconds, and br is the branching ratio.

Often, to evaluate the strength of the transition, it is convenient to express the reduced transition probabilities in terms of the single-particle estimates or Weisskopf units. In a simplified way, the Weisskopf units for E1, E2, and M1 transitions are given by the equations:

$$B_W(E1) = 0.0645A^{2/3} \ [e^2fm^2] \tag{6.5}$$

$$B_W(E2) = 0.0594A^{4/3} \ [e^2fm^4] \tag{6.6}$$

$$B_W(M1) = 1.79 \ [\mu_N^2] \tag{6.7}$$

Comparing the transition rates for electric and magnetic transitions, it may sometimes result that both the lowest allowed multipole and the next higher one become equally important, and electromagnetic transitions between two nuclear-excited states may appear as a mix of E1 and M2 or M1 and E2 transitions. For these mixed transitions, the mixing δ^2 is defined as:

$$\delta^2(E2/M1) = \frac{B(E2)}{B(M1)} \tag{6.8}$$

The mixing δ^2 can be measured experimentally based on the angular distribution of γ rays, as it will be explained in the next section.

For a mixed M1 and E2 transition, the branching fraction of a given type of transition is given by:

$$b(M1) = \frac{B(M1)}{B(E2) + B(M1)} = \frac{1}{1+\delta^2} \tag{6.9}$$

$$b(E2) = \frac{B(E2)}{B(E2) + B(M1)} = \frac{\delta^2}{\delta^2+1} \tag{6.10}$$

Finally, combining these formulas, one would get the expression for calculating the B(M1) and the B(E2) for a mixed M1+E2 transition:

$$B(M1) = \frac{56.8}{E_\gamma^3 \cdot t_{1/2}} \frac{ln2}{1+\delta^2} br \tag{6.11}$$

$$B(E2) = \frac{816 \cdot ln(2)}{E_\gamma^5 \cdot t_{1/2}} \frac{\delta^2}{\delta^2+1} br \tag{6.12}$$

6.2 Determination of the M1/E2 mixing ratio

Due to the statistics available in the present experiment described in this work, it was impossible to perform angular correlations of γ rays in order to deduce the M1/E2 mixing ratio of the 518-keV $3/2^+ \rightarrow 5/2^+$ and of the 560-keV $3/2^+ \rightarrow 1/2^+$ transition of ^{83}Se. To calculate the reduced transition probabilities for mixed transitions, one needs to know the mixing δ^2 coefficient, as shown in Eq. 6.11 and 6.12. The lifetimes of the intruder states measured in this work, and the mixing δ^2 coefficient obtained from another experiment are used to estimate the reduced transition probabilities and characterize the collectivity

of the states of interest. A summary of the results on the mixing δ^2 reported on the Bachelor thesis of F. Conca (University of Milan) with the title "Low-spin study of ^{83}Se by neutron-capture reactions and gamma-ray spectroscopy" (Supervisor S. Leoni, S. Bottoni, F. Crespi, M. Sferrazza) [72], is given in the following.

In an experiment performed at the Institut Laue-Langevin (ILL) laboratory in Grenoble (France), ^{83}Se was populated via a neutron capture reaction. An intense thermal neutron beam from a reactor was collimated to a pencil beam of 1 cm in diameter, impinging on an 85% enriched ^{82}Se target. Using the FIPPS+IFIN array [113] of 13 HPGe clover detectors, $\gamma\gamma$ coincidences allowed to expand the ^{83}Se decay scheme by identifying 28 new primary γ rays, 89 new secondary transitions, and 16 new energy levels. Angular correlations of γ rays were performed, allowing the measurement of the M1/E2 mixing of the 518-keV and the 560-keV transitions [72].

The mixing ratio δ^2 of the 518-keV transition was evaluated by the investigation of the $3/2^+ \rightarrow 5/2^+ \rightarrow 9/2^+$ γ-ray cascade. Gating on the $5/2^+ \rightarrow 9/2^+$ transition (pure E2 with $E_\gamma = 582$ keV) allowed one to measure the angular correlations. The experimental data points of the angular distribution of the 518-keV transition in coincidence with the 582-keV one are shown in the left panel of Fig. 6.1. The experimental data are fitted with the function:

$$W(\theta) = A_0 \left[1 + A_{22} Q_2 P_2(cos\theta) + A_{44} Q_4 P_4(cos\theta)\right] \tag{6.13}$$

where A_0 is a normalization constant, A_{22} and A_{44} are the correlation parameters to be derived, P_2 and P_4 are the Legendre polynomials and θ is the angle between the two γ rays in the cascade.

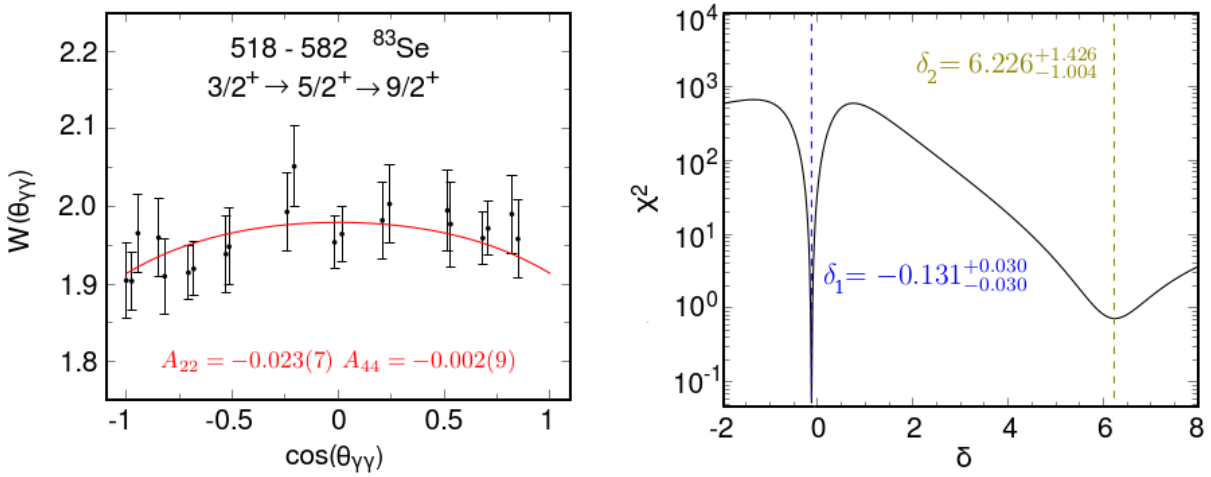

Figure 6.1: (Left) Angular distribution of the 518-keV γ rays in coincidence with the pure E2 582-keV transition. Experimental data are fitted with the function 6.13. (Right) The χ^2 function 6.14 is minimized at two mixing δ values as indicated in the figure, pointing out the two possible solutions for the 518-keV transition. The figure is taken from [72].

The experimental angular correlation coefficients obtained from the fit are compared with theoretical coefficients and the value of δ, which minimizes the χ^2 defined by the expression 6.14, is adopted as the mixing ratio of the transition:

$$\chi^2 = \left(\frac{A_{22} - A_(22)(\delta)}{A_{22}}\right)^2 + \left(\frac{A_{44} - A_(44)(\delta)}{A_{44}}\right)^2 \tag{6.14}$$

The minimization of the χ^2 for the 518-keV transition gives two solutions: δ_1=-$0.131^{+0.030}_{-0.030}$ and δ_2=$6.226^{+1.426}_{-1.004}$.

To solve the ambiguity of this result, angular correlations for the $1/2^+ \rightarrow 3/2^+ \rightarrow 5/2^+$ cascade are investigated. The $1/2^+$ state located at 5816 keV decays via 4715 keV γ-ray transition to the $3/2^+$ state at 1100 keV. The angular correlations of the 4715 keV transition, assumed as a pure M1 transition, with the 518 keV transition give two solutions: δ_1=-$0.135^{+0.050}_{-0.054}$ and δ_2=-$2.758^{+0.395}_{-0.497}$. The angular distribution of the 518-keV transition and the minimization of the χ^2 are given in Fig. 6.2. The two cascades converge in one value of delta thus, the most probable value is δ_1 in both cases. Finally, taking the weighted average of the two results, the adopted value for the 518-keV transition is δ=-0.132±0.026. The reference [72] gives more details about these results.

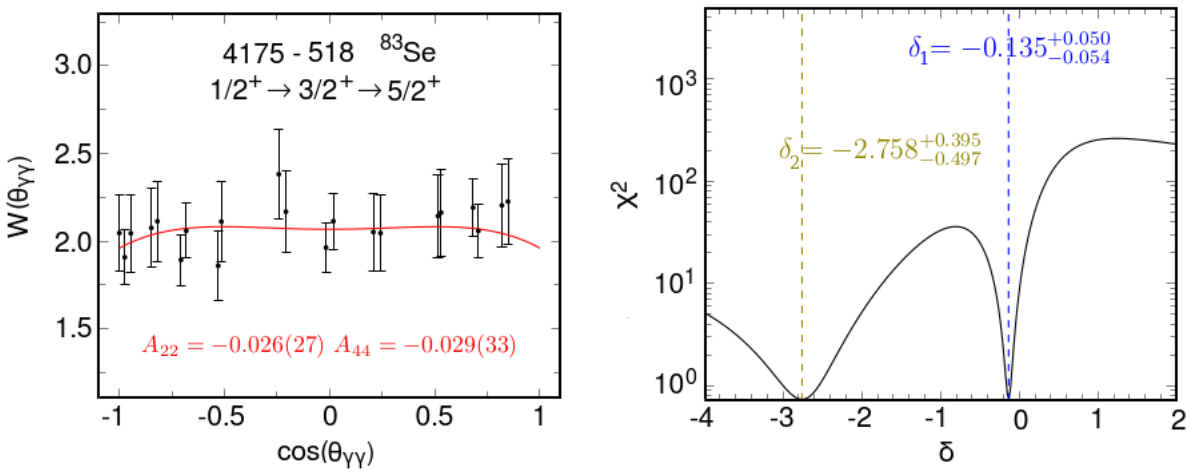

Figure 6.2: (Left) Angular distribution of 518-keV γ rays in coincidence with the pure M1 transition of 4715-keV. Experimental data are fitted with the function 6.13. (Right) The χ^2 function 6.14 is minimized at the two mixing δ values as indicated in the figure, adapted from [72].

Similarly, the mixing ratio of the 560-keV transition, connecting the $3/2^+$ with the $1/2^+$ intruder state, was evaluated by studying the coincidence between the 560 keV and the 4715 keV transition. The angular distribution of the 560-keV γ rays and the minimization of the χ^2 function is given in Fig. 6.3. The minimization of the χ^2 gives two possible solutions, δ_1=-$0.393^{+0.060}_{-0.056}$ and δ_2=-$6.669^{+1.702}_{-3.520}$, both with the same χ^2=0.079. Therefore, there is no clear evidence of the most probable solution. The study of the γ cascade $3/2^+ \rightarrow 1/2^+ \rightarrow 1/2^-$ to solve such ambiguity of the result is excluded since

this cascade does not fulfill the triangle condition. In the calculations shown later in this chapter, the value of δ_1=-0.393$^{+0.060}_{-0.056}$ is retained since it gives a B(E2) value similar to the one calculated for the $3/2^+ \rightarrow 5/2^+$ transition. The larger value δ_2 would return an unrealistically large B(E2) of 336 W.u., approximately one order of magnitude larger than B(E2) of the $3/2^+ \rightarrow 5/2^+$ transition.

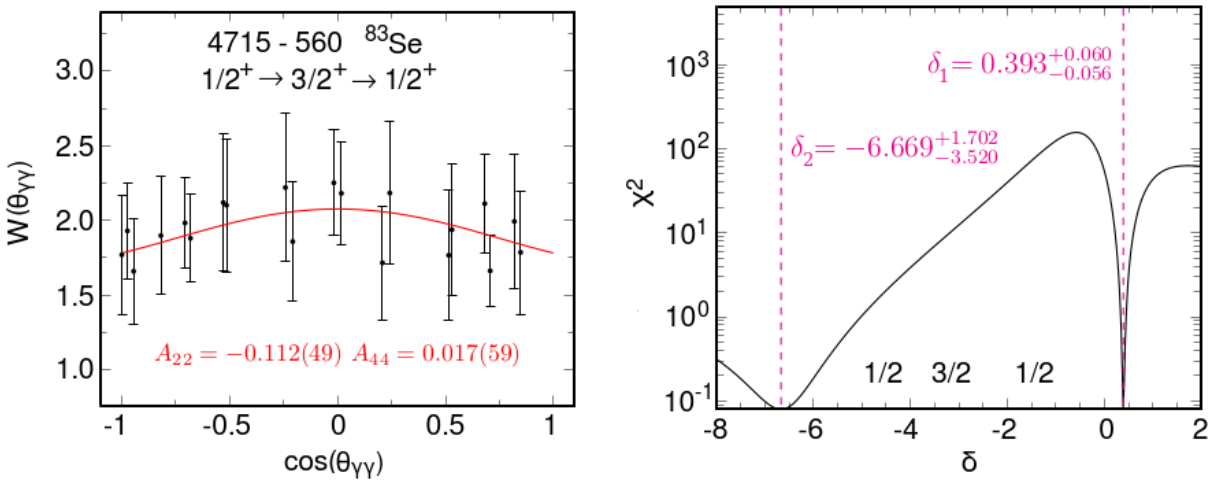

Figure 6.3: (Left) Angular distribution of 561-keV γ rays in coincidence with the pure E2 transition of 4715-keV. Experimental data are fitted with the function 6.13. (Right) The χ^2 function 6.14 is minimized at the two mixing δ values as indicated in the figure, adapted from [72].

6.3 Experimental reduced transition probabilities

The $1/2^+$ intruder state at 540 keV decays via a pure E1 transition of 311 keV to the $1/2^-$ state at 229 keV. We have measured the lifetime of the $1/2^+$ intruder state via the RDDS technique. The reduced transition probability calculated with Eq. 6.2 and converted to Weisskopf units using Eq. 6.5 is shown in Tab. 6.1.

For the other two transitions 518 and 560 keV, the mixing δ^2 must also be considered in calculating the reduced transition probability. Thus, the results obtained from the lifetimes of these transitions measured with the DSAM technique are combined with the mixing ratios from the experiment performed at the ILL laboratory. The strength of the M1 and E2 transition is calculated using the formula 6.11 and 6.12, respectively, and the results are shown in Tab. 6.1. According to the data in [6], for the 560-keV transition, a branching ratio of 22% was used in the calculation, while for the 518-keV transition, a branching ratio of 75%. The large error bars in the reduced transition probability of the E2 transition, around 30%, are related to the error bar of the mixing δ^2 coefficient. The reported values of the reduced transition probabilities have been measured for the first time in this work.

Table 6.1: The reduced transition probabilities for the $1/2^+ \rightarrow 1/2^-$, $3/2^+ \rightarrow 1/2^+$ and $3/2^+ \rightarrow 5/2^+$ transitions of ^{83}Se calculated by combining the experimental lifetimes measured in this work with the mixing ratios measured from the ILL experiment

Transition $J_i^\pi \rightarrow J_f^\pi$	E_γ (keV)	$t_{1/2}$ (ps)	δ	σL	B(σL) (W.u.)
$1/2^+ \rightarrow 1/2^-$	311	246 (5)	-	E1	$4.7(2)\cdot10^{-5}$
$3/2^+ \rightarrow 1/2^+$	560	0.298 (28)	-0.132(26)	M1	0.08(1)
$3/2^+ \rightarrow 1/2^+$	560	0.298 (28)	-0.132(26)	E2	46(12)
$3/2^+ \rightarrow 5/2^+$	518	0.298 (28)	-0.393(6)	M1	0.39(8)
$3/2^+ \rightarrow 5/2^+$	518	0.298 (28)	-0.393(6)	E2	30(11)

The two transitions, 518-keV and 560-keV, depopulating the $3/2^+$ intruder state have both large B(E2) values, 30 and 46 W.u., respectively. This indicates a strong deformation of the $3/2^+$, $5/2^+$, and $1/2^+$ intruder states.

For an axially deformed nucleus, the deformation parameter β_2 is related to the reduced transition probability B(E2) by the formula [2]:

$$B(E2 : J_i \rightarrow J_f) = \frac{5}{16\pi} e^2 Q_0^2 \langle J_i K_i 2\Delta K | J_f K_f \rangle^2 \tag{6.15}$$

where J is the angular momentum, K is the projection of the angular momentum along the z-axis, $\langle J_i K_i 2\Delta K | J_f K_f \rangle$ is the Clebsch-Gordan coefficient and Q_0 is the intrinsic quadrupole moment given by the expression:

$$Q_0 = \frac{3}{\sqrt{5\pi}} Z R_0^2 \beta_2 \tag{6.16}$$

where Z is the atomic number, R_0 is the radius of the nucleus if its shape is a perfect sphere, and β_2 is the deformation parameter.

Finally, by combining the expression 6.15 and 6.16, one gets the relation of the β_2 with the measured B(E2) value:

$$\beta_2 = \frac{4\pi}{3 Z R_0^2 \langle J_i K_i 2\Delta K | J_f K_f \rangle} \sqrt{\frac{B(E2)}{e^2}} \tag{6.17}$$

For the $3/2^+ \rightarrow 5/2^+$ transition, considering $K_i = K_f = 1/2$, the Clebsch-Gordan coefficient is $\langle J_i K_i 2\Delta K | J_f K_f \rangle = \langle \frac{3}{2}\frac{1}{2} 20 | \frac{5}{2}\frac{1}{2} \rangle = 0.29277$. Based on this estimation and using Eq. 6.17 considering $R_0 = 1.2A^{1/3}$ *fm*, the deformation parameter is $\beta_2 = 0.39(8)$.

For the $3/2^+ \rightarrow 1/2^+$ transition, considering $K_i = K_f = 1/2$, the Clebsh-Gordan coefficient is: $\langle J_i K_i 2\Delta K | J_f K_f \rangle = \langle \frac{3}{2}\frac{1}{2} 20 | \frac{5}{2}\frac{1}{2} \rangle = 0.44721$. The deformation parameter calculated with Eq. 6.17 is $\beta_2 = 0.31(6)$.

Typically for deformed nuclei, $\beta_2 > 0.3$ indicates a large deformation. From our results, it is proven that the $1/2^+$, $3/2^+$, and the $5/2^+$ intruder states of ^{83}Se are largely deformed.

6.4 Nuclear models

Several models have been developed with the goal of reproducing known properties of the nuclear medium and predicting new ones [1]. The existing models can be divided into two categories: macroscopic and microscopic models. The macroscopic models try to describe the nucleus as a whole starting from properties such as volume energy, surface energy, asymmetry energy, etc. These properties are then fitted to a wide range of nuclear properties. These models describe nicely the evolution of the nuclear binding energy along the chart. Among these models, one can mention the liquid-drop model [3].

In the microscopic models, the description of the atomic nucleus is based on the interacting nucleons. In these models, a two-body interaction (or three-body interaction) is used to solve the Schrödinger equation. Three different approaches can be mentioned aiming to describe the nucleus in the microscopic view: ab-initio [114], shell-model with effective interaction [115], and mean-field approximation [116].

- ab-initio method: This model aims to describe the atomic nucleus based on the hadronic degrees of freedom (starting from quarks and gluons). Ab-initio uses realistic nucleon-nucleon potentials from scattering data plus three-nucleon potentials derived from chiral effective field theories of QCD [117]. Within this approach, calculations can be performed only for light elements due to the computational power needed, even if recently heavier ions have started to be addressed in exploratory calculations.

- shell model - It is the most common framework used to describe atomic nuclei microscopically. In this model protons and neutrons occupy nuclear shells labeled with the quantum numbers (n,l,j,m_j). The nuclear state is calculated as a product of single-particle states. The residual interaction is obtained from general nucleon-nucleon interaction and/or fitted to experimental data. In the most commonly used calculations, an inert core is defined and only the valence nucleons outside this core contribute to the wave function that describes the nuclear state. The core excitations are taken into account in the renormalization of the nuclear Hamiltonian. The shell model describes a wide variety of nuclear phenomena and moreover, it was the first model to describe the appearance of "magic numbers".

- mean-field approximation - this method employs nuclear energy density functions based on Skyrme, Gogny, or relativistic interactions to determine the mean field and the interaction between the particles [118]. Using the Hartree-Fock-Bogoliubov (HFB) theory [116], pairing correlations are added into play. Lately, these methods are pushed beyond the mean-field approximation by restoring rotational invariance and particle number, being able to describe several properties along the nuclear chart [119, 120].

In this thesis, calculations were performed with both the shell model and the self-consistent mean field approximation. The formalism of these two theoretical models is introduced in the following sections.

6.4.1 Shell-model approach

The shell model is the basic framework for nuclear structure calculations and plays a crucial role in describing microscopically atomic nuclei [121]. The idea at the basis of this approach is the existence of a spherical mean field made of a central potential, a spin-orbit interaction, and a residual interaction containing other terms. Calculations can be performed by simplifying the nuclear many-body interaction into a problem of only a few nucleons outside an inert core. The protons and the neutrons in the inert core are coupled to angular momentum J=0 and frozen in their orbits. The nucleons outside the core are free to move in several orbits defined as the model space or the valence space. The wave function of a nuclear state is described as a product of single-particle states. The product-like states are used as a basis for this reduced Hilbert space where the Hamiltonian matrix is set up and diagonalized.

The formalism of the shell model for the description of a system of A-nucleons starts with the Schrodinger equation:

$$\hat{H}|\psi\rangle = \left(\sum_i \hat{T}_i + \hat{V}_{ij}^{NN}\right)|\psi\rangle = E|\psi\rangle \tag{6.18}$$

where $\hat{T}$ is the kinematic energy operator and $\hat{V}$ is the nucleon-nucleon interaction potential. To treat the solution perturbatively the Hamiltonian is expressed as

$$\hat{H} = \hat{H}_0 + \hat{H}_1 \tag{6.19}$$

where $\hat{H}_0$ is the unperturbed part of the Hamiltonian, a one-body term that describes the independent motion of the nucleons, whereas $\hat{H}_1$ includes the perturbation term containing the 2 body-interaction.

It is impossible to solve exactly the Schrödinger equation for the full Hilbert space. Thus, the model assumes the nucleus as an inert core plus the active nucleons in the restricted valence space. The valence space is defined in terms of the eigenvectors of $\hat{H}_0$:

$$|\phi_i\rangle = [a_1^\dagger a_2^\dagger ... a_n^\dagger]|c\rangle \qquad i = 1, ..., d \tag{6.20}$$

where $|c\rangle$ represent the inert core, the subscripts $1, 2, ..., n$ represents the single-particle states in the valence space and i the quantum number describing the state [122].

After reducing the Hilbert space, one needs to construct an effective Hamiltonian acting in the model space such as:

$$\hat{H}_{eff}\hat{P}|\psi_\alpha\rangle = \left(\hat{H}_0 + \hat{V}_{eff}\right)\hat{P}|\psi_\alpha\rangle = E_\alpha\hat{P}|\psi_\alpha\rangle \tag{6.21}$$

where E_α and ψ_α are a subset of eigenvalues and eigenfunctions of the original Hamiltonian and $\hat{P}$ the operator which projects from the full Hilbert space into the model space. The operator $\hat{P}$ is:

$$\hat{P} = \sum_i^d |\phi_i\rangle\langle\phi| \tag{6.22}$$

Different types of effective shell-model Hamiltonians are defined. The empirical interactions [123] use and fit experimental data to find the optimum values of the single-particle energies. The microscopic effective interactions (realistic interaction) [124] use many-body techniques starting from the free nucleon-nucleon potential to obtain the single-particle energies and the two body matrix elements. Finally, schematic interactions use analytical expressions with few adjustable parameters.

To summarize, the ingredients for performing shell-model calculations are: an inert core, a valence space the dimensions of which depend on the degrees of freedom of the system but are limited by the size of the matrix to be diagonalized, and an effective interaction which is a renormalization of the Hamiltonian in the model space.

6.4.2 Self-consistent mean field approximation

In the self-consistent mean-field approach, at first a set of single-particle wave functions is chosen to describe the nuclear state, $\psi_i(r,\sigma,\tau)$, where r stands for the spatial coordinates, σ for the spin ($\pm 1/2$) and τ stand for the isospin ($\pm 1/2$). The number of single-particle wave functions of the basis is bigger than the number of nucleons in the nucleus. The nuclear state ϕ can be expressed as a Slater determinant based on the single-particle wave functions defined previously.

$$|\phi\rangle = det\{(\psi_1(r_1,\sigma_1,\tau_1),\psi_1(r_1,\sigma_1,\tau_1),...,\psi_A(r_A,\sigma_A,\tau_A)\} \tag{6.23}$$

where A is the mass number of the nucleus.

It is useful to introduce the creation operator $\hat{a}_i^+$ for a nucleon in the single-particle state ψ_i(r,σ,τ) employing the creation operator $\hat{a}_x^+$ for eigenstates of position. The coordinate-space representation of the creation operator can be written as:

$$\hat{a}_i^+ = \int d^3r \sum_{\sigma\tau}(\psi_i(r_i,\sigma_i,\tau_i)\hat{a}_x^+ \tag{6.24}$$

Thus, $\hat{a}_i^+|\phi\rangle = 0$ for occupied states (i$\leq$A) and $\hat{a}_i|\phi\rangle = 0$ for unoccupied states (i>A).

To include the pairing correlations between the nucleons, the concept of the indepen-

dent quasi-particles is introduced via the unitary Bogoliubov transformation (U,V).

$$\hat{b}_n^+ = \sum_i (U_{in}\hat{a}_i^+ + V_{in}\hat{a}_i) \tag{6.25}$$

This relation connects single-particle states with the quasiparticle states.

In self-consistent mean-field models, the energy functionals are described in terms of density matrices. So, it is convenient to describe the independent-particle states in terms of the one-body density matrices. For independent quasiparticles, one has to deal with two objects: a one-body density matrix ρ and a pair tensor κ, given by the relations below;

$$\rho_{i,j} = \langle\phi|\hat{a}_j^+\hat{a}_i|\phi\rangle = (V^*V^T)_{ij} = \rho_{ji}^* \tag{6.26}$$

$$\kappa_{i,j} = \langle\phi|\hat{a}_j\hat{a}_i|\phi\rangle = (V^*U^T)_{ij} = -\kappa_{ji}^* \tag{6.27}$$

The ground state $|\phi\rangle$ of the nucleus with N neutrons and Z protons can be found by the minimization of the total energy E.

$$E = \langle\phi|\hat{H}|\rangle\phi = E(\rho, \kappa, \kappa^*) \tag{6.28}$$

Since in this approximation the number of particles is not conserved, the equation is solved under the constraint that the expectation value of the neutron and proton number operator is N and Z, $\langle\phi|\hat{N}_q|\phi\rangle = \mathrm{N}_q$.

Density-dependent interactions have been developed and are used in HFB calculations to describe nuclear structure. The most common forces are the Skyrme [125, 126] and the Gogny forces [127]. The Gogny force consists of four terms: a central term that contains the spin and isospin channel, a two-body spin-orbit term, a phenomenological density-dependent term introduced to reproduce the saturation property of the nuclear interaction, and the standard Coulomb potential between protons [116]. The Gogny interaction depends on several adjustable parameters that are obtained by performing a fit to the experimental data. In this work, calculations were performed using the Gogny force with the D1M parametrization [128].

6.5 Theoretical calculations

The experimental results are compared in the next two sections with theoretical calculations performed with the shell model and mean-field approach.

6.5.1 Shell-model calculations

Shell-model calculations were performed with the ANTOINE code [129] using the GWB interaction from the Oxbash library [130]. Modifications were applied in the interaction, extending the neutron valence space above the N=50 shell gap. In the calculations, a closed core of ^{66}Ni was considered, thus 17 nucleons (6 protons and 11 neutrons) are free to move in the valence space. The valence space for the protons includes the $2p_{1/2}$, $1f_{5/2}$, $2p_{3/2}$, $1g_{9/2}$ orbitals, while for the neutrons the $1p_{1/2}$, $1g_{9/2}$ orbitals and those above the N=50 closed shell: $2d_{5/2}$, $3s_{1/2}$, $1g_{7/2}$, $2d_{3/2}$. The standard values of the effective charges for the proton and the neutron were used: e_π = 1.5 e and e_ν = 0.5 e. The magnetic moments used in the calculations were the effective ones: for protons g_s=4.1895, g_l=1.1 and for neutrons g_s=-2.8695 and g_l=-0.1. Calculations were performed for the $1/2^+$, $3/2^+$, $5/2^+$, and $9/2^+$ states using 2p-2h and also 4p-4h excitations. A comparison of the experimental energy levels of ^{83}Se with the ones obtained from the shell model is shown in Fig. 6.4. Shell-model calculations reproduce the sequence of the energy levels of ^{83}Se. From Fig. 6.4 it appears that different truncations of the model space significantly change the energy spectrum. The ground state in both cases results to be the $9/2^+$ state, coherently with experimental observations.

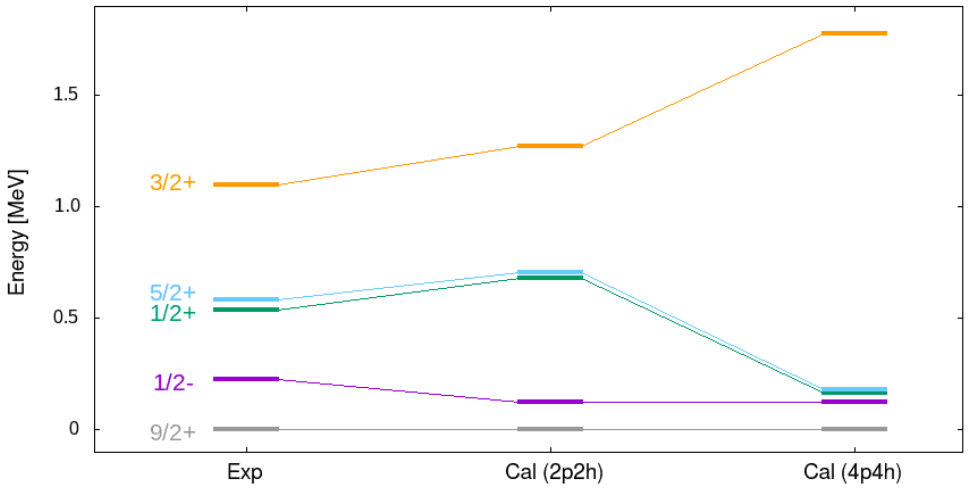

Figure 6.4: The energy of the $1/2^-$, $1/2^+$, $3/2^+$, $5/2^+$, and $9/2^+$ excited states of ^{83}Se compared to the ones calculated from shell model. Calculations are performed with 2p2h and 4p4h excitations.

The reduced transition probabilities given by the shell-model calculations are presented in Tab. 6.2 for the L=1 and L=2 transitions, and compared with the experimental values obtained in this work.

As shown in Tab. 6.2, the reduced transitions are similar for both calculations with different truncations (2p-2h,4p-4h) and the same occurs for the occupation numbers of the levels, drawn in Fig. 6.5.

The 582-keV transition

Table 6.2: The experimentally reduced transition probabilities deduced from the experimental lifetimes measured in this work and the mixing ratios measured from the ILL experiment compared to shell model calculations. The transition marked with the asterisk is not measured in this work but is included as a benchmark of the theoretical calculations.

Transition $J_i^\pi \rightarrow J_f^\pi$	E_γ (keV)	σL	B(σL)$_{exp}$ (W.u.)	B(σL)$_{cal}^{2p2h}$ (W.u.)	B(σL)$_{cal}^{4p4h}$ (W.u.)
$1/2^+ \rightarrow 1/2^-$	311	E1	$4.7(2)\cdot10^{-5}$	$5\cdot10^{-4}$	-
$3/2^+ \rightarrow 1/2^+$	560	M1	0.08(1)	0.1	0.06
$3/2^+ \rightarrow 1/2^+$	560	E2	46(12)	15	16
$3/2^+ \rightarrow 5/2^+$	518	M1	0.39(8)	0.5	0.31
$3/2^+ \rightarrow 5/2^+$	518	E2	30(11)	12	13
$^*5/2^+ \rightarrow 9/2^+$	582	E2	0.11(2)	0.06	0.09

As anticipated previously, the lifetime of the $5/2^+$ intruder state is known. The 582-keV transition which decays from this state to the ground state of ^{83}Se has a B(E2) of only 0.1 W.u. This level has been included in our shell-model calculations and it is therefore a test of their quality. The B(E2) value of this transition is quite well reproduced from the theoretical calculations, especially when including 4p4h excitation. The ground state of ^{83}Se is known to be spherical, this is why the B(E2) from the highly deformed 582-keV state to the g.s is suppressed. This makes the $5/2^+$ intruder state ($t_{1/2}$=3.6 ns [6]) a shape isomer.

The $1/2^+$ intruder state

The 311-keV transition connects the intruder state with spin $1/2^+$ with the $1/2^-$ state. The B(E1) of this transition obtained from the lifetime measured in this work results to be $(4.7\pm0.2)\cdot10^{-5}$ W.u. Shell model calculations gives B(E1)=$5\cdot10^{-4}$ W.u. Based on the shell-model calculations, the wave function of the $1/2^+$ intruder state has a strong contribution (around 60%) from $\nu g_{9/2}^{-2}\nu d_{5/2}^{1}$ coupled to 2^+ of ^{82}Se. The contribution of the $\nu g_{9/2}^{-2}\nu s_{1/2}^{1}$ in the wave function of the $1/2^+$ intruder state appears to be less dominant, of about a factor of two compared to the contribution of the $\nu d_{5/2}$ across the N=50 shell gap. The wave function of the $1/2^-$ state has a dominant contribution from the $\nu p_{1/2}^{-1}\nu g_{9/2}^{full}$ component.

The $3/2^+$ intruder state

The 1100-keV $3/2^+$ state decays via the 518-keV and the 560-keV γ-ray transitions to the $5/2^+$ and $1/2^+$ states, respectively, and both show strong M1 and E2 components. The E2 contribution, as obtained from the results of this work, implies a strong deformation, $\beta_2 \approx 0.3$. For these transitions, the shell model calculations seem to underestimate the strength of the B(E2) transitions. Compared to the experimental data, the calculated

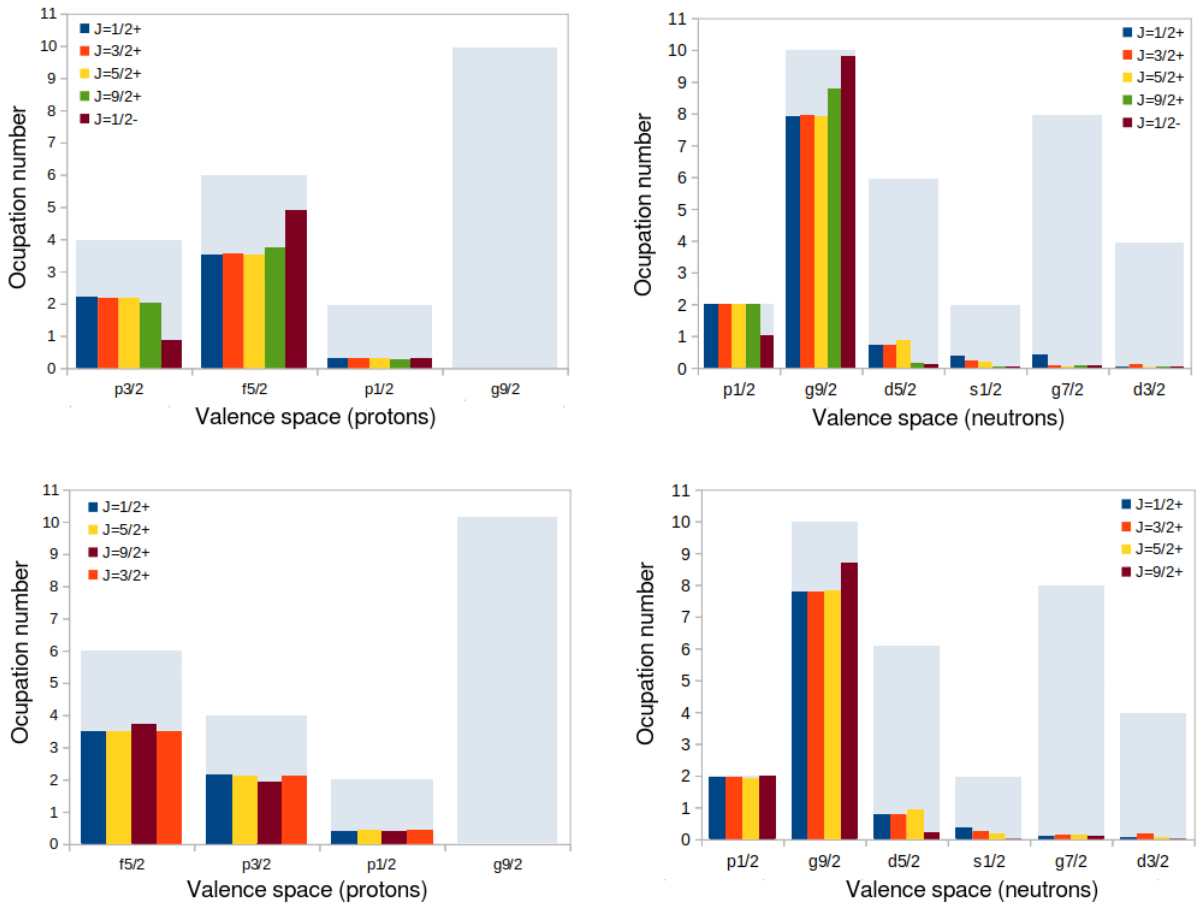

Figure 6.5: (Top) The occupation numbers of the proton and neutron valence space for the $1/2^+$, $3/2^+$, $5/2^+$, and $9/2^+$ states of ^{83}Se. Calculations are performed with 2p2h excitations. (Bottom) The same calculations with 4p2h excitations.

reduced transition probabilities for the E2 components are of a factor of three smaller. For the M1 transitions, the calculations are in good agreement with the values obtained from the measured lifetimes.

The wave function of the $3/2^+$ intruder state shows to have a large contribution (about 64%) from the $\nu g_{9/2}^{-2}\nu d_{5/2}^{1}$ configuration while the $\nu g_{9/2}^{-2}\nu s_{1/2}^{1}$ component contributes with 19%. A smaller contribution comes from the $d_{3/2}$ orbital with 9%. A contribution to the wave function of the $3/2^+$ emerges from the promotion of 2 neutrons across the N=50 shell gap. Configurations of the nature 3p-3h such as $\nu g_{9/2}^{-3}\nu d_{5/2}^{2}$, $\nu g_{9/2}^{-3}\nu d_{5/2}^{1}s_{1/2}^{1}$ or $\nu g_{9/2}^{-3}\nu d_{5/2}^{1}g_{7/2}^{1}$ contribute in total with 8% in the wave function.

6.5.2 Energy-density-functional calculations for the N=49 isotones

HFB calculations were performed for the N=49 isotones with the Gogny D1M energy density functional. This interaction has been able to reproduce a vast amount of nuclear observables [131–133].

The calculation performed for ^{83}Se by T. Rodríguez proceeds as follows. First, a basis constructed from a set of states $|\Phi(\beta_2)\rangle$ that minimizes the HFB energy is found as a function of the axial quadrupole deformation in the N=48 neighboring isotopes, represented in Fig. 6.6 and Fig. 6.7 in the left panels. This set of states is used as a basis to express the states to be calculated, $\{(\alpha^{\dagger}_{K^{\pi}}(\beta_2)|\phi(\beta_2)\rangle)\}$ where $\alpha^{\dagger}_{K^{\pi}}$ is the quasiparticle creation operator with a well defined K-value (projection of the angular momentum onto the z-axis of the nucleus and parity π). The total energy surface (TES) obtained by solving the HFB equation, with such states as the seed wave function for the $K^{\pi} = 1/2^{+}$, $3/2^{+}$, $5/2^{+}$, $7/2^{+}$ and $9/2^{+}$, gives the total energy surfaces for the N=49 isotones, represented in Fig. 6.6 and Fig. 6.7 in the right panels. If we assume that K^{π} represents the angular momentum and parity of the state, the minimum of the TES is the mean-field approximation to the energy of the K^{π} state for the N=49 isotones.

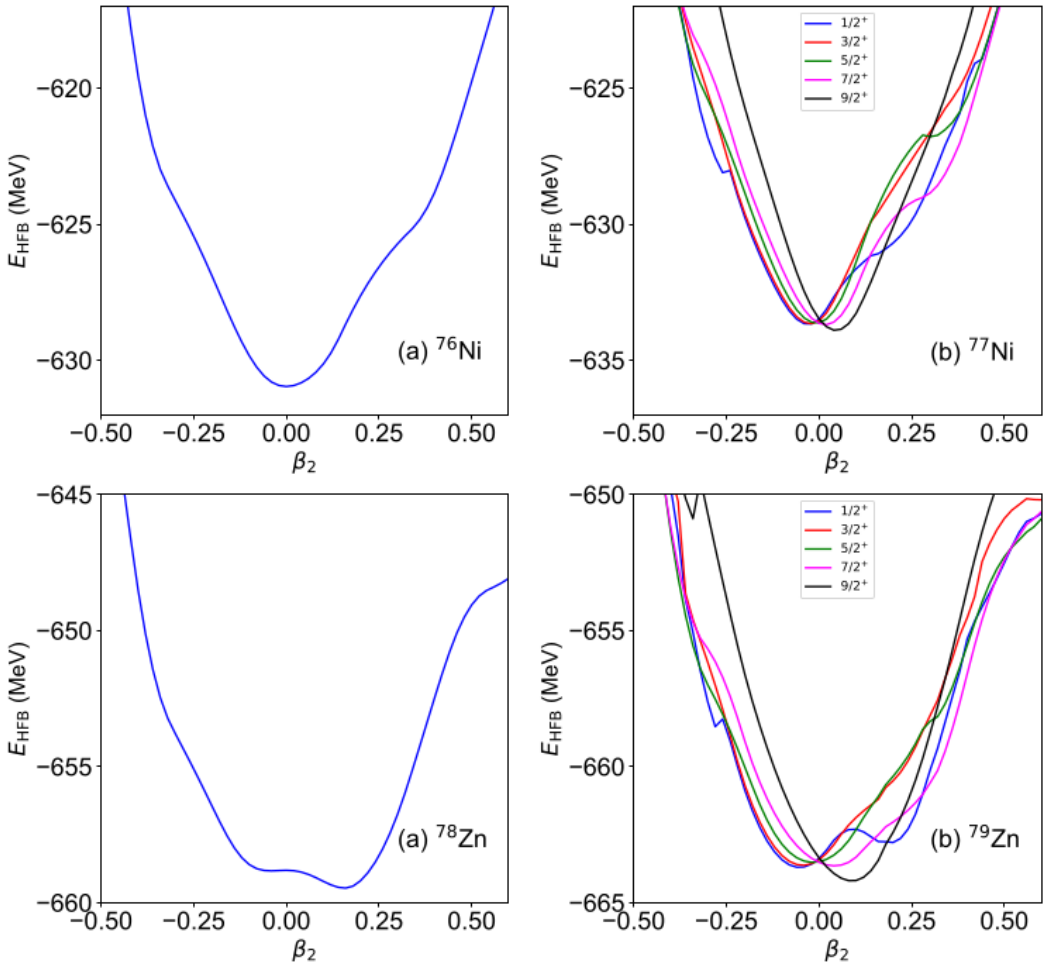

Figure 6.6: (Left) The axial quadrupole deformation for N=48 isotopes. (Right) The total energy surface for N=49 isotones. Calculations and figures provided by [134].

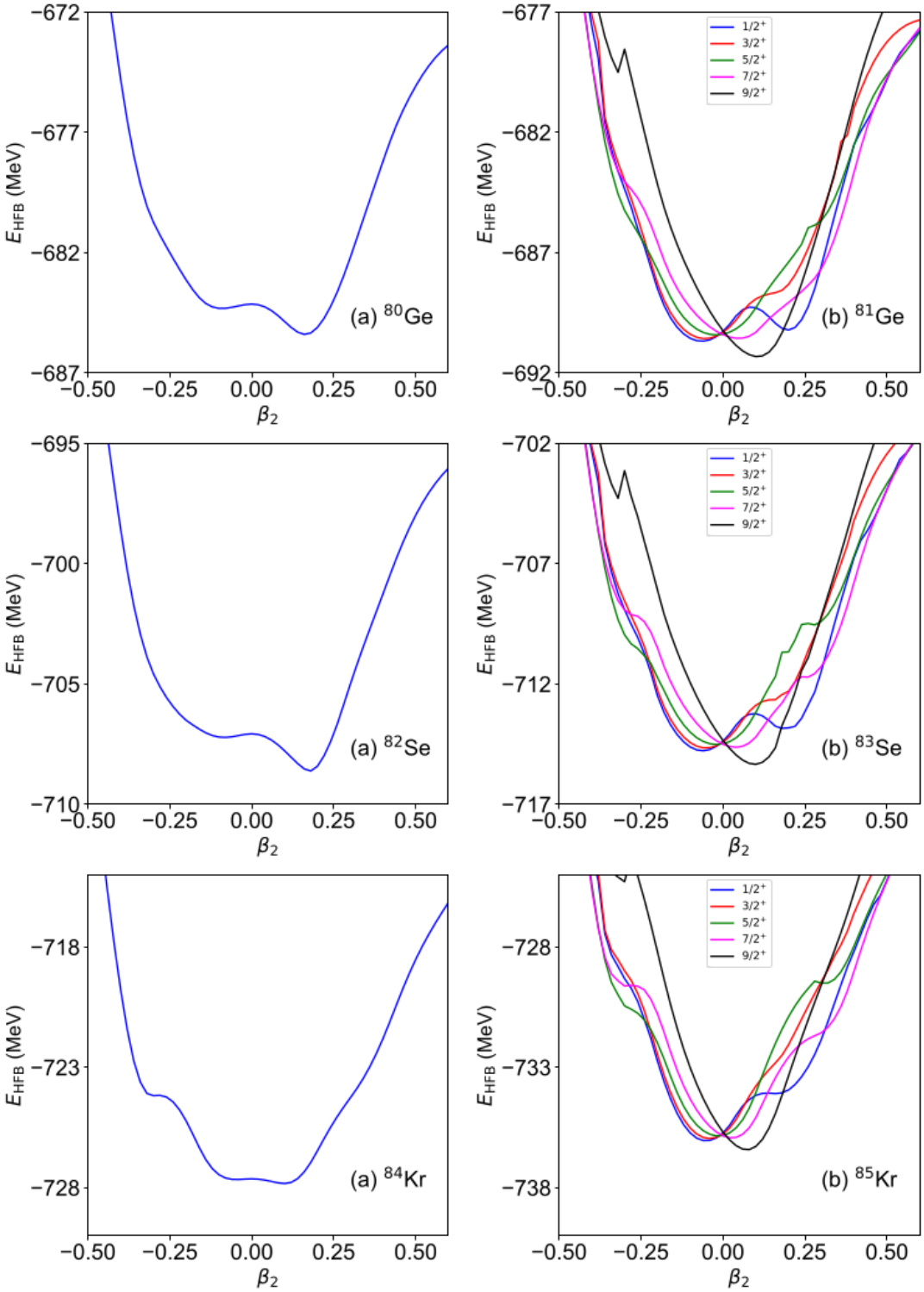

Figure 6.7: (Left) The axial quadrupole deformation for N=48 isotopes. (Right) The total energy surface for N=49 isotones. Calculations and figures provided by [134].

The energies of the excited states along N=49 isotones calculated from the density-energy-functional method are shown in Fig. 6.8. The calculations give the $9/2^+$ energy level as a ground state, the $1/2^+$ as a first excited state, then the $3/2^+$ and $7/2^+$ states very close in excitation energy and, higher up th $5/2^+$ state in all the N = 49 isotones except for ^{77}Ni, where the $1/2^+$, $3/2^+$, $5/2^+$ and $7/2^+$ are very close in excitation energy. The trend of the excitation energy of the $1/2^+$ intruder state differs from the experimental data. Experimentally, the $1/2^+$ intruder state reaches a minimum in ^{83}Se along the N=49 isotonic chain which is not reproduced by the calculations. Actual symmetry restoration (particle number, angular momentum, and parity) and shape mixing could play a role in the energy levels. Such calculations are quite challenging for even-odd nuclei and should be explored in the future for deriving reduced transition probabilities.

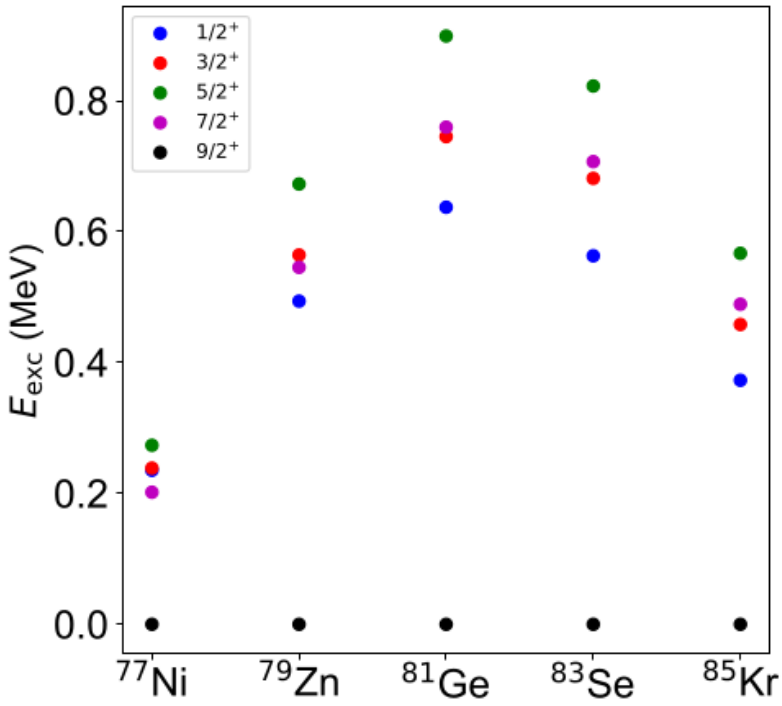

Figure 6.8: Excitation energies of the positive parity band for the N=49 isotones obtained by mean-field calculations using the Gogny force. The calculations do not reproduce the trend of the $1/2^+$ intruder state along N=49 isotonic chain. The calculations and the figure provided by [134].

6.5.3 Calculations with variational approaches using the PFSDG-U interaction

The TAURUS code allows one to perform variational calculations using real general Bogoliubov quasiparticle states represented in a spherical harmonic oscillator basis [135]. This numerical code can perform both no-core and valence-space calculations.

Calculations were performed by T. Rodríguez using the PFSDG-U interaction developed by F. Nowacki and A. Poves. This interaction is tuned to perform calculations for nuclei in the vicinity of ^{78}Ni [136]. This interaction has a closed core of ^{40}Ca and considers the full pf+gds orbits for both the protons and the neutrons. For the ^{83}Se nucleus calculations with this interaction using large-scale shell-model calculations do not provide an exact solution since the full diagonalization of the Hamiltonian is not accessible due to the number of particles outside the core. Instead, variational methods can be used to perform theoretical calculations exploiting the PFSDG-U interaction and the TAURUS code. Since the TAURUS code is being used for the first time in this region, to test its performance calculations were performed for the even-even Se isotopes, ^{82}Se and ^{84}Se, with the regular shape and K-mixing of particle number and angular momentum restoration of triaxial wave functions obtained with the Particle Number Variation After Projection method (PNVAP) [137,138]. The results are reported for the even-even neighbors of ^{83}Se in the following.

Calculations for ^{82}Se

The total energy surface of ^{82}Se obtained with the PNVAP method is shown in the (β_2, γ) plane in Fig. 6.9. The two minima in the total energy surface, one prolate and one oblate, indicate the appearance of shape coexistence in this nucleus.

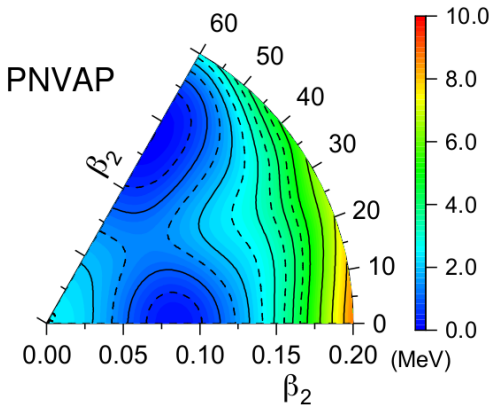

Figure 6.9: Total energy surfaces as a function of the triaxial deformations (β_2, γ) calculated for ^{82}Se within the PNVAP approach without *pn*-mixing. Calculations and figure provided by [134].

By projecting the total energy surface in good angular momentum and after mixing, the collective wave functions for several states are obtained and shown in Fig. 6.10. The ground state band is an oblate band (0_1^+, 2_1^+, 4_1^+ and 6_1^+ states) while the band build on the 0_2^+ state is prolate (0_2^+, 2_2^+, 4_2^+ and 6_2^+ excited states). The energies of the excited states obtained from the calculations using the Projected Generator Coordinate Method (PGCM) [139] are shown in Fig. 6.11 and compared with experimental data. PGCM is a beyond-mean-field method that gives excitation energies, decay probabilities,

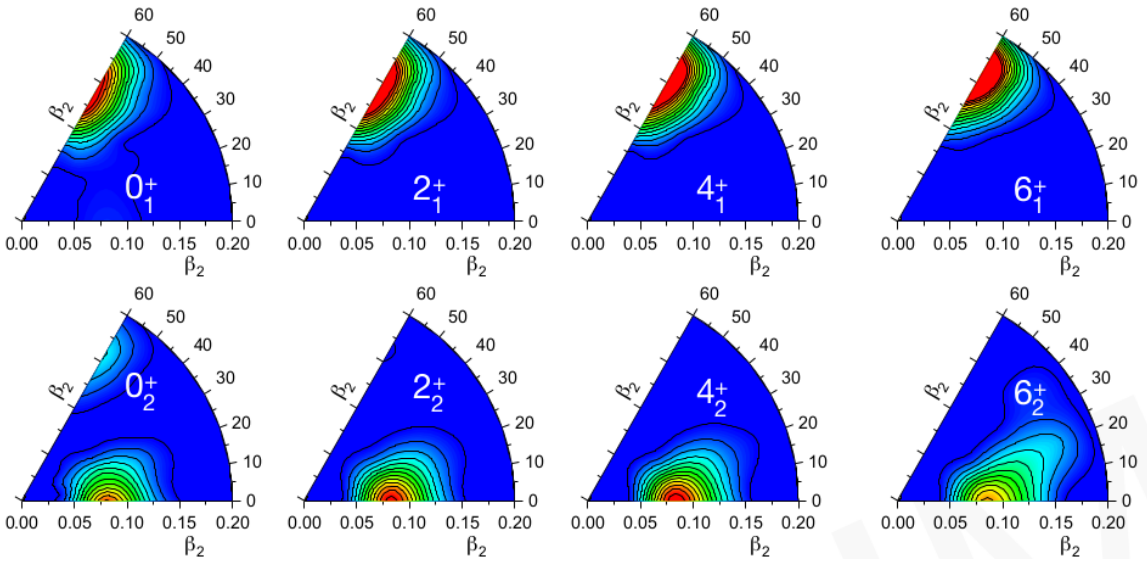

Figure 6.10: Collective wave functions of several excited states of ^{82}Se obtained by projecting the total energy surface in good angular momentum and mixing. Calculations and figure provided by [134].

and interpretations of the results in terms of collective and single-particle degrees of freedom. The calculated energy levels result to be slightly compressed with respect to the experimental ones (See Fig. 6.11), but still in good agreement.

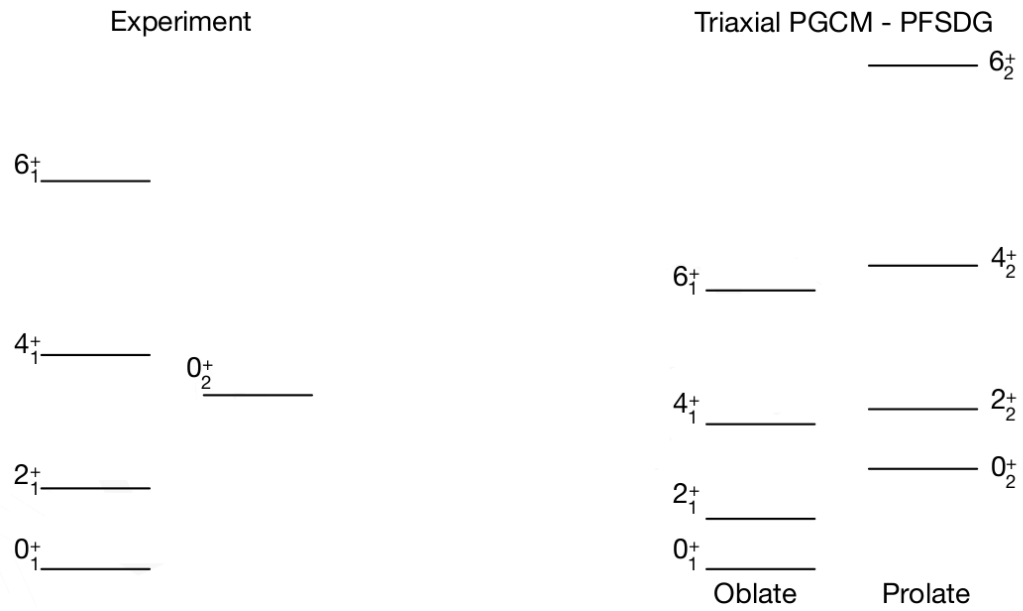

Figure 6.11: Comparison of the excitation energies of ^{82}Se with the calculated ones. Calculations and figure provided by [134].

Calculations for ^{84}Se

The total energy surface in the (β_2, γ) plane for ^{84}Se is shown in Fig 6.12. Three minima can be seen: the spherical minimum which corresponds to the N=50 shell closure, and the prolate and oblate minima.

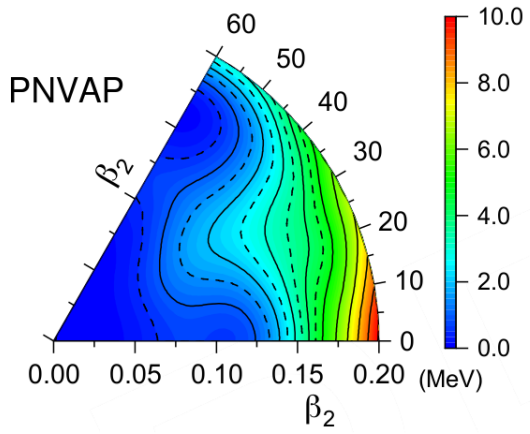

Figure 6.12: Total energy surfaces as a function of the triaxial deformations (β_2, γ) calculated for ^{84}Se within the PNVAP approach without pn-mixing. Calculations and figures provided by [134].

After projecting and mixing, the 0_1^+ ground state results in an oblate shape and two side rotational bands are also observed: One oblate band is built above the 0_2^+ state and one prolate is built above the 0_3^+ state. The collective wave functions for the excited states of this nucleus are shown in Fig. 6.13.

A comparison of the excitation energies obtained from the calculations using the PGCM method and the PFSDG-U interaction with the experimental data is shown in Fig. 6.14. The calculated energy levels are much lower than the experimental ones.

Calculations for ^{83}Se

For ^{83}Se different degrees of freedom are explored in the calculations. In the case of the negative parity band the calculations are performed with the regular shape and K-mixing of particle number and angular momentum restoration of triaxial wave functions obtained with the PNVAP method with proton-neutron mixing and blocking (the wave functions are one quasi-particle excitations on top of the even-even nuclei). In the case of the positive parity band, the calculations are performed with T=0, T=1, proton-neutron pairing and K-mixing of particle number and angular momentum restoration of wave functions obtained with PNVAP with proton-neutron mixing and blocking.

The HFB total energy surface for the positive and the negative parity bands is shown in Fig. 6.16 where indications of shape coexistence can be seen from the prolate and the oblate minima in the total energy surface both in the positive and the negative parity states.

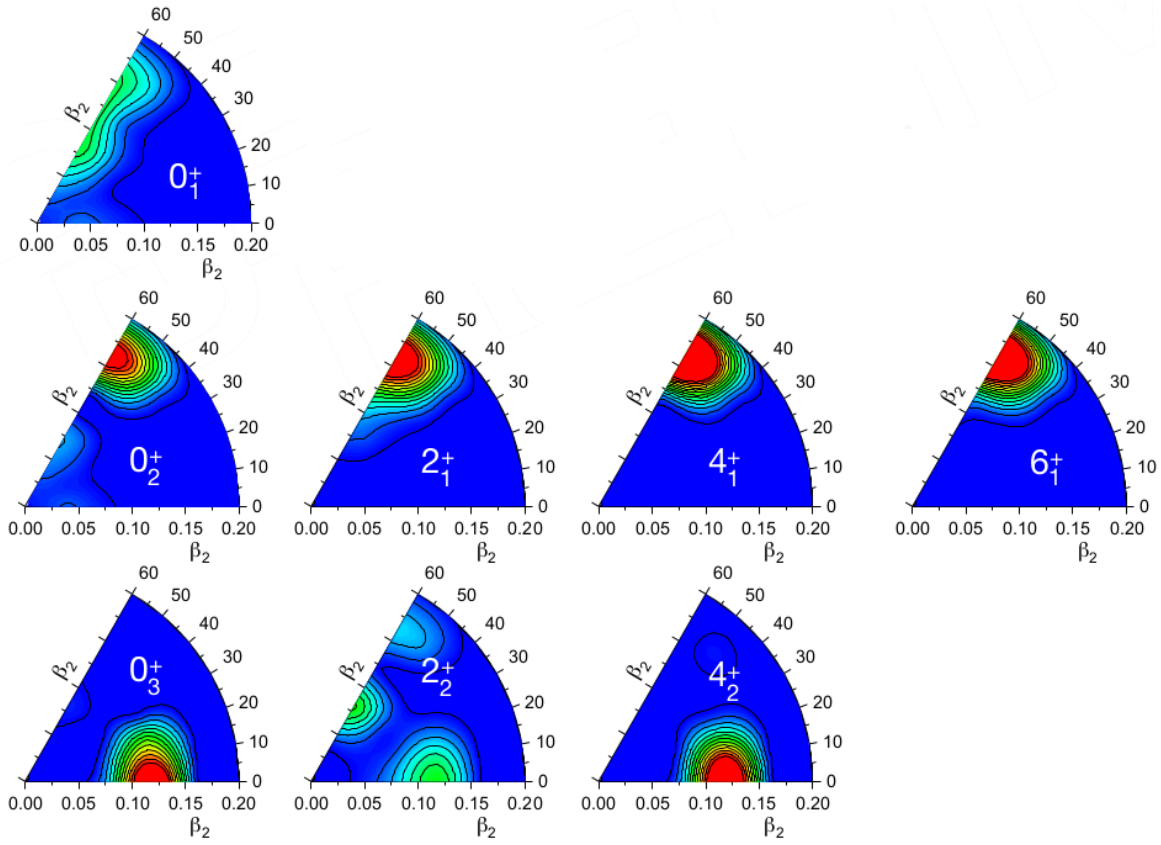

Figure 6.13: Collective wave functions of several excited states of ^{84}Se obtained by projecting the total energy surface in good angular momentum and mixing. Calculations and figures provided by [134].

The collective wave functions for the excited states of ^{83}Se are shown in Fig. 6.13. The collective wave functions of the negative parity yrast states are rather constant and peak at oblate configurations.

The energies of the excited states for the positive and the negative parity bands for ^{83}Se are shown in Fig. 6.17. At variance with the experimental data, the $5/2^+$ results to be the ground state of this nucleus. Calculations of the reduced transition probabilities are still in progress [134].

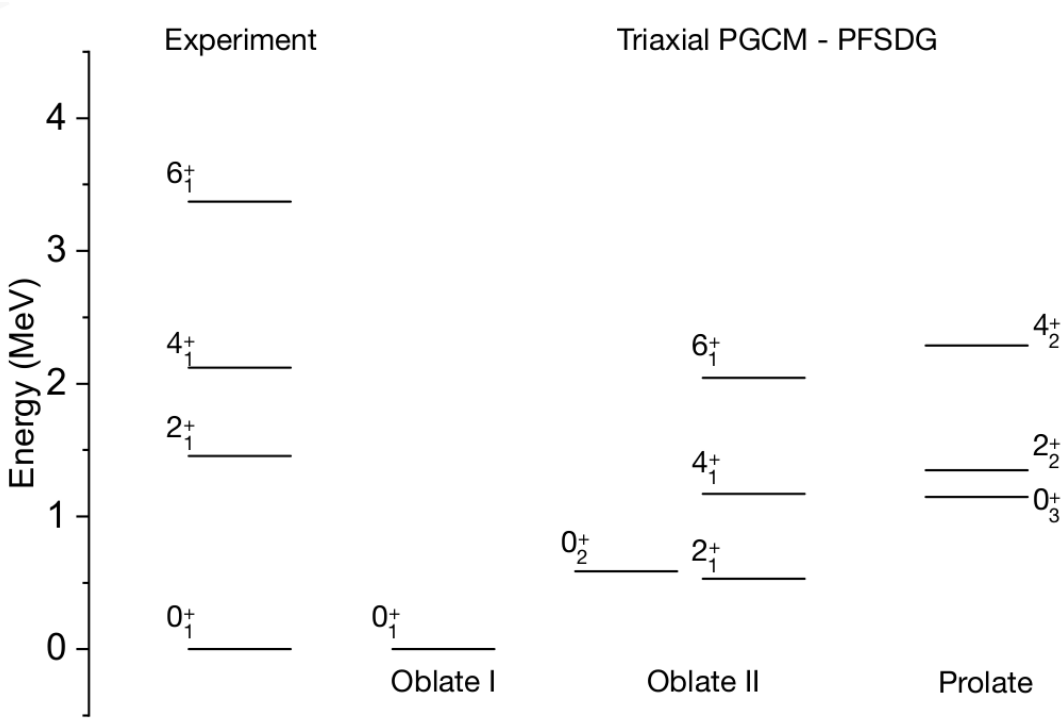

Figure 6.14: Comparison of the experimental excitation energies of ^{84}Se with the calculated ones. Calculations and figures provided by [134].

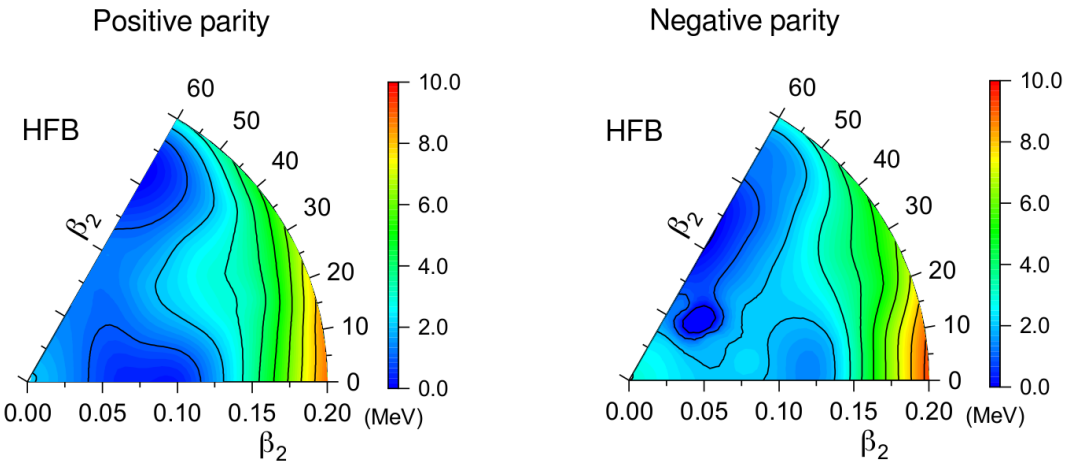

Figure 6.15: Total energy surfaces as a function of the triaxial deformations (β_2, γ) calculated for the positive and the negative parity band of ^{83}Se within the HFB approach. Calculations and figures provided by [134].

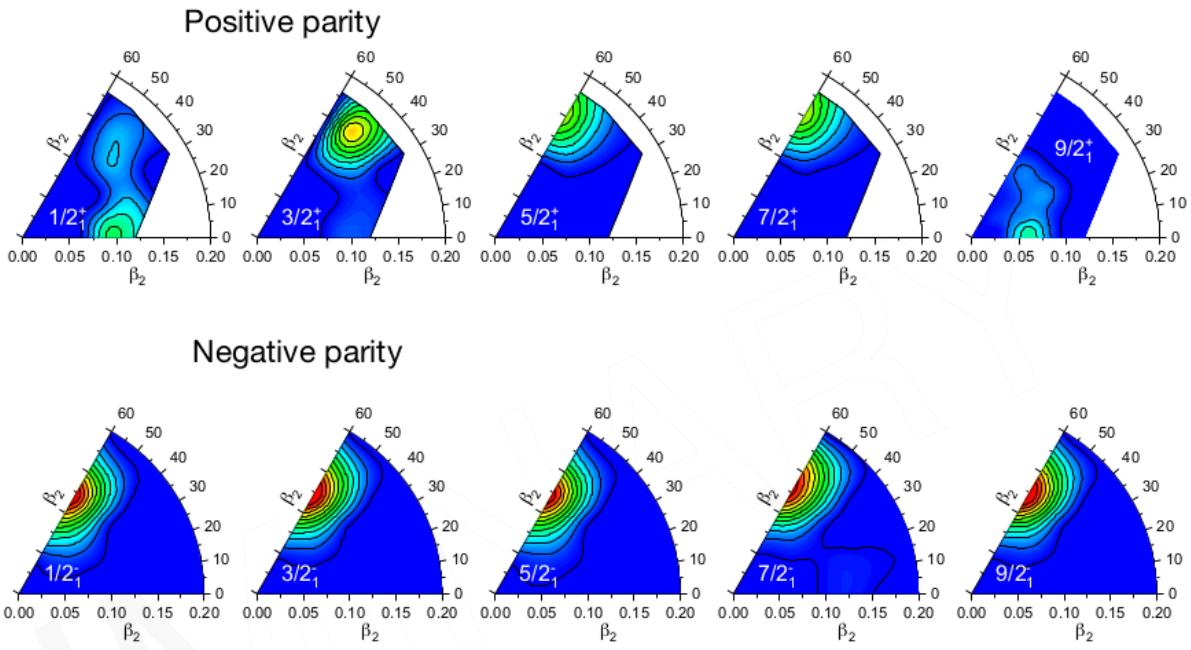

Figure 6.16: Collective wave functions of negative and positive parity states of ^{83}Se obtained by projecting the total energy surface in good angular momentum and mixing. Calculations and figures provided by [134].

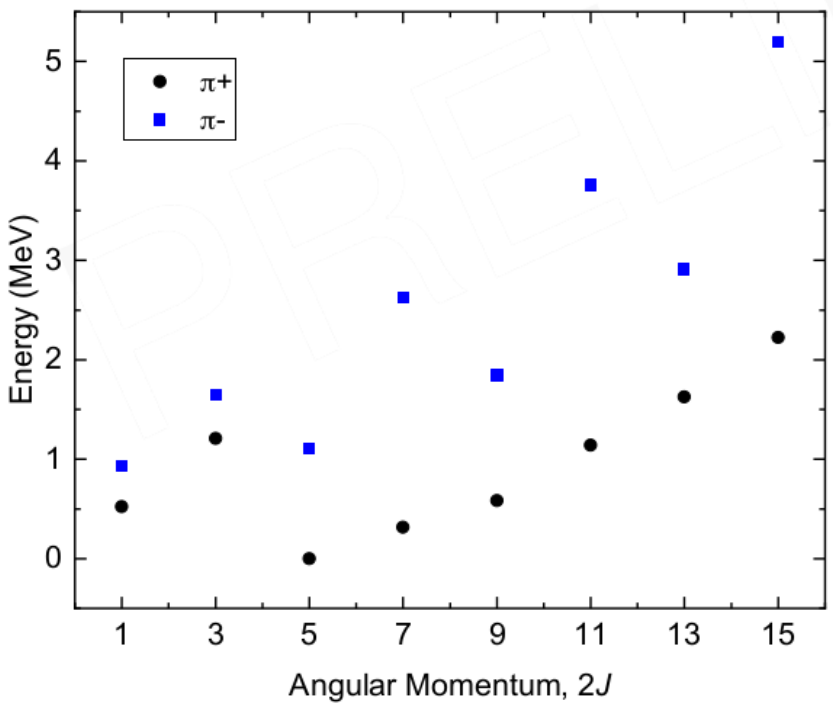

Figure 6.17: Excitation energies of the positive and negative parity states of ^{83}Se provided by theoretical calculations using the PFSDG-U interaction. The ground state of this nucleus results to be the $5/2^+$ intruder state, contradicting the experimental data. Calculations and figures provided by [134].

Chapter 7

Summary and conclusions

The intruder states with spin $1/2^+$ and $5/2^+$, emerging from the promotion of a neutron across the N=50 shell gap appear all along the N=49 isotones and reach the lowest excitation energy in ^{83}Se. The weakening of the N=50 shell gap towards ^{78}Ni favors the lowering in energy of the deformed configurations. Moreover, since ^{83}Se (Z=34) is at the middle of the proton shell (Z=28-40), quadrupole correlations are at maximum, bringing the deformed configurations lower in energy.

In this work, the intruder states of ^{83}Se, the $1/2^+$ 540-keV and the $3/2^+$ 1100-keV state, have been characterized for the first time in terms of collectivity. Lifetimes of intruder states were measured using the RDDS and the DSAM reported in this work. To populate the states of interest, a (d,p) reaction was exploited. A beam of ^{82}Se with an energy of 270 MeV impinged on a deuterated polyethylene foil with thickness 1 mg/cm^2 evaporated on a 6 mg/cm^2 Au backing. For the measurement with the DSAM technique, the deuterated target was evaporated on a 30 mg/cm^2 thick Au backing. The experiment was performed using the GALILEO γ-ray array coupled to the SPIDER silicon detector and a plunger device for lifetime measurements. The coupling of the GALILEO array with the SPIDER detector gave the possibility to measure in coincidence the scattered proton from the (d,p) reaction and γ rays, providing the needed event-by-event channels selectivity. Moreover, the use of a (d,p) reaction with a gate on the energy of the ejectile, hence on the excitation energy of the state of interest, avoids any direct feeding from other transitions. The measured lifetimes of the intruder states combined with the M1/E2 mixing ratio of the transitions of interest allowed to extract the reduced transition probabilities.

The intruder $1/2^+$ 540-keV state decays by a pure E1 γ-ray transition with energy 311 keV on the $1/2^-$ 229-keV state and the reduced transition probability deduced from the lifetime of the $1/2^+$ state is B(E1)=$(4.7\pm0.2)10^{-5}$ W.u. Shell-model calculations using the GWB interaction from the Oxbash libraries were performed and tested with the known $5/2^+ \rightarrow 9/2^+$ transition of ^{83}Se. The shell model calculations reproduce the sequence of the excited energy levels of ^{83}Se but the reduced transition probabilities are underestimated.

Based on the shell model calculations the $1/2^+$ intruder state has a contribution of 60% from the $\nu g_{9/2}^{-2}\nu d_{5/2}^{1}$ configuration coupled to the 2^+ of ^{82}Se. The contribution of the $\nu g_{9/2}^{-2}s_{1/2}^{1}$ configuration in the wave function of the $1/2^+$ intruder state is around 30%. The wave function of the $1/2^-$ state has a dominant contribution from the $\nu p_{1/2}^{-1}\nu g_{9/2}^{full}$ component. The shell model calculations give B(E1)=$5{\cdot}10^4$ for the $1/2^+ \rightarrow 1/2^-$ transition of ^{83}Se, one order of magnitude difference from the experimental value.

The 582-keV transition from the $5/2^+$ intruder state to the ground state of ^{83}Se is highly suppressed. This is due to the fact that this transition connects a highly deformed with a spherical configuration, making the $5/2^+$ intruder state a shape isomer ($t_{1/2}$=3.6 ns [6]). The shell model calculations reproduce very well the reduced transition probability for the $5/2^+ \rightarrow 9/2^+$ transition.

The intruder $3/2^+$ state decays via 518-keV and 560-keV γ ray into the $5/2^+$ and $1/2^+$ states, respectively. Both of them are mixed M1+E2 transitions. The experimental results of this work show that the E2 component of these transitions is quite strong, B(E2) approximately 30 to 40 W.u.: if one considers the intruder band built over the 582-keV state as a rotational band, a large deformation of the states with $\beta \approx 0.3$ is deduced. Shell-model calculations with the GWB interaction underestimate the reduced transition probabilities for the E2 components by a factor of three while in the case of the M1 transitions, the calculations are in good agreement with the values obtained from the experiment. These calculations yeld a wave function of the $3/2^+$ intruder state with a large contribution from the $\nu g_{9/2}^{-2}\nu d_{5/2}^{1}$ configuration. A further contribution to the wave function of the $3/2^+$ emerges from the promotion of two neutrons across the N=50 shell gap. Configurations such as $\nu g_{9/2}^{-3}\nu d_{5/2}^{2}$, $\nu g_{9/2}^{-3}\nu d_{5/2}^{1}s_{1/2}^{1}$ or $\nu g_{9/2}^{-3}\nu d_{5/2}^{1}g_{7/2}^{1}$ contribute in total with 8% in the wave function.

Even though the sequence of the energy levels of ^{83}Se is in agreement with experimental data, the reproduction of the reduced transition probabilities with shell-model calculations remains a challenge.

Calculations were performed with the PFSDG-U interaction with a core of ^{40}Ca, including the pf-sdg valence space for both protons and neutrons. The variational methods, PNVAP and the PGCM, were used to obtain the exact solutions and get the total energy surface and the excitation energies for the nucleus of interest. The quality of the calculations was tested in the even-even neighbors of ^{83}Se. The calculations reproduce the excitation energies of ^{82}Se very well, while for ^{84}Se the calculated energy levels are slightly compressed with respect to the experimental ones.

In the case of ^{83}Se, several degrees of freedom were tested for the positive and the negative parity states. The calculations suggest the appearance of shape coexistence but fail to reproduce the ground state of this nucleus. A $5/2^+$ ground state is predicted instead of the $9/2^+$ state, similar to large-scale shell-model calculations with the PFSDG-U interaction.

The collectivity of the intruder states of N=49 isotones can be used as a testing ground for the shell-model interactions used to perform calculations for nuclei in the vicinity of ^{78}Ni. The development of deuterated targets at the LNL laboratory, suitable for RDDS measurements, and the use of radioactive beams from the SPES facility [140] will provide the possibility to investigate such states via lifetime measurements in the picoseconds range. For example, intruder states in the N=49 ^{81}Ge nucleus can be measured by employing a ^{80}Ge(d,p)^{81}Ge reaction. Radioactive ion beams of ^{80}Ge with a rate of 10^7 pps will be provided by the SPES [141]. The use of the AGATA array to measure γ rays [97, 142] and the GRIT [143, 144] as a light ejectile detector would provide a large selectivity of the reaction channel of interest on an event-by-event basis. The ^{79}Zn nucleus can also be studied employing ^{78}Zn(d,p)^{79}Zn reaction, where beams of ^{78}Zn with a rate of 10^6 pps are foreseen to be provided by SPES [141].

Part II

Lifetime measurements in the N=126 region employing a new novel technique: the reversed plunger configuration

Chapter 8

Introduction

In Section 8.1 of this chapter, a brief introduction to the mechanism of multi-nucleon transfer reactions and their capabilities for studying the nuclear structure of nuclei close to the valley of stability is given. Measurements of lifetimes of nuclear-excited states employing such reaction mechanism and the differential plunger technique are described in detail in Section 8.2, focusing on the main limitations of this technique and the importance of going beyond its limits. The conceptual design of the proposed technique, the so-called reversed plunger configuration, for measuring lifetimes of nuclear-excited states in heavy neutron-rich nuclei and the physics motivation of this work are introduced at the end of this chapter, Section 8.3.

8.1 Multi-nucleon transfer reactions

Multi-nucleon transfer reactions have been used extensively to populate low-lying excited states and to study the nuclear structure of neutron-rich nuclei [145]. In these reactions, the projectile and the target nucleus exchange nucleons at the surface, and only a few are involved in the transfer process. An important role in the dynamics of the MNT reactions is played by the Coulomb barrier, which is defined in Eq. 8.1:

$$V_b = \frac{Z_1 Z_2 e^2}{r_{0c}\left(A_1^{1/3} + A_2^{1/3}\right)} \tag{8.1}$$

where Z_1 and Z_2 are the atomic numbers of the projectile and the target nucleus, A_1 and A_2 the respective mass numbers, and r_{0C} is a constant with the value approximately 1.2 fm. The primary population of the nuclei is usually followed by a secondary neutron evaporation process from the fragments, resulting in the final observed species [82].

The trajectories of the nuclei involved in this kind of reaction can often be described in a semi-classical frame since the wavelength of the relative motion is small compared to the size of the system. The grazing angle is the scattering angle corresponding to the

trajectory where the projectile and the target nucleus reach the closest distance. Based on this definition, the grazing angle is defined by Eq. 8.2.

$$sin\frac{\theta_g}{2} \approx \frac{1}{2E/V_b - 1} \tag{8.2}$$

The grazing angle θ_g depends on the energy of the projectile E and on the Coulomb barrier V_b. In a transfer reaction, the production cross-section is maximized at the grazing angle.

Magnetic spectrometers are the most powerful and sensitive setups to measure transfer reactions. The construction of large acceptance spectrometers like PRISMA at LNL [146, 147], VAMOS++ at Ganil [148, 149] or MAGNEX at LNS [150] allowed to increase the detection sensitivity and to access transfer channels with low cross sections. The large acceptance magnetic spectrometers coupled to γ-ray arrays like EXOGAM [151], CLARA [152], or AGATA [142, 153–155] become a very powerful setup to study nuclear structure. Thanks to the identification of the reaction products in mass A, in atomic number Z, and a Doppler correction applied event-by-event based on the time of flight of the recoils, the γ rays measured in coincidence can be easily assigned to the corresponding nuclei. Moreover, with such a setup, thanks to the kinematic reconstruction from the spectrometer, it is possible to reduce the background arising from neutron evaporation channels by gating on the Q value [156].

8.2 Lifetime measurements with the differential plunger

The coupling of large acceptance magnetic spectrometers to large γ-ray arrays provides the possibility to measure lifetimes of nuclear-excited states populated via MNT reactions by exploiting the 'differential plunger' technique [157]. At difference with the work described in the first part of the thesis, where reaction products are stopped in a high Z material placed after the target, in the differential plunger a thinner foil is used, namely a degrader. The degrader allows the reaction products to pass through and continue to travel towards the spectrometer where they get identified. A schematic representation of the differential plunger coupled to a magnetic spectrometer and a γ ray array is shown in Fig. 8.1 (Left panel). The target and the degrader foil mounted in the plunger device are placed parallel to the entrance of the magnetic spectrometer. The beam is tilted with respect to the normal of the target surface as much as the grazing angle θ_g, thus the beam-like fragments (BLT) travel with a given velocity $\vec{v}_{BL1}$ perpendicularly to the degrader surface as seen in the figure. The beam-like fragments lose some of their energy in the degrader foil and enter the magnetic spectrometer with velocity $\vec{v}_{BL2}$. In case an excited state with a lifetime in the sensitive range of the technique, from hundreds to a few picoseconds, decays by γ-ray emission in between the two foils or after the degrader, the observed energy of the γ-ray would be different, due to the dependence of the Doppler effect on

the velocity of the emitting particle. Consequently, two peaks corresponding to the same γ-ray transition will appear in the measured γ-ray spectrum, marked as I_1 and I_2 in the schematic γ-ray spectra in the right panel of Fig. 8.1. Getting advantage of the kinematic reconstruction from the spectrometer and the intensities of these two peaks, measured for different distances between the target and the degrader, the lifetime of the state of interest can be measured.

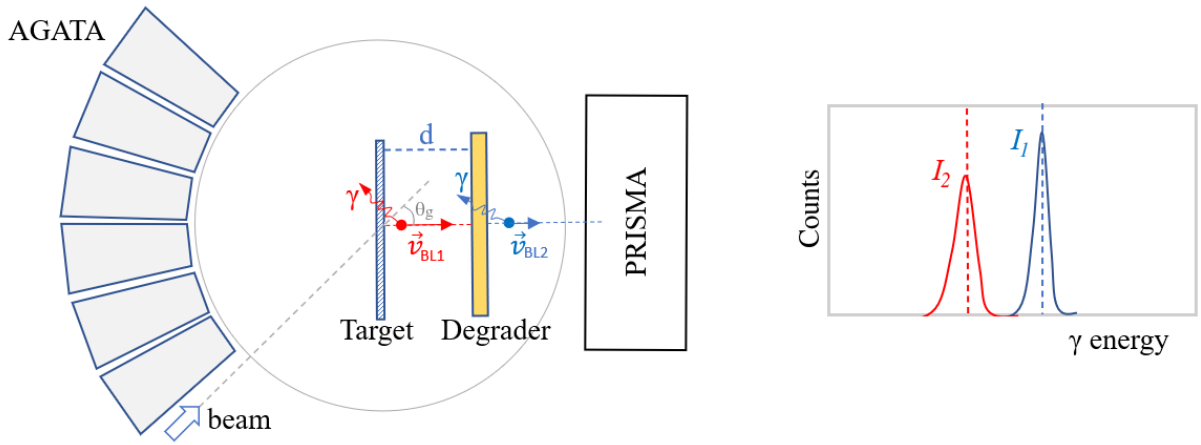

Figure 8.1: (Left) Schematic representation of the differential plunger setup configuration: AGATA (γ-ray detector array) + PRISMA spectrometer (mass spectrometer used to identify the reaction products in mass, atomic number, and charge state) + plunger device (a device used to hold and set the separation distance between the target and degrader foil). Beam-like fragments de-excite via γ-decay: in flight with velocity V_{BL1} (velocity between the target and degrader) or V_{BL2} (velocity after the degrader) and get identified in Z, mass, and velocity by the magnetic spectrometer. (Right) Schematic representation of the γ-ray spectrum measured with the differential plunger. Since $V_{BL1} > V_{BL2}$, due to the Doppler effect, for the same γ-ray transition, two different peaks are observed in the γ-ray spectrum I_1 and I_2. Their intensity will provide information on the lifetime.

With this setup, in some cases it is possible to control the side feeding of the state of interest by gating on the Q value [156, 158], reducing possible systematic errors in the measurement. The differential plunger technique has been successfully applied to measure the lifetimes of nuclear-excited states in several nuclei [157, 159–162].

In a binary reaction, the isotope identification provided by the magnetic spectrometer can be exploited to perform spectroscopic studies not only of the isotope detected by the spectrometer but also of the undetected partner, whose kinematics can be reconstructed based on the angle of entrance and the velocity vector of the ion measured the spectrometer. This technique has been successfully exploited in the past and allowed the first measurements of γ rays from excited states of ^{196}Os and ^{200}Pt [163, 164] or even heavier elements like ^{240}U [165]. The identification of beam-like particles allows one to reconstruct the kinematics of the target-like fragments and perform a Doppler correction on an event-by-event basis.

8.3 Reversed plunger configuration

The differential plunger, as mentioned in the previous section (i.e., a target followed by a degrader), is an excellent tool to measure lifetimes of nuclear-excited states. The regions of the nuclear chart that can be explored by using this technique are restricted by the identification capabilities of the magnetic spectrometer. For example, the PRISMA spectrometer has an atomic charge resolution ($\Delta Z/Z \approx 1/60$). For nuclei with $Z>54$ and relatively low energy, the identification with sufficient resolution by the spectrometer becomes difficult hence the lifetime measurements of excited states for nuclei heavier than Xe become challenging. Since heavier nuclei in the neutron-rich regions of the nuclear chart are of great interest in nuclear structure studies, with the GAMMA group at LNL we have developed a new technique to perform lifetime measurements in the picoseconds range also for these nuclei.

It is possible to extend the RDDS technique to heavier elements by using the plunger in the so-called "reversed configuration" and by employing the kinematic reconstruction of the ions from the spectrometer. In the standard configuration of the differential plunger, the target is followed by the degrader while in the reversed configuration, the degrader faces the beam. The target and the degrader, placed parallel to each other, are tilted in such a way that the target-like fragments (the heavy nuclei of interest) travel from the target toward the degrader. A schematic representation of the geometrical arrangement of the setup is shown in the left panel of Fig. 8.2. In this configuration of the plunger, the beam passes through the degrader, loses some of its energy, and interacts with the target where the MNT reaction occurs. The multi-nucleon transfer reaction may also occur from the interaction of the beam with the degrader, but by choosing them with slightly different masses, the respective grazing angle will differ (See Eq. 8.2), avoiding the products from the reaction of the beam with the degrader to enter the spectrometer. After the reaction in the target, the beam-like fragments, with a light enough mass and atomic number to be identified with sufficient resolution, enter the magnetic spectrometer. Instead, the heavy target-like fragments travel from the target to the degrader, which is thick enough to stop them completely. Therefore, one ends in a situation similar to that of the differential plunger configuration introduced previously in Section 8.2, where the nuclei of interest travel between the two foils with a given velocity. The de-excitation of the nucleus of interest in flight or at rest will give rise to the shifted and the unshifted γ-ray peak in the measured γ-ray spectra. Since the angular coverage of the solid angle from the γ-ray array is continuous and the range of the angles between the emitting particle and the γ-ray photon is larger than in the case of the differential plunger configuration, in order to distinguish between the shifted and the unshifted γ-ray component, it is convenient to represent the data in the form shown schematically in the right panel of Fig. 8.2. The non-Doppler corrected energy of the γ-rays is plotted versus the angle between the direction of

the ion and that of the photon. Gamma rays emitted at rest will appear as straight lines in the matrix since the measured energy does not depend on the angle, while, the γ-rays emitted in flight will appear as curved lines due to the Doppler effect. This 2D schematic representation of the reversed plunger data (See right panel of Fig 8.2) is referred to the rest of the thesis as the 'lineshape matrix'. The intensities of the shifted and the unshifted components can be used to determine the lifetime of the state of interest, as discussed in the first part of the thesis.

To illustrate and validate the use of this technique, realistic Monte Carlo simulations were performed and will be introduced in Chapter 9.

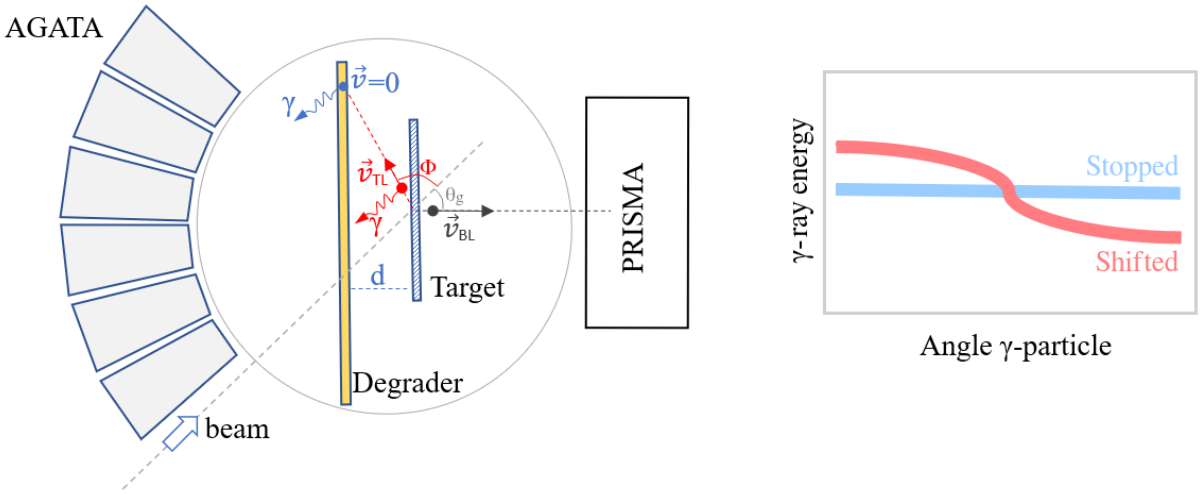

Figure 8.2: (Left) Schematic representation of the reversed plunger setup configuration: AGATA + PRISMA spectrometer + plunger in the reversed configuration. The beam passes through the degrader foil and interacts with the target. Beam-like fragments enter the spectrometer while target-like fragments (heavy neutron-rich nuclei of interest) travel towards the degrader foil. The de-excitation of target-like fragments may take place: in flight with velocity V_{TL} (velocity in between the degrader and target) or at rest after being stopped in the degrader foil. Due to the Doppler effect the stopped and the shifted component should be observed in the γ-ray spectrum. (Right) A schematic 2D plot of the energy of the γ rays versus the angle between the emitting particle and the photon (lineshape matrix). Gamma rays emitted at rest appear as straight lines in the matrix since the measured energy does not depend on the angle, while, the γ-rays emitted in flight will appear as curved lines due to the Doppler effect.

8.3.1 Physics motivation

The region of the nuclear chart with A≈190 is particularly interesting since a prolate-to-oblate shape transition has been predicted to occur from the less neutron-rich W-Os-Pt isotopes towards the more neutron-rich as the N=126 closed shell is approached [163, 166–169]. As a result, this region of nuclei has attracted a large theoretical and experimental activity in recent years.

The shape of a nucleus has a pronounced effect on the low-lying energy spectrum. For example, in an even-even nucleus, the ratio of the energy of the first 4^+ state to the energy of the first 2^+ state is approaching the value of 3.3 for a well-deformed rotational nucleus, at approximately 2.5 for a triaxial rotor and around 2 for a vibrational, spherical one [170]. This evolution of the $E(4^+)/E(2^+)$ ratio along the Hf, W, Os, and Pt isotopic chains is represented in the left panel of Fig. 8.3. For the tungsten isotopes with N<112, the ratio $E(4^+)/E(2^+)$ is close to 3.3, indicating an axial rotor character, while for heavier W isotopes, this value drops quickly to ∼2.5, indicating a triaxial rotor. For the Os isotopes, this transition is smoother, while for platinum, this ratio remains at around 2.5 along the isotopic chain. Figure 8.3 (Right panel) shows the evolution of the same parameter, $E(4^+)/E(2^+)$ ratio along different isotonic chains in the A≈190 region where a similar decreasing trend of the ratio is observed with increasing Z (from Yb towards Pt) except at N=116. When moving along the N=116 isotonic chain, a drastic change of the $E(4^+)/E(2^+)$ is noticed from ^{192}Os to ^{190}W. Even though the energies of the low-lying yrast states of ^{190}W can be understood in terms of triaxiality, the sudden drop from Z=76 to Z=74 of the $E(4^+)/E(2^+)$ along N=116 is not yet fully explained. Some studies suggested that the sudden drop in ^{190}W is caused by shell effects in this region and possibly may be evidence of the appearance of a subshell closure at Z=76 [171]. More data are required to fully understand this behavior.

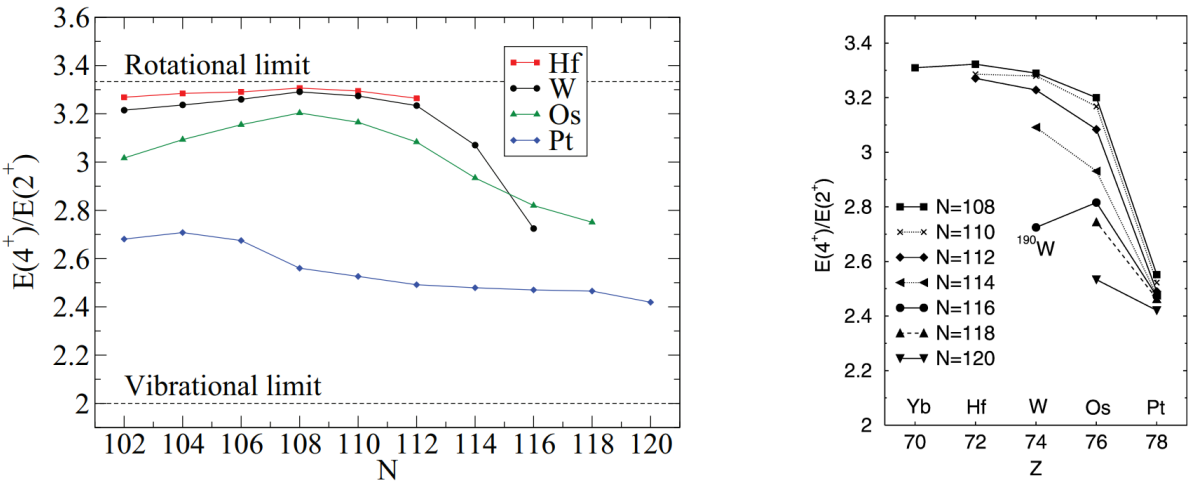

Figure 8.3: Experimental data in the A∼190 region: (Left) The evolution of the $E(4^+)/E(2^+)$ ratio along the Hf, W, Os and Pt isotopic chain. Figure taken from Ref. [166]. (Right) The evolution of the $E(4^+)/E(2^+)$ ratio along several isotonic chains in the region. Figure taken from Ref. [172].

Theoretical calculations predict a shape transition in the tungsten isotopes from prolate to oblate through a γ soft one around ^{190}W [173] as seen from the evolution of the minimum in the total energy surface plotted in the (β_2-γ) plane along the isotopic chain in Fig. 8.4. The ^{192}Os and ^{194}Pt (N=116 isotones) are well-known examples of γ-soft nuclei and therefore it is expected that the γ degree of freedom plays an important role also in

^{190}W [172].

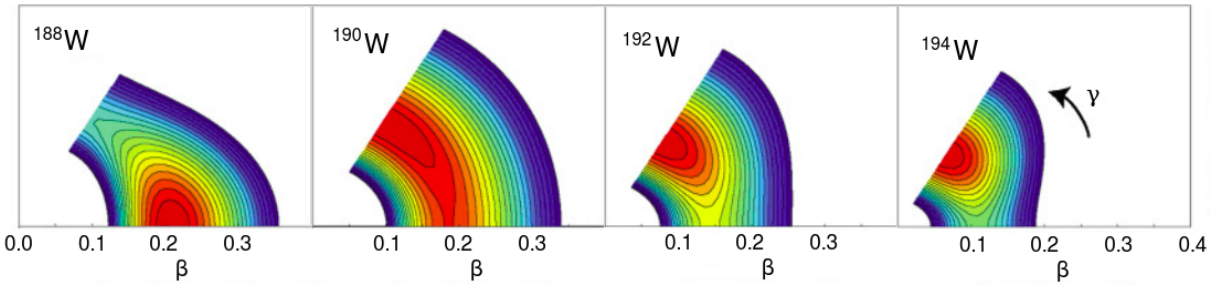

Figure 8.4: Mapped potential energy surface in terms of the deformation parameters β and γ for the W isotopes obtained with by the interacting boson model Hamiltonian determined by (constrained) Hartree-Fock-Bogoliubov calculations with the Gogny-D1S energy density functional. Figure adapted from from [173].

Theoretical calculations shown in Fig. 8.5 predict, as expected, a shape transition from a deformed to a spherical shape for the Pt isotopes as moving towards the closed shell at N=126. Due to the lack of experimental data, such behavior was not examined. The study of nuclear shape evolution along an isotopic chain would provide a further understanding of the nuclear force and is an important testing ground for nuclear models [49].

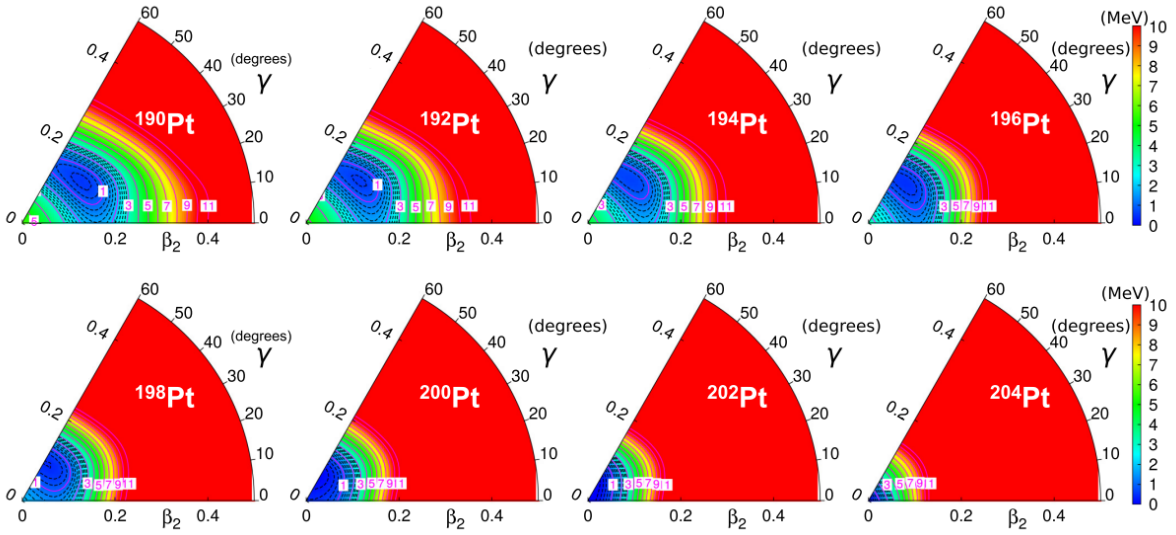

Figure 8.5: Particle-number-projected potential energy surfaces in the β-γ plane for Pt isotopes calculated with the Gogny D1S interaction. Figure taken from [164].

Shape transitions from prolate to oblate are expected to occur in the Os isotopes with increasing neutron number, as shown in Fig. 8.6. The ^{196}Os nucleus was studied previously at LNL using the AGATA+PRISMA setup and its level scheme was established [163,174]. However, up to now, no lifetimes of low-lying states of ^{196}Os have been measured.

The reversed plunger configuration provides the possibility to extend the available spectroscopic data towards more neutron-rich isotopes. This part of the thesis reports on

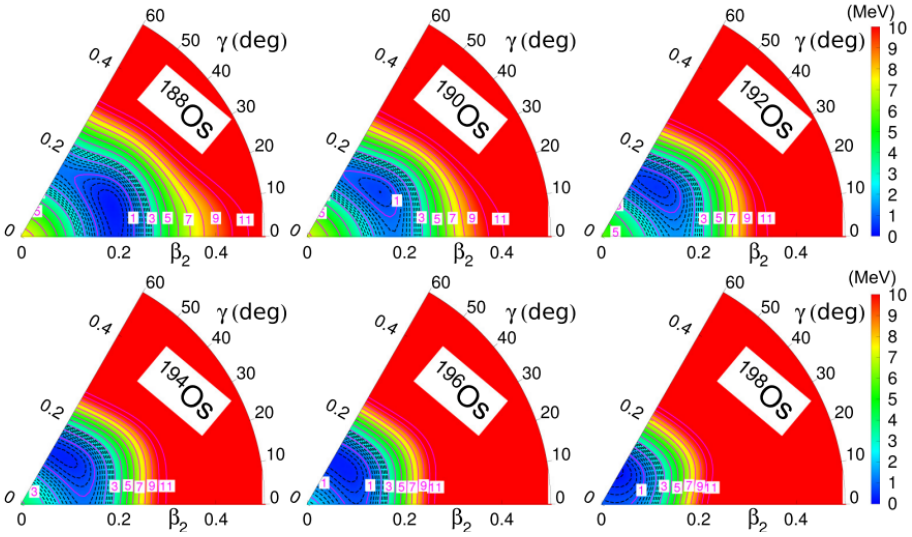

Figure 8.6: Particle number projected potential energy surfaces in the β-γ plane for the Os isotopes calculated with the Gogny D1S interaction. Figure taken from [163].

an experiment performed with such a setup at the LNL laboratory with the primary goal of measuring for the first time the lifetimes of the 2^+ and 4^+ excited states of ^{196}Os and studying the evolution of the collectivity of these states along the isotopic chain. Among the nuclei populated in the reaction chosen for such study is also ^{198}Pt, where the lifetimes of the low-lying excited states are known and can be used as a benchmark to validate the use of the new plunger configuration. The aim of this work is to extract the lifetimes of the low-lying states of ^{198}Pt by using the reversed plunger setup and compare them to the literature data.

Chapter 9

The experimental setup

The feasibility of the experiments employing the reversed plunger configuration is discussed in Section 9.1 according to GRAZING calculations and motivated with realistic Geant4 Monte Carlo simulations. The design of the experiment to measure the lifetimes of the excited states of nuclei in the region with a mass of around 190 is shown in Section 9.2. An overview of the experimental setup composed of the AGATA γ-ray array, the PRISMA magnetic spectrometer, and the plunger device is given in the last section of this chapter, Section 9.3.

9.1 Geant4 simulations to study the feasibility of the experiment

The reaction kinematics, the energy losses of the particles in the target and in the degrader, and the geometry of the setup are among the experimental conditions one has to take into account when using the plunger in the reversed configuration. The list below summarizes the experimental constraints to be considered:

- Beam-like fragments should have enough energy to be identified with enough resolution in Z by the PRISMA spectrometer. At least an energy of around 3 MeV/u is required.

- The grazing angle of the reaction should not be smaller than 20° and not larger than 150°. This is due to the mechanical constraints of the AGATA+PRISMA setup.

- The angle between the direction of target-like fragments and the incident beam direction (marked as ϕ in Fig. 8.2) should be the largest possible, allowing the target-like fragments to travel from the target to the degrader by the shortest distance possible.

- The target and degrader have to be set in the reaction chamber in such a way that

the target-like fragments reach and get stopped in the degrader foil (see Fig. 8.2). Due to mechanical constraints, the target and the degrader can be tilted up to 60° with respect to the beam direction.

- The degrader should be thick enough to stop the target-like fragments. Typically, the target-like fragments have β around 3%. If the target-like fragments are entirely stopped, the shifted and the unshifted components will be better separated.

- The energy loss of the beam-like fragments into the target should be kept as small as possible to avoid the worsening of the Q-value resolution.

Calculations were performed using the GRAZING code [175] to optimize all these experimental conditions. The feasibility of the technique was checked by performing realistic Monte Carlo simulations with Geant4 and the AGATA simulation package [106, 107].

9.1.1 Calculations with the GRAZING code

The GRAZING code [175] is a powerful tool used to calculate the angular distribution of the differential cross-sections of MNT reactions. Calculations were performed for a beam of ^{136}Xe impinging into a ^{198}Pt target. The energy of the beam was chosen to be 930 MeV since according to the GRAZING calculations the experimental conditions mentioned in Section 9.1 are better satisfied at this value. The angular distribution of the differential cross-section for the two proton pick-up channel (^{138}Ba) and of its binary (^{196}Os) is shown in Fig. 9.1 with the blue continuous and dashed line, respectively. The grazing angle for the two-proton pick-up channel is 39° and the PRISMA spectrometer was set at this angle in our experiment in order to maximize the acceptance of this reaction channel. PRISMA acceptance is marked in the figure with the blue area while the distribution of the corresponding binary partner is marked with the red area. In the left panel of Fig. 9.1 is also shown the angular distribution of the differential cross-section for the elastic channel (^{136}Xe) and of its binary (^{198}Pt), the nucleus of interest of this thesis. The kinematic lines for the target-like and beam-like fragments for the elastic channel calculated by the GRAZING code are shown in the right panel of Fig. 9.1. The beam-like fragments have an energy of 790 MeV at the grazing angle, enough to be identified in Z with a satisfactory resolution by the ionization chamber of the PRISMA spectrometer. The target-like fragments are scattered at 60° with respect to the beam direction with an energy of 220 MeV.

Based on the calculated trajectories of the target-like particles, a tilt of 50° of the target and degrader with respect to the beam direction allows them to reach the stopper foil. When this angle is defined, one must also account for the mechanical constraints of the plunger device. The cone-like shape of its holding structure sets some limits on the

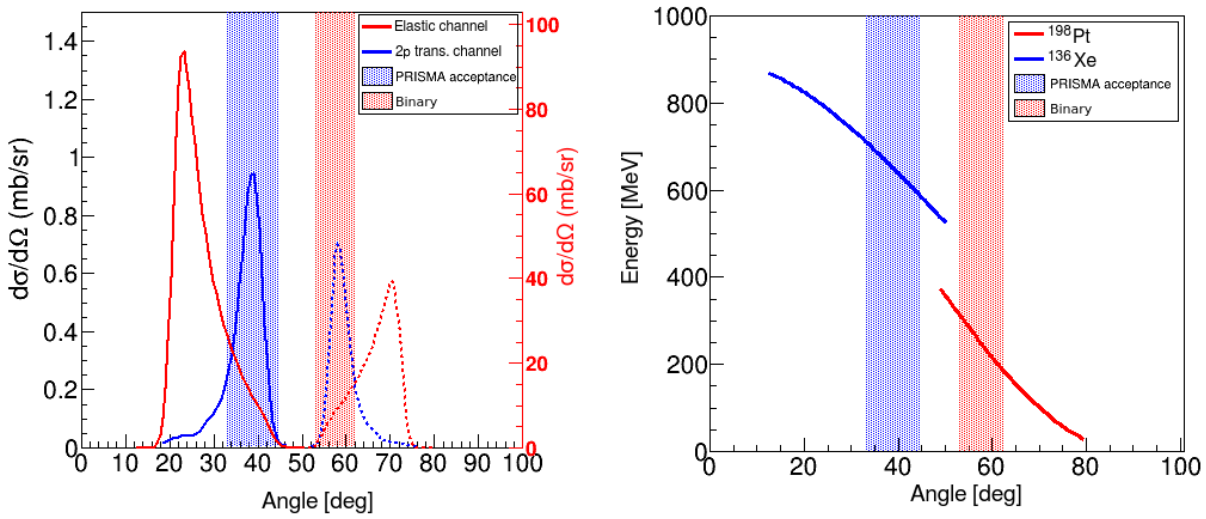

Figure 9.1: GRAZING calculations were performed for a beam of ^{136}Xe with an energy of 930 MeV impinging into a ^{198}Pt target. (Left) The angular distribution of the differential cross section of ^{198}Pt and ^{136}Xe. (Right) The kinematic line of the target-like and beam-like fragments. The PRISMA acceptance and the distribution of the corresponding binary partner are shown with the coloured areas. PRISMA configurations were centered based on the kinematics of ^{196}Os.

angles one can operate during the experiment. Moreover, the rotation will increase the beam spot as $1/\cos\theta$, which makes the focusing of the beam into the target more difficult and also affects the trajectory reconstruction of the ions by the PRISMA algorithms.

The ^{93}Nb material is chosen as a degrader since it can be produced in different thicknesses, can be a self-supporting target/degrader, and is easy to stretch in the plunger support. Moreover, as suggested by reference [176], this material does not induce a high counting rate in the HPGe detectors when used as a degrader in RDDS measurements. Calculations of the energy losses of target-like fragments in the target, considering the effective thickness and assuming the reaction point in its middle, indicate that a 3.3 mg/cm^2 thick ^{93}Nb foil is enough to stop the reaction products. Since in our configuration the degrader foil faces the beam and is followed by the target where the beam energy is optimal at a value of 930 MeV, according to energy losses calculated with Lise++ [87], it results that a ^{136}Xe beam with energy of 1134 MeV should be provided by the accelerator.

9.1.2 Geant4 Monte Carlo simulations

Simulations were performed with the Geant4 toolkit and the AGATA simulation package [106, 107]. As introduced in the first part of the thesis, these simulations consider the geometry of the setup, the response function of the detector, and the γ decay of the nucleus of interest through a complex level scheme, where the lifetimes of the populated levels are accounted for.

The 2^+ state of ^{198}Pt which decays by a γ-ray transition with the energy of 407 keV

was simulated considering no feeding from higher-lying states. The half-life of the 2^+ state was set at 22 ps, as reported in the literature [6]. The angular distributions of the differential cross-section obtained from the GRAZING calculations were included in the code and simulations were performed for several distances between the target and the degrader, at 10, 100, and 800 μm. The non-Doppler corrected γ-ray energies detected by the AGATA array, plotted as a function of the angle between the emitting particle and the photon, are presented in Fig. 9.2. This angle can be determined accurately thanks to the position sensitivity of the AGATA crystals and the reconstructed kinematics of the target-like fragments by the PRISMA spectrometer. As seen in the lineshape matrix obtained from the simulations, both the shifted and the stopped components belonging to the $2^+ \rightarrow 0^+$ transition are present. As expected, their intensity changes with the distance. At short distances, the stopped component dominates, whereas at long distances it is the shifted component that becomes more intense. According to the simulations, by using the reversed plunger setup, one is able to distinguish the shifted and the unshifted components, which carry information on the lifetime of the nuclear-excited state.

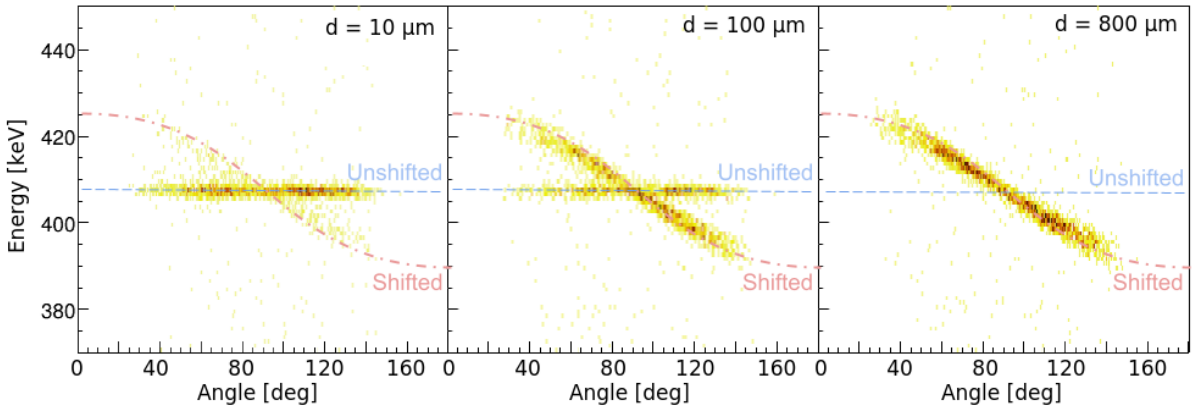

Figure 9.2: Lineshape matrix obtained by realistic Monte Carlo simulations performed with the Geant4 toolkit and the AGATA simulation package. Simulations with the AGATA+PRISMA+Plunger in the reversed configuration were performed for three different distances between the target and the degrader and with the half-life of the 2^+ state of ^{198}Pt set at 22 ps without considering any feeding from higher-lying states. The intensity of the shifted and the unshifted components varies with the distance.

9.2 The experiment with the reversed plunger configuration

The experiment with the plunger device in the reversed configuration was carried out at the 'Laboratori Nazionali di Legnaro - LNL' in Italy in May 2023. The excited states of the nuclei of interest were populated using a multi-nucleon transfer reaction. The beam

was provided by the ALPI-PIAVE accelerator complex [177].

PIAVE (Positive Ion Accelerator for Very-low Energy) [178,179] is the ion injector of the ALPI linac accelerator and can provide beams of nuclei with mass up to A≈200. The beam is extracted by a dedicated Electron Cyclotron Resonance (ECR) Ion Source [180], placed on a high voltage platform operated at a voltage from 250 kV up to 400 kV. Charge states of ions are produced without the need to accelerate and use stripper foils, as in the case of the TANDEM-XTU injector introduced in Section 3.1, which limits the mass of the nuclei that can be accelerated. The highly charged ions extracted from the ECR are accelerated from the high voltage towards a dedicated beam pipe containing magnetic dipoles and quadrupoles, where the beam is transported towards another stage of acceleration. Two Radio-Frequency Quadrupole (RFQ) operating in the superconducting regime accelerate the particles up to 3.5% of light speed. Subsequently, the ions enter eight QWR acceleration resonant cavities, being accelerated up to 4.5% of light speed, enough to be injected into the ALPI linac accelerator.

The ALPI accelerator (Acceleratore Lineare Per Ioni) is a linear accelerator at LNL that started operating in the mid-90s [181]. It uses radiofrequency-driven electromagnetic fields QWR (Quarter Wave Resonator) to accelerate the beams up to tens of MeV/A. ALPI has 20 accelerating cavities operating under superconducting working conditions (at temperatures close to 4 K where some materials show zero or minimal resistance to static or alternating currents). The resonance frequency of the first half of ALPI cavities is 80 MHz, while that of the second group is 160 MHz.

The ^{136}Xe beam with an intensity of 1 pnA, charge state 27^+ and energy of 1134 MeV impinged on a self-supporting target of ^{198}Pt with a thickness of 1.4 mg/cm^2 after passing through the degrader, a 3.3 mg/cm^2 thick Nb foil. The target and the degrader, mounted in the plunger device in the reversed configuration, were tilted at 50° with respect to the beam direction. The beam-like particles enter PRISMA, where they get identified, while the target-like particles travel towards the degrader, where they are stopped.

For the detection of the emitted γ rays, the Advanced GAmma Tracking Array (AGATA) was used [97,142]. To reach the desired channel selectivity, the AGATA array was coupled to PRISMA [146,147]. PRISMA is a magnetic spectrometer for heavy ions operating at LNL which has a very large solid angle acceptance of 80 msr, a momentum acceptance of ±10%, an excellent mass resolution of around 1/300, and the capability of rotation around the target in a wide angular range from 20° to 130°. The ion trajectories are reconstructed using the position, time, and energy measured in the focal plane detectors, and by having a detailed knowledge of the magnetic fields. Figure 9.3 shows a view of the experimental setup.

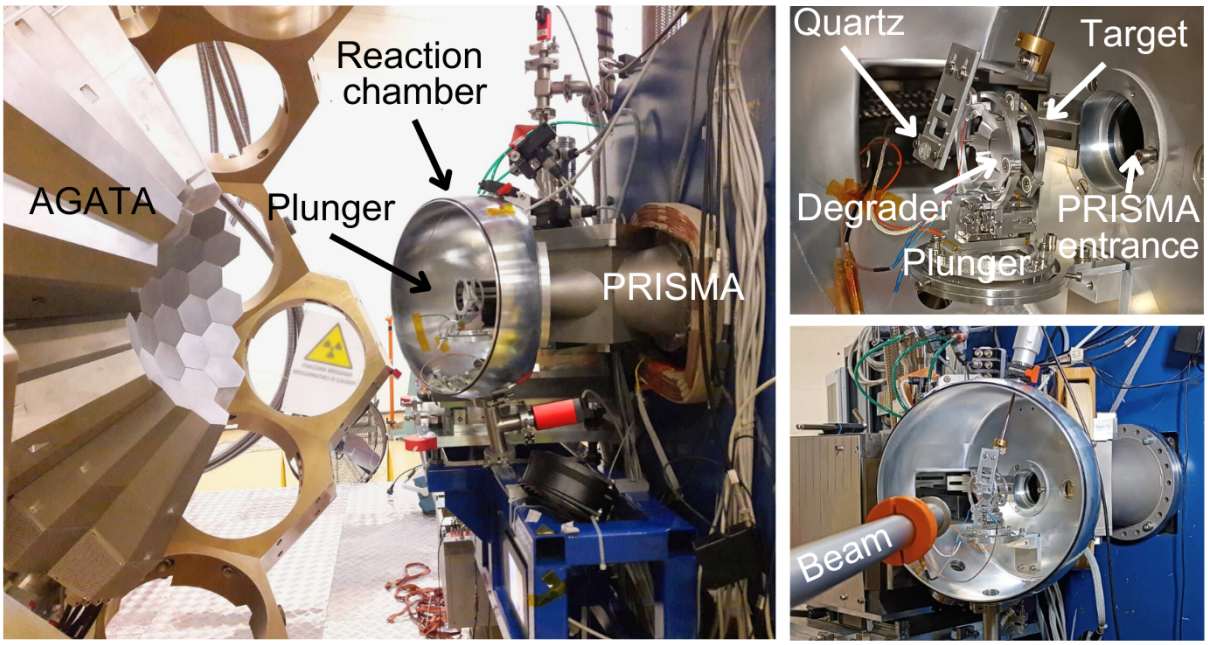

Figure 9.3: Pictures of the experimental setup. AGATA array coupled to the PRISMA magnetic spectrometer and the plunger device in the reversed configuration. The quartz crystal is used for the focusing of the beam in the target.

9.3 Experimental setup

The geometry of the AGATA array, its configuration in our experiment, and the principle of a γ-ray tracking array are introduced in this section. The main components of the PRISMA magnetic spectrometer are described and a few upgrades of the plunger device with respect to the one introduced in the first part of the thesis are discussed in this chapter.

9.3.1 PRISMA magnetic spectrometer

PRISMA is a magnetic spectrometer used to identify the mass, atomic number, velocity vector $\vec{\beta}$, and charge state of heavy ions in binary reactions. This spectrometer has been operating at LNL since 2002, working stand-alone or in conjunction with γ-ray arrays like CLARA [152] or AGATA.

A schematic representation of the spectrometer and of its components is shown in Fig 9.4. After the target, at a distance of around 25 cm, a Multi-Channel Plate detector (MCP) [182] is used for the position reconstruction of the reaction products that enter PRISMA. The ions pass through a thin carbon foil (0.02 mg/cm^2) which induces secondary electrons, which are then driven in the electric field between the carbon foil and the position-sensitive anode. The charge is collected in the anode, made of two orthogonal delay lines insulated one from the other. The difference between the time signals provides the incoming position of the ions in X and Y. The fast time signals of the MCP detector

are also used for Time of Flight (ToF) measurements.

The spectrometer has two magnetic lenses placed after the MCP detector: a quadrupole and a dipole magnet that bends the trajectories of the incoming charged particles. The quadrupole magnet is placed at a distance of 25 cm from the MCP, and it is used to focus the beam in the vertical plane and to defocus in the horizontal plane. The dipole magnet is placed 90 cm apart from the quadrupole, with a curvature of 1.2 m and a bending angle of 60°. In this experiment, magnetic fields of 0.762117 T and 0.832739 T were used in the quadrupole and the dipole magnets, respectively.

At the focal plane of the PRISMA spectrometer, a Multi Wire Parallel Plate Avalanche Counter (MWPPAC) detector [183] is used for position reconstruction. The detector is segmented into ten sections along the horizontal axis. The position in X and Y is determined by the time difference between the time signals from the two orthogonal anodes of every section. The MCP and the MWPPAC, placed at a 5.99 m distance from each other, are also used for time of flight measurements. The cathode signals from the MWPPAC are used as a start, and the delayed signals of the MCP are used as a stop signal in the Time to Amplitude Converter (TAC) modules for the ToF measurement. The information of the ToF provides the velocity of the recoil and is used to identify the mass of the ions.

The MWPPAC is followed by the ionization chamber (IC), divided into sections used to measure the energy of the ions. The active area contains 40 pads divided into ten columns, each with four pads along the trajectory of the ions (see Fig. 9.4). Each pad independently measures the energy loss of the ions. By correlating the partial and total energy loss in the gas, it is possible to identify the ions in atomic number, as will be explained further in the next chapter. Four pads, so-called side detectors, on the left and the right with respect to the ion path, are used as veto detectors for rejecting events with distorted trajectories. A carbon tetrafluoride (CF_4) gas at a pressure of 25 mb was chosen to operate the ionization chamber based on the energy of the fragments and its stopping power.

The spectrometer has an acceptance of 80 msr in solid angle and can achieve a resolution in Z$\sim$1/60 and a resolution in mass approximately 1/300.

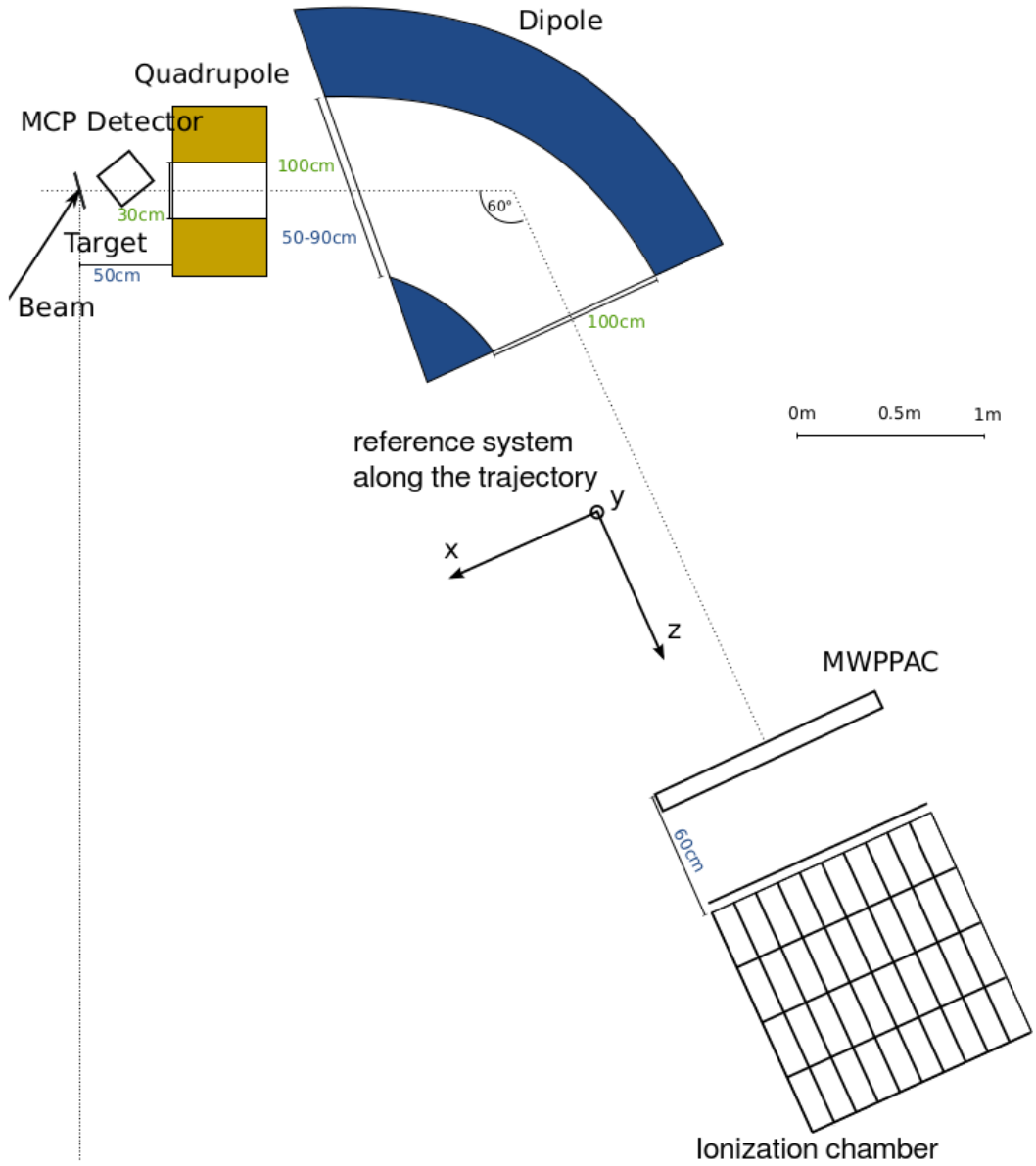

Figure 9.4: Schematic representation of the PRISMA magnetic spectrometer. After the target, an MCP detector is used for position measurement and as a stop signal in the TAC module for ToF measurements. A quadrupole magnet focuses the beam along the vertical direction and defocus in the horizontal plane. A dipole magnet is placed along the path of the ions bending their trajectories. An MWPPAC is used for the position and ToF measurement, followed by the IC used to identify in atomic number the reaction products. Figure adapted from [174].

9.3.2 AGATA γ-ray tracking array

The Advanced GAmma-ray Tracking Array (AGATA) [97, 142] is the first generation of γ-ray tracking arrays designed and constructed in a collaboration project of several European countries. It started to operate at LNL-INFN in 2009 [184] coupled to the magnetic spectrometer PRISMA and other ancillary devices. Since then, AGATA moved to GSI [155] and afterward to GANIL [154] using the beams provided in those laboratories. AGATA, since 2022 is back again at LNL-INFN, where it is being used for high-resolution γ-ray spectroscopy using stable beams and in the future, radioactive beams from the SPES facility [140].

In the final configuration, as shown in Fig 9.5 (Left panel), AGATA will cover the whole solid angle with germanium detectors. The entire sphere will comprise 180 electrically segmented HPGe detectors grouped in triple clusters where each cluster is composed of three differently shaped hexagonal tapered coaxial HPGe detectors encapsulated in a sealed thin aluminum capsule. The edge of a single crystal is roughly 90 mm and is electrically divided into 36 segments plus the central common contact, namely the core. A representation of the segmentation of the germanium crystal and its geometry is shown in Fig. 9.5 (Right panel). The high electrical segmentation of the crystals gives the possibility to extract the position of the energy deposition of a γ ray. The position and the energy deposited are used to track the trajectory of a Compton scattered photon inside the detector and the events that do not obey the Compton scattering formula are rejected. Differently from the GALILEO array, since AGATA uses tracking to reconstruct the Compton scattered events, there is no need for the Anti-Compton shielding, allowing to increase the solid angle covered by HPGe detectors effectively. The segmentation and a large number of detectors of the AGATA array result in a high selectivity and sensitivity superior to other existing γ-ray arrays.

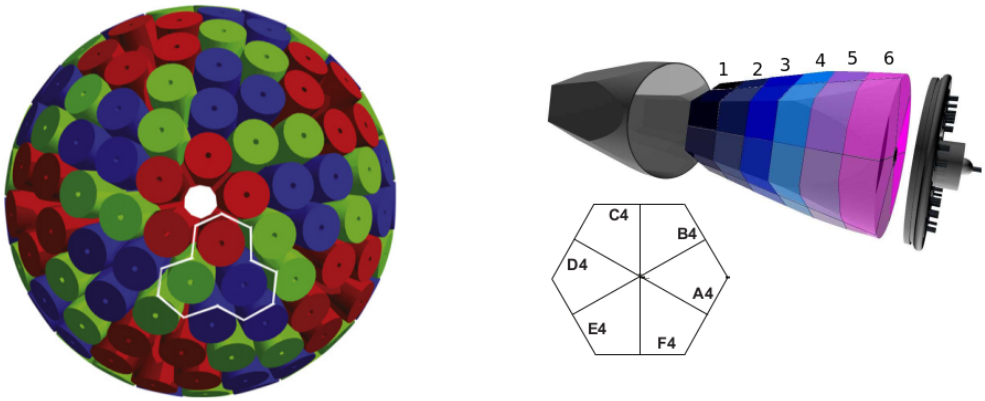

Figure 9.5: (Left) The final configuration of AGATA γ-ray tracking array, a whole sphere covered by 180 segmented HPGe detectors. (Right) The geometry of a highly segmented HPGe detector of AGATA. The detector is electrically divided into 36 segments plus the central common contact. Figure adapted from [185].

Principle of a γ-ray tracking array

When γ rays deposit totally (photoelectric) or partially (Compton) their energy in one of the segments of the crystal, electron-hole pairs are created and a net charge is collected on the electrodes while in the neighboring segments, a cross-talk signal is induced as shown in Fig. 9.6. A γ ray deposits its energy in segment B4, where the amplitude of the signal is the highest. Analyzing the shape of the signal seen by all the segments and comparing them with reference ones obtained by simulating different electric fields on the segments and saved in the AGATA libraries, it is possible to reconstruct the position of interaction with an excellent resolution of 4 mm at FWHM [186]. Once the positions of the interactions are obtained, it is possible to use properly tuned algorithms, named tracking algorithms, to reconstruct the most likely path of the γ rays inside the detector.

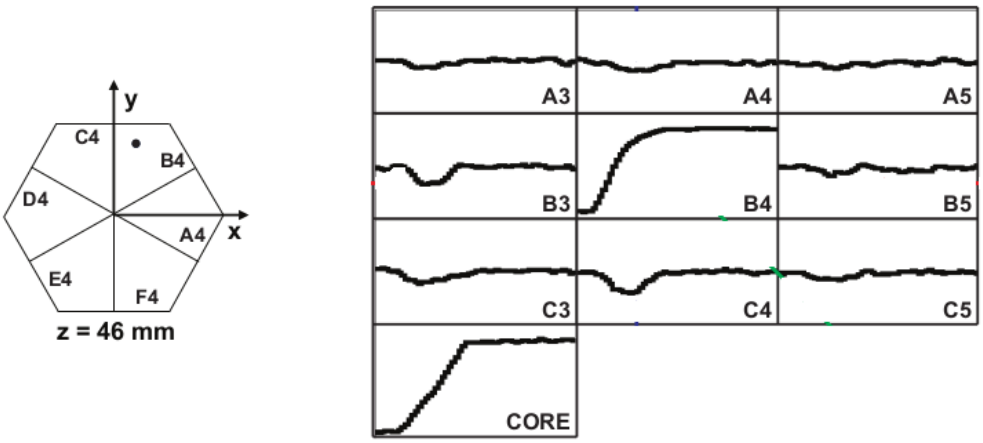

Figure 9.6: Example of the pulse shape analysis of the signals from the segments of the HPGe crystal. A drop in the net charge collected from the firing segment and the neighboring ones is seen. The most significant decrease corresponds to the segment firing. Comparison of the signals with calculated ones determines the position of interaction in X, Y, and Z coordinates with a resolution of 4 mm at FWHM. Figure adapted from [187]

Compton scattering is the primary interaction mechanism of γ-ray photons with energy from 100 keV to 10 MeV with the atoms of a germanium detector (See left panel of Fig. 9.7. When interacting via Compton scattering, the energy of the γ rays is released in a discrete number of interactions in the crystal. The purpose of the γ-ray tracking detectors is to reconstruct the path followed by the scattered γ-ray photons inside the detector on the basis of the position and energy deposit in each interaction. Based on the Compton formula (Eq. 9.1), it is possible to track the path of a γ ray inside the detector. $E_\gamma^{'}$ refers to the energy of the scattered γ-ray photon, E_γ refers to the initial energy, and θ to the scattering angle.

$$E_\gamma^{'} = \frac{E_\gamma}{1 + \frac{E_\gamma}{m_0 c^2}(1 - cos\theta)} \tag{9.1}$$

The energies of the events that follow the relation in Eq. 9.1 can be summed together since they correspond to one γ ray losing its energy via Compton scattering. Those events which partially deposit their energy in the detector are rejected.

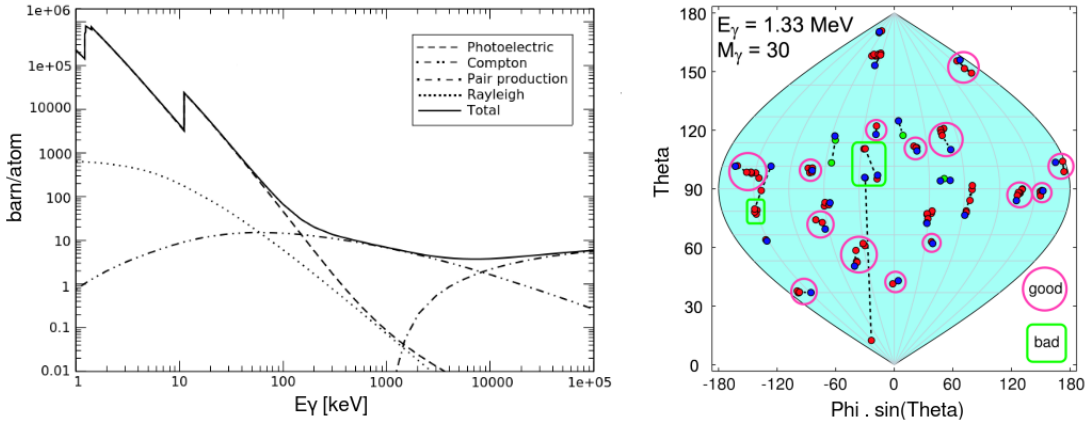

Figure 9.7: (Left) The probability of Rayleigh, pair production, Compton and photoelectric effect to occur due to the interaction of γ-ray photons in an energy range from 1 keV to 10 MeV with germanium material. (Right) Representation of 30 γ-ray events with energy E_γ=1 MeV detected in the ideal germanium shell and reconstructed with the clustering technique. Figures adapted from [188].

This calculation has to be performed for every possible sequence of interaction and for large γ-ray multiplicity this would result in a large number of cases to be computed. To avoid the enormous computational power needed, another technique is used, which is called the Clustering technique (See Fig. 9.7). The total absorption length for a γ-ray photon is of the order of a few centimeters, so the interaction position points of one γ ray should be localized in a small detector region. Based on the angular separation of the interaction points, the interactions that belong to the same track can be clustered. The points separated by an angle theta smaller than a reference one, as shown in the figure, are classified in the same cluster and then the validity of the cluster is checked by the Compton scattering formula 9.1. There are some limitations on the performance of the tracking algorithms caused by several factors, as for example: the interaction position is different from the position of the energy deposition of the electron because of the electron range in the material, electrons can lose energy via Bremsstrahlung and low-energy γ rays undergo Rayleigh scattering, resulting in a change of direction without losing energy.

A good Doppler correction when performing in-beam γ-ray spectroscopy is necessary to measure the proper energies of the detected γ rays. This can be done by knowing the angle between the emitting nucleus and the γ-ray photon, which is possible with the highly segmented germanium crystals of AGATA. Thanks to the segmented detectors and pulse shape analysis, the position interaction can be deduced with high precision.

AGATA at LNL

AGATA at LNL is coupled with the PRISMA magnetic spectrometer and both apparatus are mounted on a common mechanical structure, allowing their rotation around the target position, from 20° up to 160° with respect to the beam direction. A CAD drawing of the setup is shown in Fig. 9.8. The rotation allows the change of the experimental configuration depending on the grazing angle of the reaction. AGATA at LNL is foreseen to reach the 2π configuration, consisting of 60 HPGe segmented crystals.

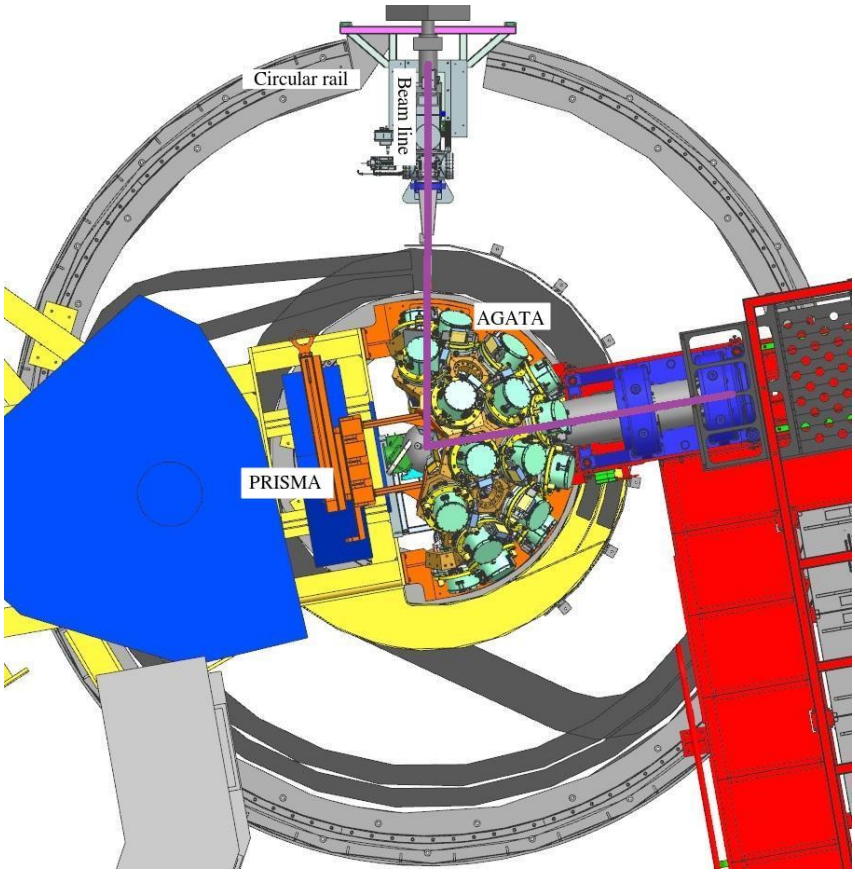

Figure 9.8: CAD drawing of the AGATA array coupled to the PRISMA spectrometer. Figure taken from [142].

In our experimental configuration AGATA was composed of 39 HPGe detectors arranged in 13 triple clusters (ATC) as shown in Fig. 9.9. The ID of each detector is marked in the figure. The triple cluster with ID 14 was not included in the acquisition during the experiment, the crystals 05A and 02B were not at the nominal value of voltage, and the 07C crystal was excluded from the analysis due to fluctuations of the baseline over time, thus ending up with 33 crystals present on the data taking process. AGATA in our experiment was placed in the so-called 'close-up' position, which means the array is translated 55 mm towards the target position with respect to the nominal position (source-detector distance equal to 235 mm)

The reaction chamber of AGATA has a radius of 17 cm which allows the installation

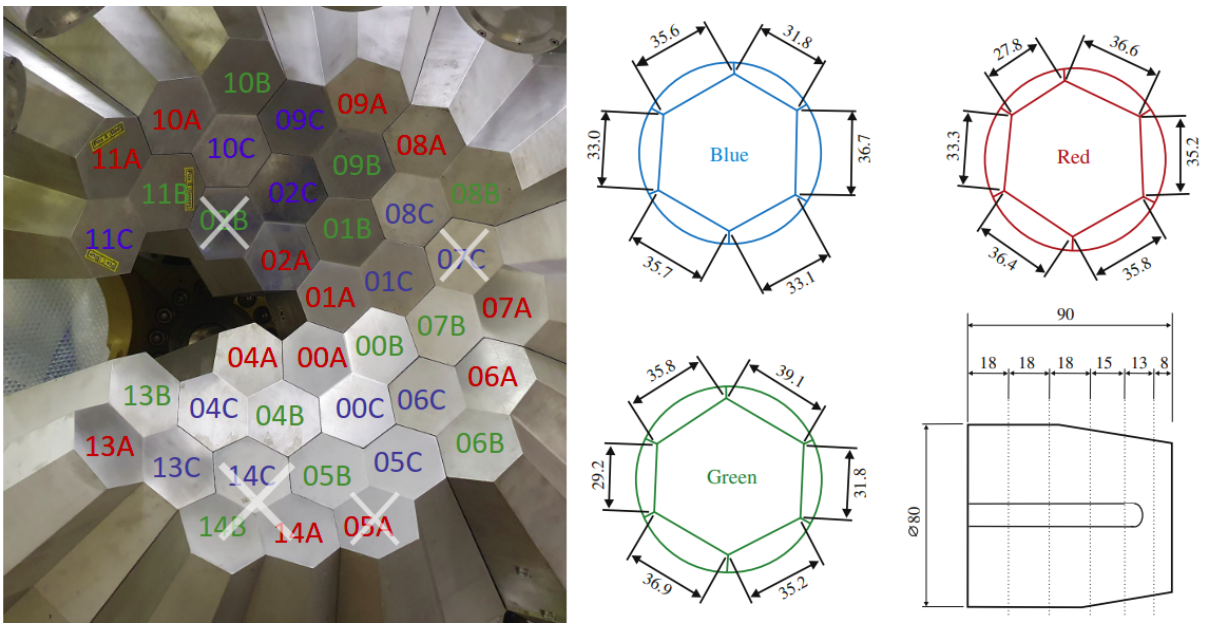

Figure 9.9: Configuration of the AGATA array at LNL composed of 39 crystals during our experiment. The crystal IDs are marked in the figure where the colors indicate the dimensions. The crystals with the white cross were not present in the acquisition or were excluded from the analysis. Figure on the right taken from [97].

of other ancillary detectors inside such as: EUCLIDES [92], TRACE [93], SPIDER [77], DANTE [189]. AGATA can also be coupled with $LaBr_3$ detectors which can be mounted in its holding structure (honeycomb) [190]. The acquisition system is similar to what was introduced before in the case of the GALILEO γ-ray array.

The signals of the AGATA detectors are read out by the AGATA digitizers similar to the ones of the GALILEO array described previously in Section 3.3.4. The Data Acquisition System provides the processing of the signals until they are stored and ready for the analysis.

The AGATA readout is composed of a local trigger generated by the Leading Edge algorithm applied to the signal of the central contact of every crystal. An external global trigger validates the trigger processor. As in the GALILEO array, the data are stored with a common clock timestamp by the Global Trigger Synchronization system (GTS). The PRISMA readout signals are collected by VME electronics. The events seen by the PRISMA detectors are correlated by the NARVAL and the Merger builds the individual events in the format to be used further in the analysis or stored on disk.

The AGATA events are merged with the events of PRISMA based on the timestamp by a dedicated VME module, AGAVA (AGATA VME Adapter) [97]. The conventional readout based on VME of the module allows the complementary detectors to participate in the trigger decisions. The flow of AGATA and Prisma data is shown schematically in Fig. 9.10.

In this experiment, in order to select the relevant events, the γ rays detected by

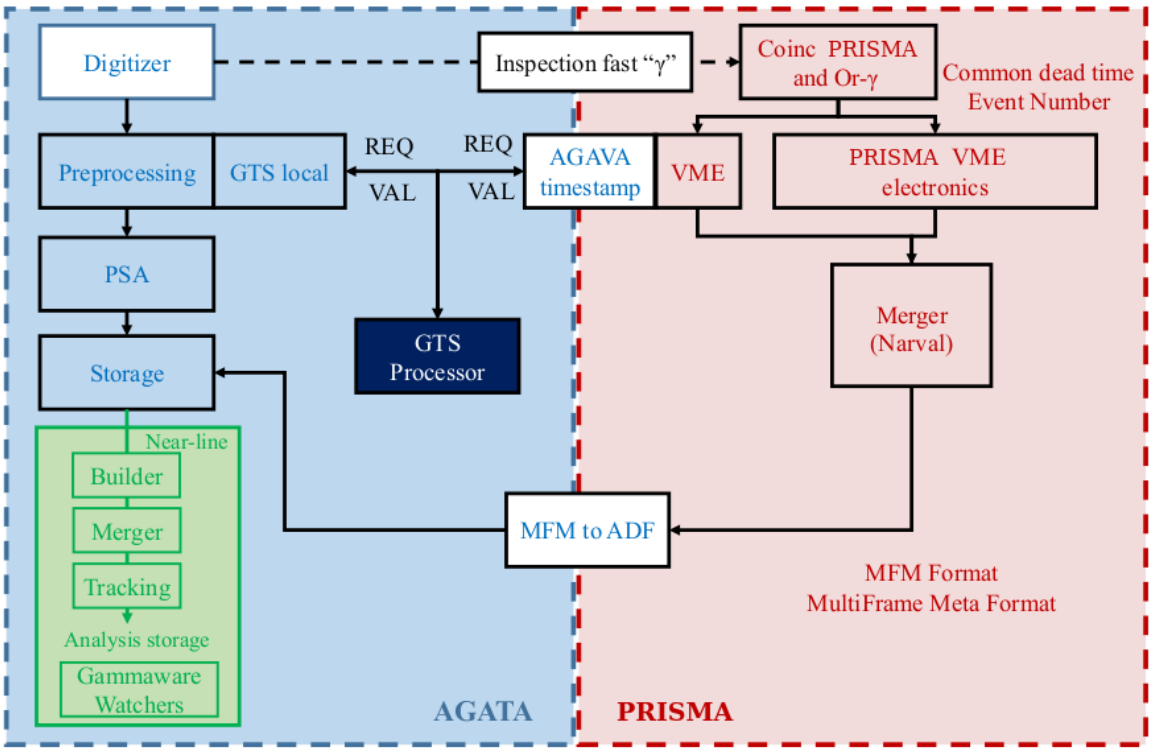

Figure 9.10: Schematic representation of the AGATA+PRISMA data acquisition system and the near-line analysis. Figure adapted from [191].

AGATA are stored only if there is a coincidence with a heavy-ion identified by the PRISMA spectrometer. The GTS system takes care to synchronize in time all the elements in the setup in order to reconstruct the coincidence events properly. The decisions made by the GTS system depend on the trigger processor configuration. In this experimental work, the standard configuration AGATA-PRISMA made of two partitions, as shown in Fig. 9.10 was used. A trigger request is sent from PRISMA if an event is detected both at the entrance of the spectrometer MCP and at the focal plane MWPPAC. A trigger request is sent by AGATA if the core signal of a crystal is larger than a given threshold.

9.3.3 The plunger device

The GALILEO plunger device described previously in Section 3.3.3 was used in this experiment but with a few upgrades. Another holding structure has been designed in order to allow its installation in the AGATA reaction chamber, as shown in the CAD drawing of Fig 9.11. The new support enables the plunger to move in the X, Y, and Z directions and rotate along the vertical symmetry axis. Another upgrade was done on the target and the degrader cone-holding structures. The aperture of the cone was increased to 60°, making it compatible with the plunger used in the reversed configuration. Moreover, the cones were built in larger dimensions because the target and the degrader

are tilted at large angles.

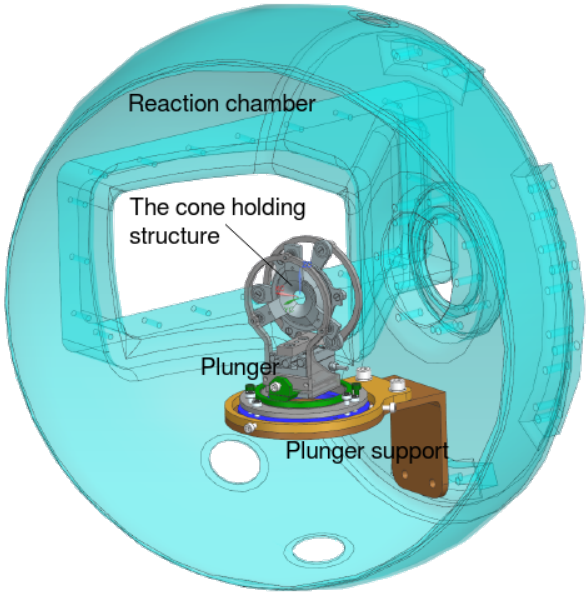

Figure 9.11: CAD drawing of the plunger device and its support structure mounted in the AGATA reaction chamber. Figure adapted from [142].

Chapter 10

Data pre-processing

An optimization of the gates and thresholds for the detectors of the PRISMA spectrometer and the steps to identify the ions in mass, charge state, atomic number, and velocity are shown in this chapter in Section 10.1. The performance of the AGATA spectrometer has also been optimized with respect to the conditions during the experiment. The HPGe crystals have been recalibrated in energy, neutron damage correction was applied and the time alignment of the signals of every crystal was performed and shown in Section 10.2.

10.1 Pre-processing of PRISMA data

The PRISMA spectrometer is composed of several detectors as it was explained in the previous chapter. Calibrations and optimizations of the performance of its components need to be carried out for the proper identification of the reaction products in mass, atomic number, and velocity $\vec{\beta}$.

- At first, the gates and thresholds are set at the optimal values for the detectors of PRISMA and the signals of the MCP and the MWPAC are calibrated.
- The IC of PRISMA is calibrated using a charge injector in the anodes of each pad. The identification of the atomic number of the ions is performed by using the IC chamber employing the ΔE-E technique.
- The time of flight is aligned between different sections of the MWPPAC. The velocity and the A/Q ratio of the ions are obtained based on the trajectory of the ions, constructed by the position in MWPPAC and MCP, the magnetic fields, and the ToF.
- The charge state of the ions is identified based on the magnetic rigidity and the energy loss in the IC. After the identification of the charge state the masses of the ions are obtained.

All these steps are described in the following.

10.1.1 MCP calibration

The MCP detector of PRISMA provides three signals: the X and Y coordinate signals and the stop signal used for the time of flight measurements. To convert the MCP detector signals from ADC channels to millimeters, a metallic cross with reference points is placed downstream of the carbon foil of the MCP, stopping the ions and creating a shadow as seen in Fig. 10.1 (Left panel), defining the reference points that can be used to perform the calibration. The reference points are marked in the figure and their coordinates are given in Tab. 10.1. The data points in the X position are calibrated using a second-order polynomial, while the Y position points are calibrated to millimeters using a third-order polynomial. Before the calibration, a linear transformation is applied to the data to rotate and stretch the raw coordinates. Figure 10.1 (Right panel) shows the final calibrated MCP matrix. The position given by the MCP is used to construct the trajectories of the ions.

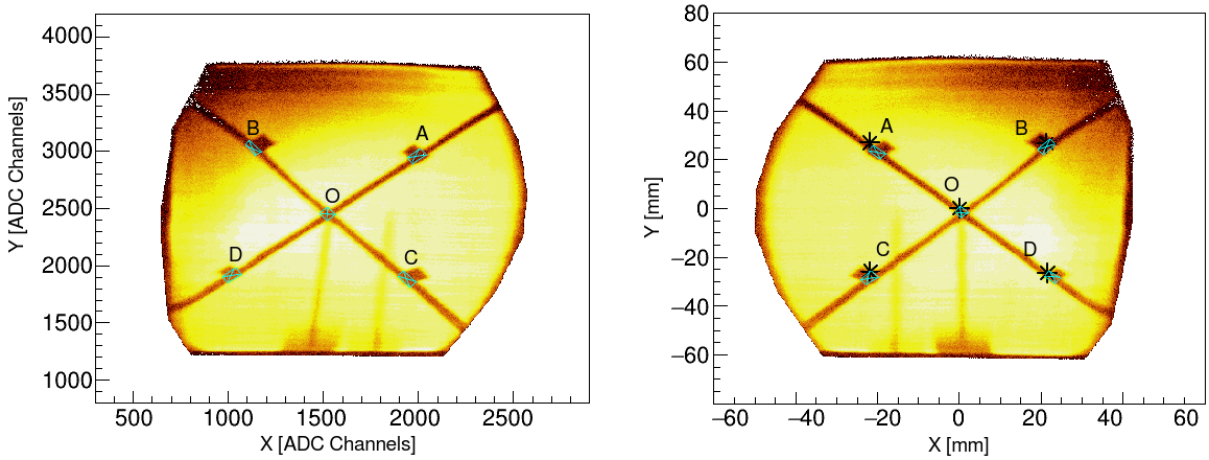

Figure 10.1: (Left) Raw X and Y MCP signals. The shadow in the matrix is produced by a metallic cross placed downstream the carbon foil of the MCP, defining the reference points used for the calibration. (Right) Final calibration in millimeters of the X and Y signals of the MCP detector. The calibrated points are shown with the blue square and the reference points with the cross symbol.

Table 10.1: The reference points used to calibrate the MCP

Position	X [mm]	Y [mm]
O	0	
A	-21.5	26.5
B	21.5	26.5
C	-21.5	-26.5
D	21.5	-26.5

10.1.2 X-focal plane calibration

The MWPPAC is segmented into ten equal sections and each of them provides six signals. The right, left, up, down and the cathode signals are used for position reconstruction. The time signal is used as a start of the TAC modules for the time of flight measurement. A threshold is applied to the signals in all the sections, and those with a smaller amplitude are discarded. The position in the horizontal plane of every event is reconstructed using the difference between the right and left signals. The difference between left and right signals for one section of the MWPPAC is shown in Fig. 10.2 (Left panel). The center of the distribution corresponds to the middle of the section, hence three points are used to calibrate each section in millimeters: the point in the middle and the two on the sides. Due to the detector inefficiencies, one of the left or right signals may be missing. Since the cathode signal is the sum of the signal measured by the anodes (left+right signal), the measured signal in the cathode reconstructs the missing signal. The recovered absent signal is used afterwards for the position reconstruction of the event, avoiding the rejection of such events. The final calibration of the sections of MWPPAC, from 0 to 1000 mm, is shown in the right panel of Fig. 10.2. As can be seen from the distribution, the Z=54 ions are not centered in the focal plane. This is because the magnetic fields of the dipole and the quadrupole magnets have been tuned in such a way that the distribution of the ions with Z=56 is centered in the focal plane.

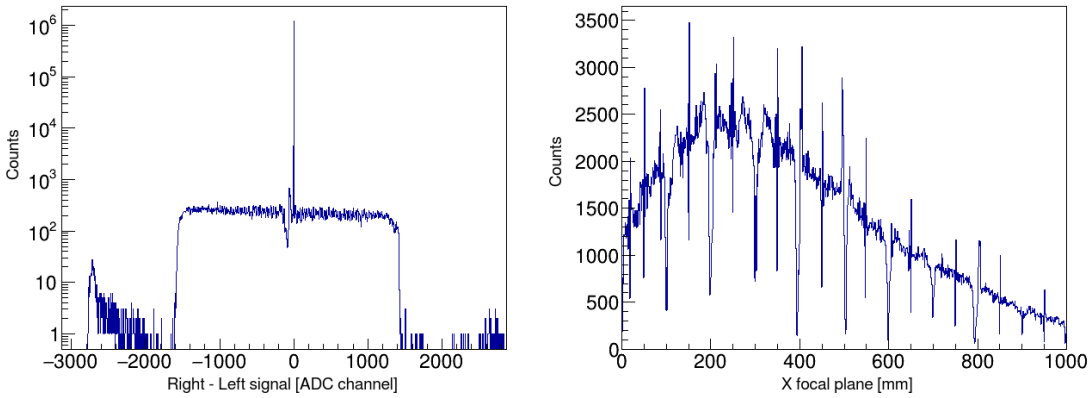

Figure 10.2: (Left) The difference between the left and right signals for one of the sections of the MWPPAC detector. Three points from this distribution are used for the position calibration: the sides and the center which corresponds to the middle of the section. (Right) The final position calibration of each section of the MWPPAC from 0 to 1000 mm.

10.1.3 The Time of Flight calibration

The time of flight is provided by ten Time to Amplitude Converter modules. As a start signal in the TAC module, the time signals from each section of the MWPPAC are used, and as a stop, the delayed signals from the MCP. This choice of the start and the stop signal avoids the coincidences with ions that enter the PRISMA spectrometer but do not

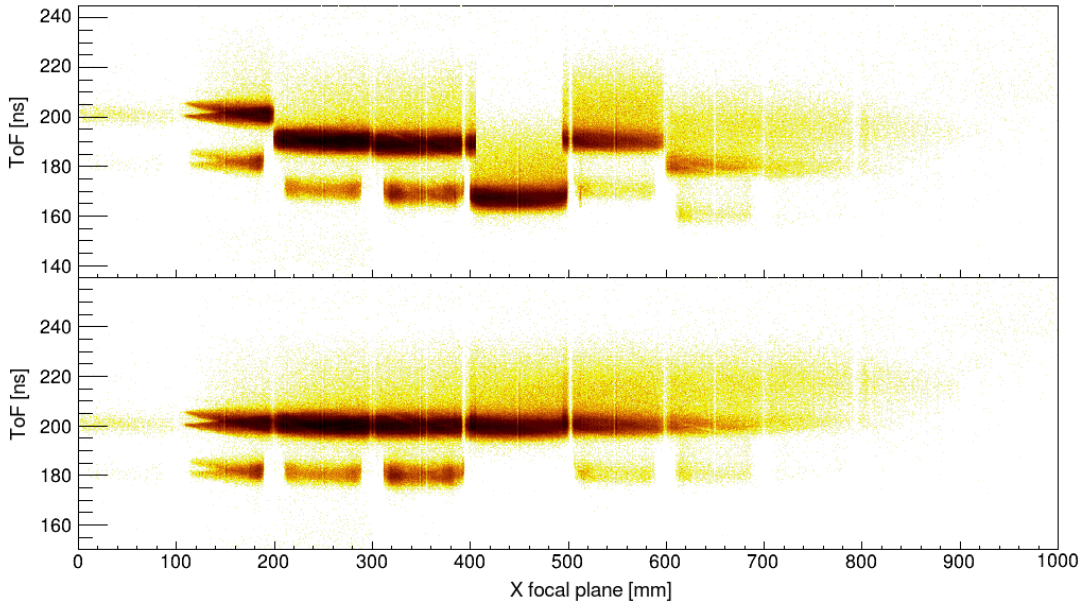

Figure 10.3: Comparison of the ToF versus X focal plane of the PRISMA spectrometer before (Top) and after the alignment of the sections (Bottom).

reach the focal plane. The calibration procedure to convert the TAC signals from ADC channels to nanoseconds is performed before the experiment. Pulse signals with known time differences from each other are used to calibrate the TAC modules. The time signals of the sections of the focal plane are then aligned by adjusting an offset in each of them. This is done in order to use the whole sections of the MWPPAC as a single detector for ToF measurements. Afterwards, a common offset is applied to retrieve the correct information on the time of flight of the ions. As a first approximation, the time of flight is obtained based on the expected velocity of the elastically scattered ^{136}Xe ions, taking into account the energy loss in the degrader and target, and the length of the trajectory from the MCP detector to the MWPPAC (approximately 5.98 m). The final alignment of the ToF is shown in Fig. 10.3 (Bottom panel). The most intense line in the matrix is aligned to 201 ns. This value was cross-checked with the γ-ray spectra measured by AGATA. Due to the emission of γ rays in flight, it is possible to deduce the velocity of the emitting ions and consequently their time of flight inside the spectrometer by considering the length of the trajectory from the MCP to the MWPPAC detector. Because of the resolution of the ToF, a finer alignment is achieved by the A/Q versus X focal plane matrix.

10.1.4 The identification of the ions

The steps to identify the ions in velocity $\vec{\beta}$, atomic number, charge state, and mass are described in the following section.

10.1.4.1 Trajectory reconstruction of the ions

After the target position, the ions pass through two optical elements of the PRISMA spectrometer, the quadrupole, and the dipole magnet. The position in the MCP and in the MWPPAC together with the knowledge of the magnetic field provides the identification of the velocity of the ions on an event-by-event basis. The PRISMA algorithms for the kinematic reconstruction consider the starting point of the trajectory of the ions in the center of the target, the motion of the ions in the horizontal plane, and ideal magnetic fields from both magnets. Using the equations of motions of a charged particle on a magnetic field is possible to calculate the trajectory of the ions. In the case of the quadrupole magnet, the magnetic field is given by:

$$\vec{B} = -\nabla U(x, y) \tag{10.1}$$

where x and y are the horizontal and the vertical coordinates, respectively, and U is given by the expression:

$$U_m = \frac{B_{max}}{R} xy \tag{10.2}$$

where B_{max} is the maximum intensity of the magnetic field and R is the inner radius of the quadrupole magnet. Considering the fact that a charged particle q in a magnetic field is under the influence of the Lorentz force:

$$\vec{F} = q\vec{V} \times \vec{B} \tag{10.3}$$

solving Eq. 10.1 for the magnetic field given by Eq. 10.3 and considering the initial direction of the ion from the center of the target and the coordinates in the MCP, the trajectory of the ions inside the quadrupole magnet and the exit coordinates can be calculated. The solution of the equations is a hyperbolic defocusing motion on the horizontal plane and a sinusoidal focusing on the vertical plane. Since the motion is considered planar, only the horizontal component is considered in the trajectory reconstruction. In the dipole magnet, the trajectory of the ions follows a uniform circular motion in the horizontal plane with a radius ρ. The radius of the curvature depends on the charge state q of the ion and on its mass A, velocity, and the magnetic field B by Eq. 10.4.

$$B\rho = \frac{Av}{q} \tag{10.4}$$

After exiting the dipole magnet, the ion continues to move on a linear path towards the focal plane where its position is measured by the MWPPAC. Since the entrance direction of the ion in the spectrometer is known from the MCP and also the position at the focal plane, the magnetic rigidity $B\rho$ can be calculated from the PRISMA algorithms. At this stage, the length of the trajectory L the ions travel from the MCP to the MWPPAC

is obtained. The velocity of the ions is determined by Eq 10.5.

$$\beta = \frac{L}{ToF \cdot c} \tag{10.5}$$

Furthermore, combining the relations 10.3 and 10.5 one gets the expression for A/Q:

$$\frac{A}{Q} = B\rho\frac{ToF}{L} \tag{10.6}$$

10.1.4.2 Z identification of the ions

The ionization chamber of PRISMA is divided into 40 pads, four columns, and ten rows. Each pad unit is calibrated before the experiment using a charge injector in each anode. Thanks to the energy deposited into each pad, it is possible to reconstruct the total kinetic energy of the reaction products. Because of the segmentation, the ionization chamber can be used as an E-ΔE telescope, helping to identify the atomic number of all the reaction products. The fraction of energy lost by a charged particle passing through a medium is given by the Bethe-Bloch formula:

$$-\frac{dE}{dx} = 2\pi N_a r_e^2 m_e c^2 \rho \frac{Z}{A}\frac{z^2}{\beta^2}\left[ln\left(\frac{2m_e v^2 W_{max}}{(1-\beta^2)I^2} - 2\beta^2\right)\right] \tag{10.7}$$

where N_a is the Avogadros number ($6.02{\cdot}10^{23}$ 1/mol), r_e is the electron radius from the classical picture ($2.817{\cdot}10^{13}$ cm), m_e the mass of the electron ($9.11{\cdot}10^{31}$ kg), z the charge of the incident particle, W_{max} is the maximum energy transfer in a single collision, I is the excitation potential, ρ is the density, Z the nuclear charge and A the relative atomic mass of absorbing material. In the case of non-relativistic particles, the formula can be simplified into:

$$\frac{dE}{dx} \approx \frac{MZ_{eff}^2}{E} \tag{10.8}$$

where M is atomic mass, Z_{eff} is the effective nuclear charge of an ion, and E is the kinetic energy energy. dE is the energy loss of the ions in the pads of the IC, dx corresponds to the range of the ions in the IC (mean free path). With the PRISMA spectrometer, it is possible to measure the total energy E by summing the energy losses in all the pads of IC, dE is typically the energy loss in the first two columns of the IC, and dx can be measured by the trajectory reconstruction algorithm of PRISMA. The pressure of the gas inside the chamber is optimized in order to stop the reaction products totally and to obtain the Bragg peak located in the third section of the ionizing chamber, improving the Z resolution and making sure to avoid punch-through events. All the events crossing the pads that correspond to different columns are discarded, thus accepting only straight trajectories of the ions along the path inside the spectrometer.

Figure 10.4 shows the energy measured by the first two columns versus the total

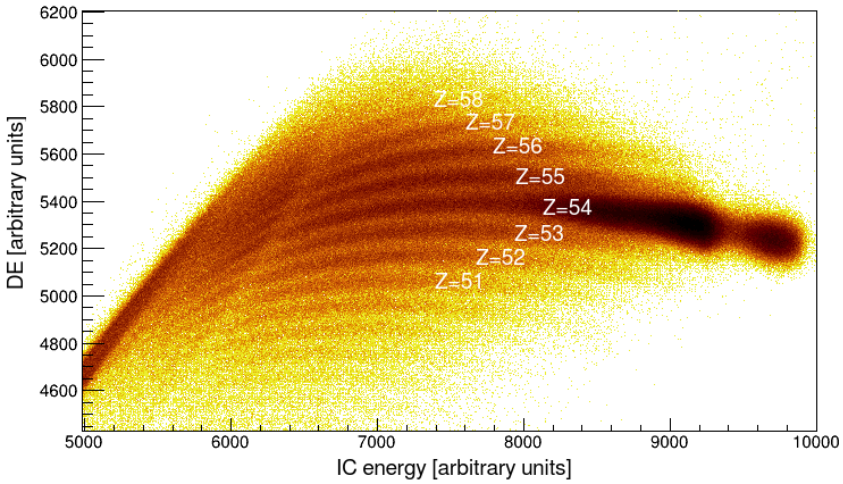

Figure 10.4: The energy of the ions measured by the first two columns versus the total energy of the IC. The structures seen in the figure correspond to nuclei with different atomic numbers. The most intense line corresponds to the elastic channel, Z=54. The different Z values are marked in the figure.

energy measured by the IC. The structures seen in the plot correspond to nuclei with different atomic numbers. The most intense line corresponds to the elastic channel of the reaction, Z=54. Going up or down in the vertical direction in the matrix in Fig. 10.4 the atomic number changes by one unit.

10.1.4.3 Charge state identification

The initial charge state identification is based on an estimate given by calculations performed with the Reaction code. For our nuclear reaction, it results that Q=41^+ is the most dominant charge state followed by Q=40^+ as shown in Tab. 10.2. The charge states identified experimentally may differ from the ones calculated since the code does not consider the carbon foil of the MCP, which may produce a change in the charge state, and the fact that the magnetic fields may impact the distribution of the charge states. As mentioned before, the fields have been set in order to center the trajectory of the ^{196}Os ions. The charge states can be separated by plotting the total kinetic energy of the ions, measured from the ionization chamber, versus the magnetic rigidity, as shown in Fig. 10.5. The structures in the figure correspond to different charge states. The masses are obtained on a first attempt based on the estimates for the charge states of the Reaction code. If the charge states are not correctly identified, this would imply a shift in the mass spectrum. Indeed, the identification based on the mass spectrum gives Q=39^+ as the most intense charge state for the ^{136}Xe ions. The final charge states of the ions identified by PRISMA are shown in Fig. 10.5.

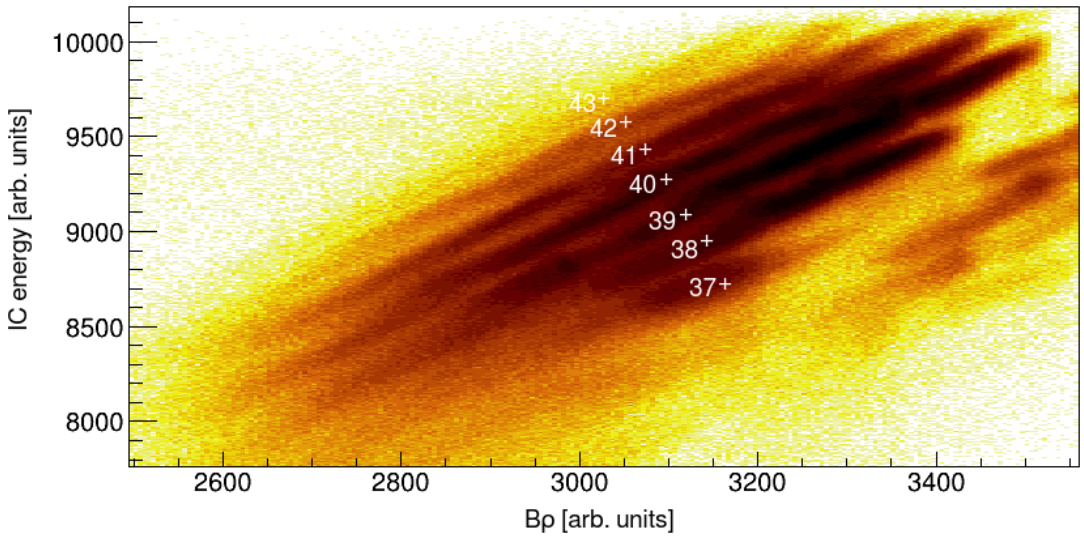

Figure 10.5: The energy of the ions measured from the ionization chamber as a function of the $B\rho$ obtained from the trajectory reconstruction. The structures in the plot indicate different charge states of the particles. When moving up along the IC energy at a fixed $B\rho$, the charge states increase by one unit.

Table 10.2: Charge states of the elastic channel calculated from the Reaction code

Charge state	%
+37	3.87
+38	8.31
+39	14.38
+40	19.64
+41	20.69
+42	16.38
+43	9.47

10.1.4.4 Mass identification for the elastic channel

After the charge identification, the A/Q value is multiplied by Q to obtain the mass spectrum. The A/Q ratio and the mass spectrum as a function of the position at the X focal plane of PRISMA are shown in Fig. 10.6. As can be seen in Fig. 10.6, the identified mass and the A/Q drift along the X focal plane position. This tendency is a result of the aberration effect. The dipole and the quadrupole magnets of PRISMA are manufactured to have a linear magnetic field but this does not prevent the higher orders from playing a role in the transmission of the ions. The algorithm for the trajectory reconstruction of PRISMA assumes a first-order approximation for the optics of the spectrometer. The trajectories can be a combination of straight lines and circular motion. Evidently, the aberrations are affecting significantly the mass resolution. Corrections may be applied to account for these effects and improve the mass resolution. One procedure to optimize the effect of the aberration is to change the effective length and position of the quadrupole

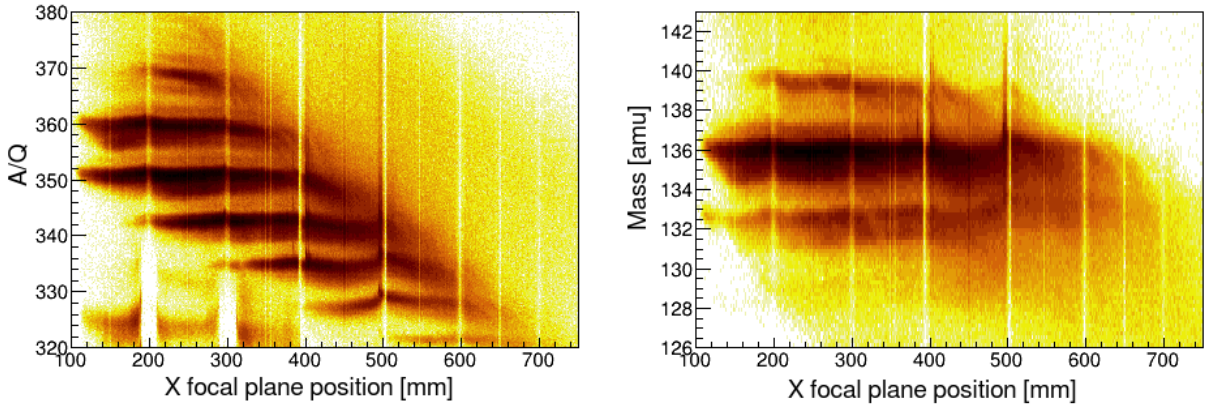

Figure 10.6: (Left) The A/Q as a function of the X focal plane position of PRISMA. The curved structures in the matrix indicate the effects of the aberrations due to the optics of the spectrometer. (Right) The mass of the ions identified by PRISMA with respect to the X focal plane position.

magnet but this procedure may partially influence the aberrations. A further improvement is reached as described in the following paragraphs.

At first, the aberration correction is performed in the A/Q versus X coordinates of the MCP by fitting a six-order polynomial in the most intense structure as shown in Fig. 10.7 (Left panel). Using the equation obtained by the fit of the experimental data, the structures could be aligned. The most intense line which corresponds to the elastic channel, is aligned at A/Q=351 as expected for this reaction channel. The alignment of the structures with respect to the X position measured by the MCP is shown in Fig. 10.7 (Right panel).

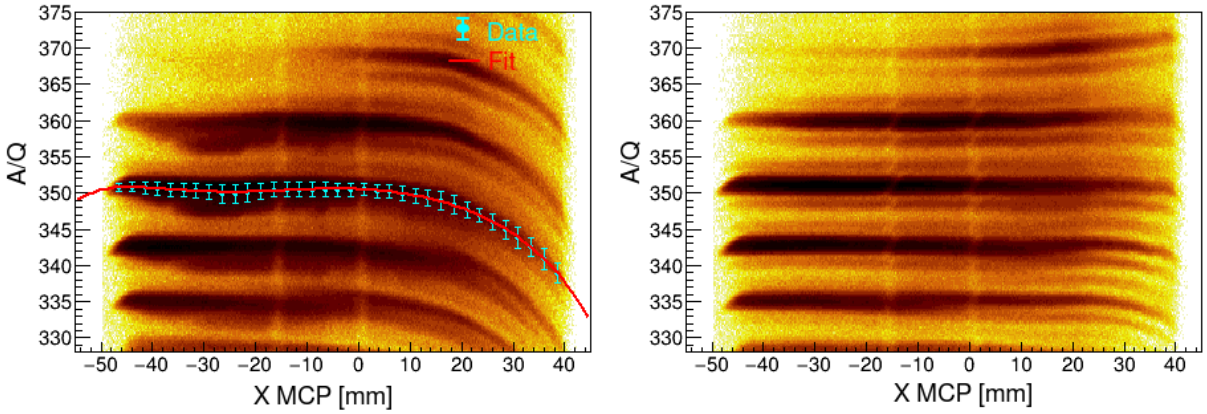

Figure 10.7: Aberration correction applied on the A/Q versus X position in the MCP matrix. (Left) The most intense structure, indicating the elastic reaction channel, is fitted with a six-order polynomial. (Right) The aberration correction applied to the data by using the polynomial function from the fit.

The same correction has also been applied on the A/Q versus Y MCP coordinate matrix. The structures appearing in the matrix, shown in Fig. 10.8 (Left panel), are aligned by using a third-order polynomial fitted in the most intense line, which corresponds

to the elastic channel. The alignment can be appreciated in Fig. 10.8 (Right panel).

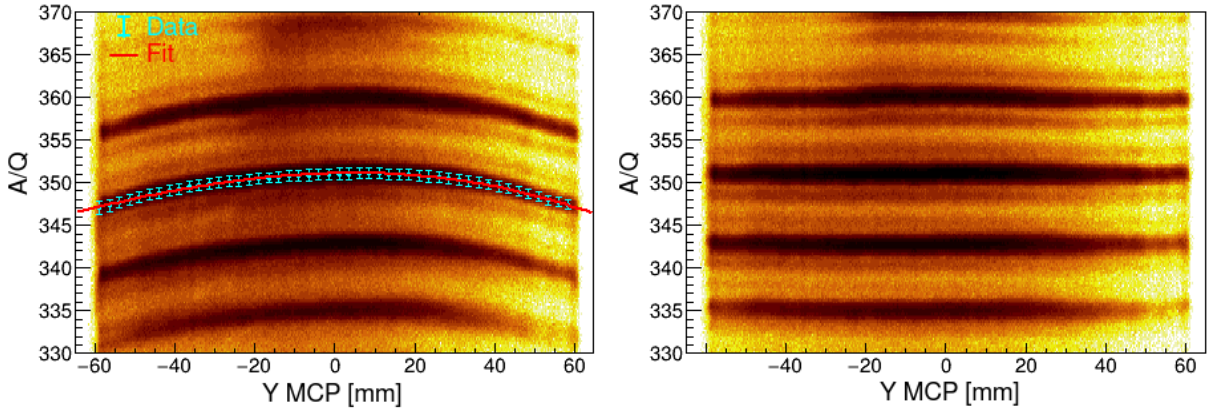

Figure 10.8: Aberration correction applied on the A/Q versus Y position in the MCP matrix. (Left) The most intense structure, indicating the elastic reaction channel, is fitted with a third-order polynomial. (Right) The aberration correction applied to the data by using the polynomial function from the fit.

After applying the aberration correction of the A/Q in the X and Y position of the MCP, the resolution of the A/Q, when plotted with respect to the X focal plane position, changes significantly (Compare the right panels of Fig. 10.6 and Fig. 10.9). In order to obtain a better resolution a finer alignment is applied by using a six-order polynomial fitted to the experimental data corresponding to the elastic channel as shown in Fig. 10.9 (Left panel). The final result is shown in Fig. 10.9 (Right panel). The difference before and after the corrections is noticeable.

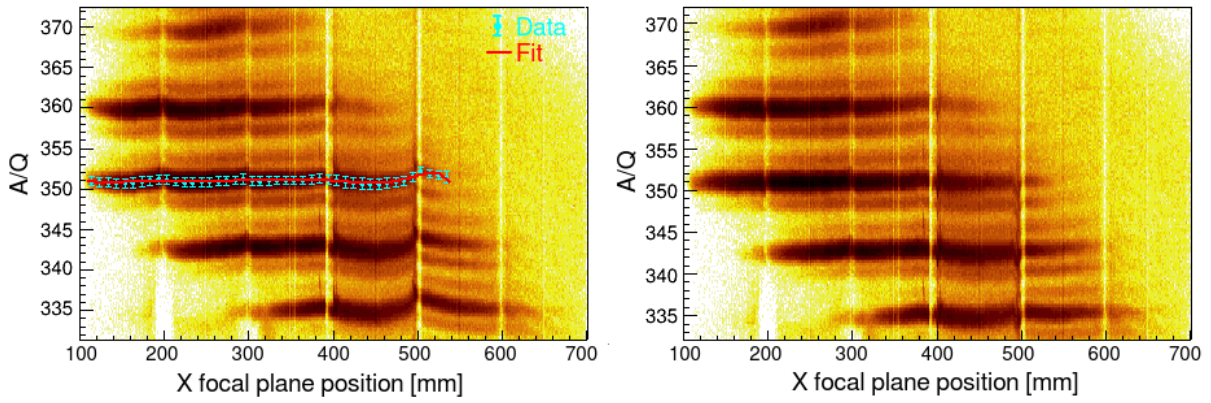

Figure 10.9: Aberration correction applied on the A/Q versus X focal plane position matrix. (Left) The most intense structure, indicating the elastic reaction channel, is fitted with a six-order polynomial. (Right) The aberration correction applied to the data by using the polynomial function from the fit.

The mass spectrum for the elastic channel gated on Z=54 is shown in Fig. 10.10. As expected, the elastic channel is identified with mass A=136, confirming the charge state identification. The resolution in mass results to be ∼1/240.

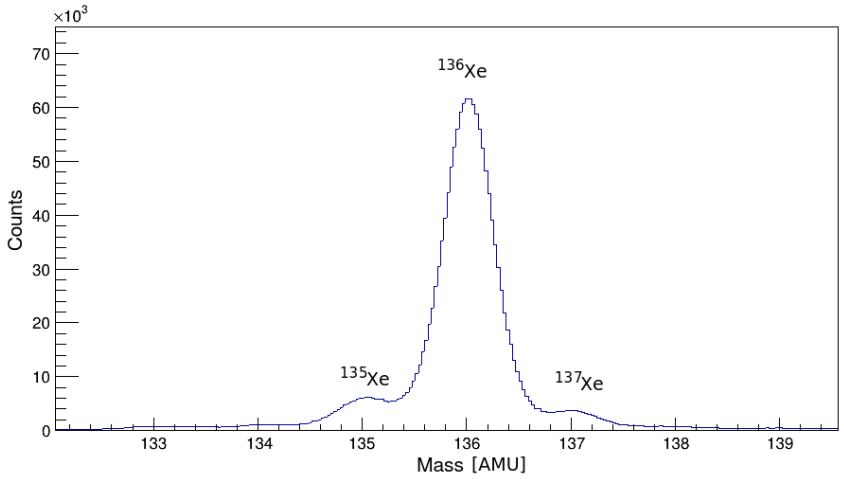

Figure 10.10: Mass spectrum for the elastic channel gated in Z=54 after the aberration corrections. The resolution in mass results to be ∼1/240.

10.2 Pre-processing of the AGATA data

The processing of the AGATA data is divided into two parts: the Local processing stage, where the performance of each crystal is optimized individually, and the Global processing, where the performance of the array is characterized as a whole.

At the Local stage of the pre-processing of the data, the energy calibration is performed using a ^{60}Co source. Using the source data, the cross-talk correction is applied, and also the time alignment of the segments with the core itself. Afterwards, a recalibration is performed using the ^{152}Eu source, the linearity of the detectors is checked, the time alignment of all the cores, and the neutron damage correction is applied. These steps are all performed by the NARVAL actors in consecutive order, as shown schematically in Fig. 10.11. The processing of the data by each NARVAL actor is described in the following section.

10.2.1 The local level of the AGATA data processing

All the optimization steps up to the PSA filter are performed before the beginning of the experiment using a ^{60}Co source.

10.2.1.1 The crystal producer

The crystal producer actor is the first filter applied to the AGATA data. At this stage, the raw binary data are read and converted into spectra. This filter reads the amplitude, the time stamp, and the traces for every event in every channel present in the acquisition. Each crystal has 38 channels (36 channels of the segments and the two channels from the central contact). The energy spectra obtained at this stage are used to extract the calibration coefficients for every channel of every crystal. Due to the huge amount of channels, 1254

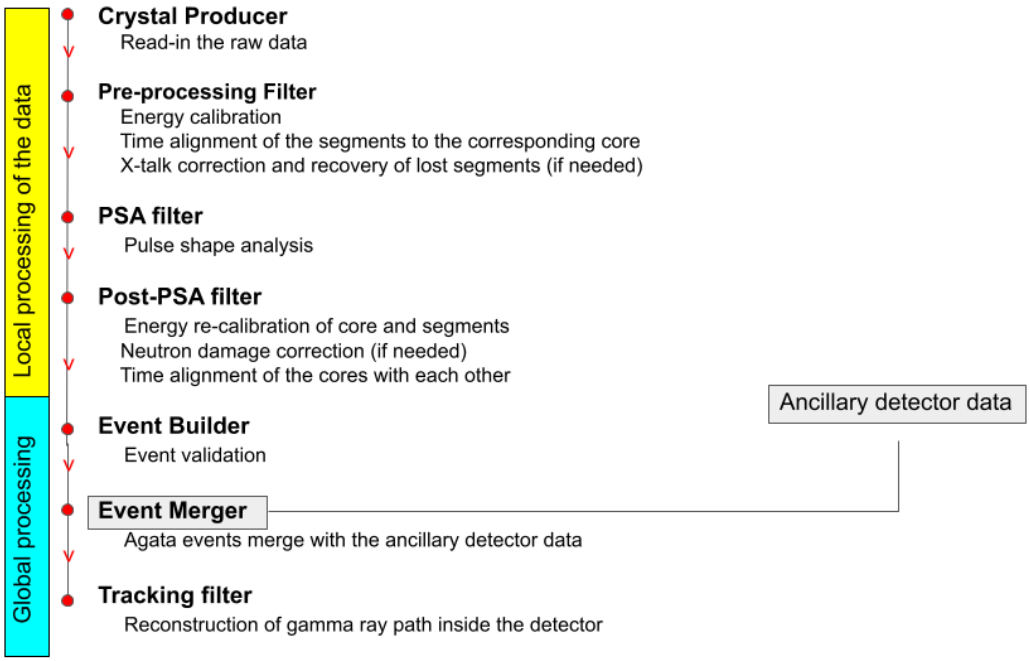

Figure 10.11: Schematic representation of the stages of the processing of the data of AGATA. The Local processing stage, where the performance of each crystal is optimized individually, and the Global processing where the performance of the array is characterized as a whole.

in total in the actual configuration of the array (33 crystals x 38 channels), the calibration is performed by an automatic peak finder program called ReCalEnergy [192]. The two γ-ray transitions of ^{60}Co (1.1 and 1.3 MeV energy) are fitted with a linear function with offset forced to zero. The coefficients are saved and will be used from the Pre-processing filter to produce the calibrated spectra for every channel. The spectra from the producer filter shown in Fig. 10.12 are also a way to check the status of the detectors, like missing signals from segments, gain fluctuations, etc.

10.2.1.2 Pre-processing filter

Besides the energy calibration performed at this stage, several additional steps are also necessary to be performed such as: cross-talk and time alignment.

Cross-talk correction

In an electrically segmented detector, if the γ rays do not lose their entire energy in the same segment, a deficit is produced in the sum energy of the segments. This deficit becomes bigger as the multiplicity increases (number of segments firing at the same time) as shown in the left panel of Fig 10.13. The same effect happens when signals are induced to the neighboring segments. To account for these effects the cross-talk correction has been applied to all the crystals using the xTalkSort code [192]. The shift from the nominal

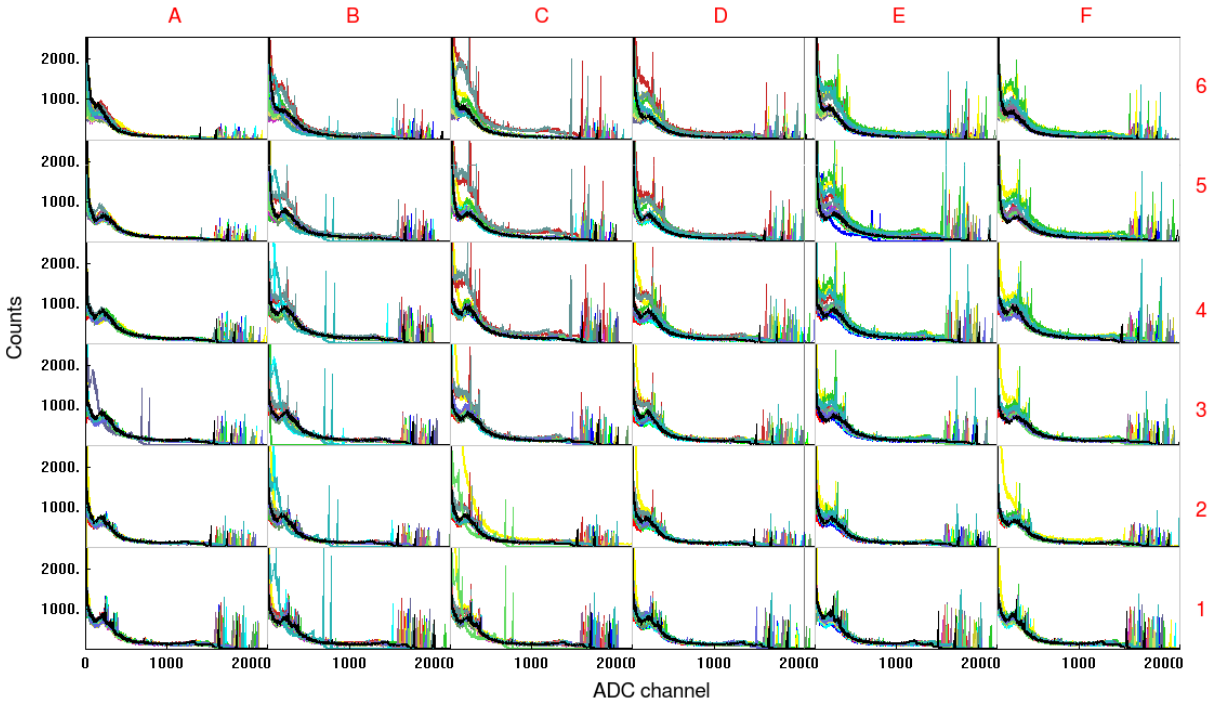

Figure 10.12: Energy spectra of every segment given by the Producer filter for all the crystals in the acquisition.

energy of the two ^{60}Co γ-ray transitions is used to correct the cross-talk effects. The correction can be seen in Fig. 10.13 (Right panel).

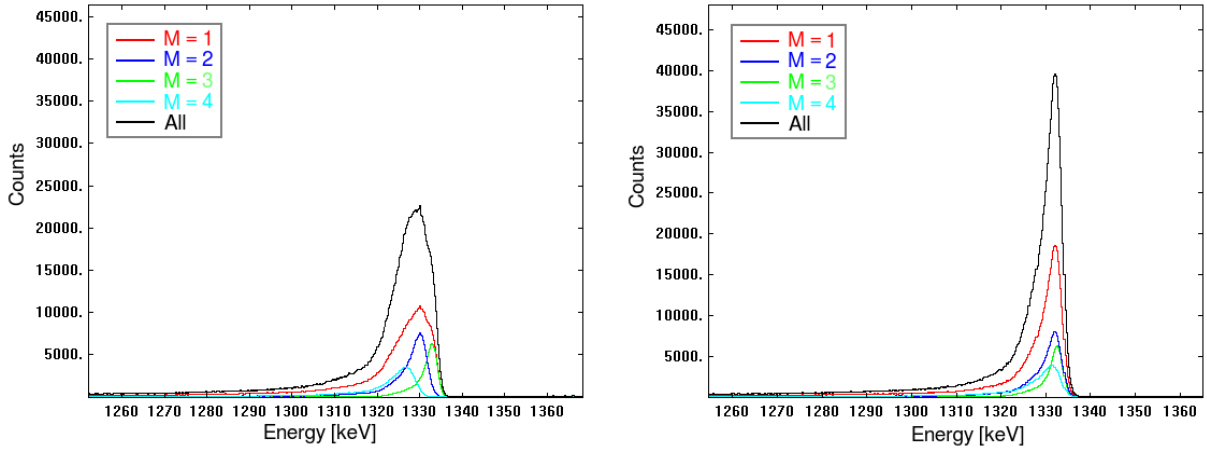

Figure 10.13: Comparison of the γ-ray spectrum at the 1.3 MeV transition of ^{60}Co for different multiplicities of segments (coloured lines) and for all multiplicities (black line). (Left) The γ-ray spectrum before and (Right) after applying the cross-talk correction.

In cases of missing signals from one segment of an AGATA crystal, it is possible to recover its correct information using the signals of the core. Since the central core measures the same signals as seen from all 36 segments, in cases one of them is broken, subtracting from the core signal the sum of signals of all the working ones, it is possible to recover the signals from the missing segment.

Several detectors showed this behavior in our experiment: detectors 01B, 04A, 08A, and 11A. The recovery of their missing segment was successful in all of them.

Time alignment of the segments

The pulse shape analysis used for the position reconstruction of the hits in the HPGe detector requires that the traces are aligned in time. As mentioned previously, for position reconstruction, the signals seen in every segment are compared to calculated ones. The signals calculated for the PSA assume an ideal detector where signals are well aligned in time. Time differences between measured signals would lead to inaccurate calculation of the position of interaction. For this reason, an alignment in time of the signals of the segments in every detector is performed. Due to the huge number of channels present in the acquisition, the ReCalEnergy program is used to automatize the procedure. The alignment in time of all the segments at 500 ns is shown in Fig. 10.14.

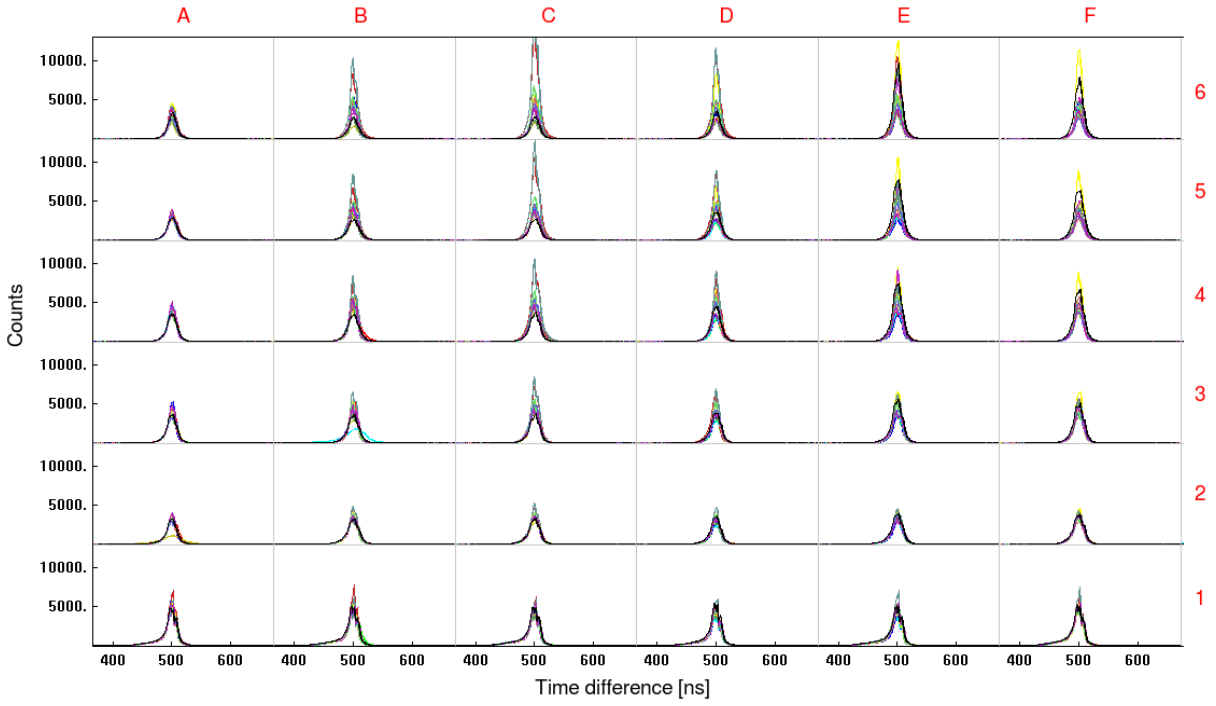

Figure 10.14: Time alignment at 500 ns of the signals measured by the segments of every detector present in the acquisition.

In order for all the detectors to have the same reference time, all the cores are aligned to each other to have the same starting time reference. This time reference is called Tzero. The TZero aligned for all the crystals present in the experimental setup is given in Fig. 10.15.

10.2.1.3 The PSA filter

As anticipated previously, the PSA filter calculates the position of interaction event-by-event of the γ rays in the germanium medium. The signals generated in the detector due

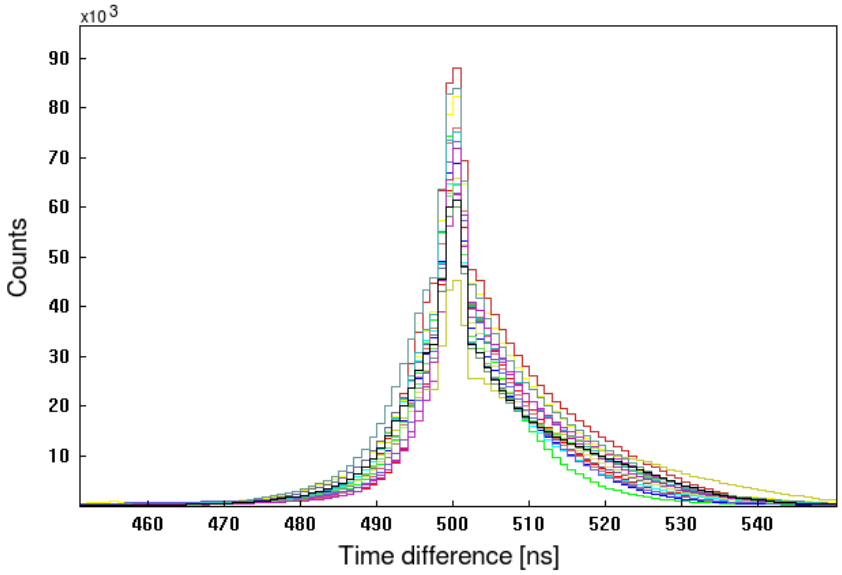

Figure 10.15: The alignment of the signals of the cores at 500 ns in order to have the same starting time reference.

to the interaction with the γ ray are compared with a calculated dataset [193]. The best fit between the detector signals and the calculated ones defines the interaction position with a resolution of 4 mm in FWHM. The distribution of the hits in one crystal is shown in Fig. 10.16 in the XY, XZ, and YZ planes. A clustering of the events in the center of the segments can be noticed even though one would expect a uniform distribution. This accumulation of the data in the center of the crystal can be related to limitations of the PSA algorithm or of the calculated signals.

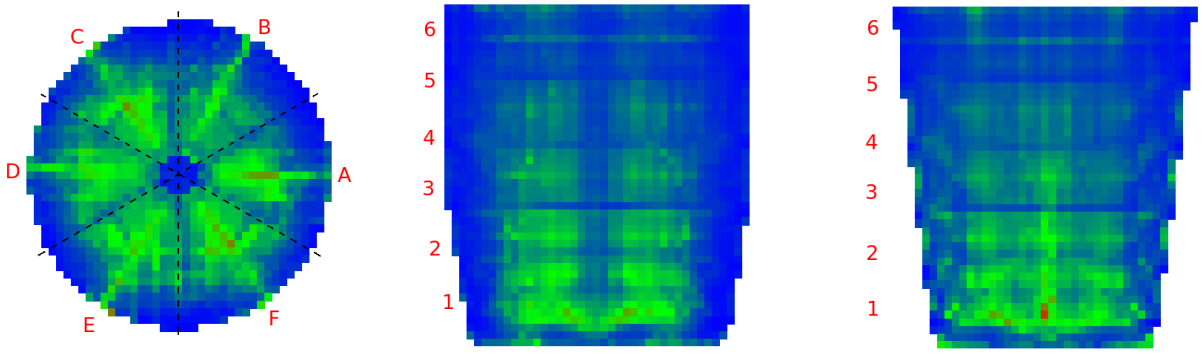

Figure 10.16: The distribution of the hits in one crystal of AGATA, reconstructed by the PSA filter. (Left) The distribution in XY plane (Middle) XZ and (Right) YZ plane.

Figure 10.17 shows the hit pattern of the AGATA array based on the position reconstruction of the events from the PSA filter. The ID of each crystal is marked in the figure.

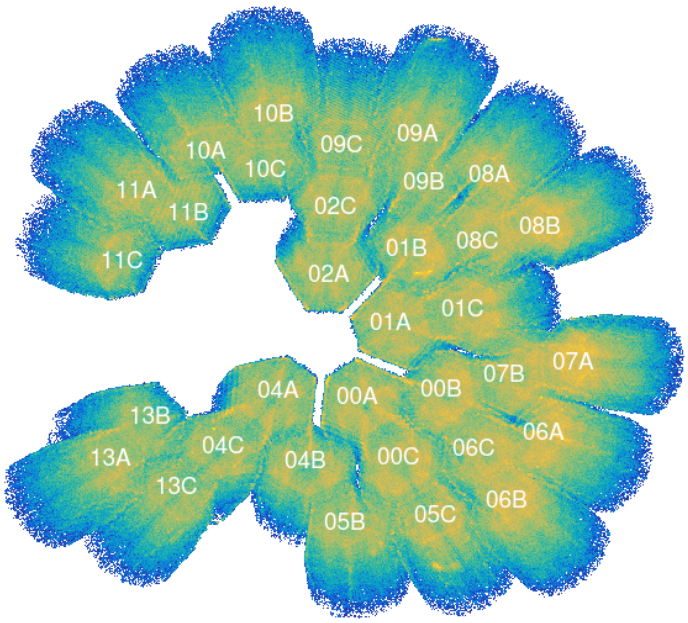

Figure 10.17: Hit pattern of the AGATA array generated by the PSA filter using the experimental data. The IDs of the 33 detectors present in the acquisition are marked in the figure.

10.2.1.4 The Post-PSA filter

At this stage, several more corrections can be applied, improving further the performance of the detectors in terms of energy resolution. As described in Section 1.2, a calibration was performed using the ^{60}Co source, and the offset of the linear fit was forced to zero. A recalibration is performed at this step using data points covering a wide γ-ray energy range. In this experiment, the recalibration was performed using a ^{152}Eu source covering energies from tens of keV up to 1.5 MeV. The neutron damage correction was applied, significantly improving the energy resolution of the detectors. Finally, a global time alignment was performed.

Neutron damage

The germanium crystals are very sensitive to fast neutrons (neutrons with energy of a few MeV). The interaction of the neutrons with the germanium causes some defects in its lattice which interact with the charge carriers (electrons and holes) inside the detector, causing a decrease in the charge collection efficiency. Consequently, the γ-ray peaks in the spectrum appear with a tail on the left side. This can be seen in the γ-ray spectra obtained for one crystal of the AGATA array in Fig. 10.18. Data from the AGATA spectrometer show that the segments are more sensitive to neutron damage compared to the central core contact. Since the defects are negatively charged, the e^- carriers are not trapped as much as the holes. The deficiency in the charge collection due to trapping can be determined as a function of the interaction position of the γ rays within

the crystal. Based on the deficiency of the charge collection and on the exact information of the position of interaction given by the pulse shape analysis, it is possible the correct the measured energy by employing specific trapping parameters in the HPGe volume, resulting in a much better energy resolution [194]. The trapping parameters for each crystal are determined by using data collected with an ^{60}Co source and the effect of the neutron damage correction can be appreciated in Fig. 10.18 and Fig. 10.19.

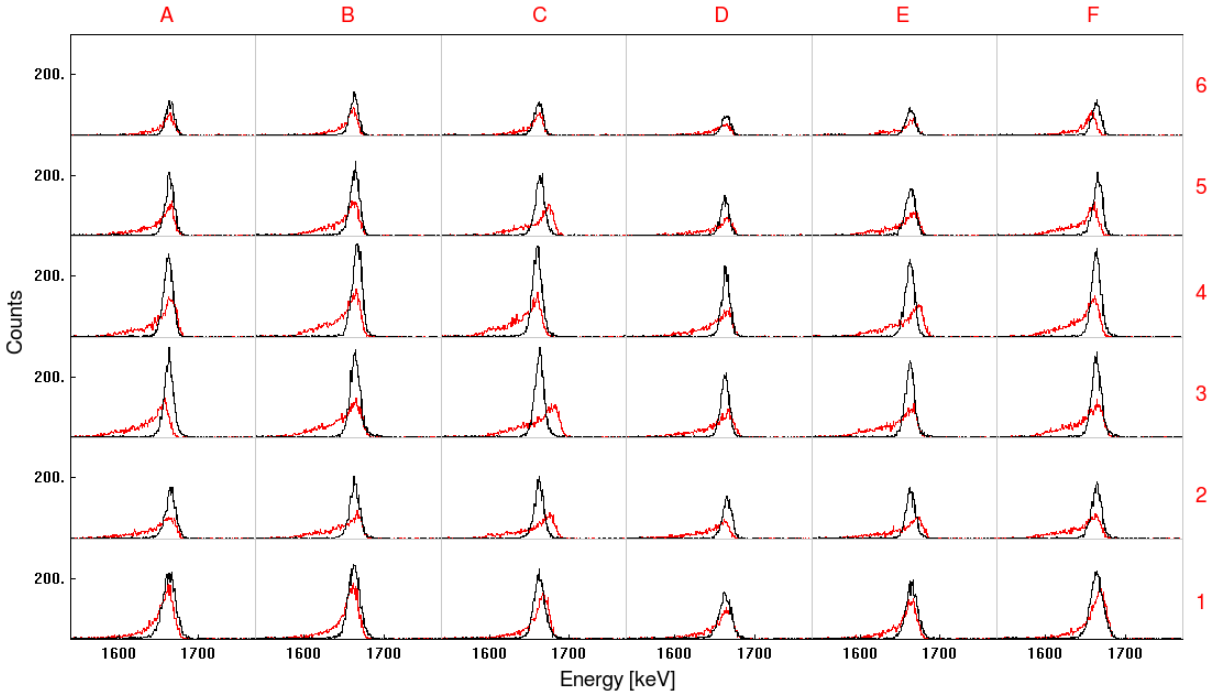

Figure 10.18: Comparison of the γ-ray energy spectrum taken with a source of ^{60}Co before (red) and after applying the neutron damage correction (black). The comparison is shown for the segments of detector 00A. The ID of the segments is marked in the figure.

Energy recalibration

After applying the neutron damage correction to the data, a final recalibration is performed using an ^{152}Eu source. At this step, linear or higher-order polynomials can be used to calibrate the detectors. In this experiment all the HPGe detectors show linear behavior (measured energy of the γ rays versus ADC channel), so a first-order polynomial is used for the calibration.

Another option when applying the recalibration is the "ForceSegToCore" which normalizes the energy measured by all the segments in one crystal with the energy measured by the core. This function reduces the effect of the neutron damage in the segments and any other possible malfunctioning of the segment. This option was applied in this data set since it improves the energy resolution of the sum of the segments γ-ray spectra.

Global time alignment

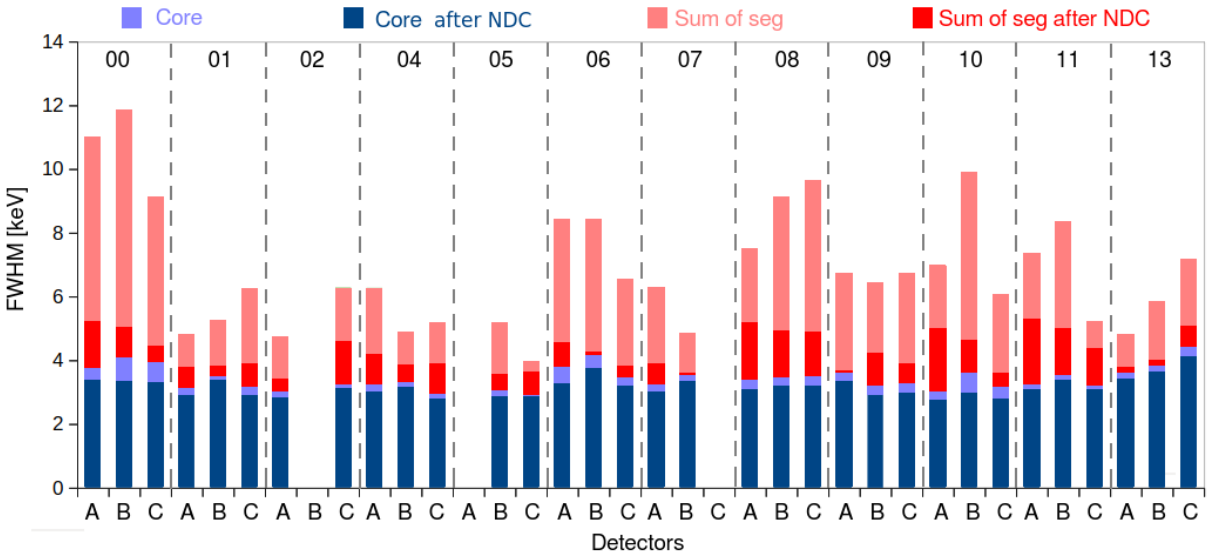

Figure 10.19: The energy resolution of the spectra obtained from the core and the sum of segments for each AGATA detector present in the acquisition at 1.3 MeV before and after the neutron damage correction.

To avoid random coincidences, the alignment in time of all the crystals is performed at the Post-PSA step of the data processing. The time difference between each combination of a pair of two detectors is calculated. The program SolveTT [192] is used to optimize the time shift coefficient for each detector. The alignment in time of the detectors is shown in Fig. 10.21.

10.2.2 The global level of the data processing

The global level of the data processing includes three Narval actors: the Event Builder, the Event Merger, and the Tracking Filter.

10.2.2.1 The Event Builder and Merger

The signals of the AGATA HPGe crystals and those of the ancillary detectors are synchronized in time by the GTS tree. The AGATA data is then merged with the ancillary data (in this case, the PRISMA spectrometer data) based on the timestamp of the events. The events processed at the local level within a time window of 1 μs are assembled in units by the Event Builder. This time window is quite large in order not to miss events but in the offline analysis, narrower gates can be set to further reduce the background events. The time difference between the PRISMA events time stamp and the AGATA events time stamp is shown in Fig. 10.22 where the time window set for the coincidence measurements is indicated with the red dashed lines.

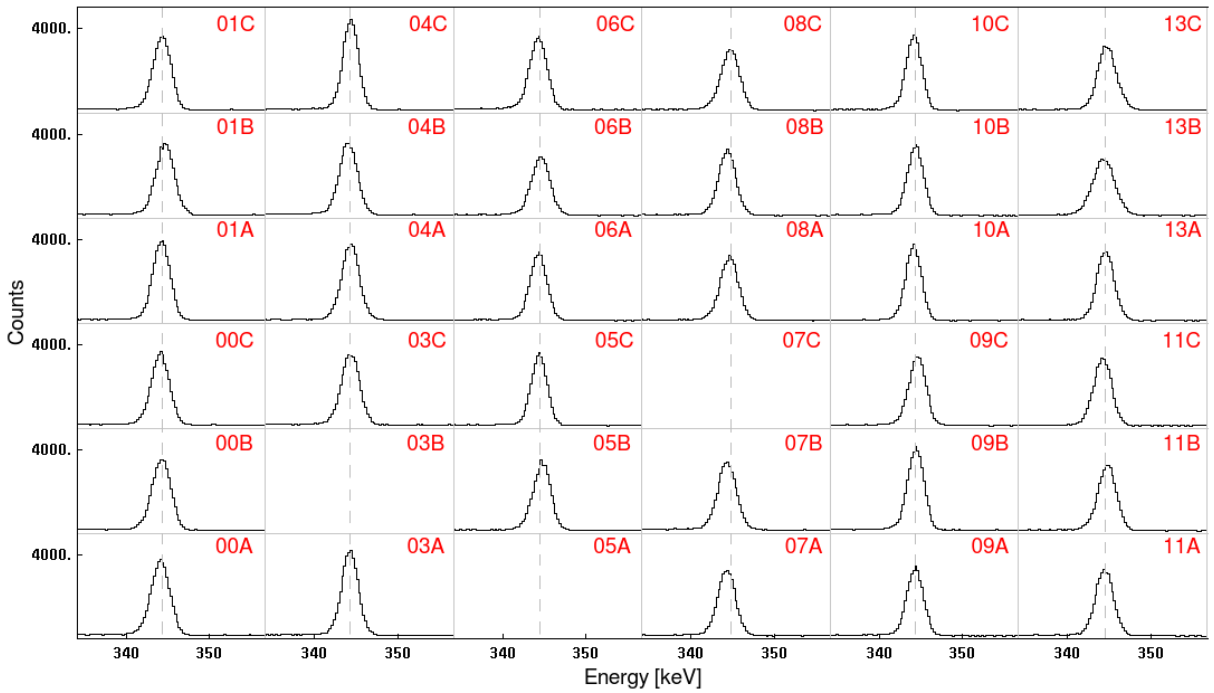

Figure 10.20: Final energy calibration of the detectors of AGATA using the ^{152}Eu source. The peak shown in the figure corresponds to the 344 keV peak. The ID of each core is shown in the figure

10.2.2.2 The tracking filter

The reconstruction of the path of γ rays inside the crystal is performed by the tracking filter based on the position, time, and energy deposited for every interaction. The Orsay Forward Tracking (OFT) algorithm [195] was used to reconstruct the events. In this code, four empirical parameters have to be optimized to improve the performance of the tracking:

- SigmaTheta (σ_θ) - the average interaction-point position resolution
- MinProbTrack (P_{track}) - the minimum probability for a γ ray to interact via the Compton effect
- MinProbSig (P_{sig}) - the minimum probability for a γ ray to have penetrated a given depth in the detector and to have been absorbed via the photoelectric effect
- Clustering Angle and Reduction Factor (ClAngRed) - Reduce the area where the cluster events are tested to fulfill the Compton scattering formula

From a recent update of the OFT code, the P_{sig} parameter is set to a constant value. Thus, to optimize the tracking for our data, a series of replays of the ^{60}Co data was performed by fixing two parameters and varying the third one. These parameters affect the efficiency and the Peak-to-Total ratio in opposite directions and a compromise

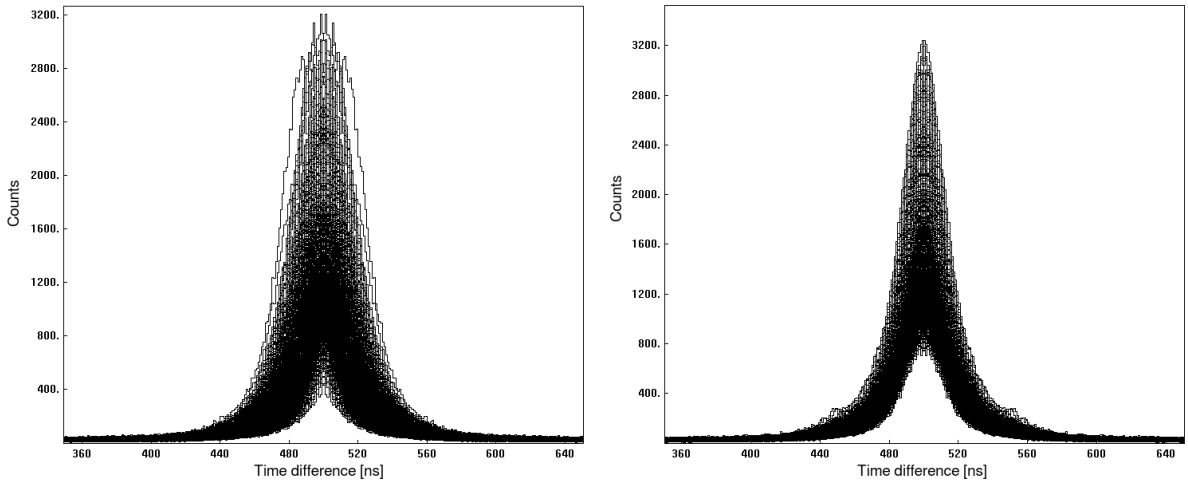

Figure 10.21: The global time alignment: Alignment in time of the signals of every combination of two detectors.

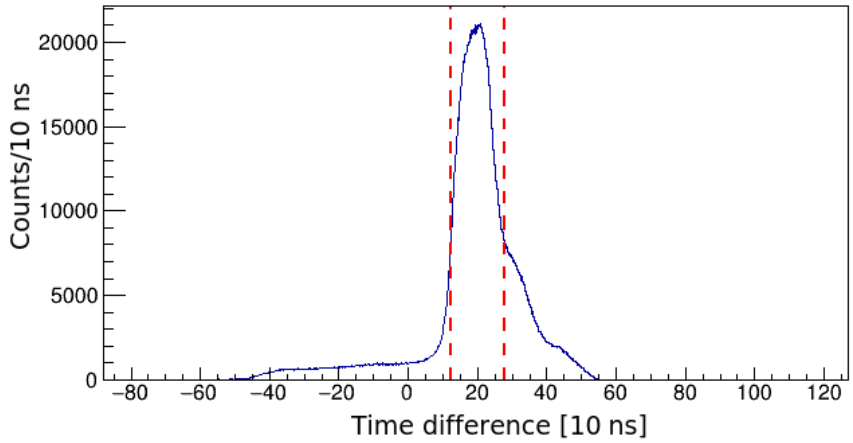

Figure 10.22: The difference between the time stamp of the PRISMA and AGATA events. The time gate set for the coincidence measurements between the two detectors is marked with the red dashed lines.

between these two tendencies has to be found. The efficiencies and the P/T ratio are shown for each case in Fig. 10.23. The best parameters for the tracking are σ_θ=2.0 , P_{track}=0.05 and ClAngRed=0.2.

10.2.3 Efficiency calibration of the array

After the optimization of the array, the characterization in terms of detection efficiency is performed by using a ^{152}Eu source with known activity for different analysis modes:

- Core: the energy spectrum is obtained by the signals of the central contact of each crystal of the array
- Add-back: sum of all the simultaneous hits of neighboring crystals in one single event

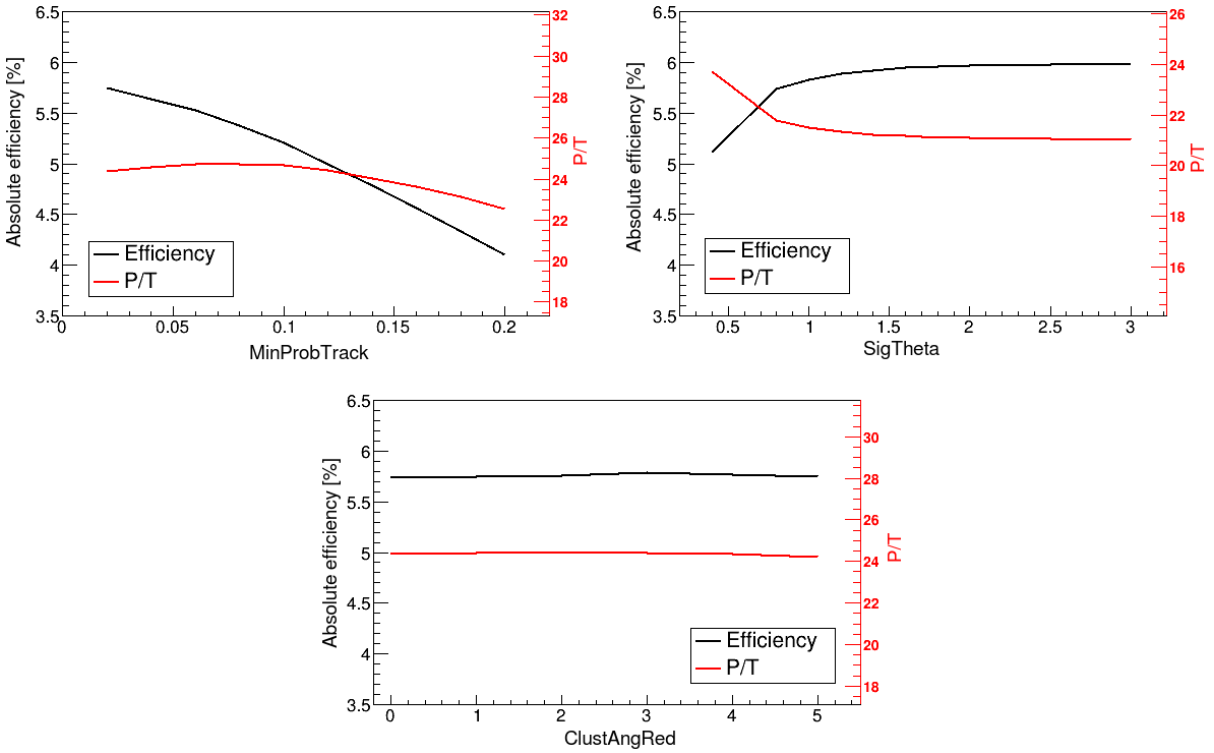

Figure 10.23: Optimization of the tracking parameters. A series of replays of the data are performed by varying one parameter and fixing the two others. The absolute efficiency and the P/T ratio are plotted for each parameter.

- Tracked: energy of the events reconstructed by the tracking algorithm

The absolute efficiency is obtained for each of the modes using the procedure explained in Section 4.1.6. The absolute efficiency of the AGATA array at the close-up position composed of 33 operational crystals is shown in Fig. 10.24 for the core, add-back, and the tracked γ-ray spectra. The add-back is used as a reference for the ideal efficiency of the array and the tracked analysis mode is close to the ideal efficiency for γ rays with energy above 500 keV. Even though the tracking mode provides a better P/T ratio, the add-back mode has been used in the analysis due to its higher efficiency in low energies.

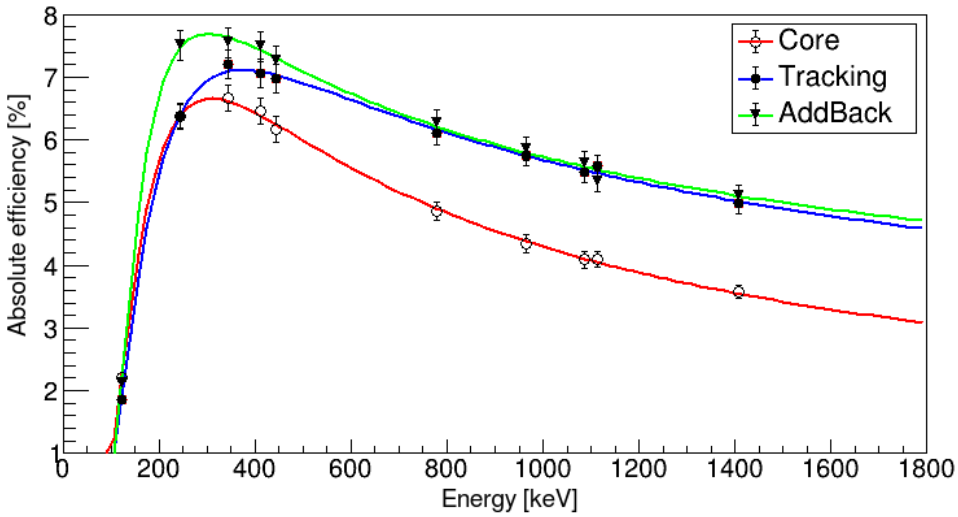

Figure 10.24: The absolute efficiency of the AGATA array in close-up position composed of 33 crystals for: the core, add-back, and the tracked γ-ray spectra. The experimental data points are fitted with Eq. 4.3

Chapter 11

Data analysis and results

Several levels in ^{198}Pt have lifetimes in the range of picoseconds and can be measured with the reversed plunger configuration as demonstrated in this chapter. The γ-ray spectrum measured in coincidence with PRISMA shows both shifted and unshifted components for the $4^+ \rightarrow 2_1^+$, $2_2^+ \rightarrow 2_1^+$, and $2_1^+ \rightarrow 0^+$ transitions. In this chapter, the lifetimes of the 2_1^+, 2_2^+ and 4^+ states of ^{198}Pt are measured using the Decay Curve Method and the Differential Decay Curve Method and compared to the literature data.

11.1 Spectroscopy of the ^{198}Pt nucleus

The identification of the ions in mass and atomic number from the PRISMA spectrometer provides the possibility to identify event-by-event the γ rays that belong to a specific nucleus. The γ-ray spectrum measured in coincidence with PRISMA is shown in Fig. 11.1.a and the one gated on the ions with Z=34 and A=136 is shown in Fig. 11.1.b. Figure 11.1.c shows the Doppler-corrected γ-ray spectrum based on the velocity of the ^{136}Xe ions measured by the PRISMA spectrometer. The peak at 1313 keV, which belongs to the $2^+ \rightarrow 0^+$ transition of ^{136}Xe, stands up clearly in the spectrum. Based on the kinematics of the beam-like fragments (in this case ^{136}Xe), the kinematics of the corresponding binary partner (^{198}Pt) can be reconstructed and used for the Doppler correction of the γ-ray spectrum, shown in Fig. 11.1.d. The γ-ray peaks which belong to transitions of ^{198}Pt are marked in the figure with gray dashed lines. The observed γ-ray transitions of ^{198}Pt are well known and their energies in the literature are the same as the ones measured in this experiment. The intensities of the observed γ-ray transitions of ^{198}Pt relative to the one of the $2^+ \rightarrow 0^+$ are given in Tab. 11.1.

A partial level scheme of ^{198}Pt relevant for our study is shown in Fig. 11.2. The assignment of the spin and parity to the states is based on literature [6]. The width of the γ-ray transitions is proportional to the intensities of each transition, relative to the one of $2^+ \rightarrow 0^+$.

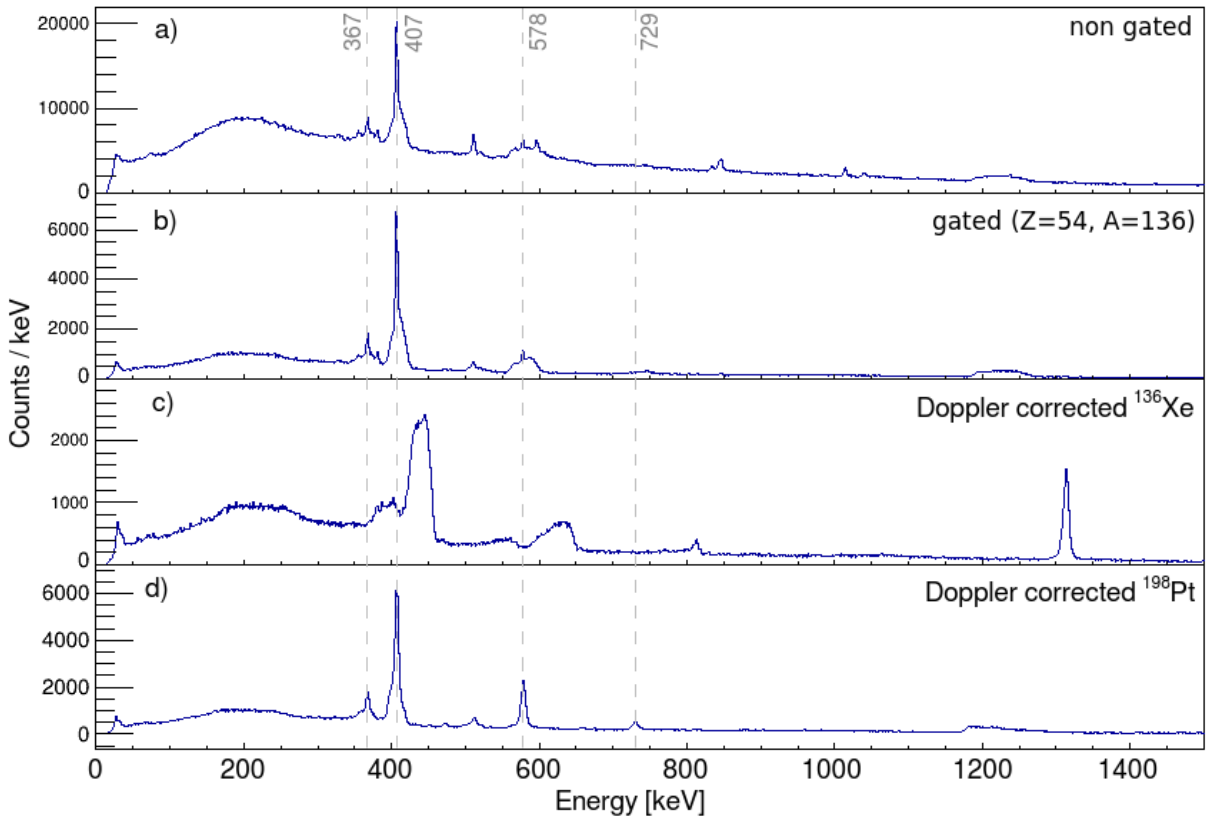

Figure 11.1: a) Gamma-ray spectrum measured by AGATA in coincidence with the PRISMA spectrometer. b) Gamma-ray spectrum in coincidence with the ^{136}Xe ions identified by PRISMA. c) Gated γ-ray spectrum and Doppler corrected event by event based on the kinematics of the ^{136}Xe ions. d) Gated γ-ray spectrum and Doppler corrected event-by-event based on the kinematics of the ^{198}Pt reconstructed using the velocity vector of the ^{136}Xe ions measured by PRISMA. The γ-ray peaks of ^{198}Pt are marked in the figure with the dashed gray lines.

Table 11.1: The intensities of the γ-ray transitions of ^{198}Pt identified in this experiment, relative to the intensity of the $2_1^+ \rightarrow 0^+$ transition.

E_i [keV]	J_i^π	E_f [keV]	J_f^π	E_γ [keV]	I_γ [%]
407	2_1^+	0	0^+	407.0 (11)	100.0 (2)
775	2_2^+	407	2_1^+	367.4 (11)	18.9 (1)
985	4^+	407	2_1^+	578.0 (12)	25.9 (1)
1714	6^+	985	4^+	730.1 (13)	6.8 (1)

11.2 The lineshape matrix of ^{198}Pt

The left panel of Fig. 11.3 shows the sum of the lineshape matrices of ^{198}Pt for all the plunger distances. For the $2_1^+ \rightarrow 0^+$ transition both the shifted and the unshifted components are present in the matrix and the same can be observed for the $2_2^+ \rightarrow 2_1^+$ and for the $4^+ \rightarrow 2_1^+$ transition at 367 keV and 578 keV, respectively. The $6^+ \rightarrow 4^+$ γ-ray transition

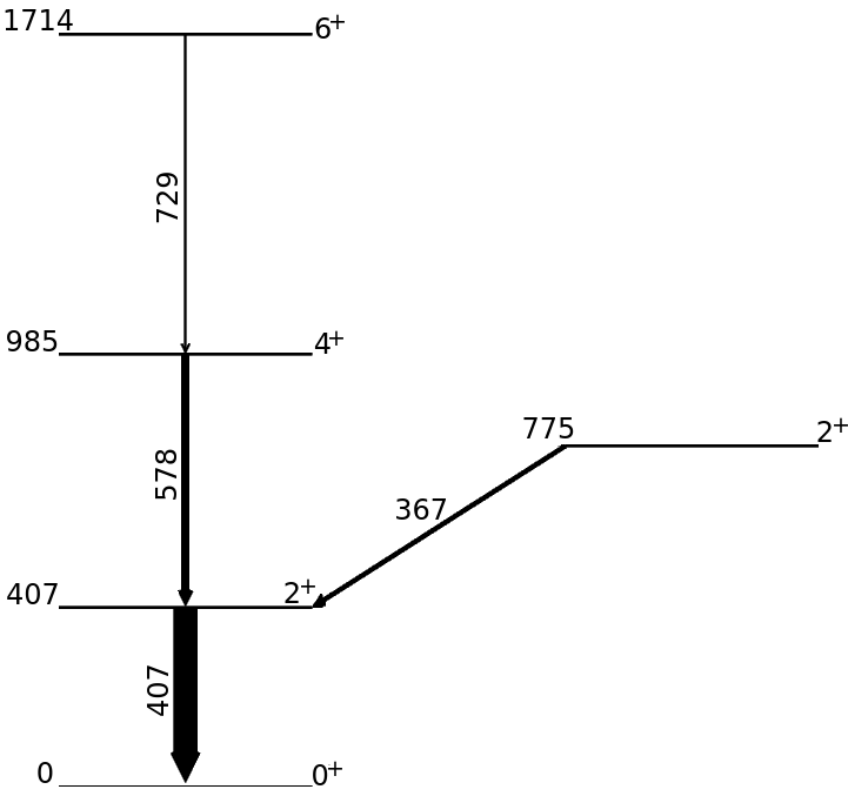

Figure 11.2: Partial level scheme of ^{198}Pt based on the transitions observed in this experiment. The width of the γ-ray transitions is proportional to the measured intensity, relative to the one of the $2_1^+ \rightarrow 0^+$ transition.

with energy 729 keV appears in the matrix only with the shifted component which means that the lifetime of the 6^+ state is too short to be measured by our technique and γ rays depopulating this level are constantly emitted in flight. In fact, the 6^+ state of ^{198}Pt has a lifetime of 0.7 ps [196]. The fact that this transition appears completely shifted in the spectra proves that all the target-like particles escape the target, otherwise, the opposite would impact the measured lifetimes by introducing a systematic error.

Figure 11.3 (Right panel) shows a projection on the energy axis of the matrix for the angles from 20° to 40°. The shifted and the unshifted components for the mentioned transitions are indicated in the figure with the red and blue dashed lines, respectively.

11.3 Velocity determination

The velocity of the ^{198}Pt ions can be obtained by the PRISMA algorithms based on the kinematics of its binary partner (^{136}Xe) or otherwise by the γ-ray spectrum. The derived from the γ-ray spectrum is more precise since, in the case of the identification by PRISMA, the reaction interaction position in the target has to be known precisely. This information is not accessible and typically the interaction position is assumed to be in the middle of the target which may lead to uncertainties since the energy loss of the ions is not properly

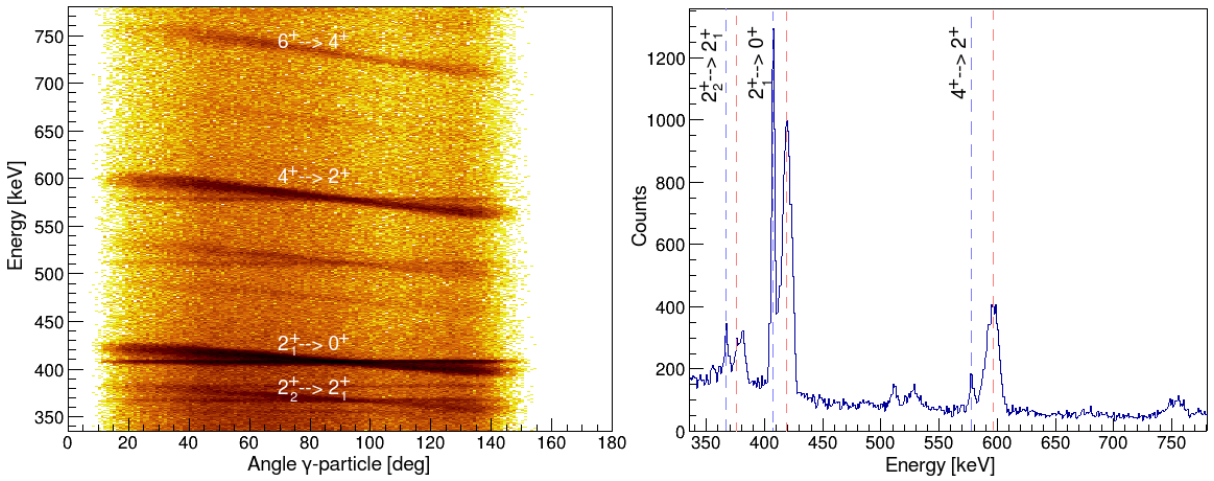

Figure 11.3: (Left) The energy of the γ rays as a function of the angle between the emitting ion and the photon. The matrix is obtained by adding the data from all the plunger distances. Several transitions show shifted and stopped components. The transitions are marked in the figure. (Right) Projection of the matrix on the energy axis for the angles from 20° to 40°. The stopped and the shifted components for the transitions displaying lifetimes in the RDDS range are marked with dashed lines.

evaluated. Instead, the energy splitting of the shifted and the unshifted components of a γ-ray transition can provide better information on the velocity of the recoils from the Doppler Shift formula 3.3.

The lineshape matrix for the $2_1^+ \rightarrow 0^+$ transition at the plunger distance 120 μm is shown in Fig. 11.4 (Left panel). The projection of the matrix on the energy axis at specific angles between the emitting ion and the γ-ray photon is shown in the right panel of Fig. 11.4. The energy of the shifted and the unshifted γ-ray peak at each angle for the 407 keV transition is given in Tab. 11.2 together with the β value calculated from the Doppler Shift formula. The weighted average of the results obtained at different angles gives β=(3.4±0.5)%. This value is used in the analysis to determine the lifetime of the low-lying excited states of ^{198}Pt.

11.4 The distance from target to degrader

In the standard plunger configuration, the ions travel perpendicular to the degrader foil as shown schematically in Fig. 8.1. In this case, the mechanical plunger distance is equal to the path that the ions pass through: from the target to the degrader. In the case of the reversed plunger configuration, due to the geometry of the setup, the ions travel between the two foils at angles different than 90° as shown in the schematic representation in the left panel of Fig. 11.5. The length of the path traveled by the ions, from the target to the degrader, has to be known in order to determine the lifetime of the nuclear-excited states. Based on the drawing in Fig. 11.5 (Left panel), the length of the path traveled by

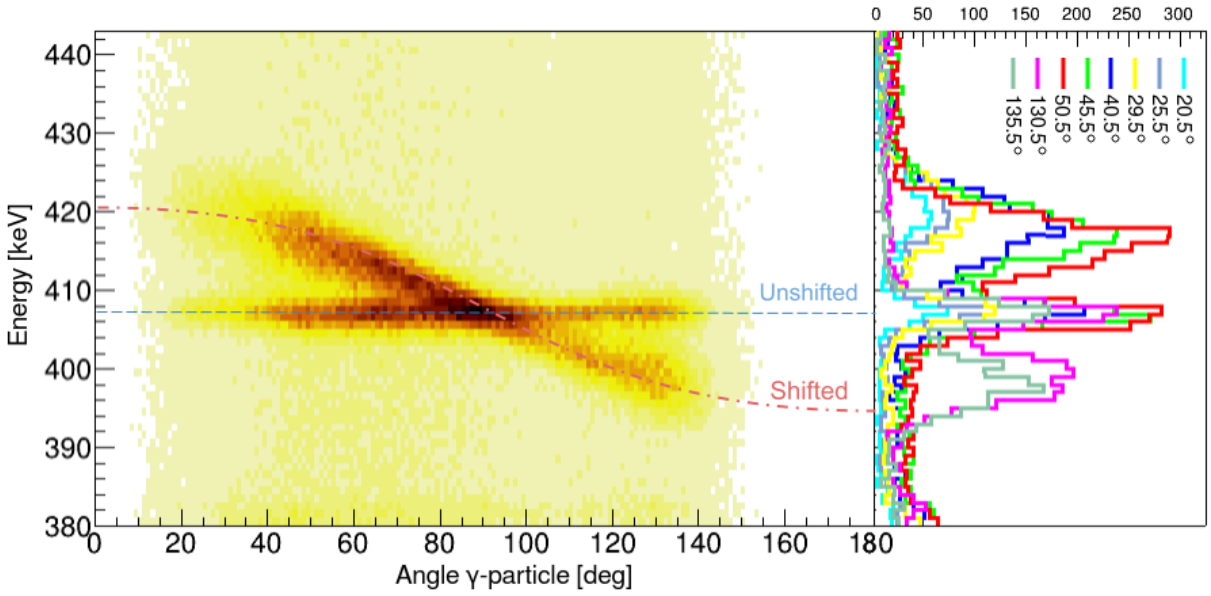

Figure 11.4: The γ-ray energy as a function of the angle between the emitting ion and the photon for the $2_1^+ \rightarrow 0^+$ transition of ^{198}Pt. The projections of the matrix on the energy axis at several angles are shown. The energy difference between the shifted and the unshifted component is used to determine the velocity of the recoils.

Table 11.2: The β value determined from the energy splitting of the shifted and the unshifted components of the $2_1^+ \rightarrow 0^+$ transition of ^{198}Pt taken at several projections on the energy axis of the lineshape matrix of Fig. 11.4. The weighted average of these results obtained independently for each projection gives β=(3.4±0.5)%.

Projection [°]	E_γ [keV]	E'_γ [keV]	β [%]
20.5	407.0±1.3	420.4±3.9	3.5±1.1
25.5	407.4±1.7	419.6±3.4	3.3±1.1
29.5	407.4±1.8	419.5±3.6	3.4±1.2
40.5	407.2±2.1	417.4±3.1	3.3±1.4
45.5	406.7±1.8	416.7±3.3	3.4±1.3
50.5	406.6±1.8	415.6±3.1	3.4±1.2
130.5	407.2±1.5	398.8±3.1	3.2±1.0
135.5	407.1±1.6	397.7±3.0	3.2±1.3

the ions 'D' can be calculated with Eq. 11.1:

$$D = \frac{d}{cos(\theta_{TL} - \alpha)} \tag{11.1}$$

where d is the mechanical plunger distance, θ_{TL} is the angle of the target-like fragments with respect to the beam direction reconstructed by PRISMA based on the detected information of its binary partner, and α is the angle between the beam direction and the target foil (See Fig. 11.5). The ion path length D can be measured event-by-event,

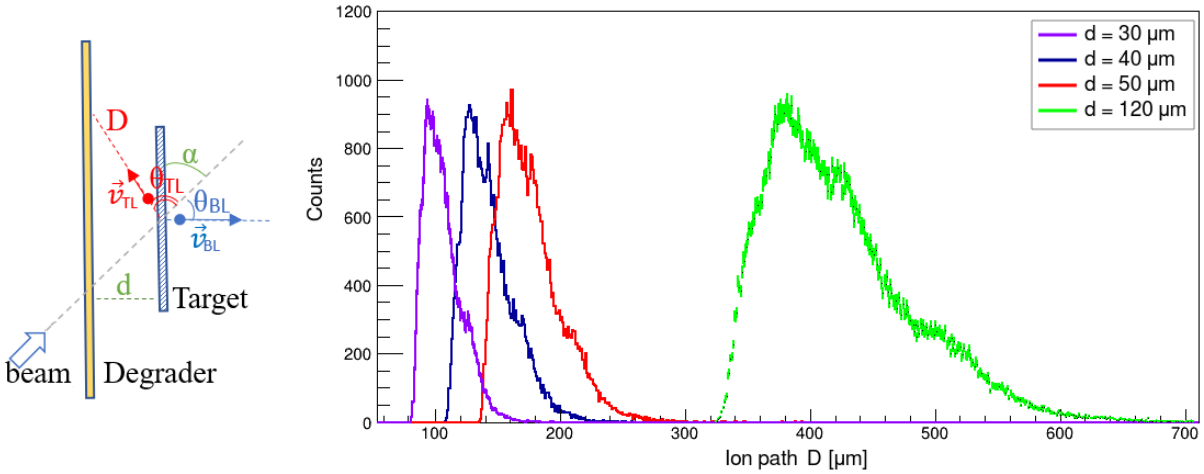

Figure 11.5: The length of the path between the target and the degrader traveled by the ions when using the plunger in the reversed configuration calculated event-by-event.

and the distribution for each mechanical plunger distance can be seen in the left panel of Fig. 11.5.

In a first attempt, we use in the analysis the average value of the ion path length distribution D: 107, 144, 179, and 423 μm. Since the distribution becomes broad, especially at long plunger distances, attempts were made to divide the distances D into smaller ranges and measure the lifetime on each division, and this kind of analysis is shown in Section 11.8.

11.5 Measurement of the half-life of the 2_2^+ state

The second 2^+ state has a lifetime in the time range that can be measured using the plunger technique. From the lineshape matrix of the $2_2^+ \rightarrow 2_1^+$ transition at a plunger distance of 120 μm shown in the left panel of Fig. 11.6, one can observe that the shifted component both at angles smaller and higher than 90° is contaminated by two γ-ray transitions appearing at 356 and 383 keV. These γ rays are emitted at rest, so they affect one part of the distribution of the shifted component of the $2_2^+ \rightarrow 2_1^+$ transition. The projection of the matrix on the energy axis for the angles around 90° is shown in the left panel of Fig. 11.6 where the contaminant γ-ray peaks are marked with an asterisk.

Since the lifetime of the nuclear state is obtained from the intensity of the shifted and unshifted components, the presence of the contaminant peaks would introduce a systematic error on the determined lifetime. To avoid the contribution of the contamination on the shifted component of the $2_2^+ \rightarrow 2_1^+$ transition, the matrix is projected on the energy axis for angles from 40° to 50°. The lineshape matrix of the $2_2^+ \rightarrow 2_1^+$ transition for each plunger distance is shown in Fig. 11.7 (Right panel) and the projection of the matrix on the energy axis for angles from 40° up to 50° is shown in the left panel of Fig. 11.7. As it can be seen in the projected spectra, the contaminant peaks (marked with an as-

terisk) do not influence the shifted component (marked with the red dashed line) of the $2_2^+ \rightarrow 2_1^+$ transition and the intensities of the shifted and unshifted components vary with the distance as expected.

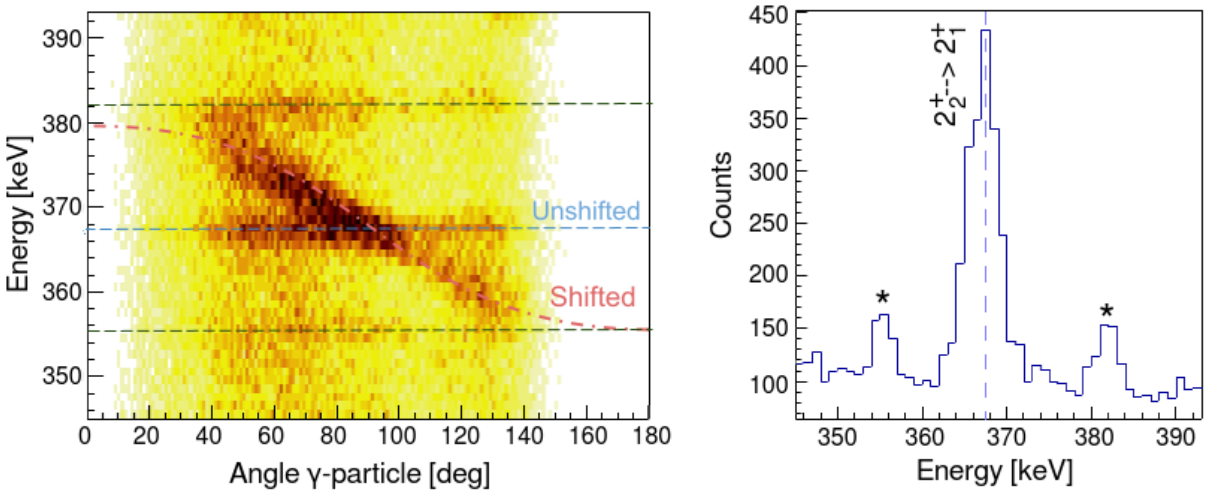

Figure 11.6: (Right) The lineshape matrix for the $2_2^+ \rightarrow 2_1^+$ transition of ^{198}Pt at the plunger distance of 120 μm. The shifted component is contaminated by two γ-ray transitions at 356 and 383 keV. (Left) The projection of the matrix on the energy axis at 90°. The peaks from the contamination are marked with an asterisk in the figure.

To obtain the lifetime of the 2_2^+ state, the data were analyzed using the DCM method which was introduced in Section 5.2.3. Based on the intensities of the shifted and the unshifted components of the projected spectra, the ratio R defined in Eq. 5.3 for each plunger distance is obtained and shown in the right panel of Fig. 11.8. The experimental data points in the plot are fitted using Eq. 5.4 and a half-life of $t_{1/2}$=(30.7±1.1) ps was obtained for the 2_2^+ state. The right panel of Fig. 11.8 shows the same function but on a linear scale in order to draw attention to the error bars.

The analysis was also performed using the DDCM technique which was introduced in Section 5.2.3. Since no direct feeding of the 2_2^+ is observed from other higher-lying states, the half-life for the 2^+ state was obtained using Eq. 5.7. From the DDCM analysis, the half-life of this state results to be $t_{1/2}$=(30.3±0.4) ps (See Fig. 11.9). The lifetime of the 2_2^+ state of ^{198}Pt obtained from our experiment is compared to the literature value in Section 11.9.

11.6 Measurement of the half-life of the 4^+ state

The lifetime of the 4^+ state of ^{198}Pt is also known from the literature as it will be discussed in Chapter 12. The lifetime of this state, which decays via a 578-keV γ ray over the 2_1^+ state, is relatively short and lies at the limits of the lifetimes that can be measured with our technique, thus requesting very short plunger distances. The lineshape matrices for

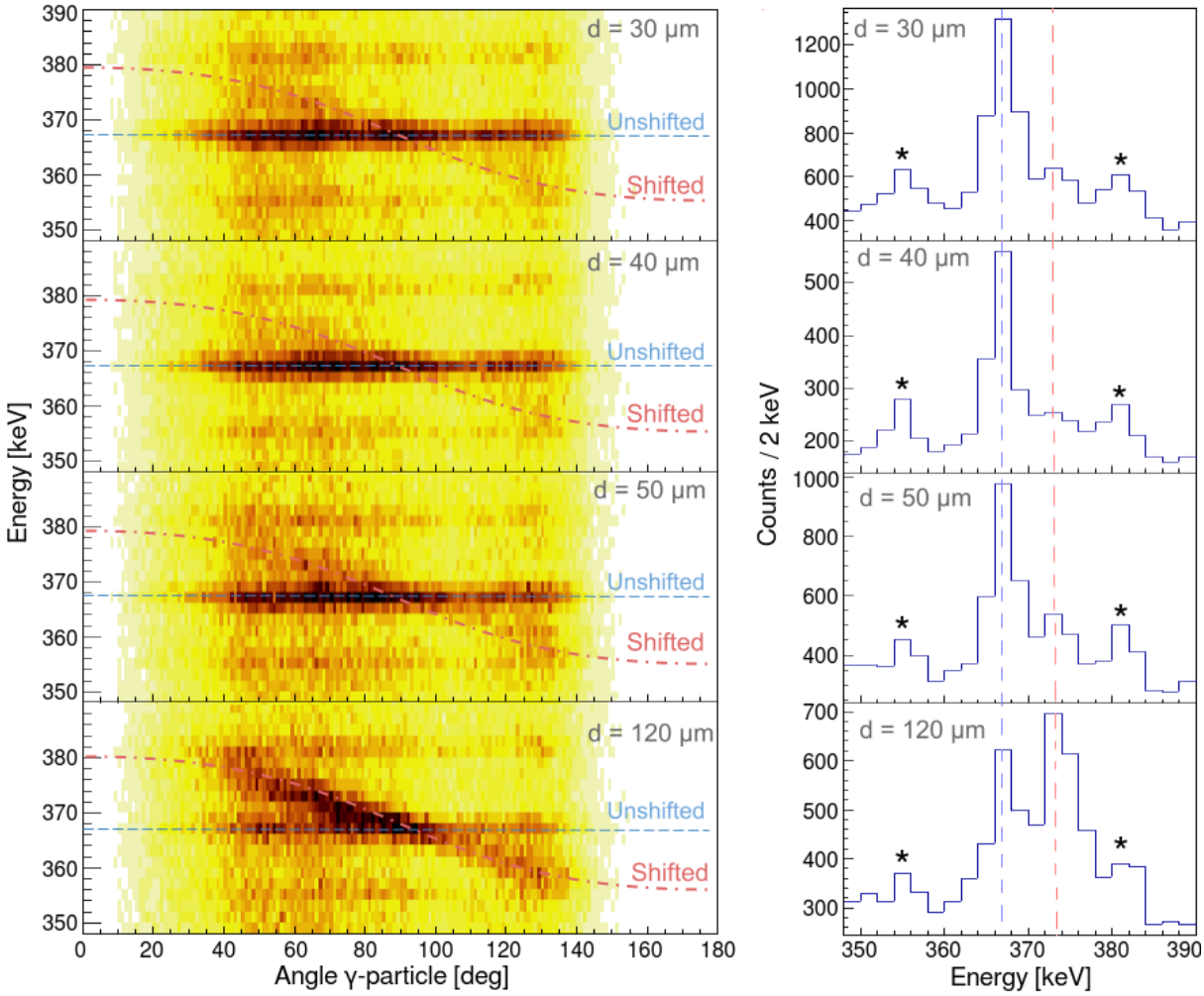

Figure 11.7: (Left) The lineshape matrix for the plunger distance at 30, 40, 50, and 120 μm for the $2_2^+ \rightarrow 2_1^+$ transition of ^{198}Pt. The shifted and the stopped components are marked in the figure. (Right) The projection of the lineshape matrix on the energy axis for the angles 40° to 50° to avoid the two contaminant transitions at 356 and 383 keV. The contaminant peaks are marked with an asterisk.

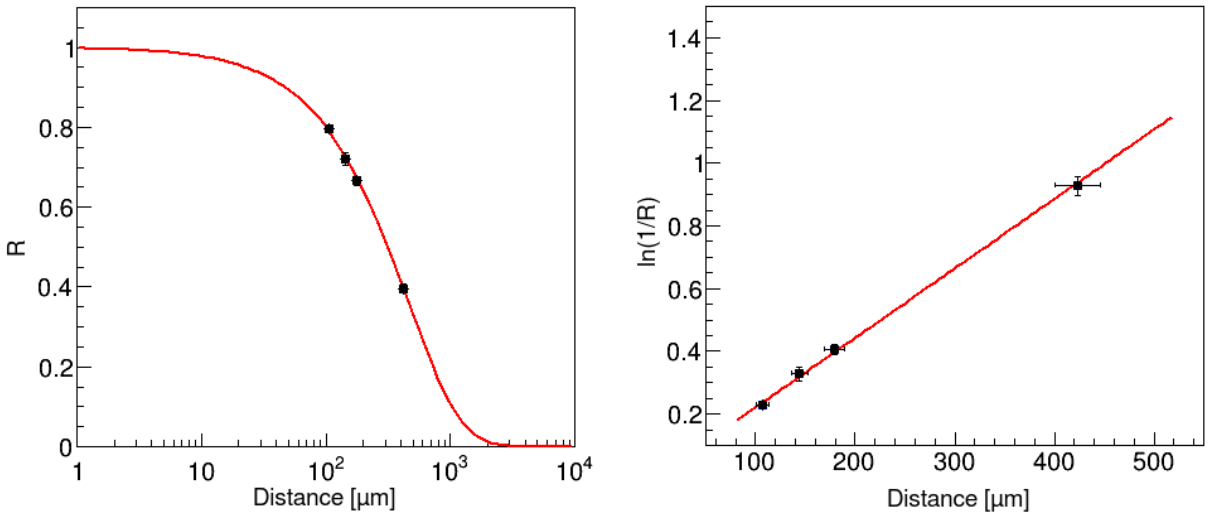

Figure 11.8: (Left) The decay curve of the 2_2^+ state of ^{198}Pt obtained with the DCM analysis based on the intensities of the shifted and the unshifted component. (Right) The logarithmic of the 1/R as a function of the ion path length where the error bars on the experimental points are more visible.

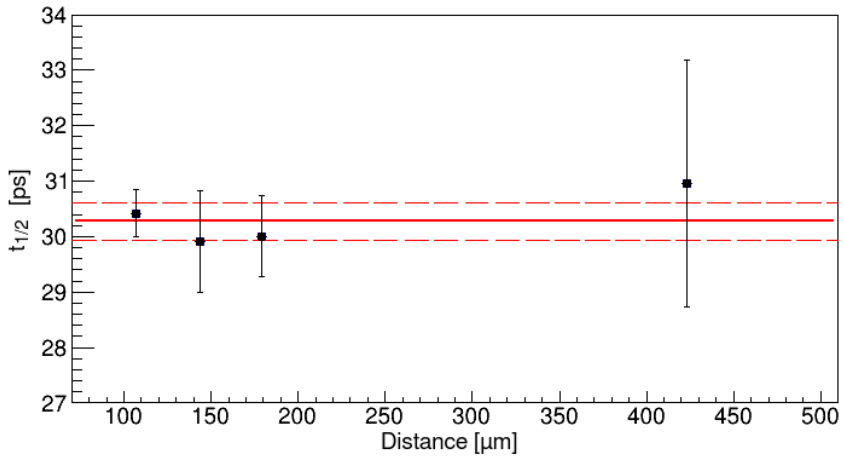

Figure 11.9: The half-life of the 2_2^+ state of ^{198}Pt measured at various distances with the DDCM technique. The fit to the experimental results is shown with the red line and the dashed red line represents the experimental uncertainty at one standard deviation level.

the $4^+ \rightarrow 2^+$ transition for the mechanical plunger distances at 30, 40, and 50 μm are shown in the left panel of Fig. 11.10 and the projection of the matrix on the energy axis at forward angles is shown in the right panel of the same figure.

The lifetime of the 4^+ state of ^{198}Pt is obtained using the same analysis methods as it was done previously for the 2_2^+ state. From the analysis with the DCM, the lifetime of the 4^+ state results to be $t_{1/2}$=(4.7±0.2) ps. The decay curve of this state is shown in Fig. 11.11.

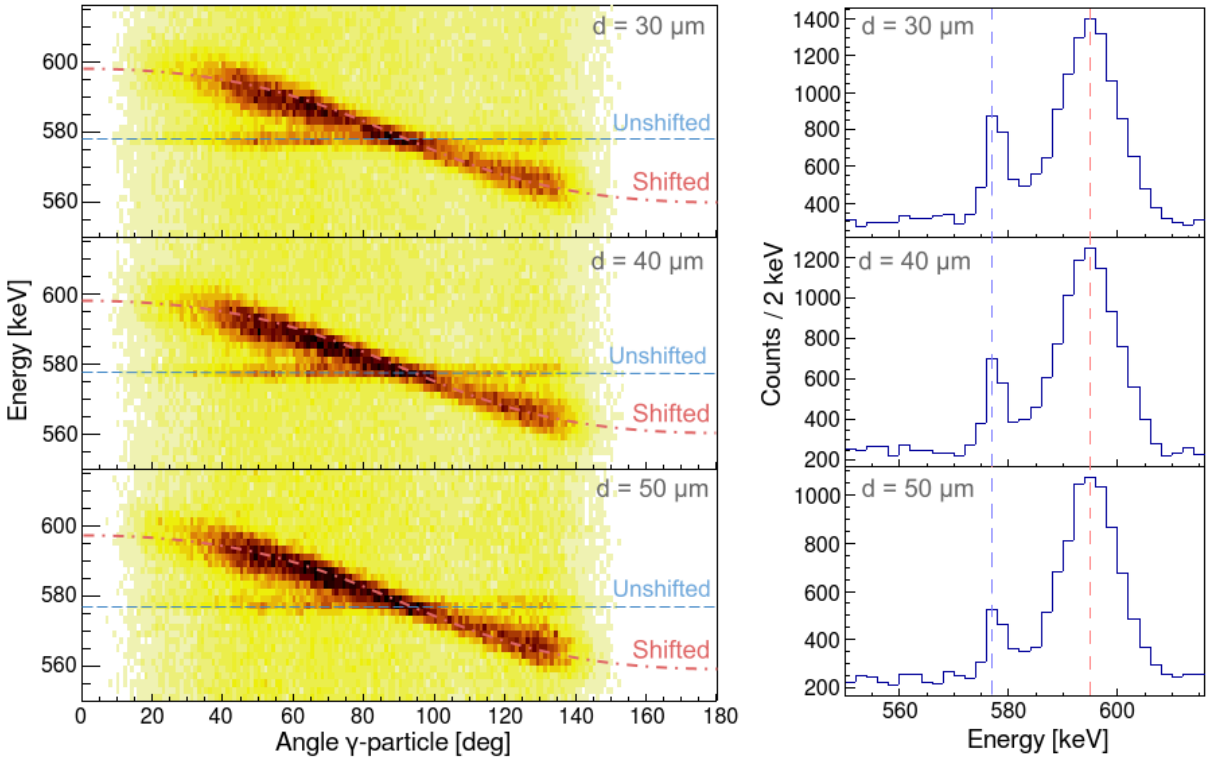

Figure 11.10: (Left) The lineshape matrix for the plunger distance at 30, 40, and 50 μm for the $4^+ \rightarrow 2_1^+$ transition of ^{198}Pt. The shifted and the stopped components are marked in the figure. (Right) The matrix projection on the energy axis for the angles between 0° and 50°. The stopped component is marked in the figure with the dashed line.

From the analysis with the DDCM technique, the lifetime of the 4^+ state results to be: $t_{1/2}$=(4.7±0.4) ps. Figure 11.12 shows the fit to the experimental data. The feeding of the 4^+ state from the short-lived 6^+ state is not taken into account since its contribution is very small. The lifetime obtained from our experiment is compared to the literature value in Section 11.9.

11.7 Measurement of the half-life of the 2_1^+ state

The lineshape matrix for the $2_1^+ \rightarrow 0^+$ γ-ray transition gated in the ions with Z=56 and A=136 is shown for several plunger distances between the target and the degrader in Fig. 11.13 (Left panel) where it is evident that the intensity of the shifted component

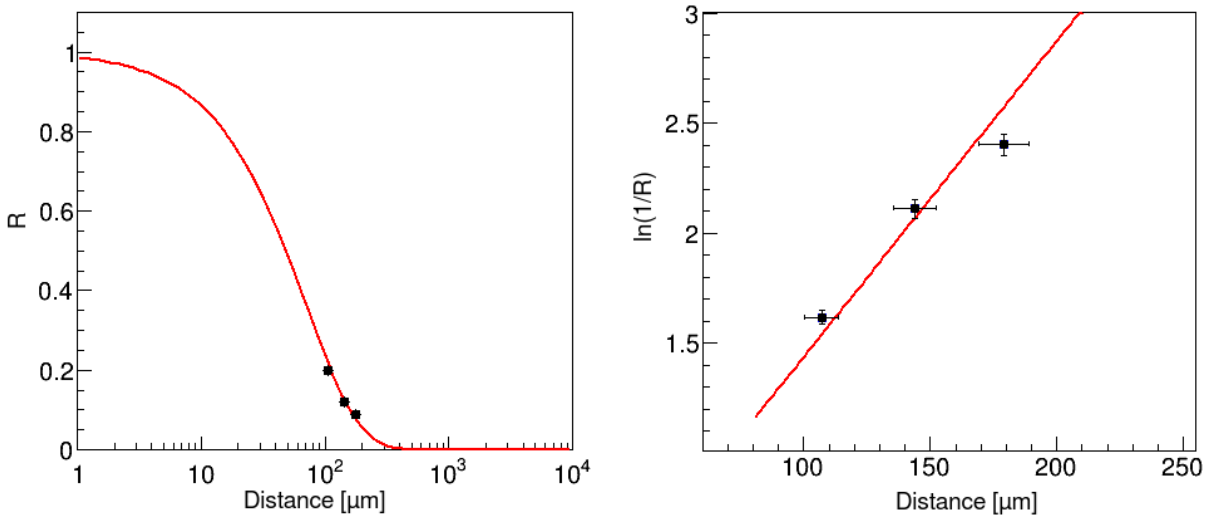

Figure 11.11: (Left) The decay curve of the 4^+ state of ^{198}Pt obtained with the DCM analysis based on the intensities of the shifted and the unshifted component. (Right) The logarithmic of the 1/R as a function of the ion path length D where the error bars on the experimental points are more visible.

increases with the distance. The projection of the matrices on the energy axis from 20° to 40° is shown in Fig. 11.13 (Right panel) where the stopped component with the energy of 407 keV is indicated with the red dashed line. The projection of the matrix is performed for a small angular range at very forward angles since the splitting in energy between the two components is more evident.

For the determination of the lifetime of the 2_1^+ state the direct feeding from the two other higher-lying states, the 2_2^+ and the 4^+ has to be accounted. In Section 5.2.3 the analysis of RDDS data was performed with the DCM method since events that directly populate the level of interest could be selected, but in the case of feeding of the level of interest i from higher-lying levels k, the Bateman equations have to be solved. In general, one would write:

$$\frac{d}{dt}n_i(t) = -\lambda_i \cdot n_i(t) \sum_{k=i+1}^{N} \lambda_k \cdot n_k(t) \cdot b_{ki} \tag{11.2}$$

where λ is the decay constant, b_{kj} the branching rations from levels k to level j and n the number of nuclei in the levels at time t. The solution of the differential equation is given by:

$$R_i(t) = P_i e^{-t\lambda_i} + \sum_{k=i+1}^{N} M_{ki} \left[\frac{\lambda_i}{\lambda_k} e^{-t\lambda_k} - e^{-t\lambda_i} \right] \tag{11.3}$$

where P_j denotes the direct feeding intensity of the level j and M_{ki} is given by:

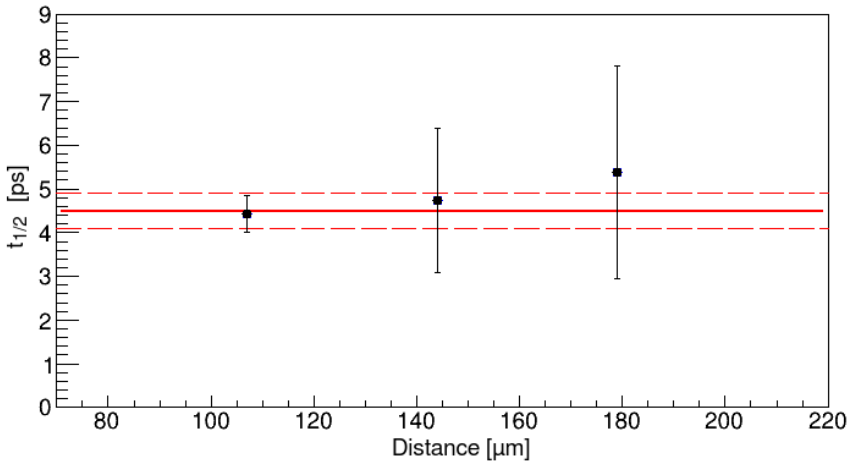

Figure 11.12: The half-life of the 4^+ state of ^{198}Pt measured at various distances with the DDCM technique. The fit to the experimental results is shown with the red line and the dashed red line represents the experimental uncertainty at one standard deviation level.

$$M_{ki}(\lambda_i/\lambda_k - 1) = b_{ki}P_k - b_{ki}\sum_{m=k+1}^{N} M_{mk} + \sum_{m=i+1}^{k-1} M_{km}b_{mi}(\lambda_m/\lambda_k) \tag{11.4}$$

The function $R_i(t)$ is fitted to the experimental data in order to determine the lifetime of the level i. The fit in the case of direct feeding involves a significant number of free parameters like lifetimes, branching rations, and initial populations of the levels involved. To avoid the complexity of such a fitting procedure, the DDCM method is used instead to determine the lifetime of the 2_1^+ state.

In the case of feeding from higher-lying states, the data can be fitted using the function:

$$\tau_i(t) = \frac{-R_i(t) + \sum_k b_{ki}\alpha_{ki}R_k(t)}{\frac{d}{dt}R_i(t)} \tag{11.5}$$

where R_i is the ratio of the counts in the unshifted component with the sum of the counts of the shifted and the unshifted component for the transition i, b_{ki} is the intensity of the $k \rightarrow i$ transition and α_{ki} is determined by the detector efficiencies for the $E_\gamma i$ and $E_\gamma k$ and their angular distribution.

The 2^+ state is fed by two states, the 4^+ with an intensity of 25%, and the second 2^+ state with an intensity of 19%. Taking into account also the respective efficiencies of the γ-ray transitions involved and the Eq. 11.5, one gets the lifetime of the 2_1^+ state. The results for each distance are shown in Fig. 11.14. By fitting with a constant function, the lifetime of the 2_1^+ result to be $t_{1/2}$=(19.3±0.3) ps.

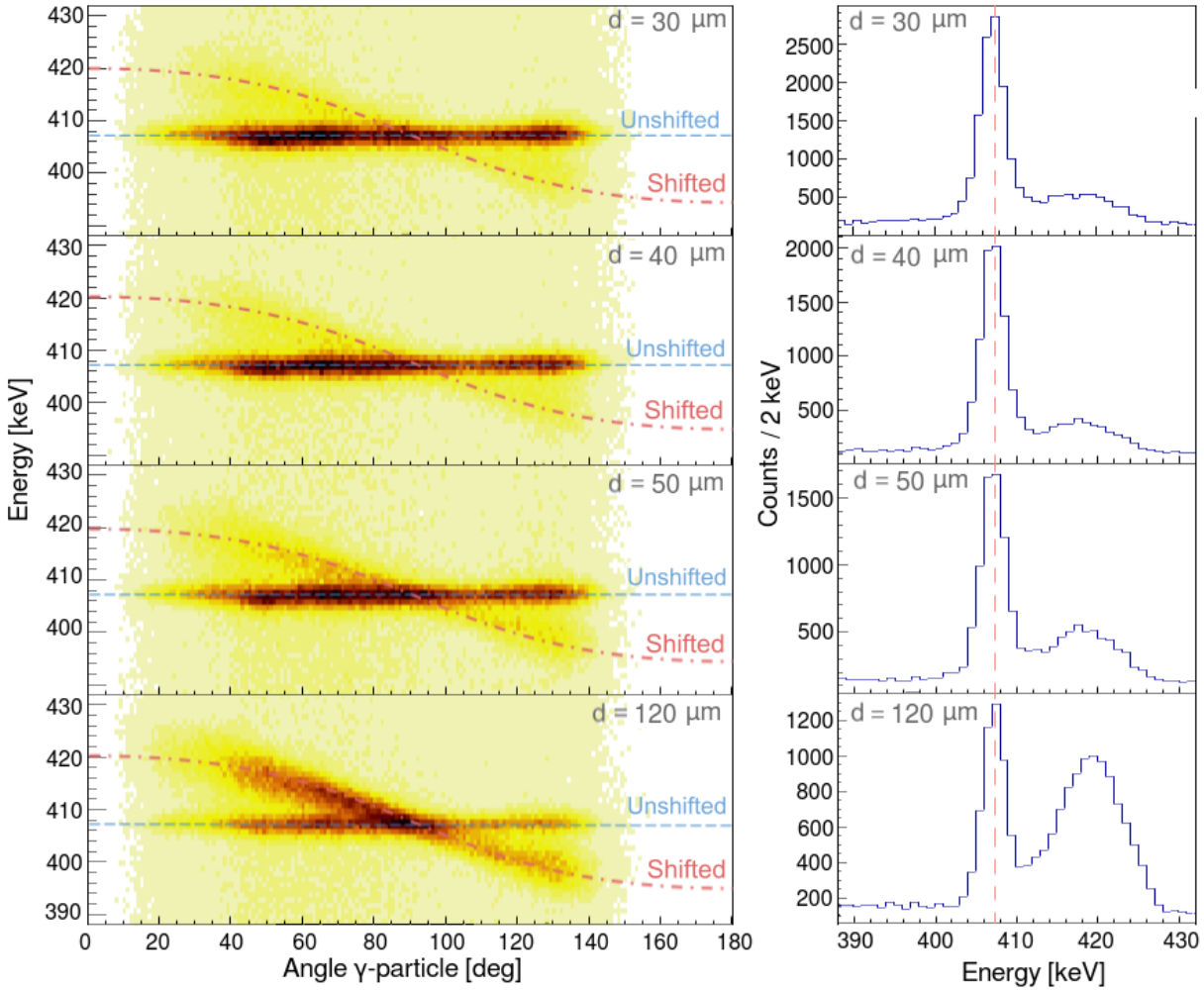

Figure 11.13: (Left) The lineshape matrix of the $2_1^+ \rightarrow 0^+$ transition of ^{198}Pt for different plunger distances. The shifted and the unshifted components are marked in the figure. The two components cross at 90° as expected. The intensity of the two components changes with the distance. (Right) Projection of the matrix in the energy axis for the angles from 20° to 40°. The change in the intensity of the two components with the distance is evident. The stopped component at 407 keV of the 2^+ state of ^{198}Pt is marked with the red dashed line.

11.8 The half-life of the 407-keV 2^+ state with the restriction on the distance

As shown previously, the trajectory of the heavy ion can be reconstructed by the PRISMA spectrometer based on the information of the detected binary partner. This also allowed one to derive event-by-event the length of the path that the ions travel from the target to the degrader, as it was shown in Fig. 11.5. Due to the angular distribution of the target-like and beam-like fragments shown in Fig. 11.15 (Left panel), the ion path length is broad, especially at long mechanical plunger distances, as shown in Fig. 11.15 (Right panel). Thus, it is convenient to group events in smaller ranges and analyze the data with

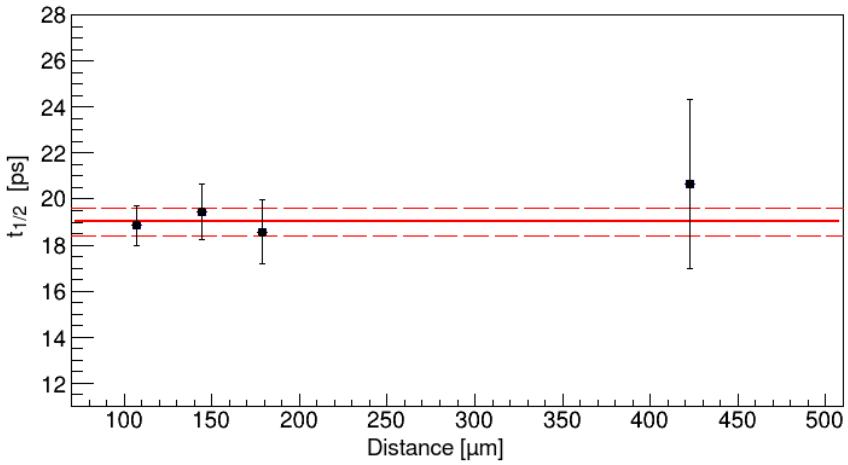

Figure 11.14: The half-life of the 2_1^+ state of ^{198}Pt measured at various distances with the DDCM technique. The fit to the experimental results is shown with the red line and the dashed red line represents the experimental uncertainty to the one standard deviation level.

the aim of obtaining the decay curve of the energy levels of ^{198}Pt that display lifetimes in the sensitive time range accessible from our technique. The total ion path length D distributions is divided into smaller ranges as shown in Fig. 11.15: 80-110, 110-140, 140-170, 170-200, 300-400, and 400-600 μm ranges. Analyzing each of these data sets will provide six data points while the plunger was set at four different mechanical distances. The lineshape matrix is shown for each range of distances in the left panel of Fig. 11.16.

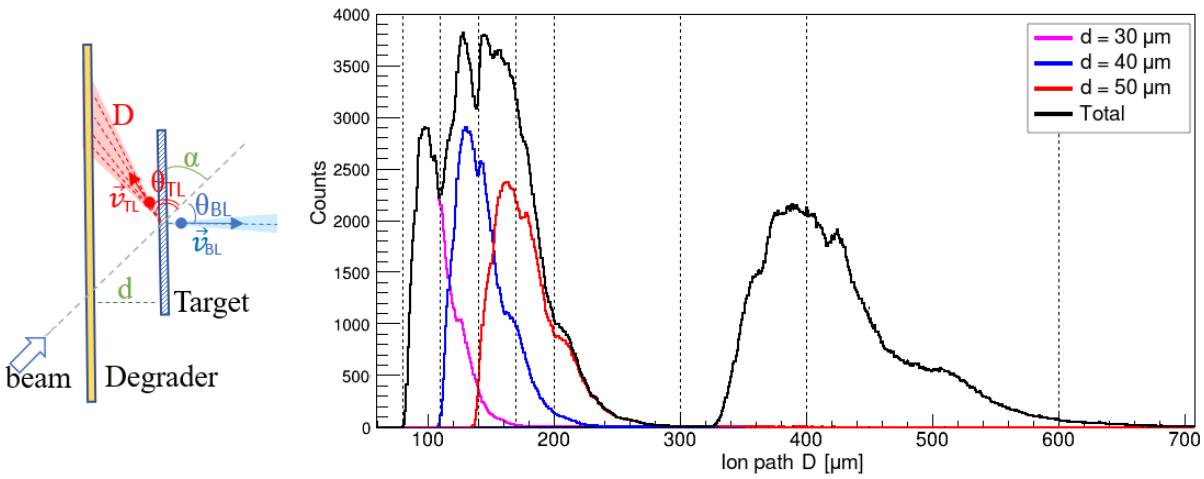

Figure 11.15: The ion path length D calculated event-by-event and the division of the total distribution of all the plunger distances into smaller ranges.

The projected spectra on the energy axis at 0° to 50° are shown in the right panel of Fig. 11.16.

The analysis of the data restricted on the distance is performed in the same way as it has been done so far, using the DDCM techniques. Analyzing with the DDCM technique, one obtains $t_{1/2}$=(18.6±0.5) ps. Fig. 11.17 shows the fit to the experimental data.

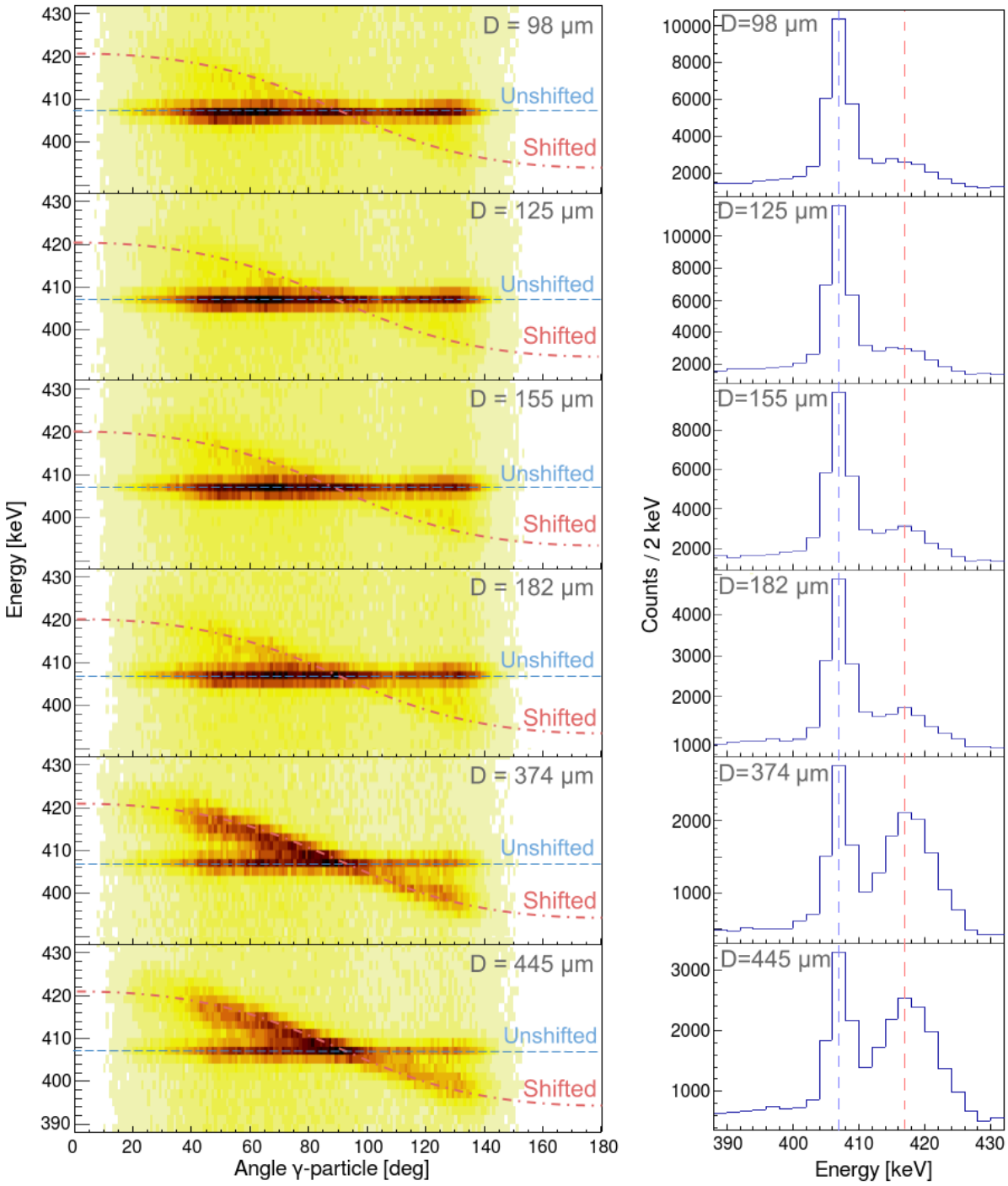

Figure 11.16: (Left) The lineshape matrix of the $2_1^+ \rightarrow 0^+$ transition of ^{198}Pt restricted on the ion path distance. (Right) The projections of the lineshape matrix on the energy axis for the angular range from 0° to 50°. The shifted and the unshifted components are marked with the red and the blue dashed lines, respectively.

It is important to note that the result obtained when restricting on the distance is similar to the previously obtained in Section 11.7 with the DDCM technique. This should demonstrate the possibility of measuring several data points simultaneously with the plunger device fixed at the same position. One drawback is the amount of statistics needed in order to be able to extract information from the data.

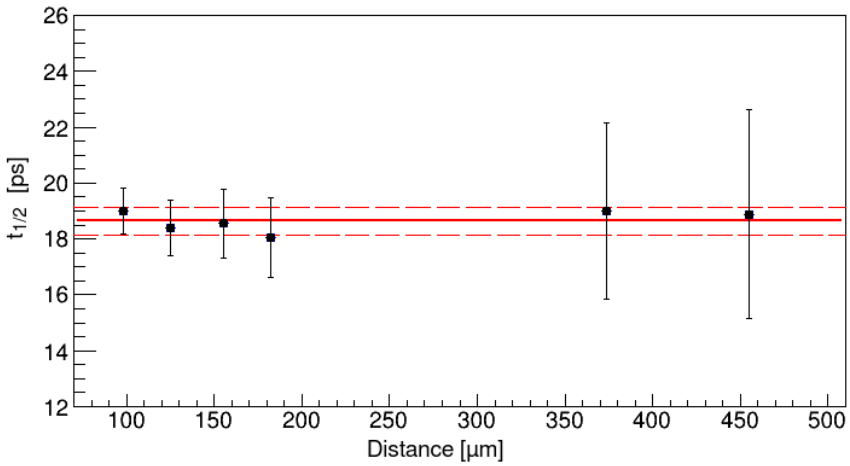

Figure 11.17: The half-life of the 2_1^+ state of ^{198}Pt measured at various distances with the DDCM technique after the division of the ion path length D into smaller ranges. The fit to the experimental results is shown with the red line and the dashed red line represents the experimental uncertainty at one standard deviation level.

11.9 Discussion of the results

The lifetimes of the low-lying excited states of ^{198}Pt are well-known from previous studies. Direct measurements of lifetimes for the states up to 6^+, were performed by using the RDDS technique [196,197] and also indirectly from measured B(E2) values using Coulomb excitation experiments [198–205]. The reported half-lifes of the 2^+ state vary from 16 ps up to 25 ps, with the adopted value 22.25 ps [6]. The half-lifes of the 2_2^+ and 4^+ state are only reported by RDDS measurements, 27 ps and 3.3 ps [196], respectively. Our experimental results are in excellent agreement with the literature values shown in Tab. 11.3.

Therefore, one can conclude, that the reversed plunger configuration, discussed for the first time in this thesis, is successfully working. We have demonstrated in this chapter that with such a setup it is possible to separate the two components (stopped and in flight) of a γ-ray transition depopulating excited states with a lifetime in the picoseconds range. The reversed plunger configuration, coupled with large γ-ray arrays and magnetic spectrometers, will open the possibility to further explore the heavy neutron-rich region of the nuclear chart. Several experiments intend to use this plunger configuration with

Table 11.3: The measured half-lifes of the low-lying excited states of ^{198}Pt using the plunger in the reversed configuration compared with the adopted values from previous studies [6]. Our results were obtained from the DCM, DDCM, and from the analysis with the condition on the ion path length.

E_{lev} [keV]	J_i^π	$t_{1/2}^{DCM}$ [ps]	$t_{1/2}^{DDCM}$ [ps]	$t_{1/2}^{Cond}$ [ps]	$t_{1/2}^{Lit}$ [ps]
407	2_1^+		19.3(3)	18.6(5)	22.25(15)
775	2_2^+	30.7(1.1)	30.3(4)		27(4)
985	4^+	4.7(2)	4.7(4)		3.3(3)

AGATA and PRISMA spectrometers at Laboratori Nazionali di Legnaro to perform lifetime measurements of low-lying excited states of the neutron-rich isotopes such as W and Pb.

Chapter 12

Summary and future perspectives

A new configuration of the plunger has been proposed to access the lifetimes of nuclear-excited states in heavy neutron-rich nuclei, the so-called reversed plunger, working in conjunction with a γ-ray array and a large magnetic spectrometer. Differently from the standard configuration, in the reversed plunger the degrader faces the beam. Taking profit from the kinematics of the multi-nucleon transfer reaction and from the geometrical arrangement of the setup, the beam-like particles enter the magnetic spectrometer while the target-like fragments (the heavy neutron-rich nuclei of interest) travel from the target to the degrader foil. Thus, the situation is similar to the standard plunger configuration where the particles of interest travel with a given velocity from the target foil towards the degrader. The identification of the beam-like fragments from the spectrometer provides the needed channel selectivity event-by-event and the reconstruction of the kinematics of the corresponding target-like fragments.

To test the use of the proposed plunger setup in such a configuration, an experiment was performed at Laboratori Nazionali di Legnaro by coupling the plunger device with the Advanced Gamma-ray Tracking Array - AGATA and the large magnetic spectrometer PRISMA. A beam of ^{136}Xe with energy of 1134 MeV impinged on a ^{198}Pt target with a thickness of 1.4 mg/cm^2 after passing and a degrader of ^{93}Nb with a thickness of 3.2 mg/cm^2. The target and the degrader were mounted in the plunger device and placed in the center of the AGATA reaction chamber tilted by 50° with respect to the beam direction. Measurements were performed at several distances between the target and the degrader: 30, 40, 50, 120, and 370 μm. The aim of this experiment was to measure for the first time the lifetimes of the 2^+ and 4^+ states of ^{196}Os, while the known lifetimes of the low-lying states of ^{198}Pt have been used as a benchmark to validate the use of the plunger device in such a configuration. The lifetime of the energy levels with spin 2_1^+, 2_2^+, 4_1^+ of ^{198}Pt were measured using such setup. The data were analyzed by projecting the line-shape matrix and based on the intensities of the shifted and the unshifted components, the lifetimes of the excited states were derived using the standard analysis techniques: the Decay Curve Method -DCM and the Differential Decay Curve Method - DDCM. The

lifetimes of low-lying states of ^{198}Pt derived from our data are compatible with the values reported in previous studies, thus validating the use of this technique.

As shown in this work the kinematics of the reaction and the geometry of the setup plays an important role in the feasibility of this technique. Besides the reversed plunger also the 'mirror configuration' is proposed here to measure the lifetimes of nuclear-excited states of heavy elements populated via MNT reactions. The use of one or the other has to be evaluated depending on the projectile-target combination and beam energy, which has a direct consequence on the grazing angles of the beam-like and target-like fragments. The configuration that is more suitable for an experiment has to be evaluated based on the kinematics of the reaction and Geant4 simulations to test the quality of the spectra.

The mirror plunger configuration is shown in Fig. 12.1. In this configuration, the plunger is tilted with respect to the beamline at the same angle as the one expected for the trajectory of the target-like fragments, and consequently the particles of interest travel at 90° degrees with respect to the degrader foil. This would allow better control of the length of the path that the ions travel from the target to the degrader, corresponding to the mechanical plunger distance.

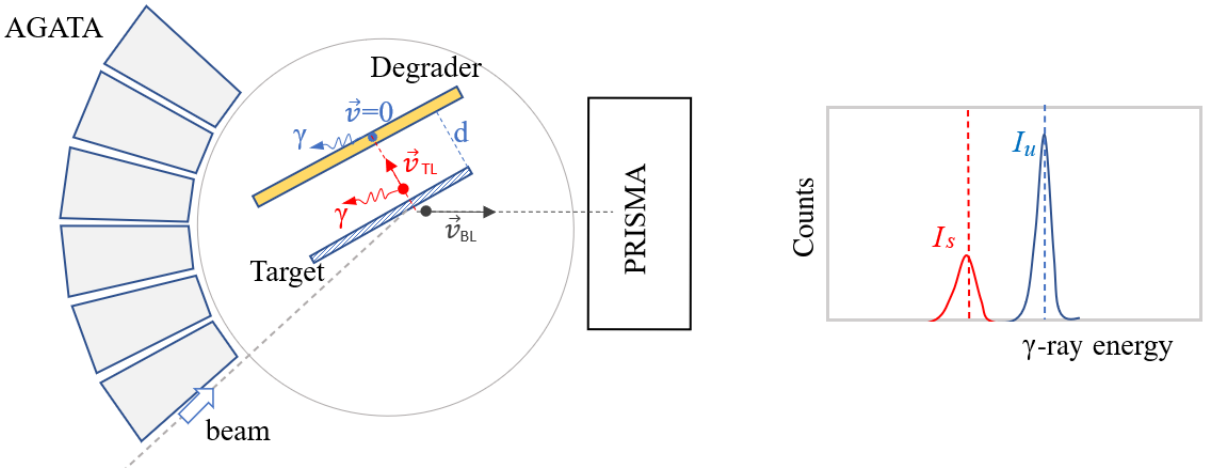

Figure 12.1: (Left) The mirror configuration of the plunger device proposed for measuring lifetimes of nuclear-excited states of heavy neutron-rich nuclei. The target and the degrader are tilted in such a way to allow the beam-like fragments to enter the PRISMA spectrometer and the target-like fragments travel towards the stopper at 90° degrees with respect to its surface. (Right) Schematic representation of the γ-ray spectrum expected to be measured with such a configuration of the plunger. I_s and I_u denote the intensity of the shifted and the unshifted components, respectively.

However, several difficulties may arise by using the mirror configuration of the plunger. First, the energy loss of the beam-like particles in the target may affect their identification from the magnetic spectrometer. In such a configuration of the plunger, the angle between the direction of the beam-like fragments and the normal of the target surface is large, resulting in a significant effective thickness of the target seen by the beam-like fragments. Thus, the thickness of the target has to be chosen in such a way that the en-

ergy loss of the reaction products does not affect their identification by the spectrometer. Secondly, some technical difficulties may arise from the mechanical holding structure of the plunger device itself. The aperture of the cone holding structure and the support of the cone which is around 60° (See Fig. 9.11), may shadow the entrance of the PRISMA spectrometer.

Future prespectives

The possibility of developing a new analysis procedure to investigate data from the reversed plunger configuration needs to be elaborated more in the future. The projection of the lineshape matrix on the energy axis at a certain angular range, and the analysis of this projected γ-ray spectrum using the standard DCM and DDCM method, showed that lifetimes of nuclear-excited states could be extracted from the data and are consistent with literature results. The use of only a part of the information contained in the lineshape matrix employing the previously mentioned analysis methods may be a simplified approach, therefore a more efficient exploitation of the dataset will be considered in the near future.

Stahl et al. proposed the APCAD (Analysis program for the continuous-angle DSAM) to analyze data [206] from DSAM experiments that employ in the setup position-sensitive detector systems like AGATA. Simulations are performed taking into account the geometry of the setup, the angular distribution of the γ rays, the response function of the detectors, the reaction mechanism and the kinematics of the reaction products, the interaction of the ions with the materials (target and degrader), and the decay of the nucleus of interest following complex level schemes. The simulated lineshape matrix, the structure of which depends on the lifetime of the state, is compared with the experimental one and the agreement between the two matrices is quantified in terms of the χ^2 value. The best fit between the simulation and the experimental data provides the lifetime of the state of interest.

A similar analysis technique can be employed in the case of the reversed plunger configuration, where a 2D fit of the lineshape matrix (non-Doppler corrected γ-ray energy versus the angle between the emitting ion and the γ-ray photon) is performed. A three-dimensional plot of the lineshape matrix for the $2_1^+ \rightarrow 0^+$ transition of ^{198}Pt (407 keV) obtained at the mechanical plunger distance 120 μm is shown in Fig 12.2.The geometry of the setup is very well under control thanks to the AGATA simulation package while a few more additional steps would be needed to perform such analysis:

- implement in the simulations the kinematics of the reaction products in the simulations based on the experimental information provided by the PRISMA spectrometers
- add background events on the simulated data described by polynomial functions

- account for the angular distribution of the γ rays
- scale the number of the simulated events based on the number of ions detected from the magnetic spectrometer

The χ^2 can be calculated with the expression:

$$\chi^2 = \sum_{i,j} \frac{E_{ij} \cdot S_{ij}(t)}{E_{ij}} \tag{12.1}$$

where E_{ij} is the number of counts on the energy bin i and angle bin j of the experimental lineshape matrix and $S_{ij}(t)$ is the number of counts in the same i, j bins of the simulated lineshape matrix. The minimization of the χ^2 would provide the best parameter of the fit and consequently the lifetime of the state of interest. The two-dimensional fit was never implemented in any DSAM experimental work employing position-sensitive detectors, even though the APCAD code was developed for such measurements. Typically a one-dimensional fit is applied to the data, regardless of the use of position-sensitive γ-ray detectors, as it was introduced in the first part of the thesis in Section 5.3.2. The data set with the reversed plunger configuration could be a testing ground of such analysis techniques and the gain in terms of statistical uncertainty between the one-dimensional and the two-dimensional fit can be tested.

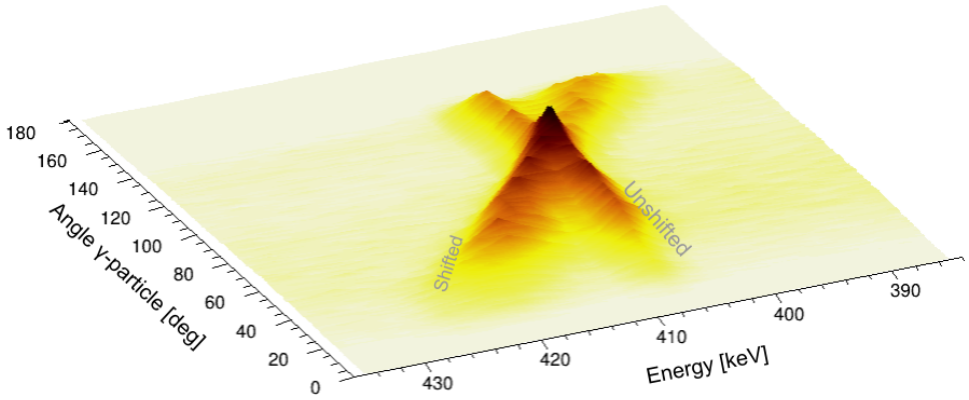

Figure 12.2: Three-dimensional plot of the lineshape matrix for the $2_1^+ \rightarrow 0^+$ transition of ^{198}Pt (407 keV) obtained with the plunger set at a mechanical distance of 120 μm.

When performing measurements with the reversed plunger configuration, additional information is obtained based on the non-Doppler corrected γ-ray energy plotted with respect to the ion path length D at a fixed mechanical plunger distance. Due to the trajectory of the heavy ions from the target to the degrader and the geometry of the setup, the ion path length distribution is large, and the division of this distribution into smaller ranges confirmed that the intensity of the two components is changing. Figure 12.3 shows the non-Doppler corrected γ-ray energy of ^{198}Pt versus the ion-path length D restricted on the angle between the emitting particle and the γ-ray photon (angle$<50°$).

The distribution of the shifted and the unshifted component along the ion path length D depends on the geometry of the setup, the kinematics of the ions, the angular distribution of the γ rays, besides the lifetime of the state. These conditions can be adjusted in the simulation code based on the experimental information, and perform a fit of the simulated data to each pixel of the matrix as explained above. It is still to be understood, if one could perform a multi-parameter fit with the information shown in Fig 12.2 and Fig 12.3.

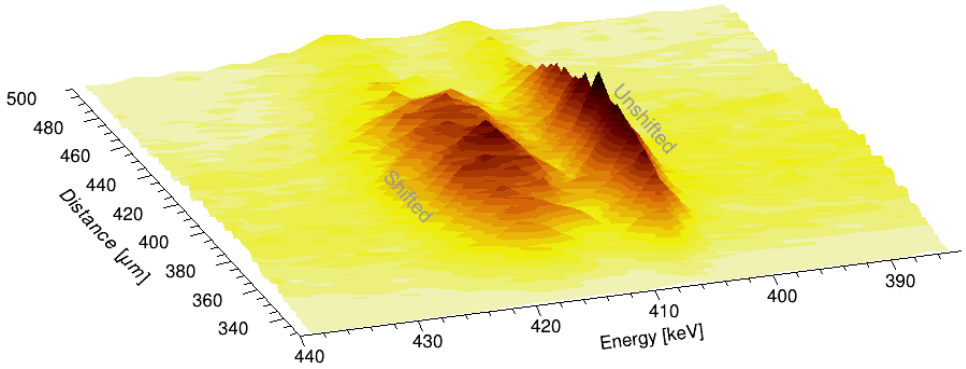

Figure 12.3: Non-Doppler corrected γ-ray energy versus the ion path length D, restricted on the angle between the emitting particle and the γ-ray photon (angle$<50°$), for the plunger mechanical distance 120 μm. The two components of the $2_1^+ \rightarrow 0^+$ transition can be observed in the plot.

The use of the proposed techniques to analyze data from the reversed plunger is foreseen to be explored in the near future, complementing the use of such configuration and maximizing the outcome of such data.

Bibliography

[1] K. S. Krane. *Introductory Nuclear Physics.* John Wiley Sons, 2^{nd} edition (1988).

[2] R. F. Casten. *Nuclear Structure from a Simple Prespective.* Oxford University Pres (2000).

[3] N. Bohr. *Neutron capture and nuclear constitution.* Nature 137, 344–348 (1936).

[4] E. B. Shera et al. *Systematics of nuclear charge distributions in Fe, Co, Ni, Cu, and Zn deduced from muonic x-ray measurements.* Phys. Rev. C 14, 731 (1976).

[5] Sonia Bacca. *Structure models: from shell model to ab-initio methods.* Eur. Phys. J. Plus 131, 107 (2016).

[6] National Nuclear Data Center website.

[7] Maria Geoppert Mayer. *On Closed Shells in Nuclei.II.* Phys. Rev. 75, 1969 (1949).

[8] Otto Haxel, J. Hans D. Jensen, and Hans E. Suess. *On the "Magic Numbers" in Nuclear Structure.* Phys. Rev. 75, 1766 (1949).

[9] S. G. Nilsson. *Binding States of Individual Nucleons in Strongly Deformed Nuclei.* Dan. Mat. Fys. Medd. 29, 16 (1955) pp.1-69.

[10] A. Navin et al. *Direct Evidence for the Breakdown of the N=8 Shell Closure in* ^{12}*Be.* Phys. Rev. Lett. 85, 266 (2000).

[11] C. Détraz et al. *Beta decay of Na and their descendants.* Phys. Rev. C 19, 164 (1978).

[12] T. Motobayashi et al. *Large deformation of the very neutron-rich nucleus* ^{32}*Mg from intermediate-energy Coulomb excitation.* Phys. Lett. B 346 (1995) 9-14.

[13] B. Bastin et al. *Collapse of the N = 28 Shell Closure in* ^{42}*Si.* Phys. Rev. Lett. 99, 022503 (2007).

[14] K. Tshoo et al. *N = 16 Spherical Shell Closure in* ^{24}*O.* Phys. Rev. Lett. 109, 022501 (2012).

[15] T. Otsuka et al. *Magic Numbers in Exotic Nuclei and Spin-Isospin Properties of the NN Interaction.* Phys. Rev. Lett. 87, 082502 (2001).

[16] F. Wienholtz et al. *Masses of exotic calcium isotopes pin down nuclear forces.* Nature, 498 (7454), 346-9 (2013).

[17] D. Steppenbeck et al. *Evidence for a new nuclear "magic number" from the level structure of ^{54}Ca.* Nature 502, 207–210 (2013).

[18] E. K. Warburton, J.A. Becker, and B. A. Brown. *Mass systematics for A=29–44 nuclei: The deformed A∼32 region.* Phys. Rev. C 41, 1147 (1990).

[19] A. P. Zuker. *Monopole, quadrupole, and pairing: a shell model view.* Phys. Scr. 2000 157.

[20] C. Bahri, J. Escher, and J.P. Draayer. *Monopole-pairing and deformation in atomic nuclei.* Nucl. Phys. A 592 (1995) 171-193.

[21] Takaharu Otsuka, Alexandra Gade, Olivier Sorlin, Toshio Suzuki, and Yutaka Utsuno. *Evolution of shell structure in exotic nuclei.* Rev. Mod. Phys. 92, 015002 (2020).

[22] T. Otsuka, T. Suzuki, R. Fujimoto, H. Grawe, and Y. Akaishi. *Evolution of Nuclear Shells due to the Tensor Force.* Phys. Rev. Lett. 95 232502 (2005).

[23] T. Otsuka and Y. Tsunoda. *The role of shell evolution in shape coexistence.* J. Phys. G: Nucl. Part. Phys. 43 024009 (2016).

[24] Yusuke Tsunoda et al. *Novel shape evolution in exotic Ni isotopes and configuration-dependent shell structure.* Phys. Rev. C 89, 031301(R) (2014).

[25] S. Leoni et al. *Revealing microscopic origins of shape coexistence in the Ni isotopic chain.* EPJ Web of Conferences 223, 01032 (2019).

[26] Klaus Blauma. *High-accuracy mass spectrometry with stored ions.* Physics Reports 425 (2006) 1 – 78.

[27] Bernhard Franzke, Hans Geissel, and Gottfried Münzenberg. *Mass and lifetime measurements of exotic nuclei in storage rings.* Mass Spectrometry Reviews 27(5), 428 (2008).

[28] N. K. Glendenning. *Direct Nuclear Reactions.* WORLD SCIENTIFIC (1983).

[29] S. Pain et al. *Structure of ^{12}Be: Intruder d-Wave Strength at N=8.* Phys. Rev. Lett. 96, 032502 (2006).

[30] Zs. Dombrádi et al. *Evolution of the N = 20 shell gap.* J. Phys.: Conf. Ser. 49 140 (2006).

[31] O. Sorlin and M.G. Porquet. *Evolution of the N = 28 shell closure: a test bench for nuclear forces.* Phys. Scr. (2013) 014003.

[32] T. Rzaca-Urban, W. Urban, J.L. Durell, A.G. Smith, and I. Ahmad. *New excited states in ^{82}Ge: Possible weakening of the N = 50 closed shell.* Phys. Rev. C 76, 027302 (2007).

[33] A. Prévost et al. *Medium-spin excitations of the neutron-rich ^{84}Se isotope: Possible decrease in energy of the N = 50 neutron-core excitation.* Eur. Phys. J. A 22, 391–395 (2004).

[34] J. A. Winger et al. *New subshell closure at N = 58 emerging in neutron-rich nuclei beyond ^{78}Ni.* Phys. Rev. C 81, 044303 (2010).

[35] D. Verney et al. *Low-energy states of $^{81}_{31}Ga^{50}$: Proton structure of the nuclei close to ^{78}Ni.* Phys. Rev. C 76, 054312 (2007).

[36] Giacomo de Angelis. *Nuclear Structure far from Stability at LNL: From high intensity stable to radioactive nuclear beams.* Nucl. Phys. A 787 (2007) 74c–83c.

[37] J. Van de Walle et al. *Low-energy Coulomb excitation of neutron-rich zinc isotopes.* Phys. Rev. C 79, 014309 (2009).

[38] P. Delahaye et al. *High-accuracy mass measurements of neutron-rich Kr isotopes.* Phys. Rev. C 74, 034331 (2006).

[39] G. Audi, A. Wapstra, and C. Thibault. *The Ame2003 atomic mass evaluation: (II). Tables, graphs and references.* Nucl. Phys. A 729 (2003) 337.

[40] J. Hakala et al. *Evolution of the N = 50 Shell Gap Energy towards ^{78}Ni.* Phys. Rev. Lett. 101, 052502 (2008).

[41] S. Baruah et al. *Mass Measurements beyond the Major r-Process Waiting Point ^{80}Zn.* Phys. Rev. Lett. 101, 262501 (2008).

[42] Paul E. Garrett, Magda Zielińska, and Emmanuel Clément. *An experimental view on shape coexistence in nuclei.* Prog. Part. Nucl. Phys. 124 (2022) pp.103931.

[43] R.K. Sieja and F. Nowacki. *Three-body forces and persistence of spin-orbit shell gaps in medium-mass nuclei: Toward the doubly magic ^{78}Ni.* Phys. Rev. C 85, 051301(R) (2012).

[44] K. Sieja and F. Nowacki. *Three-body forces and persistence of spin-orbit shell gaps in medium-mass nuclei: Toward the doubly magic* ^{78}*Ni*. Phys. Rev. C 85, 051301(R) (2012).

[45] H. Okuno, N. Fukunishi, and O. Kamigaito. *Progress of RIBF accelerators*. Prog. Theo. and Exp. Phys., 2012 (2012) 03C002.

[46] P. Senger. *The heavy-ion program of the future FAIR facility*. J. Phys.: Conf. Ser. 798 (2016) 012062.

[47] J. Wei et al. *Advances of the FRIB project*. Int. Jour. Mod. Phys. 28, 1930003 (2019).

[48] R. Taniuchi et al. ^{78}*Ni revealed as a doubly magic stronghold against nuclear deformation*. Nature, 569, 53-58 (2019).

[49] K. Heyde and J.L. Wood. *Shape coexistence in atomic nuclei*. Rev. Mod. Phys. 83, 1467 (2011).

[50] J. Bonn, G. Huber, H.J. Kluge, L. Kugler, and E.W. Otten. *Sudden change in the nuclear charge distribution of very light mercury isotopes*. Phys. Lett. B 38, 308 (1972).

[51] J. H. Hamilton et al. *Crossing of Near-Spherical and Deformed Bands in* ^{186,188}*Hg and New Isotopes* ^{186,188}*Tl*. Phys. Rev. Lett. 35, 562 (1975).

[52] A. N. Andreyev et al. *A triplet of differently shaped spin-zero states in the atomic nucleus* ^{186}*Pb*. Nature 405, 430-433 (2000).

[53] J. Bron et al. *Collective bands in even mass Sn isotopes*. Nuc. Phys. A 318(3) (1979) 335-351.

[54] J.L. Wood, E.F. Zganjar, C.D. Coster, and K. Heyde. *Electric monopole transitions from low energy excitations in nuclei*. Nucl. Phys. A 651 (1999) 323.

[55] P. Federman and S. Pittel. *Unified shell-model description of nuclear deformation*. Phys. Rev. C 20, 820 (1979).

[56] J. H. Hamilton et al. *Evidence for Coexistence of Spherical and Deformed Shapes in* ^{72}*Se*. Phys. Rev. Lett. 32, 239 (1974).

[57] R.A. Meyer, O.G. Lien, and E.A. Henry. *Coexisting intruder bands in* ^{83}*Se and evidence for the role of proton subshell closure in inhibiting formation of odd-neutron intruder bands*. Phys. Rev. C 25, 682(R) (1982).

[58] P. Hog and B. Fogelberg. *Properties of strongly Neutron-rich isotopes of germanium and arsenic.* Nucl. Phys. A 368 (1981) 210-236.

[59] S.L. Heller and J.N. Friedman. *Coriolis-coupling model applied to odd-neutron nuclear spectra of the $1g_{9/2}$ shell.* Phys. Rev. C 10, 1509 (1974).

[60] E. K. Lin et al. *Nuclear Structure Studies in the Selenium Isotopes with (d,p) and (d,t) Reactions.* Phys. Rev. 139, B340 (1965).

[61] X. F. Yang et al. *Isomer Shift and Magnetic Moment of the Long-Lived $1/2^+$ Isomer in $^{79}_{30}Zn_{49}$: Signature of Shape Coexistence near ^{78}Ni.* Phys. Rev. Lett. 116, 182502 (2016).

[62] A. Gottardo et al. *First Evidence of Shape Coexistence in the ^{78}Ni Region: Intruder 0_2^+ State in ^{80}Ge.* Phys. Rev. Lett. 116, 182501 (2016).

[63] F.H. Garcia et al. *Absence of Low-Energy Shape Coexistence in ^{80}Ge: The Nonobservation of a Proposed Excited 0_2^+ Level at 639 keV.* Phys. Rev. Lett. 125, 172501 (2020).

[64] C.M. Shand et al. *Shell evolution beyond $Z = 28$ and $N = 50$: Spectroscopy of $^{81,82,83,84}Zn$.* Phys. Lett. B 773 (2017) 492–497.

[65] S. Ahn et al. *Direct neutron capture cross section on ^{80}Ge and probing shape coexistence in neutron-rich nuclei.* Phys. Rev. C 100, 044613 (2019).

[66] P.-A. Söderström et al. *Two-hole structure outside ^{78}Ni: Existence of a μs isomer of ^{76}Co and decay into ^{76}Ni.* Phys. Rev. C 92, 051305(R) (2015).

[67] Luis A. Montestruque et al. *Study of the $^{77,79,81,83}Se$ level structure with the $^{76,78,80,82}Se(d,p)$ reaction.* Nucl. Phys. A 305 (1978) 29-62.

[68] Robert G. Cochran and William W. Pratt. *Radioactive decay of ^{83}Se.* Phys. Rev. 109, 878 (1958).

[69] K.W. Marlow and M.A. Waggoner. *Radioactive decay of ^{83}Se.* Phys. Rev. 163, 1098 (1967).

[70] N. Fotiades et al. *First observation of high-spin states in ^{83}Se.* Phys. Rev. C 74, 034308 (2006).

[71] N. Fotiades et al. *First observation of high-spin states in ^{83}Se.* Phys. Rev. C 74, 034308 (2006).

[72] F. Conca. *Low-spin study of ^{83}Se by neutron-capture reactions and gamma-ray spectroscopy.* Master's thesis, Universitá Degli Studi di Milano (2023).

[73] C. Wraith et al. *Evolution of nuclear structure in neutron-rich odd-Zn isotopes and isomers*. Phys. Lett. B 771 (2017) 385-391.

[74] C. Signorini et al. *The 16 MV Tandem of the Laboratori Nazionali di Legnaro*. Revue de Physique Appliquee 12 (1977) 1361-1367.

[75] C. Müller-Gatermann et al. *A new dedicated plunger device for the GALILEO γ-ray detector array*. Nucl. Instr. and Meth. A 920 (2019) 95-99.

[76] A. Goasduff et al. *The GALILEO γ array at the Legnaro National Laboratories*. Nucl. Instr. and Meth. A 1015 (2021) 165753.

[77] M. Rocchini et al. *SPIDER: A Silicon PIe DEtectoR for low-energy Coulomb-excitation measurements*. Nucl. Instr. and Meth. A 971 (2020) 164030.

[78] P. M. Brewster. *Thermal Neutron Capture Studies in Five Isotopes of Selenium*. PhD thesis, McMaster University (1979).

[79] J.V Kratz, H. Franz, N. Kaffrel, and G. Herrmann. *Gamma-ray emission from $^{80-86}As$ isotopes*. Nucl. Phys. A 250 (1975) 13-37.

[80] N. Fotiades et al. *First observation of high-spin states in ^{83}Se*. Phys. Rev. C 74, 034308 (2006).

[81] M. G. Porquet et al. *High-spin excitations of $^{81,82,83,85}Se$: Competing single-particle and collective structures around $N = 50$*. Eur. Phys. J. A 39, 295-306 (2009).

[82] G. Montagnoli and A.M. Stefanini. *Lecture Notes: Heavy-Ion Reactions*. University of Padova (2022).

[83] I. Thompson. *Nuclear Reactions for Astrophysics: Principles, Calculation, and Applications of Low-Energy Reactions*. Cambridge: Cambridge University Press, (2012).

[84] Fresco website (Coupled Reaction Channels Calculations).

[85] A. Haixia and C. Chonghai. *Global deuteron optical model potential for the energy range up to 183 MeV*. Phys. Rev. C 73, 054605 (2006).

[86] A.J. Koning and J.P. Delaroche. *Local and global nucleon optical models from 1 keV to 200 MeV*. Nucl. Phys. A 713 (2003) 231-310.

[87] M.P. Kuchera, O.B. Tarasov, D. Bazin, B. Sherril, and K.V. Tarasova. *LISE ++ Software Updates and Future Plans*. J. Phys.: Conf. Ser. 664 (2015) 072029.

[88] Lise++ website.

[89] M. Febbraro, D. Walter, S.C. Shadrick, S.D. Pain, K.A. Chipps, C. Thornsberry, and E. Lesser. *Improved technique for preparation of deuterated-polyethylene targets.* Nucl. Instr. and Meth. B 410 (2017) 53-59.

[90] D. Bazzacco et al. *The gamma-ray spectrometer GASP.* Proc. AECL 10613 2, (1992).

[91] F.A. Beck. *EUROBALL: Large γ-ray spectrometers through European collaborations.* Prog. Part. Nucl. Phys. 28 (1992) 443-461.

[92] D. Testov et al. *The 4π highly-efficient light-charged-particle detector EUCLIDES, installed at the GALILEO array for in-beam γ-ray spectroscopy.* Eur. Phys. J. A 55, 47 (2019).

[93] D. Mengoni. *Trace: a highly-segmented Silicon detector for light-charged particles emitted in fusion-evaporation and direct nuclear reactions.* PhD thesis, University of Camerino (2008).

[94] O. Skeppstedt et al. *The EUROBALL neutron wall - design and performance tests of neutron detectors.* Nucl. Instr. and Meth. A 421 (1999) 531–541.

[95] M. Rocchini. *Coulomb excitation of low-lying states in ^{66}Zn with the SPIDER array.* PhD thesis, Universitá Degli Studi di Firenze (2018).

[96] A. Pullia, G. Pascovici, and C. Ur. *A versatile low-noise wide-range charge-sensitive preamplifier for HPGe detectors.* 2012 IEEE Nuclear Science Symposium and Medical Imaging Conference Record (NSS/MIC).

[97] S. Akkoyun et al. *AGATA - Advanced gamma tracking array.* Nucl. Instr. and Meth. A 668 (2012) 26-58.

[98] D. Barrientos et al. *Performance of the fully digital FPGA-based front-end electronics for the GALILEO array.* IEEE Trans. Nucl. Sci. 62, 3134–3139 (2015).

[99] A. Pullia et al. *A 12-Channel 14/16-Bit 100/125-MS/s digitizer with 24-gb/s optical output for AGATA/GALILEO.* Proc. 2012 IEEE Nucl. Sci. Symp. Med. Imag. Conf. Rec., 819–823.

[100] J. Collado. *Contribution to Phase Two of AGATA electronics.* PhD thesis, University of Valencia (2019).

[101] M. Bellato et al. *Sub-nanosecond clock synchronization and trigger management in the nuclear physics experiment AGATA.* JINST 8 P07003 (2013).

[102] I. Deloncle et al. *Fast timing: Lifetime measurements with $LaBr_3$ scintillators.* J. Phys.: Conf. Ser. 205 (2010) 012044.

[103] A. Matta et al. *NPTool: a simulation and analysis framework for low-energy nuclear physics experiments.* J. Phys. G: Nucl. Part. Phys. 43 045113 (2016).

[104] A. Dewald, O. Möller, and P. Petkov. *Developing the Recoil Distance Doppler-Shift technique towards a versatile tool for lifetime measurements of excited nuclear states.* Prog. in Part. and Nucl. Phys. 67 (2012) 786 – 839.

[105] A. Dewald, S. Harissopulos, and P. von Brentano. *The differential plunger and the Differential Decay Curve Method for the analysis of Recoil Distance Doppler-Shift data.* Z. Physik A - Atomic Nuclei 334, 163–175 (1989).

[106] S. Agostinelli et al. *Geant4 – a simulation toolkit.* Nucl. Instr. and Meth. A 506 (2003) 250-303.

[107] E. Farnea et al. *Conceptual design and Monte Carlo simulations of the AGATA array.* Nucl. Instr. and Meth. A 621 (2010) 331–343.

[108] I. Zanon. *Testing three-body forces in light nuclei: Lifetime measurements in ^{20}O in the femtosecond range.* PhD thesis, Universitá Degli Studi di Ferrara (2022).

[109] R. Escudeiro. *Excited states lifetime in the fp-shell mirror nuclei.* PhD thesis, Universitá Degli Studi di Padova (2023).

[110] J. Pellumaj, R. Escudeiro, F. Recchia, and S. Lenzi. *Lifetime measurements for ^{46}Ti and ^{50}Cr using the AGATA spectrometer.* Acta Phys. Pol. B Proc. Suppl. 16, 4-A13 (2023).

[111] J. Pellumaj. *Lifetime measurements for nuclei in the $f_{7/2}$ shell using the AGATA spectrometer.* Master's thesis, Universitá Degli Studi di Padova (2020).

[112] SRIM - The Stopping and Range of Ions in Matter.

[113] C. Michelagnoli. *FIPPS (FIssion Product Prompt γ-ray Spectrometer) and its first experimental campaign.* EPJ Web of Conferences 193, 04009 (2018).

[114] A. Ekström, C. Forssén, G. Hagen, G.R. Jansen, W. Jiang, and T. Papenbrock. *What is ab-initio in nuclear theory?* Front. Phys. 11:1129094 (2023).

[115] E. Caurier, G. Martínez-Pinedo, F. Nowacki, A. Poves, and A.P. Zuker. *The shell model as a unified view of nuclear structure.* Rev. Mod. Phys. 77, 427 (2005).

[116] M. Bender, P.H. Heenen, and P.G. Reinhard. *Self-consistent mean-field models for nuclear structure.* Rev. Mod. Phys. 75, 121 (2003).

[117] Heiko Hergert. *A Guided Tour of Ab-Initio Nuclear Many-Body Theory.* Front. Phys. 8, 379 (2020).

[118] L. M. Robledo et al. *Mean field and beyond description of nuclear structure with the Gogny force: a review.* J. Phys. G: Nucl. Part. Phys. 46 013001 (2019).

[119] Tomás R. Rodríguez and J. Luis Egido. *Triaxial angular momentum projection and configuration mixing calculations with the Gogny force.* Phys. Rev. C 81, 064323 (2010).

[120] Tomás R. Rodríguez, Alfredo Poves, and Frédéric Nowacki. *Occupation numbers of spherical orbits in self-consistent beyond-mean-field methods.* Phys. Rev. C 93, 054316 (2016).

[121] A. Gargano, L. Caroggio, A. Covello, and N. Itaco. *Realistic shell-model calculations and exotic nuclei.* Journal of Physics: Conference Series 527, 012004 (2014).

[122] L. Caroggio, A. Covello, A. Gargano, N. Itaco, and T.T.S. Kuo. *Realistic shell-model calculations and exotic nuclei.* Prog. Part. Nucl. Phys. 62 (2009) 135-182.

[123] B.A. Brown and B.H. Wildenthal. *Status of the Nuclear Shell Model.* Ann. Rev. Nucl.Part.Sci. 38 (1988).

[124] M. Hjorth-Jensen, T.T.S. Kuo, and E. Osnes. *Realistic effective interactions for nuclear systems.* Physics Reports 261 (1995) 125-270.

[125] J.W. Negele and D. Vautherin. *Density-Matrix Expansion for an Effective Nuclear Hamiltonian.* Phys. Rev. C 5, 1472 (1972).

[126] Y.M. Engel, D.M. Brink, K. Goeke, S.J. Krieger, and D. Vautherin. *Time-dependent Hartree-Fock theory with Skyrme's interaction.* Nucl. Phys. A, 249(2) (1975) 215–238.

[127] D.M. Brink and E. Boeker. *Effective interactions for Hartree-Fock calculations.* Nucl. Phys. A 91 (1967) 1-26.

[128] S. Goriely, S. Hilaire, M. Girod, and S. Péru. *First Gogny-Hartree-Fock-Bogoliubov Nuclear Mass Model.* Phys. Rev. Lett. 102, 242501 (2009).

[129] E. E. Caurier, G. Martínez-Pinedo, F. Nowacki, A. Poves, and A.P. Zuker. *The shell model as a unified view of nuclear structure.* Rev. Mod. Phys. 77, 427 (2005).

[130] B. A. Brown et al. *The computer code OXBASH.* MSU-NSCL Report No. 524 (1988).

[131] R. Rodríguez-Guzmán, P. Sarriguren, L.M. Robledo, and S. Perez-Martin. *Charge radii and structural evolution in Sr, Zr, and Mo isotopes.* Phys. Lett. B, 691(4) (2010) 202 – 207.

[132] R. Rodríguez-Guzmán, P. Sarriguren, and L.M. Robledo. *Shape evolution in yttrium and niobium neutron-rich isotopes.* Phys. Rev. C 83, 044307 (2011).

[133] R. Rodríguez-Guzmán, P. Sarriguren, and L.M. Robledo. *Signatures of shape transitions in odd-a neutron-rich rubidium isotopes.* Phys. Rev. C 82, 061302 (2010).

[134] Tomás Rodríguez. *Private communication.*

[135] B. Bally, A. Sánchez-Fernández, and T.R. Rodríguez. *Symmetry-projected variational calculations with the numerical suite TAURUS.* Eur. Phys. J. A (2021) 57: 69 (2021).

[136] F. Nowacki, A. Poves, E. Caurier, and B. Bounthong. *Shape Coexistence in ^{78}Ni as the Portal to the Fifth Island of Inversion.* Phys. Rev. Lett. 117, 272501 (2016).

[137] B. Bally, A. Sánchez-Fernández, and T.R. Rodríguez. *Variational approximations to exact solutions in shell-model valence spaces: Calcium isotopes in the pf shell.* Phys. Rev. C 100, 044308 (2019).

[138] P. Ring and P. Schuck. *The Nuclear Many-Body Problem.* Springer-Verlag (1980).

[139] James J. Griffin and John A. Wheeler. *Collective Motions in Nuclei by the Method of Generator Coordinates.* Phys. Rev. 108, 311 (1957).

[140] T. Marchi et al. *The SPES facility at Legnaro National Laboratories.* J. Phys.: Conf. Ser. 1643 012036 (2020).

[141] G. de Angelis et al. *The SPES Radioactive Ion Beam facility of INFN.* J. Phys.: Conf. Ser. 580 (2015) 012014.

[142] J. J. Valiente Dobón et al. *Conceptual design of the AGATA 2π array at LNL.* Nuc. Instr. and Meth. A 1049 (2023) 168040.

[143] GRIT webpage.

[144] M. Assié et al J.-J. Dormard. *Pulse shape discrimination for GRIT: Beam test of a new integrated charge and current preamplifier coupled with high granularity Silicon detectors.* Nucl. Instr. and Meth. A 1013 (2021) 165641.

[145] R.M. Pérez-Vidal et al. *Nuclear structure advancements with multi-nucleon transfer reactions.* Eur. Phys. J. A (2023) 59:114.

[146] A.M. Stefanini et al. *The heavy-ion magnetic spectrometer PRISMA*. Nucl. Phys. A 701 (2002) 217-221.

[147] S. Szilner et al. *Multinucleon transfer reactions in closed-shell nuclei*. Phys. Rev. C 76, 024604 (2007).

[148] H. Savajols and the VAMOS collaboration. *VAMOS: a VAriable MOde high acceptance spectrometer*. Nucl. Phys. A 654 (1999) 1027c.

[149] M. Rejmund et al. *Performance of the improved larger acceptance spectrometer: VAMOS++*. Nucl. Instr. and Meth. A 646 (2011) 184–191.

[150] F. Cappuzzello, C. Agodi, D. Carbone, and M. Cavallaro. *The MAGNEX spectrometer: Results and perspectives*. Eur. Phys. J. A 52, 167 (2016).

[151] J. Simpson et al. *The EXOGAM array: A radioactive beam gamma-ray spectrometer*. Acta Physica Hungarica, Series A: Heavy Ion. Physics 11, 159 (2000).

[152] A. Gadea et al. *Coupling a CLOVER detector array with the PRISMA magnetic spectrometer*. Eur. Phys. J. A 20, 193-197 (2003).

[153] A. Gadea et al. *Conceptual design and infrastructure for the installation of the first AGATA sub-array at LNL*. Nucl. Instr. and Meth. A 654 (2011) 88.

[154] E. Clémentet et al. *Conceptual design of the AGATA 1π array at GANIL*. Nucl. Instr. and Meth. A 855 (2017) 1-12.

[155] N. Pietralla et al. *On the Road to FAIR: 1st Operation of AGATA in PreSPEC at GSI*. EPJ Web of Conferences 66, 02083 (2014).

[156] M. Siciliano, J.J. Valiente-Dobón, and A. Goasduff. *Nuclear structure in the neutron-deficient Sn nuclei TKEL effects on lifetime measurements*. EPJ: Web Conf. 223, 01060 (2019).

[157] Jose Javier Valiente Dobón et al. *Lifetime Measurements of the Neutron-Rich N=30 Isotones ^{50}Ca and ^{51}Sc: Orbital Dependence of Effective Charges in the fp Shell*. Phys. Rev. Lett. 102, 242502 (2009).

[158] Mengoni.D, J.J Valiente-Dobón, E. Farnea, A. Gadea, A Dewald, A. Latina, and the CLARA-PRISMA Collaboration. *Lifetime measurements of neutron-rich nuclei around ^{48}Ca with the CLARA-PRISMA setup*. Eur. Phys. J. A 42, 387–391 (2009).

[159] E. Sahin et al. *Shell evolution beyond N=40: ^{69,71,73}Cu*. Phys. Rev. C 91, 034302 (2015).

[160] M. Doncel et al. *Determination of lifetimes of nuclear-excited states using the Recoil Distance Doppler Shift Method in combination with magnetic spectrometers.* Eur. Phys. J. A 53, 211 (2017).

[161] M. Siciliano et al. *Pairing-quadrupole interplay in the neutron-deficient tin nuclei: First lifetime measurements of low-lying states in* $^{106,108}Sn$. Phys. Lett. B 806 (2020) 135474.

[162] R.M. Pérez-Vidal et al. *Evidence of Partial Seniority Conservation in the* $\pi g_{9/2}$ *Shell for the N=50 Isotones.* Phys. Rev. Lett. 129, 112501 (2022).

[163] P.R. John et al. *Shape evolution in the neutron-rich osmium isotopes: Prompt* γ*-ray spectroscopy of* ^{196}Os. Phys. Rev. C 90, 021301 (2014).

[164] P.R. John et al. *In-beam* γ*-ray spectroscopy of the neutron-rich platinum isotope* ^{200}Pt *toward the N=126 shell gap.* Phys. Rev. C 95, 064321 (2017).

[165] B. Birkenbach et al. *Spectroscopy of the neutron-rich actinide nucleus* ^{240}U *following multinucleon-transfer reactions.* Phys. Rev. C 92, 044319 (2015).

[166] P. J. R. Mason et al. *Half-life of the yrast* 2^+ *state in* ^{188}W*: Evolution of deformation and collectivity in neutron-rich tungsten isotopes.* Phys. Rev. C 88, 044301 (2013).

[167] P.D. Stevenson, M.P. Brine, Zs. Podolyak, P.H. Regan, P.M. Walker, and J. Rikovska Stone. *Shape evolution in the neutron-rich tungsten region.* Phys. Rev. C 72, 047303 (2005).

[168] J. J. Jolie and A. Linnemann. *Prolate-oblate phase transition in the Hf-Hg mass region.* Phys. Rev. C 68, 031301(R) (2003).

[169] R. Bengtsson, J. Bengtsson, T. Dudek, G. Leander, W. Nazarewicz, and J. Zhang. *Shape coexistence and shape transitions in even-even Pt and Hg isotopes.* Phys. Lett. B 183 (1987), 1-6.

[170] P. D. Stevenson. *Shape evolution in the neutron-rich tungsten region.* Phys. Rev. C 72, 047303 (2005).

[171] H. Mach. *Subshell closure at Z=76 and a uniform* N_pN_n *systematics for the rare-earth region.* Phys. Let. B 185 (1987) 20.

[172] Zs. Podolyák et al. *Isomer spectroscopy of neutron rich* $^{190}W_{116}$. Phys. Let. B 491 (2000) 225-231.

[173] K. Nomura et al. *Spectroscopic calculations of the low-lying structure in exotic Os and W isotopes.* Phys. Rev. C 83, 054303 (2011).

[174] P.R. John. *Study of shape evolution in the neutron-rich osmium isotopes with the advanced gamma-tracking array AGATA*. PhD thesis, University of Padova (2012).

[175] A. Winther. *A Fortran program for estimating reactions in collision between heavy nuclei*. Nucl. Phys. A, 572 (1994) 191-235.

[176] A. Goasduff et al. *Counting rate measurements for lifetime experiments using the RDDS method with the new generation γ-ray array AGATA*. Nucl. Instr. and Meth. A 758 (2014) 1–3.

[177] C. A. Ur. *The Tandem-ALPI-PIAVE accelerator complex of LNL*. AIP Conference Proceedings 1530, 35–43 (2013).

[178] A. Lombardi et al. *The new positive ion injector PIAVE at LNL*. Proceedings of the 1997 Particle Accelerator Conference, Vancouver, BC, Canada, 1129-1131.

[179] G. Bassato et al. *First Operation of PIAVE, the Heavy Ion Injector Based on Superconducting RFQs*. Proceedings of the 2005 Particle Accelerator Conference, Knoxville, TN, USA, 2621-2623.

[180] M. Cavenago et al. *Alice ion source and its high voltage platform*. Rev. Sci. Instr. 71, 758-760 (2000).

[181] G. Fortuna et al. *The ALPI project at the Laboratori Nazionali di Legnaro*. Nucl. Instr. and Meth. A 287 (1990) 253–256.

[182] G. Montagnoli et al. *The large-area micro-channel plate entrance detector of the heavy-ion magnetic spectrometer PRISMA*. Nucl. Instr. and Meth. A 547 (2005) 455–463.

[183] S. Beghini et al. *The focal plane detector of the magnetic spectrometer PRISMA*. Nucl. Instr. and Meth. A 551 (2005) 364-374.

[184] A. Gadea et al. *Conceptual design and infrastructure for the installation of the first AGATA sub-array at LNL*. Nucl. Instr. and Meth. A 654 (2011) 88-96.

[185] A. Boso. *Study of Isospin Symmetry Breaking effects in the A=23 and A=46 multiplets*. PhD thesis, University of Padova (2019).

[186] M. Siciliano et al. *Position uncertainties of AGATA pulse-shape analysis estimated via the bootstrapping method*. Eur. Phys. J. A 57, 64 (2021).

[187] C. Michelagnoli. *The lifetime of the 6.79 MeV state in ^{15}O as a challenge for nuclear astrophysics and γ-ray spectroscopy: a new DSAM measurement with the AGATA Demonstrator array*. PhD thesis, University of Padova (2019).

[188] D. Bazzacco et al. *AGATA, Technical Proposal for an Advanced Gamma Tracking Array for the European Gamma Spectroscopy Community.* HAL open science 87 (1991).

[189] A. Gottardo and J.J. Valiente-Dobón. *Performance of the DANTE detector.* Nucl. Phys. A 805 (2008) 606-608.

[190] A. Giaz et al. *Characterization of large volume 3.5"'×8"' LaBr3:Ce detectors.* Nucl. Instr. and Meth. A 729 (2013) 910–921.

[191] R.M. Pérez-Vidal. *Collectivity along N=50: Nuclear Structure studies on the neutron-magic nuclei ^{92}Mo and ^{94}Ru with AGATA and VAMOS++.* PhD thesis, University of Valencia (2019).

[192] AGATA softwares and user guide website.

[193] F. C. L. Crespi et al. *A pulse shape analysis algorithm for HPGe detectors.* Nucl. Instr. and Meth. A 570 (2007) 459-466.

[194] B. Bruyneel et al. *Correction for hole trapping in AGATA detectors using pulse shape analysis.* Eur. Phys. J. A 49, 61 (2013).

[195] A. López-Martens, A. Hauschild, K. Korichi, J. Roccaz, and J.P. Thibaud. *γ-ray tracking algorithms: a comparison.* Nucl. Instr. and Meth. A 533 (2004) 454–466.

[196] H.H. Bolotin, A.E. Stuchbery, I. Morrison, D.L. Kennedy, C.G. Ryan, and S.H. Sie. *Lifetimes of excited states in ^{196,198}Pt; Applications of Interacting Boson Approximation Model to even Pt isotopes systematics.* Nucl. Phys. A 370 (1981) 146.

[197] D.L. Kennedy, A.E. Stuchbery, and H.H. Bolotin. *The extraction of lifetimes of weakly-populated nuclear levels in Recoil Distance Method experiments.* Nucl. Instr. and Meth. A 171 (1980) 361-367.

[198] G.J. Gyapong, R.H. Spear, M.T. Esat, M.P. Fewell, A.M. Baxter, and S.M. Burnett. *Electric quadrupole moments of the first excited states of ^{194}Pt, ^{196}Pt and ^{198}Pt.* Nucl. Phys. A 458 (1986) 165-187.

[199] S.J. Mundy, J. Lukasiak, and W.R. Phillips. *The spin(6) scheme and electromagnetic transitions in ^{191}Ir and ^{193}Ir.* Nucl. Phys. A 426 (1984) 144-162.

[200] F. Todd Baker, Alan Scott, T.H. Kruse, W. Hartwig, E. Ventura, and W. Savin. *Nuclear shapes of the transitional nuclei ^{194,196,198}Pt.* Nucl. Phys. A 266 (1976) 337-345.

[201] W.T. Milner, F.K. McGowan, R.L. Robinson, P.H. Stelson, and R.O. Sayer. *Coulomb excitation of* $^{182,184,186}W$, $^{186,188,190,192}Os$ *and* $^{192,194,196,198}Pt$ *with protons,* ^{4}He *and* ^{16}O *ions.* Nucl. Phys. A 177 (1971) 1-32.

[202] E.J. Bruton, J.A. Cameron, A.W. Gibb, D.B. Kenyon, and L Keszthelyi. *Coulomb excitation of Pt nuclei.* Nucl. Phys. A 152 (1970) 495-502.

[203] J.E. Glenn, R.J. Pryor, and J.X. Saladin. *Measurement of the Static Quadrupole Moments of the First* 2^{+} *States of* ^{194}Pt, ^{196}Pt, *and* ^{198}Pt. Phys. Rev. 188, 1905 (1969).

[204] L. L. Grodzins, R.R. Borchers, and G.B. Hagemann. *Coulomb excitation in the platinium isotopes.* Nucl. Phys. 88 (1966) 474-480.

[205] P.H. Stelson and F.K. McGowan. *Gamma-Ray Yields from Coulomb Excitation.* Phys. Rev. 99, 112 (1955).

[206] Christian Stahl, Jörg Leske, Marc Lettmann, and Norbert Pietralla. *APCAD - Analysis program for the continous-angle DSAM.* Computer Physics Communications 214 (2017) 174-198.